Department of Physics and Astronomy, University of Canterbury,
Private Bag 4800, Christchurch, New Zealand

Radioluminescence of $NaMgF_3$ Characterisation for Radiotherapy Dosimetry

Jethro Donaldson

A thesis submitted in partial fulfilment of the requirements for the degree of
Doctor of Philosophy in Medical Physics

Supervisor: Dr. Michael Reid
Co-supervisor: Dr. Grant Williams

Abstract

This study seeks to evaluate doped synthetic $NaMgF_3$ as a luminescence material for applications in radiotherapy dosimetry. Two largely independent investigations were undertaken: a basic radiotherapy characterisation of a pre-existing prototype system incorporating $NaMgF_3$ activated with europium and manganese, and the fundamental characterisation of infrared emitting species in the same crystal host.

During the radiotherapy characterisation it was found that the tested system was in many regards unsuitable for use in radiotherapy, suffering from radiation damage, stem effects, and statistical uncertainty imposed by optical inefficiency. Radiation damage effects were found to be predominantly caused by radiation induced F–centres in $NaMgF_3$, while stem effects were dominated by Čerenkov radiation as seen in other fibre coupled systems at megavoltage x-ray energies. It was identified that both of these difficulties could be substantially mitigated by exploiting luminescence at near infrared rather than visible wavelengths, spurring the subsequent investigation into infrared emitters.

A range of rare earth and transition metal dopants were then investigated in the same crystal host, of which divalent nickel was identified as the most promising. With this dopant a broad emission band occurs in the region of 1600 nm, at which wavelength the Čerenkov stem effect is theoretically reduced by at least an order of magnitude with respect to that detected in the near ultraviolet with a europium dopant. No colour centre absorptions were observed in undoped $NaMgF_3$ beyond 1000 nm, and the radiation damage effects measured with the nickel dopant are correspondingly negligible, on the order of 10^{-6} sensitivity loss per Gy of absorbed dose.

Samarium was also identified as a dopant with potential for dosimetry applications. Line emissions were observed from both divalent and trivalent ions, each with markedly different evolution of intensity with absorbed dose. In principle, tracking of total absorbed dose is possible by monitoring the intensity of each, although this is likely to be complicated by the radiation induced F–centre absorptions. The manganese dopant remains of interest as it provides relatively high sensitivity for a low atomic number, while activation with europium yields an efficient phosphor which may have applications in reusable planar dosimeters. The near ultraviolet emission of the latter is detected against both a larger background of Čerenkov radiation and the F–band absorption in $NaMgF_3$, rendering it unsuitable for real-time fibre coupled dosimetry.

Engineering refinements to facilitate infrared luminescence and improve optical efficiency of the prototype dosimetry system are also reported.

Acknowledgements

Like any doctorate project, this work would not have been possible without the professional and personal support I have received from a wide range of people. I cannot hope to mention them all here by name, but would like to acknowledge those whose contributions have been most valuable.

First and foremost, my gratitude goes to my co-supervisor Dr Grant Williams for encouraging me to further develop my MSc project into this work, providing day-to-day guidance, and for tolerating my initial ignorance of solid state and luminescence physics. Similarly, I would like to thank the remainder of my past and present supervisory team, Dr Michael Reid, Dr Jürgen Meyer, and Lynne Greig, for their various contributions to this work. In particular, my thanks go to the Wellington Blood and Cancer Centre chief physicist Lynne Greig for facilitating both access to irradiating equipment at Wellington Regional Hospital and doctoral research concurrent with clinical training.

At Victoria University of Wellington, where much of this project played out, I would like to thank Professor Andy Edgar for his seasoned and often timely scientific advice and assistance with laboratory work, and also past PhD students Christin Gädkte, Nicola Winch, and Stefaan Janssens, for assistance with equipment and measurements at Victoria University and Callaghan Innovation. I would also like to thank Evelyn Bauer of the Malaghan Institute for Medical Research for performing irradiations as part of radiation damage study, which would have otherwise been impractical if not impossible.

Engineering support for the fibre optic dosimeter prototype, across the various upgrades and breakdowns, was kindly provided by Sebastiampillai Raymond of Callaghan Innovation, without whom the radiotherapy characterisation aspects of this research would not have been possible. In addition, the eventual redevelopment of this system would never have left the drawing board without the ongoing support of Rodney Brown of the SCPS electronic workshop, Nick Grinter and Manu Pouajen-Blakiston of the SCPS mechanical workshop, and Don Peat of i2M Labs.

Finally, special thanks are due to my partner, friends, and family for putting up with me during the years spanned by this project, and for their invaluable assistance in proofing what follows.

Some aspects of this work have been funded by grants from the Ministry of Business, Innovation and Employment and its previous incarnation, the Ministry of Science and Innovation.

Contents

List of Figures

List of Tables

Chapter 1

Introduction

The study of luminescence phenomena dates back to at least 1664, when the emission of light from diamond under the application of heat was first reported by Sir Robert Boyle.[1] Theoretical understanding did not develop for many centuries, and consequently the exploitation of such phenomena to measure radiation dose did not emerge until the 20^{th} century. The earliest applications of luminescence in the dosimetry of ionising radiation were dating techniques in the field of archaeology, which involved the thermal or optical stimulation of latent luminescence in quartz and feldspar exposed to naturally occurring radioactivity.[2] Similar techniques also have a history in radiotherapy, the most prolific being the estimation of medical radiation doses from the luminescence emitted by lithium fluoride under thermal stimulation.[3] Historically, this has been of significant value but the experimental uncertainty typically associated with this technique has arguably not kept pace with the requirements of state of the art radiation therapy.

The past two decades have seen significant advances in the routine use of ionising radiation in oncology. In particular, the proliferation of intensity modulated external beam and high dose rate brachytherapy has brought new challenges to the task of dosimetric verification of radiotherapy treatments. With more precise shaping of radiation dose around targeted tissues, high dose gradients regularly occur near critical organs at risk where verification of delivered dose is of clinical interest. Despite the power of modern computing and increased availability of Monte Carlo dose calculation, the ability to accurately predict dose to patients in a clinical setting is not yet assured and so the hospital physicist still relies heavily in experimental measurement to assure safety for more complex treatment modalities. The limitations of existing dosimetry tools therefore remains somewhat of a barrier to the advancement of radiation therapy,[4] and so research into new or complimentary measurement technologies is of interest.

This work builds on a previous doctorate project[2] within the same research group, in which $NaMgF_3$:Eu and $NaMgF_3$:Mn were identified as potential candidates for luminescence dosimetry where radiological tissue equivalence is important, namely dosimetry for radiation protection and therapy. These two materials are tested as radiotherapy dosimeters in a fibre coupled configuration herein, and the experience gained has guided further materials research involving the $NaMgF_3$ host and a wider range of transition metal and rare earth dopants. The endpoint of the work reported is the selection of a more promising material, $NaMgF_3$:Ni, in which potentially lies solutions to some of the more significant challenges faced by fibre coupled dosimeter systems employing inorganic compounds. The practical difficulties in implementing fibre coupled dosimeter systems are also explored and the engineering of the requisite prototype hardware is detailed.

In chapter 2 an introductory summary of the theoretical and practical considerations of radiotherapy dosimetry, luminescence dosimetry, and fibre coupled dosimeter systems is given. This chapter is relatively detailed in an attempt to make this work accessible to both the clinical medical physicist and the solid state physicist. Chapter 3 details the experimental methods used to characterise the materials studied in both the laboratory and a radiotherapy setting. Results of characterisation studies are given in chapter 4 for all materials in the study, including those ultimately deemed of little value for applications. Finally, in chapters 5 and 6 the prototype fibre coupled dosimeters used and the radiotherapy testing is described.

An emphasis is given throughout to real-time dosimetry, in which a dosimeter is exposed to radiation and a surrogate for dose rate is recorded. Key radiotherapy applications for this type of system include beam characterisation measurements, patient specific dose verification, and potentially also *in vivo* dosimetry. While it is not reported in this work, many of the investigated materials exhibit latent forms of luminescence and so also lend themselves to future applications in planar or volumetric dose imaging.

Chapter 2

Background Theory

Fibre coupled dosimeter (FCD) research for radiotherapy applications encompasses a number of distinct disciplines, the theoretical aspects of which are presented in this chapter. Radiation dosimetry in the context of radiotherapy will be addressed foremost, followed by the solid state and luminescence physics relevant to the materials science undertaken. The engineering aspects of implementing a working fibre coupled dosimeter are also considered.

2.1 Radiotherapy Context

The currently accepted international framework for radiation safety[5] dictates that intentional exposures, including consented medical therapy, be both justified in terms of net benefit to the exposed individual and optimised to minimise the inherent risks. In the context of modern radiotherapy, justification mandates a high level of certainty in dose delivery while optimisation requires intimate knowledge of the radiation used. It follows that reliable radiation dosimetry is crucial to safely achieving the aims of therapeutic radiation exposure. The principal requirements for radiotherapy dosimeter hardware and the theoretical framework supporting existing technologies will be discussed in following sections.

2.1.1 Clinical Motivation

Modern radiobiology models the response of both malignant and normal tissues to radiation with steep sigmoidal dose response curves exhibiting highly similar isoeffective doses (see figure 2.1). These models attempt to quantitatively reflect the clinically observed delicate balance between destruction of malignant cells and depopulation of proliferating healthy tissues or permanent damage in late responding physiology.[6–8] Successful radiotherapy requires delivery of radiation doses inside this narrow window between the radiobiological response of the targeted and collateral tissues.

In the modern radiotherapy clinic, it is generally expected that uncertainty in dose delivery can be constrained to within 3% for targeted tissues.[8–10] This uncertainty budget is often dominated by the geometric uncertainties surrounding delivery of treatment to patients, particularly in persons with deteriorating health, leaving little latitude for dosimetric uncertainty. Of those uncertainties allotted to dosimetry in general, much is tied up in the maintenance of a local standard for absorbed dose to water. Consequently, instrumentation used in radiotherapy clinics must deliver minimal type A measurement uncertainty, ideally well under 1%, if the aforementioned limit in overall uncertainty is to be achieved.

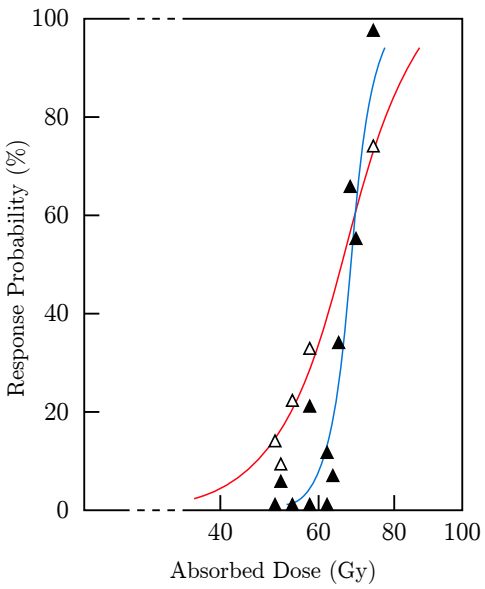

Figure 2.1: Biological response curves of a nominal healthy (blue) and malignant (red) tissue type to x-ray photons, illustrating the high sensitivity of both to small deviations in dose delivery. While the radiobiology of specific tumours and normal tissues varies widely, the steep gradient and narrow separation of isoeffective doses is typical.[6,7] *Adapted from IPEM 81.*[8]

Most dosimeters to see use in radiotherapy departments do perform at this level, but all existing instruments are limited in some other aspect, most often in terms of spatial resolution. Thus investigation into more novel techniques remains an active area of research.

2.1.2 Radiometric and Dosimetric Quantities

Physical quantities used in this thesis are defined in this section. Preference is given to SI units where appropriate.

Particle and energy fluence, Φ and Ψ, are the number of particles, N, and the radiant energy, R, of said particles excluding rest mass, incident to a given area. As implied by the units given in equations 2.1a and 2.1b below, Ψ may be calculated as the product of Φ and the energy of said particles. Fluence rate, $\dot{\Phi}$, and energy fluence rate, $\dot{\Psi}$, are the time derivatives of particle fluence and energy fluence respectively. While time derivative of fluence is often called flux, this terminology will be avoided as potentially ambiguous, with at least one authoritative source[11] defining flux and energy flux instead as the time derivative of particle count and radiant energy respectively.

$$\text{(a) } \Phi = \frac{\mathrm{d}N}{\mathrm{d}A} \quad (\mathrm{m}^{-2}) \qquad \text{(b) } \Psi = \frac{\mathrm{d}R}{\mathrm{d}A} = \Phi E \quad (\mathrm{J\,m}^{-2}) \tag{2.1}$$

Where the particle fluence is not monoenergetic, as is typical of radiotherapy sources, the concept of particle and energy fluence spectra are useful.[12] These are represented using differential notation as below, with Φ_E and Ψ_E to be used as shorthand. An integration over these fluence spectra should replace the monoenergetic Φ and Ψ where any of the subsequent formulae are applied to polyenergetic radiations.[11,12]

$$\text{(a) } \Phi_\mathrm{E}(E) = \frac{\mathrm{d}\Phi}{\mathrm{d}E}(E) \qquad \text{(b) } \Psi_\mathrm{E}(E) = \frac{\mathrm{d}\Psi}{\mathrm{d}E}(E) \tag{2.2}$$

The cross section, σ, is the fundamental interaction coefficient, defined as the probability of an interaction occurring under a given particle fluence. All other interaction coefficients discussed here may be expressed in terms of cross sections or differential cross sections. While not explicitly shown in equation 2.3, the interaction probability, P, has energy dependence. As cross sections tend to be numerically small in terms of m^2, the unit barn, b, equal to 10^{-28} m^2 is also common.[11]

$$\sigma = \frac{P}{\Phi} \quad (\mathrm{m}^2) \tag{2.3}$$

Linear attenuation coefficient, μ, describes the probability that an uncharged particle will interact with an absorber. This is expressed in equation 2.4 both in terms of particle interactions per unit length and the sum of constituent cross sections. N_A is the Avogadro constant, 6.022×10^{23} mol^{-1}, and M the molar mass in kg mol^{-1}. As the probability of photon interactions depends strongly on the density of the absorber, the mass attenuation coefficient, μ/ρ, is preferred where comparisons between μ for different substances are desired. The reciprocal of μ is the mean free path, ℓ.[11]

$$\frac{\mu}{\rho} = \frac{1}{\rho\,\mathrm{d}l}\frac{\mathrm{d}N}{N} = \frac{N_\mathrm{A}}{M}\,\Sigma_i \sigma_i \quad (\mathrm{m}^2\,\mathrm{kg}^{-1}) \tag{2.4}$$

For photons in the energy regime of therapeutic and diagnostic x-rays, the mass attenuation coefficient can be split into the cross sections for the relevant interactions,[12,13] as in equation 2.5. The cross sections for photon interactions by the photo electric effect, Rayleigh scattering, Compton scattering, and pair production are denoted σ_E, σ_R, σ_C, and σ_P respectively.

$$\frac{\mu}{\rho} = \frac{1}{\rho}\left(\sigma_\mathrm{E} + \sigma_\mathrm{R} + \sigma_\mathrm{C} + \sigma_\mathrm{P}\right) \tag{2.5}$$

For application to dosimetric quantities, mass linear attenuation coefficients are further decomposed into mass energy transfer, μ_tr/ρ, and mass energy absorption, μ_ab/ρ, coefficients. These are related to μ/ρ by equations 2.6a and 2.6b, and to each other by equation 2.6c. E_tr is the energy transferred to secondary charged particles by a photon fluence, and E_ab the energy eventually absorbed by the attenuator from said charged particles. $\overline{g}$ is the radiative fraction, representing energy lost to Bremsstrahlung, fluorescence, and annihilation photons. This decomposition of μ is necessary in the context of radiation dosimetry as energy transfer and absorption are typically separated in space.[12,14]

Below approximately 1 MeV μ_tr/ρ and μ_ab/ρ are effectively equal, with departure at higher energies[12] due largely to the increasing probability of pair and triplet production. These processes generate annihilation photons, which at 511 keV each are liable to transport the radiated energy significant distances in materials of intermediate density.

$$\text{(a) } \mu_\mathrm{ab} = \frac{E_\mathrm{ab}}{h\nu} \qquad \text{(b) } \mu_\mathrm{tr} = \frac{E_\mathrm{tr}}{h\nu} \qquad \text{(c) } \mu_\mathrm{ab} = \mu_\mathrm{tr}\,(1-\overline{g}) \tag{2.6}$$

Total stopping power describes the energy loss per unit path length for charged radiations in a given substance, as per the definition given in equation 2.7a. This is the sum of radiative stopping power, S_rad, electronic or collision stopping power, S_col, and nuclear stopping power, S_nuc. These correspond to energy radiated as Bremsstrahlung, fluorescence, or annihilation photons, lost through Coulombic interactions with atomic electrons, and lost to Coulombic interactions with atomic nuclei respectively. Restricted stopping power or linear energy transfer (LET), L_Δ, excludes all charged particles above an arbitrary threshold energy, Δ.[11,12] As with mass attenuation coefficients, the influence of the absorber density is mitigated by normalising by mass density.[11]

For photons, which partake in neither electrostatic or radiative interactions, stopping power is not strictly meaningful. However, values are often formulated in terms of the spectrum of energetic electrons generated by the photon radiation of interest,[12] an important use of which is found in small cavity theory (see § 2.1.3).

$$\text{(a) } \frac{S}{\rho} = \frac{1}{\rho}\frac{\mathrm{d}E}{\mathrm{d}l} \quad (\mathrm{J\,m^2\,kg^{-2}}) \qquad \text{(b) } L_\Delta = S_{\mathrm{col}} - \frac{E_{>\Delta}}{\mathrm{d}l} \tag{2.7}$$

Energy imparted to charged particles by a fluence of uncharged radiation per unit mass of an absorber is called kerma, and is related to μ_{tr} by equation 2.8 below. Kerma is an acronym for the *k*inetic *e*nergy *r*eleased in *ma*tter, and so the ionisation energy is excluded. The portion of kerma expended via interactions with atomic electrons is denoted as collision kerma, K_{col}, and the portion converted to Bremsstrahlung, fluorescence, or annihilation photons as radiative kerma, K_{rad}.[12,13]

$$K = \frac{\mathrm{d}E_{\mathrm{tr}}}{\mathrm{d}m} = \Psi\frac{\mu_{\mathrm{tr}}}{\rho} = K_{\mathrm{col}} + K_{\mathrm{rad}} \quad (\mathrm{J\,kg^{-1}}) \tag{2.8}$$

A more directly measurable dosimetric quantity is the total charge of one sign released per unit mass, known as exposure. Charge from ionisations generated by secondary Bremsstrahlung, fluorescence, and annihilation photons is excluded in the formal definition and assumed an insignificant contribution to measurements made with suitably small instruments. As shown below, exposure can be related to collision kerma using the mean energy expended per ion pair created, W, and the elementary charge, e. The accepted value of W in air is 33.97 eV, and is usually assumed to be independent of the incident photon energy.[12]

$$X = \frac{\mathrm{d}Q}{\mathrm{d}m} = \frac{e}{W}K\,(1-\overline{g}) \quad (\mathrm{C\,kg^{-1}}) \tag{2.9}$$

The end point of interactions of ionising radiation with matter, absorbed dose, is the energy deposited in a given mass. If said mass is a living cell or tissue, there exists an undisputed, if poorly defined, causal relationship between absorbed dose and biological effect, and so this is the principle quantity of interest in clinical radiation oncology. Where charged particle equilibrium (CPE) exists absorbed dose is equal to collision kerma.[12,14]

$$D = \frac{\mathrm{d}E_{\mathrm{ab}}}{\mathrm{d}m} = \Psi\frac{\mu_{\mathrm{ab}}}{\rho} = K(1-\overline{g}) \quad (\mathrm{J\,kg^{-1}}) \tag{2.10}$$

Under appropriate measurement conditions, exposure as measured in an air filled ionisation chamber can be used to determine kerma and therefore absorbed dose to the air volume, which may then be related to the dose in the surround medium using cavity theory.

2.1.3 Cavity Theory

As implied in the preceding discussion of dosimetric quantities, absorbed radiation dose is not a directly measurable quantity. While dose to a detector may be inferred under the assumption that the detector response is proportional to the energy deposited within a sensitive volume of known mass, this is not typically the quantity of interest. A more useful result is the dose to the medium into which the detector has been introduced, which often differs in atomic number and composition. This is determined by the application of cavity theory.[12,15]

A typical scenario in radiotherapy would be the determination of absorbed dose to a water phantom from the response of the air filled cavity of an ionisation chamber. For a given radiation quality, cavity size is described qualitatively with respect to the linear range of charged particles in the medium surrounding the cavity. In the case of large cavities in photon radiations, energy deposition is dominated by interactions within the cavity itself with a negligible contribution made by electrons originating from photon interactions outside the cavity.

Under these conditions, dose in the cavity is effectively independent of kerma in the surrounding medium, and so the ratio of collision kerma in the cavity to that in the medium is used to calculate dose absorbed in the latter.[12,14] This simplifies to a ratio of mass energy absorption coefficients as in equation 2.11 below. The notation $(x)_{\mathrm{a,b}}$ denotes the ratio of the value of x for material a to that of material b.

$$D_{\mathrm{med}} = D_{\mathrm{cav}} \left(\frac{\overline{\mu}_{\mathrm{ab}}}{\rho} \right)_{\mathrm{cav,med}} \tag{2.11}$$

$\overline{\mu}_{\mathrm{ab}}/\rho$ is the mass energy absorption coefficient (see equation 2.6a) weighted by the energy fluence spectra of a polyenergetic photon radiation (equation 2.2b), as discussed in § 2.1.2. This is formally defined by equation 2.12, in which Ψ_{tot} is the total energy fluence integrated across all energies present.

$$\frac{\overline{\mu}_{\mathrm{ab}}}{\rho} = \frac{1}{\rho \Psi_{\mathrm{tot}}} \int_0^{E_0} \Psi_{\mathrm{E}}(E) \mu_{\mathrm{ab}}(E) \, \mathrm{d}E \qquad \Psi_{\mathrm{tot}} = \int_0^{E_0} \Psi_{\mathrm{E}}(E) \, \mathrm{d}E \tag{2.12}$$

In the megavoltage bremsstrahlung radiations used in external beam radiotherapy, where the range of individual electrons in water is on the order of centimetres, detectors designed for useful spatial resolution are necessarily small cavities, for which the Bragg-Gray and Spencer-Attix theories apply instead. The formal conditions for the application of either theory are that the cavity is small enough to not perturb the charged particle fluence and that, in contrast to large cavities, energy is deposited in the cavity solely by charged particles completely traversing it.

Under these constraints, the fluence of charged particles set in motion by the primary photon fluence does not change between the cavity and the medium, thus differences in absorbed dose between the cavity and the medium are attributed simply to differences in interactions with this charged radiation fluence. Mass stopping power ratios are therefore used to relate dose in the cavity to the medium. In the case of Bragg-Gray theory, which neglects both secondary ionisations and charges coming to rest within the cavity, the ratio of unrestricted collision mass stopping powers (see equation 2.7a) is used, as in equation 2.13 below.[12] $\overline{S}_{\mathrm{col}}/\rho$ is a fluence spectra weighted average stopping power, defined similarly to $\overline{\mu}_{\mathrm{ab}}/\rho$ (equation 2.12).

$$D_{\mathrm{med}} = D_{\mathrm{cav}} \left(\frac{\overline{S}_{\mathrm{col}}}{\rho} \right)_{\mathrm{cav,med}} \tag{2.13}$$

Spencer-Attix theory, which operates under the same conditions but does not neglect track-end electrons or secondary ionisations, employs restricted collision mass stopping power ratios, as in equation 2.14 below.

$$D_{\mathrm{med}} = D_{\mathrm{cav}} s_{\mathrm{med,cav}} \tag{2.14}$$

A cavity size dictated threshold energy, Δ, is required, below which electrons are assumed to deposit energy locally. For completeness, an expression for the Spencer-Attix stopping power, s, is given in equation 2.15. L_{Δ} (see equation 2.7b) is defined with threshold such that electrons with range greater than the mean chord length of the cavity, which may deposit energy outside the sensitive volume, are excluded. The term outside the integral approximates the contribution from electrons with energy above the threshold but low enough to fall below Δ while traversing the

cavity.[12] In calculating the ratio of stopping powers for use in equation 2.14, the electron particle fluence in the medium is used to determine s in both the cavity and the medium, as the cavity is by definition too small to generate any significant perturbation of this fluence.

$$s = \frac{1}{\rho \Phi_{\text{tot}}} \left[\int_{\Delta}^{E_0} \Phi_{\text{E}}(E) L_{\Delta}(E)\, \mathrm{d}E + \Delta \Phi_{\text{E}}(\Delta) S(\Delta) \right] \qquad \Phi_{\text{tot}} = \int_{\Delta}^{E_0} \Phi_{\text{E}}(E)\, \mathrm{d}E \tag{2.15}$$

Due to the weak energy dependence of stopping power ratios for materials typically employed in radiotherapy dosimeters and phantoms, the difference in dose to a medium calculated with Bragg-Gray versus Spencer-Attix is minimal, although not negligible. Modern codes of practice for absorbed dose to water in radiotherapy typically use Spencer-Attix cavity theory.[16,17]

The aforementioned conditions for the application of both Bragg-Gray and Spencer-Attix theory cannot be completely satisfied for practical detectors. For ionisation chambers, perturbation correction factors are used to mitigate the impact of necessary departures from the ideal small cavity. These include corrections for the presence of a central electrode, p_{cel}, and the conductive cavity wall, p_{wall}, both of which are required for charge collection. A correction is also required for the minimal perturbation of the secondary electron fluence induced by any cavity of finite size, p_{cav}, which is otherwise assumed absent. The slight displacement of the effective point of measurement in a directional radiation field is corrected by p_{dis}. These are all chamber specific corrections with values close to unity, typically determined by Monte Carlo simulation.[12,17]

2.1.4 Energy Dependence

The response of real dosimeters is typically not independent of incident radiation energy.[12,14] This is a direct and unavoidable consequence of the fundamental interactions of ionising radiation with matter being dependent on both radiation energy and the composition of matter.[13] In the context of radiotherapy it is desirable to perform radiation measurements using detectors with radiological properties similar to the substance used most often as a tissue surrogate phantom: water. This both minimises perturbation of radiation flux in the region of the phantom displaced by the detector and ensures that dose deposition in the detector, and therefore the measurement outcome, is reasonably representative of that in soft tissue. While the response of a water inequivalent detector could, in principle, be corrected using cavity theory, in practice Ψ_{E} is only known with sufficient accuracy under well defined experimental conditions.

Compton scattering cross-sections are predominantly dependent on bulk electron density, which is straightforward to calculate using equation 2.16 for elemental materials, where N_A is the Avogadro constant, ρ the mass density, and Z and A the atomic number and relative atomic mass (in amu) respectively.[13]

$$\rho_{\text{e}} = N_A \frac{Z}{A} \rho \tag{2.16}$$

With the exception of hydrogen, the ratio of Z to A does not deviate significantly from 0.5, resulting in ρ_{e} roughly proportional to ρ and on the order of N_A for most substances. For crystalline compounds, including metals and many covalent solids, both ρ and ρ_{e} can be estimated from the contents and dimensions of the unit cell, although correctly accounting for the impact of dopants requires accurate knowledge of mechanisms of integration and charge compensation.

While Compton scattering is the dominant interaction of high energy radiations with tissue and

is largely uninfluenced by atomic number, detectors composed of high Z materials are nonetheless observed to respond inappropriately in therapeutic radiations. This is due to the unavoidable presence scattered photon fluence at reduced energies, for which photoelectric interactions become significant. Unlike Compton scattering, the photoelectric effect is strongly dependent on atomic number.[13,14]

Effective atomic number, Z_{eff}, is formally defined by equation 2.17, where f_i^{e} is the electronic fraction contributed by the i^{th} chemical element with atomic number Z_i. The exponent n varies with photon energy as determined experimentally, with a value of 3.5 employed herein. This is an energy dependent quantity with limited applicability to the polyenergetic Bremsstrahlung radiations typical of radiotherapy.[13,14]

$$Z_{\text{eff}} = \sqrt[n]{\sum_i f_i^{\text{e}} \text{Z}_i^n} \qquad 3 \geq n \geq 4 \tag{2.17}$$

Values of Z_{eff} calculated using equation 2.17 are valid primarily in the keV energy regime, while Z_{eff} for MeV radiations are typically lower ($\sim$3.5) and vary considerably less between light materials.[18] While the use of Z_{eff} to draw comparisons between dosimeter materials is very common, it is at best an indicative, but inconclusive measure of appropriate energy response. Comparison in terms of mass attenuation absorption co-efficients is generally more meaningful. Consideration should also be given to relative stopping powers if determination of absorbed dose with a given detector involves the application of small chamber cavity theories.

The response of a given material relative to water may be quantified for the purposes of inter-comparison between dosimeter materials by using equation 2.18, in which E_0 is a suitable reference energy,[2] perhaps the average emission energy of ^{60}Co. In substituting μ_{ab}/ρ of water for that of a standard tissue type[i], this expression also provides a quantifiable description of the often poorly defined concept of tissue equivalence.

$$\epsilon(E) = \frac{\left(\mu_{\text{ab}}\left(E\right)/\rho\right)_{\text{det,water}}}{\left(\mu_{\text{ab}}\left(E_0\right)/\rho\right)_{\text{det,water}}} \tag{2.18}$$

When working with the Compton interaction dominated low megavoltage energies, error arising from the use of a non-water equivalent dosimeter can often be mitigated by calibration under an approximation of the conditions of use.[13,21] This approach often suffices where measurement uncertainty is dominated by geometric errors, such as may occur during *in vivo* dosimetry.

2.1.5 Radiation Quality

A number of radiations are employed in radiotherapy. External beam therapy may be delivered using kilovoltage or megavoltage x-ray, γ-ray, electron, neutron, proton, or heavy ion radiations,[12,14] although in practice most modern clinics employ isocentric gantry mounted electron accelerators. While largely obsolete in first world medicine due to the dosimetric[ii] and safety advantages of modern linear accelerators, ^{60}Co γ-ray teletherapy units remain relatively common in developing nations. Modern high dose rate (HDR) brachytherapy almost exclusively utilises ^{192}Ir tipped wires

[i] Composition of many body tissues are standardised by the ICRU,[19] and the corresponding mass attenuation coefficient data is available from NIST.[20]

[ii] The extended sources used in ^{60}Co teletherapy result in comparatively poor geometric penumbrae, complicating the deployment of modern small field techniques.[22,23]

while low dose rate radioactive seed implants typically involve encapsulated ^{125}I, ^{90}Sr, or ^{103}Pd radionuclides.[14,21]

Higher LET radiations, specifically neutrons, protons, and selected heavy ions, have potential therapeutic advantage[7,21] but are prohibitively expensive to generate with only a handful of treatment centres existing worldwide. With such facilities being largely absent from the southern hemisphere these radiation qualities are necessarily outside the scope of this work, as are the technical considerations[17] of their dosimetry.

Spectral differences between different radiation types are most often described in terms of radiation quality. While for radionuclide sources the energy spectrum is almost always well known, for Bremsstrahlung x-ray sources the emitted radiation spectrum may be difficult to directly measure, and may even change between devices of the same manufacture. In the absence of a complete energy spectrum, radiation quality may be specified in terms of the first attenuation half value layer (HVL), a ratio of depth dose values ($\mathrm{TPR}_{20,10}$), nominal acceleration potential (NAP), percentage depth dose (PDD) characteristics, or the effective monoenergetic energy for an equivalent HVL.[12,14] In this work, the radiation quality is abstractly denoted q and numerically defined by one of the aforementioned measurable quantities as appropriate for the radiation in question.

2.1.6 Reference Dosimetry

Reference dosimetry is concerned largely with establishing and maintaining an absorbed dose calibration traceable to a recognised primary standard. New Zealand radiotherapy clinics are required[24] to perform calibration measurements in accordance with the code of practice embodied in the IAEA Technical Report Series No. 398 (TRS-398). Consequently, reference dosimetry measurements for this work was governed by these recommendations, the pertinent features of which are summarised in this section.

The directly measured quantity in ionisation chamber dosimetry is the ionisation current, which combined with the known mass of air in the sensitive volume yields exposure. Under conditions of CPE, the exposure can be related to absorbed dose to the chamber by combination of equations 2.9 and 2.10. Dose to the surrounding water phantom is then determined by application of Spencer-Attix cavity theory, as given in equations 2.14 and 2.15.

In practice, an experimentally determined instrument calibration co-efficient is used and the formalism given in equation 2.19 below is applied. In this expression, D_{w} is dose to a water phantom, Q is the charge measured, and $N_{\mathrm{D,w,q_0}}$ the instrument calibration in a reference radiation quality q_0. The remaining variables are corrections for departures in environmental conditions and radiation quality with respect to the conditions of calibration. In this formalism, the above discussion of exposure is embodied in Q and $N_{\mathrm{D,w,q_0}}$ and the Spencer-Attix theory in $k_{\mathrm{q_0}}$. The remainder of this section will address the aforementioned correction factors.

$$D_{\mathrm{w}} = QN_{\mathrm{D,w,q_0}}k_{\mathrm{pol}}k_{\mathrm{s}}k_{\mathrm{TP}}k_{\mathrm{q_0}} \tag{2.19}$$

Response of air filled chambers depends on the mass density of the air within the sensitive volume, itself varying as a function of temperature and pressure. The multiplicative factor k_{TP}, defined in equation 2.20, corrects the chamber response to that expected at the temperature and pressure for which the instrument calibration applies, T_0 and P_0. This factor may be derived from the ideal gas law and is considered accurate for corrections up to a few percent.[25]

$$k_{\mathrm{TP}} = \frac{P_0 T}{P T_0} \qquad T_0 = 293.15\,\mathrm{K} \qquad P_0 = 101.325\,\mathrm{kPa} \tag{2.20}$$

Polarity of the high voltage supply typically has negligible influence on the response of a well designed ionisation chamber when used in megavoltage x-ray energies.[12,17] This can be verified for a given instrument by evaluating equation 2.21 with charge collected using polarising voltages of the opposite sign and equal magnitude, Q_+ and Q_-. If the chamber was calibrated using a negative voltage then k_{pol} is used as a correction, else all occurrences in equation 2.21 of Q_+ and Q_- should be swapped. It is not unusual to determine k_{pol} to be unity to more than four significant figures when using a cylindrical ionisation chamber.

$$k_{\mathrm{pol}} = \frac{|Q_+| + |Q_-|}{2Q_-} \tag{2.21}$$

Loss of charge collection efficiency due to recombination is typically negligible for continuous radiation sources at therapeutic dose rates. In low duty cycle pulsed radiations where the instantaneous dose rate can be very high, a correction can be inferred from the variation in collected charge with polarisation voltage, $Q(V)$. Equation 2.22 is based on a series of quadratic fits to the reciprocal of collection efficiency against the ratio of chamber response for a range of different polarisation voltages. It compares very well to corrections derived from numeric solutions to the equations of Boag[26,27] for the dose rates and polarisation voltages typically used in modern radiotherapy departments. The empirically determined co-efficients a_0, a_1, and a_2 are supplied in TRS-398 for a range of values of N. For an air filled chamber the magnitude of the k_{s} correction is typically less than 1%.

$$k_{\mathrm{s}} = a_0 + a_1 \frac{Q(V)}{Q(V/N)} + a_3 \frac{Q(V)^2}{Q(V/N)^2} \quad N \geq 3 \tag{2.22}$$

In New Zealand, $N_{\mathrm{D,w,q_0}}$ factors are ultimately derived the ^{60}Co secondary standard maintained by the Institute of Environmental Science and Research, in turn traceable to the graphite calorimetry primary standard held by the Australian Radiation Protection and Nuclear Safety Agency. The megavoltage x-ray radiation qualities used in clinics are related to the ^{60}Co standard by application of the quality correction factor $k_{\mathrm{q_0}}$. This correction is well approximated by the quotient of Spencer-Attix stopping power ratios of water to air for ^{60}Co and the quality of interest, as shown in equation 2.23. Perturbation corrections for departures from the ideal small cavity are also radiation quality dependent and so are included in this quotient. Their determination is discussed in TRS-398.[17] Values for $k_{\mathrm{q_0}}$ may in principle be calculated using equation 2.15, but in practice are obtained from tables in TRS-398 for standard ionisation chamber types and radiation qualities.

$$k_{\mathrm{q_0}} \approx \frac{\left(s_{\mathrm{w,air}}\, p_{\mathrm{cav}}\, p_{\mathrm{cel}}\, p_{\mathrm{dis}}\, p_{\mathrm{wall}}\right)_{\mathrm{q}}}{\left(s_{\mathrm{w,air}}\, p_{\mathrm{cav}}\, p_{\mathrm{cel}}\, p_{\mathrm{dis}}\, p_{\mathrm{wall}}\right)_{\mathrm{Co}}} \tag{2.23}$$

Radiation quality corrections are the dominant source of uncertainty in absorbed dose calibration for radiotherapy, but cannot be avoided in the absence a primary absorbed dose to water standard or a direct megavoltage x-ray cross-calibration service.

Reference dosimetry is almost exclusively performed under an approximation of the reference conditions for which the instrument calibration applies. For the megavoltage x-ray dosimetry incorporated in this work, the reference conditions are dictated by TRS-398. The dosimeter is

positioned 100 cm from the x-ray target, at 10 cm depth in a homogeneous water phantom, ideally at standard temperature and pressure to minimise the required correction (see equation 2.20), and exposed on the central axis of a 10×10 cm square radiation field.[17]

2.1.7 Absolute Dosimetry

Except for the calibration of instruments and accelerator x-ray output, dosimetry of clinical interest is not typically performed under reference conditions. Experiments in which an instrument with a calibration established via reference dosimetry is used to determine absorbed dose in a substantially different irradiation geometry is termed absolute dosimetry. Examples include *in vivo* dosimetry where a dosimeter is used to directly measure dose delivered during treatment, and verification dosimetry in which a radiotherapy treatment is delivered to a phantom to validate the delivery of a specific treatment prior to exposure of patients.[21]

Absolute dosimetry demands detectors with excellent long term stability, approximate radiological equivalence to water, minimal and correctable dependence on environmental influence factors, and a repeatable means of calibration. A sound theoretical basis relating the measured quantity to absorbed dose is also desirable, such as the average energy of ionisation, W/e, which links exposure to kerma for ionisation chamber dosimetry.

2.1.8 Relative Dosimetry

Dosimeters which do not meet the criteria require for absolute dosimetry may still be employed to collect data subsequently normalised to an absolute measurement made with another instrument. This approach provides scope for the use of dosimeters unsuitable for calibration but otherwise possessing some technical advantage, such as high sensitivity or spatial resolution.[12] Relative measurements also simplify the consideration of the previously discussed corrections usually required for absolute dosimetry, the effects of which may be ignored where the influence quantity in question can be shown to remain constant.[14,21]

Typical relative dosimetry measurements include dose profiles, scatter factors, and central axis depth dose data. Relative dose profiles, also called off axis ratios (OAR), are used to describe changes in absorbed dose at points off the central beam axis with respect to the central axis dose at a given depth. Scatter factors capture the changes in dose at a reference depth on the central axis as a function of field size (r), expressed relative to a reference field size. Often these are separated into scatter components originating from the accelerator collimation (S_c) and from the irradiated volume of patient tissues or water phantom (S_p). On the central beam axis, percentage depth dose (PDD) expressed relative to the depth of dose maximum ($d_{\max}$) for a given source-to-skin distance (SSD) is the most practical quantity to directly measure.

For an isocentrically mounted accelerator the somewhat ambiguously named tissue phantom ratio (TPR) is a more useful description of central axis dose. Here the changes in dose with depth are given for a fixed distance from the radiation source, typically the source-to-axis distance (SAD), and expressed relative to the calibration depth (d_{ref}) under varying SSD. TPR has the advantage of being intrinsically independent of SSD, in that $\text{SSD}(d) = \text{SAD} - d$, and relating directly to the depth of calibration. While TPR can be directly measured, in practice it is calculated from PDD and scatter factors using a formalism published in BJR supplement 25.[28]

The relationship between SAD, SSD, and depth is shown diagrammatically in figure 3.9.

2.1.9 Small Fields

A photon radiation field is said to be small if the collimated beam radius is less than the maximum lateral range of secondary charged particles, resulting in a loss of lateral electronic equilibrium (LEE). This reduces the fluence of track-end electrons on the central axis and so modifies the energy spectrum of secondary charged radiation, which is otherwise almost independent of collimation in broader fields.[29] While spectral changes will influence the response of all dosimeters, ionisation chambers in particular are affected by the loss of CPE, a condition for the application of cavity theory.[12,13]

The minimum radius for LEE in water, $r_{\mathrm{LEE,w}}$, has been found by Monte Carlo techniques to be linear with beam quality as specified by $\mathrm{TPR}_{20,10}$, and may be calculated for clinical x-ray fields using equation 2.24.[30] This expression only holds for a NAP in the range of 1 to 15 MV. A medical accelerator producing 6 MV x-rays, for which a $\mathrm{TPR}_{20,10}$ of 0.7 is typical, maintains LEE in water for field sizes down to approximately 3×3 cm. In lower density media, such as lung tissue, the transition to electronic disequilibrium occurs at larger field sizes due to the increased range of secondary charged particles.

$$r_{\mathrm{LEE,w}} = 5.973\,\mathrm{TPR}_{20,10} - 2.688 \tag{2.24}$$

Significant spectral changes in the primary x-ray radiation are also expected as field sizes are reduced to a degree where the distributed x-ray source is partially occluded.[29] Such effects are highly dependent on the design of the accelerator beam conditioning and collimation systems, and so will be addressed where required for the interpretation of results in the context of the actual accelerators used for the experimental work herein.

Difficulties in the dosimetry of small fields arise largely from the limitations of detector technologies, predominantly energy dependence and spatial averaging.[14,31] With modern stereotactic and IMRT techniques routinely employing small megavoltage x-ray fields,[14,29,31] such limitations are among the primary motivations for research into optical solid state dosimetry materials of the type investigated in this work.

2.2 Luminescence Fundamentals

Often set apart from incandescence with the colloquial description of 'cold light', luminescence is the emission of light that utilises energy derived from sources other than the thermal content of a body. These include chemical reactions, atomic and sub-atomic processes, and the conversion of electrical or mechanical potential.[32,33] Of particular interest for luminescence dosimetry are the processes that produce infrared, visible, and ultraviolet photoluminescence (PL), radioluminescence (RL) and stimulated luminescence (SL). Collectively, these three phenomena are the fundamental mechanisms by which the wider range of luminescent phenomena discussed herein may be accounted for, including those exploited for radiation dosimetry.[2,34,35] The theoretical basis of these will be outlined in this section.

2.2.1 Optical Electronic Transitions

It is well established that the energies of a bound electron are discrete. Theoretically, this arises when solutions to the Schrödinger equation, $\mathcal{H}\psi = E\psi$, are constrained such that the complex

conjugate of the electron wavefunction, $\psi^*\psi$, may be interpreted as a probability density. This requires that ψ be continuous, smooth, finite, and single valued in 3-space, so that $\int \psi^*\psi \, \mathrm{d}\mathbf{x}$ may be normalised. In this way, the troublesome interpretation of probabilities which are neither single valued nor confined to $[0, 1]$ is avoided.[32,36]

When the electron in question is a valence electron bound by the electrostatic potential of an atomic nuclear charge, the energy of discrete electronic states typically fall on the magnitude of eV, and so resonant absorption and emission of photons at optical energies can occur. In a somewhat simplified description, energy is transferred via interaction of the photon electromagnetic field with the net electric or magnetic dipole moments of the valence electrons. The transition probabilities are proportional to $|\langle\psi_f|\mathcal{H}^{\mathrm{e}}_{if}|\psi_i\rangle|^2$ and $|\langle\psi_f|\mathcal{H}^{\mathrm{m}}_{if}|\psi_i\rangle|^2$ for the electric and magnetic dipole interaction Hamiltonians $\mathcal{H}^{\mathrm{e}}_{if}$ and $\mathcal{H}^{\mathrm{m}}_{if}$, and the initial and final state wavefunctions ψ_i and ψ_f. To a first approximation, electric dipole transitions are 10^5 times more probable than those of magnetic dipole character.[37]

Permitted transitions between states are those which conserve parity, spin, and orbital momentum. The operator $\mathcal{H}^{\mathrm{e}}_{if}$ has odd parity, thus for electric dipole transitions in which ψ_i and ψ_f have equal parity $\langle\psi_f|\mathcal{H}^{\mathrm{e}}_{if}|\psi_i\rangle = 0$, and the transition is forbidden. With the $\mathcal{H}^{\mathrm{m}}_{if}$ operator being of even parity, the inverse applies for magnetic dipole transitions.[36,38] If the electronic system is not isolated, the symmetry of the environment must also be considered, in which case intraorbital transitions are similarly forbidden for ions on a lattice site possessing a centre of inversion.[37,39]

If the electronic states are described in terms of spectroscopic term symbols[iii] of general form ${}^{2S+1}L_J$, the transitions which conserve spin and orbital momentum across interactions with photons are limited to those between terms which satisfy equations 2.25a through 2.25d. In these equations, L is the total orbital angular momentum, S the total spin angular momentum, and J the total angular momentum.[32,37]

$$\text{(a) } \Delta S = 0 \qquad \text{(b) } \Delta L = 0, \pm 1 \qquad \text{(c) } \Delta J = 0, \pm 1 \qquad \text{(d) } J = 0 \not\leftrightarrow 0 \tag{2.25}$$

Selection rules are discussed here both because they are useful in the interpretation of electronic features in optical spectra, and also to highlight their limitations. For the complex multi-electron systems of the higher Z elements, neither the term symbol description of an electronic state nor the above selection rules are strictly applicable. This is because values of S and L from which J is derived become poorly defined when determined under the assumption of negligible spin-orbit coupling, an assumption that does not hold for heavier atoms.[32,40] While spectroscopic term symbols remain useful for labelling electronic states in general, the predictive power of the associated selection rules is limited beyond the fourth period of elements.

For the valence electrons of ions in the crystalline lattice of an insulator or semiconductor, the binding potential has a periodic time dependence as the lattice vibrates at temperatures above absolute zero. The potential may be locally approximated by that of the harmonic oscillator, for which solutions to the Schrödinger equation describe a ladder of equally spaced energies for the lattice atoms, with which excited electronic states may interact.[36] Such interactions are modelled by emission or absorption of quanta of vibrational energy called phonons. These quantum pseudo particles have an energy quantum of $\hbar\omega$, where ω is the angular frequency describing the motion of the nuclear potential.[41,42]

[iii] Spectroscopic term symbols may be likened to alphabet soup, in that $L = \mathbb{N} \cup \{0\} \mapsto \{\mathrm{S}, \mathrm{P}, \mathrm{D}, \mathrm{F}, \mathrm{G} \ldots \mathrm{Z}\} \setminus \{\mathrm{J}\}$ for reasons best described as historical.

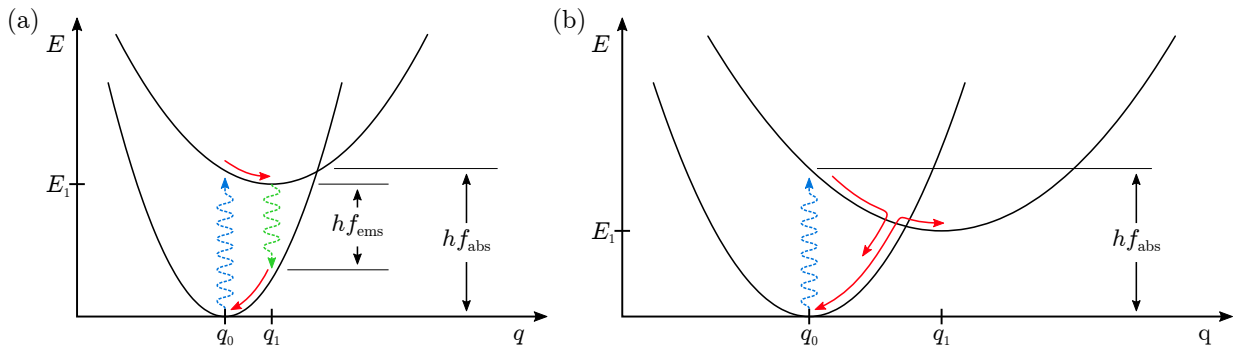

Figure 2.2: Configurational co-ordinate representation of multi-phonon processes as they occur for (a) the Stokes shift and (b) complete non-radiative relaxation. In (a) a photon of energy hf_{abs} is absorbed (blue), promoting a valence electron to an elevated vibrational level of an excited state. This is followed by rapid decay to the lowest vibrational level by emission of multiple phonons (red). Eventually, the excited state relaxes radiatively to a vibrational level of the ground state by emission of a photon with energy hf_{ems} (green). In (b) a similar process occurs but radiative relaxation from the lowest vibrational level of the excited state is not possible. Instead, a phonon may be emitted at the intersection of the states and absorbed in the other. As illustrated, it is also possible to thermally populate the excited state via the same mechanism.[37,46]

At room temperature the frequency of lattice vibrations is on the order of 10^{13} Hz[43,44] for which $\hbar\omega$ is on the order of 10^{-3} eV. The precise value depends primarily on the nature of the host lattice, and so is comparable for impurity ions of a given size and electronic configuration.[45] Being several orders of magnitude smaller than the energy quantum of electronic transitions, vibrational modes give rise to observable fine structure in optical spectra measured at low temperatures. This disparity in the frequencies of optical radiation and lattice vibration also admits electric dipole interactions when the electronic system is displaced from equilibrium. The resultant loss of inversion symmetry at the time of the interaction is reflected in a partial relaxation of the previously stated parity selection rules.[32,37]

Phonons are also implicated in non-radiative relaxation and generation of the Stokes shift. The latter occurs when an electronic state interacts strongly with the lattice vibrational modes, permitting the loss of excitation energy to the crystal environment in the form of heat, followed by optical emission at a lower energy.[33,37] This description is only meaningful for excitation and emission from the same electronic state. For states with minimal energy separation, completely non-radiative relaxation becomes possible, if not dominant.[32,37,46]

Both these processes are illustrated by the configurational co-ordinate diagrams in figure 2.2, in which the vibrational levels are those of the harmonic oscillator. The configurational co-ordinate, q, describes the displacement of the optically active ion with respect to its mean position in a vibrating lattice. Oscillator potentials are then placed relative to the outer electrons of the neighbouring ions in q, and the electronic ground state in E. Use of a single co-ordinate describes only the simplest 'breathing' mode of the lattice vibration,[37,46] a substantial simplification with respect to real crystals. The optical transitions depicted in figure 2.2 are vibronic, in that they simultaneously move between different electronic and vibrational states.[32]

2.2.2 Crystal Field Theory

For the isolated ion, the energy of electronic states partaking in optical transitions are dictated largely by the interactions between valence electrons and the net binding potential of the nucleus

and core electrons. The Hamiltonians for each are denoted here as $\mathcal{H}_e$ and $\mathcal{H}_0$ respectively, and the generalised free ion Hamiltonian is the sum of these terms, $\mathcal{H} = \mathcal{H}_e + \mathcal{H}_0$. $\mathcal{H}_0$ remains dominant while the electron of interest remains bound. In the absence of external electromagnetic magnetic fields, orbitals within each electronic configuration of the free ion may be degenerate in energy.[37,38]

When this ion is incorporated into a crystal lattice, the effect on the energies of states can be explored with the addition of an crystal field term, $\mathcal{H}'$, to the Hamiltonian of the free ion. This term describes the interaction between the ion and the rest of the crystal, predominantly the adjacent ligands for metal ion complexes. For $\mathcal{H}' \ll \mathcal{H}_e$, the so-called 'weak field' scenario, the crystal field affects a small perturbation of the free ion states.[37] Small shifts in the energy of states and additional fine structure due to weak splitting are observed, but in general the $^{2S+1}L_J$ notation remains useful in identifying the resulting energy levels.[47] This is the case with the $4f$ configurations of the rare earth elements, which are effectively shielded from the lattice environment by the larger radial extent of the $5s$ orbitals.[48]

In the 'strong field' case, $\mathcal{H}' > \mathcal{H}_e$, the crystal field significantly shifts the free ion energies and usually reduces degeneracy with respect to an isolated system. In the case of the $3d$ configuration to which crystal field theory is frequently applied, the five degenerate free ion d orbitals split into a pair, denoted e_g, and a triplet, $t_{2\mathrm{g}}$, the separation of which is defined as $10Dq$. This grouping reflects the symmetries of the d orbital wavefunctions in 3-space and only occurs strictly as described when the crystal field itself has high symmetry. When the ion resides on a distorted site these groupings will split further, completely removing degeneracy of the free ion states for the $3d$ configuration.[37,38]

The arrangement of partially occupied split d orbitals is subject to the magnitude of $10Dq$ relative to the electron pairing energy, E_p, which is essentially the electrostatic repulsion which must be overcome in order to pair two electron spins in the same orbital. Where $10Dq < E_\mathrm{p}$ all of the e_g and $t_{2\mathrm{g}}$ orbitals may be occupied individually, while for $10Dq > E_\mathrm{p}$ it becomes energetically favourable to pair spins in the lower energy set. This results in a discontinuity at $10Dq = E_\mathrm{p}$ in the energy of crystal field states as a function of $10Dq$.[38,49] The net magnetic moment arising from the angular momentum of unpaired spins should also change across this discontinuity.[39] Metal-ligand complexes are classified as low or high spin for $10Dq$ above and below E_p.

Term symbols used for the free ion energies are insufficient to describe the crystal field states and so group theory labels, specifically Mulliken notation, are typically used instead. In this work, the term symbol of the parent free ion state usually will be suffixed to avoid ambiguity.

2.2.3 Band Theory of Solids

It follows from the discussion in § 2.2.2 that the energy levels of the ions belonging to the lattice should also be perturbed by the crystal field. Splitting of the corresponding free ion energies occurs similarly, but due to the very large number of ions involved the lattice collectively takes on a large number of states distributed about the free ion energy levels. With the number of split states being of the order of N_A, these energy levels are effectively spread into continuous bands.[32,36]

In insulators and semiconductors the Fermi energy, E_f, resides intermediate to these bands and the valence electrons remain localised on the lattice ions, occupying states within the band immediately below E_f, the valence band. The conduction band is that which lies immediately above E_f, and charge carriers promoted to states within this band are bound only to the lattice at large. Effective insulators possess a band gap between the valence and conduction states of several eV.[32,37]

Defects in the lattice structure, such as atomic vacancies, substitutions, chemical impurities, and exterior surfaces, can result in additional allowed states within the prohibited energy ranges between bands. As these states exist only in the spatial locality of the corresponding defect, charge carriers occupying defect states are consequently confined in space.[35] Such charge carriers are said to be 'trapped' at the defect. Point defects may be introduced intentionally by doping a crystalline substance with trace amounts of impurities.

While trapping defects can in principle have permitted energies anywhere in the band gap of the material in question, the role played by a given defect played in luminescence is heavily influenced by proximity to the valence and conduction bands. Those at energies closer to the valence band have a higher probability of trapping holes, while those nearer the conduction band are more likely to localise electrons. Such defects are often classified as hole and electron traps,[35,50,51] reflecting only the probability of localising a given sign of charge carrier. Defects with energy roughly equidistant from both bands have similar probability of trapping either charge carrier and thus act predominantly as recombination centres, sequentially acquiring a hole and then an electron or vice versa.

The difference between the energy of the localised state and the delocalised band is referred to as the trap depth, representing the threshold of stimulation energy required to release a trapped charge from the defect. With all luminescent materials necessarily being semiconductors or insulators in order to possess a band gap[32] a significant range of depths is possible, from shallow traps thermally accessible at room temperature to those not readily stimulated by visible light or easily attained temperatures.[34,35]

2.2.4 Charge Carrier Kinetics

Interaction of ionising radiation with atomic electrons readily imparts sufficient energy to cross the band gap and promote charge to the conduction band, leaving unoccupied states in the valence band. These vacancies behave as charge carriers complimentary to the absent electron and so may facilitate the transportation of positive charge via the valence band.

Once delocalised, charge carriers may either recombine directly across the band gap or with previously trapped charge, giving rise to excitons and potentially luminescence (see figure 2.3a). Direct cross band gap recombination demands both spatial and temporal co-incidence and so is relatively rare. Consequently, the presence of defects, specifically those acting as recombination centres, can significantly enhance the efficiency of this type of luminescence.[35]

Alternatively, delocalised charge carriers may relax to the localised intermediate states permitted about defects and thus become spatially trapped. Subsequent thermal excitation or irradiation at optical wavelengths will re-excite a portion of trapped charge back to the delocalised energy bands and the aforementioned processes of recombination and trapping recur. This is referred to herein as stimulated luminescence (see figure 2.3b).

Trapping defects also constitute finite potential wells from which a confined charge may potentially escape by quantum tunnelling, a purely stochastic process requiring no external perturbation of the state.[36] A charge carrier liberated by tunnelling has insufficient energy to attain states in the delocalised bands and so must tunnel to a nearby recombination centre or another trap of similar depth (see figure 2.3c). It may do so from the ground state of the defect or, with somewhat higher probability, from an excited but still localised state attained by thermal or optical stimulation.[52,53]

The fate of electronically excited states arising after recombination is somewhat more compli-

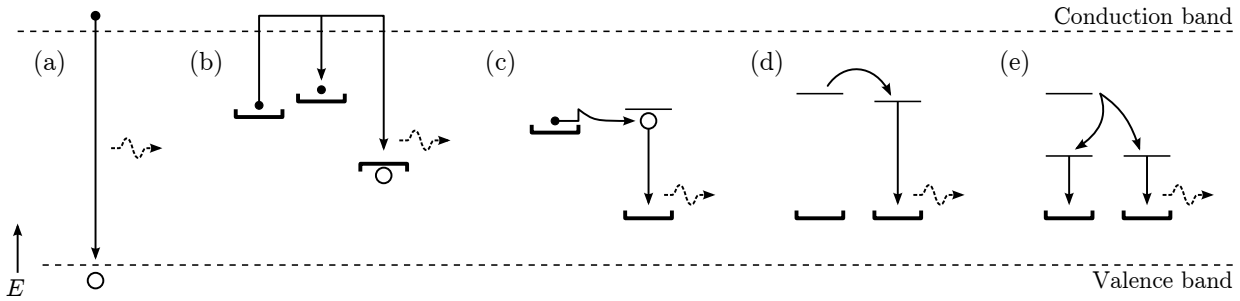

Figure 2.3: Examples of charge recombination and relaxation processes in materials exhibiting stimulated luminescence. (a) Direct recombination across the band gap, which occurs with relatively low probability. (b) Optically or thermally stimulated recombination via a delocalised band, a process with which vacant traps may compete. (c) Quantum tunnelling to a recombination centre followed by radiative relaxation. (d) Energy transfer of an excited state from one centre to another, quenching the emission from the donor site. (e) Cross relaxation in which excitation energy is distributed between the lower excited states across multiple centres. In (a) through (c) an electron recombining with a previously trapped hole is illustrated, although the inverse also occurs. While emission of a photon is pictured, each of these processes may also terminate with non-radiative relaxation.

cated than the purely radiative relaxation suggested so far. Excited states in real solids are subject to the multi-phonon processes illustrated in figure 2.2. This impacts luminescence efficiency and may even facilitate complete quenching of luminescence at elevated temperatures.[35] Further complexity arises when non-radiative energy transfer is considered, a process in which excitation energy is shifted between spatially distinct centres via multi-pole electromagnetic, quantum exchange, or cross relaxation interactions (see figures 2.3d and 2.3e). The probability of each is dependent on the physical separation of the donor and acceptor centres, and so is influenced by the concentration of defects. These mechanisms are usually identified by a reduction in the lifetime of luminescence decay.[37]

The processes of charge transport and recombination described above can, to some extent, be modelled by the system of rate equations 2.26 through 2.29.[44,54] In this system, n_c is the number of delocalised electrons in the conduction band, and m_v the corresponding holes in the valence band. n_i and m_j are the populations of trapped electrons and holes at defects of the i^th and j^th unique depths, and N_i and M_j are the concentrations of these defects. Probabilities of trapping charge carriers from the delocalised bands into electron and hole traps are A_i^n and A_j^m respectively, and A_j^{mn} is the probability of recombination for a delocalised electron at the site of a trapped hole.

$$\frac{\mathrm{d}n_\mathrm{c}}{\mathrm{d}t} = \Gamma\dot{\Phi} + n_i\left[\dot{\phi}(\lambda)\sigma_i(\lambda) + se^{-E_a/kT}\right] - n_\mathrm{c}A_i^n\left(N_i - n_i\right) - n_\mathrm{c}m_jA_j^{mn} \tag{2.26}$$

$$\frac{\mathrm{d}m_\mathrm{v}}{\mathrm{d}t} = \Gamma\dot{\Phi} - A_j^m m_\mathrm{v}\left(M - m\right) \tag{2.27}$$

$$\frac{\mathrm{d}n_i}{\mathrm{d}t} = n_\mathrm{c}A_i^n\left(N_i - n_i\right) - n_i\left[\dot{\phi}(\lambda)\sigma_i(\lambda) + se^{-\Delta/kT}\right] \tag{2.28}$$

$$\frac{\mathrm{d}m_j}{\mathrm{d}t} = A_j^m m_\mathrm{v}\left(M_j - m_j\right) - n_\mathrm{c}m_jA_j^{mn} \tag{2.29}$$

External influences included in this model are ionising irradiation, optical illumination, and application of heat. Ionisation is modelled as the product of the fluence rate at ionising energies, $\dot{\Phi}$, and the ionisation cross section, Γ, directly populating the valence and conduction bands.

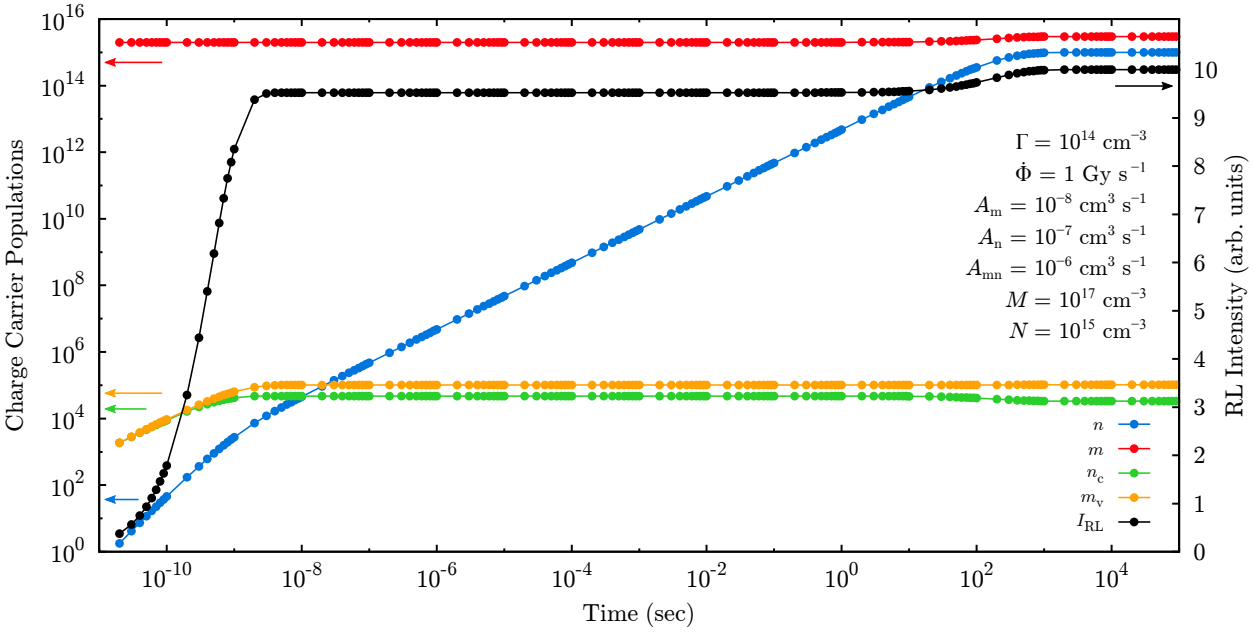

Figure 2.4: Numerical solution to equations 2.26 through 2.29 using the parameters shown and initial conditions $[n(0), m(0), n_{\mathrm{c}}(0), m_{\mathrm{v}}(0)] = [0, 2 \times 10^{15}, 0, 0]$ cm^{-3}. Intensity of RL as calculated using equation 2.30 is plotted linearly against the secondary vertical axes. At the indicated dose rate, an equilibrium population of delocalised carriers (green and orange) and RL intensity (black) occurs after about 10^{-9} seconds. For t on the order of minutes the population of trapped holes (red) increases and saturates, leading to a corresponding inflation of RL intensity, as is typically observed in defective luminescence materials. The initial equilibrium intensity is largely dictated by $m(0)$, which has a non-zero finite value for all any realistic system.

Similarly, optical stimulation of trapped charge into the conduction band occurs in proportion to the incident fluence rate at optical energies, $\dot{\phi}(\lambda)$, and the photoionisation cross section of the trapping defect, $\sigma_i(\lambda)$. Both of these typically have strong wavelength dependence. Probability of thermal stimulation is governed by temperature, T, and the attempt to escape frequency, s, which depends on the lattice vibration frequency.[44]

The modelled observable is intensity of luminescence, taken to be proportional to the rate of recombination of negative charge carriers from the conduction band with trapped holes.[54] The relevant term is isolated in equation 2.30 and an example solution for the entire system is illustrated in figure 2.4. This model specifically addresses systems in which a luminescent ion behaves as a hole trap, converting the recombination energy of electrons captured from the conduction band into excited electronic states which then relax radiatively. This is by no means the only process by which luminescence arises in inorganic solids.

$$I \propto \sum_j n_{\mathrm{c}} m_j A_j^{mn} \tag{2.30}$$

As a simplification, this system of rate equations considers only electron transport, holes being assumed stationary. This assumption is probably valid for many materials at room temperature. Self-stimulation is also neglected, in that the photons produced in the radiative recombination are not taken as input via the $\dot{\phi}(\lambda)\sigma(\lambda)$ term in equation 2.26, the effect of which is assumed negligible when modelling physically small samples. The equations are coupled by requiring that the system remain electrically neutral, specifically that $\Sigma n_i + n_{\mathrm{c}} = \Sigma m_j + m_{\mathrm{v}}$, which is strictly the case only for modelling of stimulated luminescence. During irradiation, this condition holds only in localities where CPE exists.

While this type of model is a powerful tool for understanding the dynamics of optical systems containing trapping defects, it is ultimately limited by the knowledge available concerning said traps in a given material. This information is difficult extract experimentally as the nature of traps in a given material are notorious for sensitivity to crystal fabrication conditions and techniques.[55] Thus a configuration of traps which may well describe one sample of an optical material of interest does not necessarily apply generally.

2.2.5 Photoluminescence

PL photons are generated by the optical excitation of a luminescent species, typically as a defect in an inorganic material, resulting in either fluorescent or phosphorescent emissions. In the majority of materials a Stokes shift or relaxation via intermediate electronic states occurs, and the emission is detected at longer wavelengths. In a few cases emission can also be detected at wavelengths shorter than the excitation light where mechanisms of multi-photon absorption, energy transfer, or excited state absorption occur.[56,57] Fluorescent emissions arise from transitions which are permitted in the quantum mechanical sense and so re-emit the excitation energy promptly, on the order of 10^{-9} seconds after excitation.[32] This is not always the case, with the emissions from many materials being phosphorescent, the result of weakly forbidden transitions where the lower probability of relaxation causes the excitation energy to be re-emitted over seconds or longer.[33,35]

Generally, PL does not directly involve the population of trapped charge in defective materials and so emission intensity is often independent of previously absorbed dose.[35] However, where radiation induced photochemical changes occur, the character of the PL may change significantly. In this case it is termed radiophotoluminescence (RPL) and can often be quantitatively related to absorbed dose.[58,59] The RPL exhibited by silver activated phosphate glass was exploited in a relatively crude casualty dosimeter for military use,[60] more recently for environmental dosimetry,[61] and in at least one commercial personal monitoring system.[62] RPL does not encompass cases where a change in detectable PL emission arises from radiation damage effects, such as the creation of colour centres.

2.2.6 Stimulated Luminescence

SL encompasses both optically stimulated luminescence (OSL) and thermally stimulated luminescence (TSL), which are fundamentally the same process, distinguished only by the form of stimulation energy.[34,35] Consequently, all materials in which TSL is observed are expected to also exhibit OSL, and vice versa. The defining feature of SL is the latent nature of the emission, with trapping defects facilitating the phenomenon potentially being stable for periods of months to years.[35]

During SL emission, a portion of the charge carrier recombination energy is recovered as luminescence via the electronic excitation of an optically active defect at or near the site of recombination. The emission spectrum will therefore typically have features in common with the PL emission.[34,35] The processes of stimulation and recombination preceding optical emission are described in § 2.2.4.

Ideally, integration of the total SL emissions from a previously irradiated sample yields a figure directly proportional to absorbed dose, but in reality there exist a number confounding aspects. In real materials, the energy distribution of traps is varied, some are too shallow to prevent charge from being thermally released at room temperature, while others are too deep for practical thermal or optical stimulation. Occupation of deeper traps directly influences the competition between

said traps and those at the dosimetrically relevant energies, potentially generating changes in the sensitivity of reused dosimeters. The finite number of traps at any depth also implies a saturation dose, which is approached asymptotically.[34,35] Furthermore, the fraction of recombination energy lost to the environment via non-radiative relaxation processes will typically depend on temperature, perhaps significantly so.[35,63,64]

Not surprisingly, OSL and TSL are difficult to isolate in practical SL applications where measurements are necessarily performed at or near room temperature under normal lighting conditions. Packaging TSL dosimeters for light tightness interferes with accurate and repeatable heating, while maintaining OSL dosimeters at cryogenic temperatures is impractical at best and impossible if used *in vivo*. The interplay of different SL processes is part of the reason so few of the thousands of stimulable luminescent materials studied to date have been utilised as radiation dosimeters.

The practice of exploiting SL for dosimetric measurements is referred to as optically stimulated luminescence dosimetry (OSLD) or thermoluminescence dosimetry (TLD). In imaging applications the term photo-stimulated luminescence (PSL) is common.

2.2.7 Radioluminescence

Luminescence during irradiation is observed in defective materials exhibiting SL, arising from precisely the same processes, but prior to localisation of charge carriers at trapping defects. RL and SL are thus competing processes, in that charge carriers which recombine and give rise to RL photons are unavailable for trapping, and so do not contribute to SL emissions, and vice versa.[35] This situation is also dynamic, with the population of trapped charge increasing during irradiation and the probability of trapping falling correspondingly, partially suppressing competition from trapping defects and so effectively increasing RL efficiency.[54,65,66] Therefore, measured RL emission intensity cannot be directly interpreted as a surrogate for rate of dose deposition as this observable reflects both instantaneous dose rate and previously absorbed dose.

Materials without a significant concentration of charge trapping centres, and thus no significant capacity for SL, can still exhibit radioluminescence. This is usually referred to as scintillation, but the underlying mechanisms are essentially the same: radiative relaxation from excited states attained either by interaction of bound electrons with ionising radiation or the recombination of secondary charges.[65,67,68] The principle characteristic for which scintillation is usually defined as distinct from radioluminescence is prompt decay of emissions, although this definition leads to misnomers in the literature such as 'long lifetime scintillators'.[69]

A wide range of organic, inorganic, artificial, and naturally occurring materials scintillate, with numerous well established applications in radiation detection and medical imaging. Popular high light yield inorganic scintillators, including NaI:Tl, $Bi_3Ge_4O_{12}$, and $Lu_2(SiO_4)O$:Ce, make for effective x-ray detector or imaging systems when coupled with photomultiplier tubes.[67,68] Such materials also tend to be fragile, hygroscopic, susceptible to radiation damage, exhibit poor tissue equivalence, and so while effective as radiation detectors, are generally poor candidates for applications involving clinical radiation dosimetry.[70]

In this work, luminescence observed during irradiation of materials in which charge trapping and transport occur will be referred to as RL, and scintillation otherwise. The term x-ray luminescence, seemingly synonymous with radioluminescence, occurs frequently in the literature.

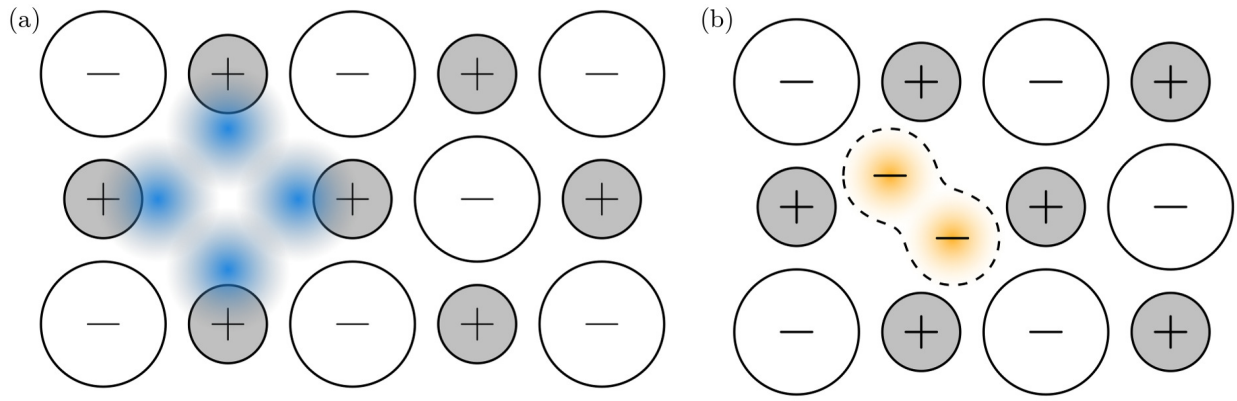

Figure 2.5: Pictorial illustration of typical models the (a) F–centre and (b) H–centre in a generalised alkali halide lattice. The approximate spatial distribution of the probability density function for the single electron in the F–centre is shown in blue and a possible configuration for accommodating the interstitial halide of the H–centre in orange. Some degree of localised lattice distortion (not illustrated) is also expected. *Adapted from literature*.[71]

2.2.8 Colour Centres

The term 'colour centre' broadly encompasses all optically active defects involving the intrinsic constituents of a crystal lattice, specifically excluding impurities.[46] These defects may be innate or induced by exposure to radiation, and so play a key role in radiation damage effects in inorganic crystals. Perhaps foremost for this reason, colour centres have been heavily researched during the latter half of the 21$^{\text{st}}$ century.[72] The concepts introduced in this section are derived largely from studies of the alkali halides, and as such may only be tentatively applied to more complex fluorides and oxides.[73]

By far the most prevalent and well-studied example is the F–centre, consisting of a single electron trapped at an anion vacancy. It is illustrated in figure 2.5a. Containing only one unpaired electron, the F–centre is paramagnetic and exhibits hydrogenous optical spectra with significant temperature dependence and Stokes shifts.[46] The latter is a consequence of the electron wavefunction being spatially distributed across the adjacent lattice sites, generating strong interaction with lattice vibrational modes. In many materials the F–centre is immobile at room temperature.[46,72]

Radiolytic creation of F–centres occurs following the localisation of an exciton on the anion sublattice, with the hole trapped between two anions in the local distortion of the crystal environment caused by the exciton itself. Such a defect is known as a V_{k} centre, also termed X_2^-. This defect is unstable above cryogenic temperatures[2,73] and so dissociates promptly at room temperature, displacing one of the anions involved into an interstitial position and leaving behind an F–centre. The efficiency of this process depends on the anion atomic displacement energy for the lattice and the available space for interstitials, the latter of which may be characterised in terms of anion separation and ionic diameter.[73] In the case of halide crystals, the associated interstitial is referred to as an H–centre (see figure 2.5b) and will migrate to annihilate with F–centres at sufficiently elevated temperatures.[46,72]

If either the oscillator strength[iv] for an optical absorption or the corresponding defect concentration is known, then the other can be approximated using Smakula's equation,[37,74] the general form of which is given in equation 2.31 below. In this expression, N is the defect concentration, f

[iv] Indication of the number of electric dipole oscillators which can be stimulated by the electromagnetic field of optical radiation, interpreted as a transition probability which approaches unity for strongly allowed transitions.[37]

the oscillator strength, n the refractive index of the host crystal, $\mu(E)$ the optical absorption as a function of energy, and the constants m_e, c, $\hbar$, and e take on their usual values. Refractive index is assumed to not change significantly in the neighbourhood of the absorption, and the host medium must be transparent.[74]

$$Nf = \frac{m_{\mathrm{e}}c}{2\pi^2 e^2 \hbar} \frac{n}{(n^2+2)^2} \int \mu(E)\,\mathrm{d}E \tag{2.31}$$

If the absorption band is assumed to have a Gaussian character then equation 2.31 can be simplified to equation 2.32 below, in which $\mu_{\max}$ is the peak absorption co-efficient in cm^{-1} and Δ the absorption bandwidth at half maximum in eV.[75]

$$Nf = 8.7 \times 10^{16} \frac{n}{(n^2+2)^2} \Delta\mu_{\max} \tag{2.32}$$

A number of colour centres derive from the F–centre through the acquisition and loss of charge carriers or association with other intrinsic defects. The F^-–centre, for example, consists of two electrons trapped at an anion vacancy. This is possible due to the aforementioned distribution of the electron wavefunction in the F–centre, which does not effectively screen the positive charge of the vacancy. The second electron is only weakly bound and so the F^-–centre is not generally stable at room temperature. In the case of divalent anions such as O^{2-}, two electrons trapped on an anion vacancy are electrically neutral, and so are termed F^0. Optically this behaves more like an F^-–centre than an F–centre. In a similar vein, an ionised F–centre is an anion vacancy, and is referred to as an F^+–centre, V_{a}–centre, or occasionally an α–centre.[2,46,72]

At sufficiently high temperature F–centres are liable to aggregate, forming F_2, F_3, and occasionally higher order defects. The F_2 and F_3 defects are also referred to as M and R centres respectively,[76] with optical absorption always occurring at lower energies than the F–centre.[46] Aggregates may be formed during exposure to irradiation, either by direct creation of multiple F–centre defects in close proximity or by ionisation of existing F–centres. In the latter case, the resulting F^+–centre, which is more likely to be mobile at room temperature, will diffuse through the lattice and localise against other defects.[46] When created by ionising radiation, the equilibrium concentration of F_2–centres is expected to be proportional to the square of the concentration of F–centres.[76]

When an F–centre or H–centre occurs immediately adjacent to an impurity on a cation site it is denoted F_{A} or H_{A} accordingly.[77,78] If the cation impurity is a luminescence species, the optical character of the impurity may be significantly influenced by the resulting change in the local crystal field.[79]

2.3 Dosimetry Materials

The past century of research has yielded countless potential SL materials, only a few of which have seen uptake in medical and personal dosimetry. These include lithium fluoride (LiF) with a range of dopant elements,[3,80] carbon doped aluminium oxide (α-Al_2O_3:C),[34,81] and silver-activated phosphate glasses.[59,60] This apparent limited success in medical applications stems primarily from the requirement for approximate radiological equivalence to water. A selection of materials of interest for luminescence dosimetry applications are introduced in this section, including those investigated in this work. A summary of physical and radiometric properties for these materials is

presented in table 2.1 along with those of general materials of interest to radiotherapy dosimetry: air, water, and silicon. Properties are further discussed in the context of dosimeter applications in § 2.4.4.

2.3.1 Lithium Fluoride

While not investigated in this study, impurity doped lithium fluoride (LiF) has seen widespread use in personal and medical dosimetry for many decades[3] and so constitutes a valuable benchmark. The undoped crystal is chemically inert, mechanically robust and insoluble. Like many alkali halides, the lattice structure is cubic (see figure 2.6a). Non-dosimetric applications are found in industrial and scientific optics as bulk monocrystalline LiF exhibits a wide window of transparency extending from mid-infrared wavelengths well into the vacuum ultraviolet. This is due to an unusually wide band gap of 13.6 eV.[102–104]

Complex colour centre luminescence is observed after exposure to ionising radiation, attributed primarily to F_2–centres and F_3^+–centres.[105,106] This occurs in undoped LiF, but it is usual dope with multiple transition metals to increase sensitivity. Both OSLD[106] and TLD[103] is possible with LiF, with very rapid TSL readout when heated using infrared lasers.[107–109] Tribothermoluminescence[v] is observed at least for LiF:Mg,Ti, particularly when using powdered material heated without isolation in an inert atmosphere.[103]

At the time of this writing, LiF:Mg,Ti and LiF:Mg,Cu,P remain among the most tissue equivalent dosimetry materials available for use in radiotherapy clinics,[111,112] and so are still the standard luminescence dosimeters of choice.[14,35] However, the most commonly used variant, LiF:Mg,Ti, is subtly non-linear in the dose range 1 to 5 Gy, a range which is often of interest in radiotherapy.[80] This increases measurement uncertainty and severely limits the applicability of the material for *in vivo* dosimetry of hypo-fractionated or brachytherapy treatments.

Sintered LiF:Mg,Ti is commercially available as TLD-100, and the more sensitive LiF:Mg,Cu,P as TLD-100H. Isotope enriched flavours TLD-600(H) and TLD-700(H) also exist for differential dosimetry of thermal neutrons, exploiting the $^6\mathrm{Li}\,(\mathrm{n},\alpha)\,^3\mathrm{He}$ nuclear reaction.[103]

[v] TSL induced mechanically rather than by exposure to radiation[110]

	ρ_m (g/cc)	ρ_e (e/cc)	†Z_{eff}	$\mu_{\mathrm{ab}}/\rho_{\mathrm{m}}$ (cm^2/g)	λ_{ems} (nm)	τ (s)
Air	1.20×10^{-3}	3.61×10^{20}	7.8	0.002789	—	—
Diamond	3.51	1.06×10^{24}	6.0	†0.00454	—	—
H_2O	1.00	3.34×10^{23}	7.5	0.007072	—	—
Si	2.33	6.99×10^{23}	14	0.006361	—	—
BC-*XXX*	1.03	3.37×10^{23}	5.7	0.006894	420 . . . 580	$10^{-9} \ldots 10^{-7}$
BCF-*XX*	1.05	3.40×10^{23}	5.7	0.006847	430 . . . 530	$\sim 10^{-9}$
α-Al_2O_3:C	3.97	1.18×10^{24}	11	0.006252	415	3.5×10^{-2}
BeO	3.01	7.71×10^{23}	7.1	0.006113	380	2.5×10^{-5}
LiF	2.64	7.40×10^{23}	8.3	0.005894	410	$\sim 10^{-8}$
$NaMgF_3$	†3.07	8.87×10^{23}	11	0.003912	—	—

Table 2.1: Selected physical and dosimetric properties of luminescence materials and substances of interest, compiled from scientific and engineering texts,[2,12–14,35,82] published literature,[66,80,83–95] Bicron/Saint-Gobain datasheets,[96–101] and the NIST x-ray mass attenuation coefficient tables.[20] Values marked † were calculated. Densities apply at temperature and pressure in the region of 300 K and 100 kPa, attenuation coefficients at 1 MeV, and lifetimes at the emission wavelength.

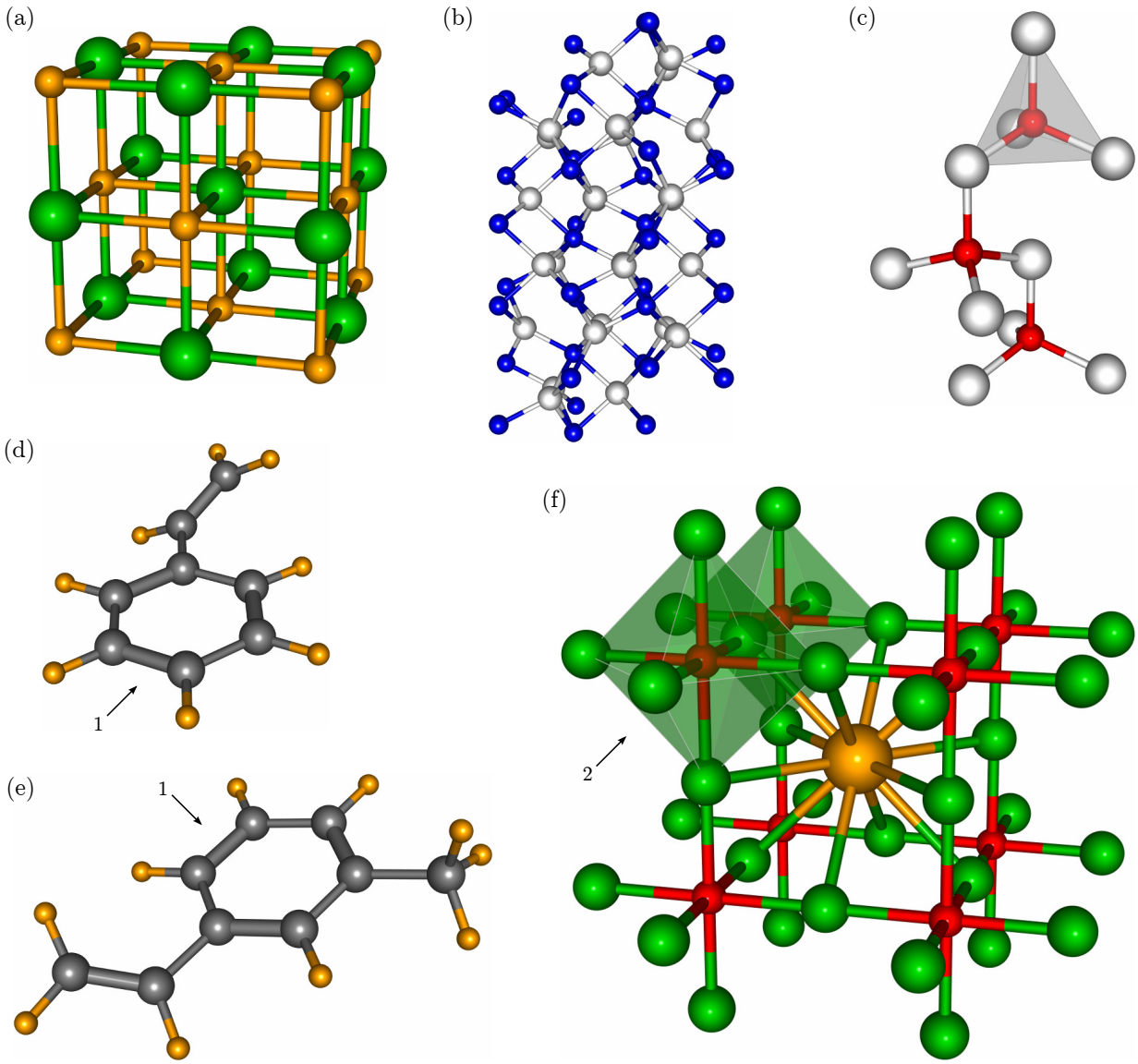

Figure 2.6: Crystal and molecular structure of (a) LiF, (b) α-Al_2O_3, (c) BeO, (d) styrene monomer, (e) vinyl toluene monomer, and (f) $KMgF_3$. Ions are coloured by valence, with monovalent cations (H^+, Li^+, and K^+) in orange, divalent cations (Be^{2+} Mg^{2+}) in red, trivalent cations (Al^{3+}) in blue, tetravalent cations (C^{4+}) in grey, monovalent anions (F^-) in green, and divalent anions (O^{2-}) in white. Luminescence in structures (a) through (c) is anion defect related, with various doping employed to increase sensitivity. For the monomers depicted in (d) and (e), luminescence is intrinsic to the aromatic molecular structure, in this case (1) benzene rings. With the perovskite structure the co-ordination polyhedra influence the luminescence of impurity cations, particularly those integrating as (2) BF_6 octahedra. *Structure graphics generated using VESTA*[113].

2.3.2 Aluminium Oxide

Anion deficient α-Al_2O_3:C, a synthetic sapphire, has been studied in depth over the past two decades and proved an effective dosimeter material characterised with radioisotope sources,[114–116] kilovoltage[117–122] and megavoltage[50,51,122–124] radiotherapy beams, and also for neutron,[125,126] proton,[122,127] and heavy ion[122,128–130] radiations. α-Al_2O_3:C was initially investigated as a high sensitivity TLD material,[131] but being sensitive to visible light and subject to thermal quenching it has found wider acceptance in OSLD applications.[35] This compound is the active material employed in the Luxel+® and InLight® personal monitoring systems from Landauer Inc.[132,133]

Undoped Al_2O_3 has numerous industrial applications ranging from semiconductor substrates

and laser hosts to insulation of fission reactors.[134] There are two known phases, α-Al_2O_3 and γ-Al_2O_3, occurring naturally as the minerals corundum and boehmite respectively. Monocrystalline α-Al_2O_3 has a trigonal lattice structure, consisting of oxygen anions in an approximate hexagonal close packed (HCP) arrangement (see figure 2.6b) with two thirds of the octahedral interstices regularly occupied by aluminium.[135–137] This structure has unusually high mass and electron density (see table 2.1) for the relatively low atomic number of the constituent elements. In contrast, γ-Al_2O_3 is a defective spinel in which anions reside in a cubic close packed (CCP) lattice with both tetrahedral and octahedral interstices occupied at random.[134,138] Only the more extensively studied α phase, which also possesses a larger band gap,[134] has seen successful application in radiation dosimetry.

When grown in a reducing atmosphere the presence of carbon demonstrably promotes the formation of oxygen vacancies in α-Al_2O_3, effectively activating luminescence assigned to F–centres and F^+–centres upon examination of absorption spectra.[139] Beyond this, the precise mechanism of integration of carbon into the α-Al_2O_3 lattice and any direct luminescent role played by the activator appears poorly understood. Substitution of tetravalent carbon ions on O^{2-} sites with anion vacancies providing charge compensation is suggested,[140] as is integration of divalent carbon on Al^{3+} sites,[131] although neither substitution is favoured upon consideration of ionic radii[141] or valency. The relatively small size of the tetravalent carbon anion may also permit the formation of α-Al_2O_3:C crystals with interstitial carbon.[140]

F–centre luminescence in α-Al_2O_3:C produces a band emission at 415 nm attributed to transitions between the excited ^{3}P state, often termed an F*–centre, and the ^{1}S ground state of the defect.[35,72,140] This transition is spin forbidden, explaining the relatively long lifetime of emission (10^{-2} seconds) exploitable during pulsed OSL readout and for Čerenkov stem signal suppression.[66] A far shorter-lived (10^{-9} seconds) and weaker ultraviolet emission centred on 330 nm due to F^+–centre luminescence is also reported in the literature.[35,72]

When used as an RL dosimeter the intensity of emissions from this material exhibit severe dependence on previously absorbed dose with up to 37 fold changes in sensitivity observed.[66] Radiologically, α-Al_2O_3:C compares well to silicon diodes having Z_{eff} of 11, but poorly to both LiF and BeO. At least one study has attempted characterisation of this material in a planar form.[126] α-Al_2O_3:C is also sold commercially for TLD use under the name TLD-500.[142]

With the addition of a magnesium dopant, α-Al_2O_3 is potentially suitable for RPL dosimetry. A near infrared PL emission occurs after irradiation and is attributed to F^+–centre aggregates with local charge compensation provided by Mg^{2+} ions. Dose response is linear up to at least 2 Gy, rendering the material useful for radiation protection dosimetry. While Al_2O_3:C,Mg was originally developed for applications in optical data storage, it has also been proposed as a nuclear track detector, and most recently as an RPL dosimeter material.[143–145]

2.3.3 Beryllium Oxide

Also known as beryllia, BeO is an opaque ceramic which, like Al_2O_3, has existing industrial and aerospace applications, rendering it cheap and obtainable. Initially studied as a TL powder,[146,147] this material has been recently revisited in the solid ceramic form with highly tissue equivalent OSL applications in mind,[148–153] including dosimetric imaging[154,155] and fibre coupled dosimetry.[156,157] BeO exhibits pronounced sensitivity of TL signal to light and thermal quenching of OSL response.[148]

With an attractive Z_{eff} of 7.1, BeO represents the primary alternative to α-Al_2O_3:C, albeit

with lower sensitivity and reduced linear range, saturating above 5 Gy.[35] When powdered, BeO is both chemically toxic and a confirmed human carcinogen.[35,158] However, as the primary vector for toxicity is inhalation, the use of ceramic largely mitigates any immediate biological hazard.

BeO possesses a Wurtzite crystal structure, beryllium and oxygen atoms being arranged in topologically equivalent HCP sublattices tetrahedrally co-ordinated with respect to one another[159,160] (see figure 2.6c). As with α-Al_2O_3:C luminescence arises from anion vacancies, although spectral accounts in the literature differ somewhat, possibly due to variations in fabrication technique. A TSL emission near 335 nm,[35] and an optically excited emission bands at 320 nm and 365 nm attributed to F^+ and F-centres are reported for synthetic beryllia.[161,162] More recent measurements of the OSL emission describe a band emission at 370 nm with a shoulder near 310 nm,[35] while an RL emission peaking near 380nm under ^{137}Cs irradiation is also reported.[88]

2.3.4 Organic Plastic Scintillators

Due to the relative ease of fabricating large or convoluted sensitive volumes from plastics, organic plastic scintillators are favoured in numerous particle detection systems from large area contamination monitors to high energy particle physics research.[70,163] Research into radiotherapy dosimetry applications dates back at least two decades[164,165] and is driven primarily by excellent radiological equivalence to water. The majority of published radiotherapy applications research involving organic scintillators utilises the prefabricated PVT scintillators (BC-xxx) and PST scintillating optical fibres (BCF-xx) from Bicron/Saint-Gobain listed in table 2.1. These detectors typically have short wavelength emissions, rapid decay of luminescence, and superior water equivalence in comparison to current inorganic materials. Radiation tolerance is acceptable, with BC-404 and BC-408 reported to withstand up to 10^4 Gy, albeit with considerable loss of transparency and light output.[166,167]

While plastics possess many of the properties highly desirable for radiotherapy dosimeters, none of the base materials commonly employed have useful scintillation efficiency or transparency at the wavelength of their near ultraviolet emission. The addition of an aromatic[vi] primary fluor is required to raise light output to levels comparable to reference scintillator materials such as crystalline anthracene or NaI. Concentrations up to 4% are typical,[169] for which the transfer of excitation energy from the solvent to the primary fluor can occur non-radiatively. As the Stoke's shift of the primary fluor is rarely sufficient to clear the absorption spectrum of the base plastic, additional fluors are usually required to shift the emission wavelength into the visible spectrum, with only the final emission detected in any significant intensity in all but the geometrically smallest samples. Shifting fluors are usually present in concentrations in the region of 0.1%,[169] resulting in radiative energy transfer from the primary fluor to the wavelength shifter(s). Organic compounds employed as both primary and wavelength shifting fluors include oxazoles, oxadiazoles, benzoxazoles, pyrazolines, oligophenylines, and polyphenol hydrocarbons.[70,163,169]

For organic scintillators, the luminescence is an intrinsic property of individual molecules rather than material structure, permitting the presence of other substances and thus wider scope for the creation of materials with general characteristics tailored to a given application. Plastic scintillators investigated as radiotherapy dosimeters utilize organic luminophors suspended in polystyrene

[vi] Aromatic compounds are cyclic, planar ring structures with a total of $4n+2$ atomic p orbitals, one on each atom of the ring. The prototypical example is the benzene ring (C_6H_6), of which many aromatic substances are derivatives, including the polycyclic benzine chains of anthracene and naphthalene.[168]

(PST), polyvinyl toluene (PVT), polyvinyl xylene (PVX), or polymethyl methacrylate (PMMA). If desired for specific applications, the solvent may also be a liquid.[67] In the case of PMMA, which does not possess the aromatic structure favoured for scintillation, an aromatic co-solvent such as naphthalene is required.[70] PST and PVT monomers are illustrated in figure 2.6d and 2.6e.

As implied above, the intrinsic emission of typical organic scintillators resides in the near ultraviolet. Wavelength shifting luminescent dyes are required in order to obtain longer wavelength emissions. Achieving red emissions may involve multiple shifts, reducing efficiency and also radiation tolerence, with each fluor in the series of emissions and absorptions presenting additional targets for damage.[170]

2.3.5 Fluoroperovskites

Fluoroperovskites are ternary fluorides of general form ABF_3 possessing a crystalline structure related to that of $CaTiO_3$, the mineral known as perovskite. This requires that A and B be monovalent and divalent cations respectively and that A have ionic radius in excess of B. Such materials have been studied in depth in past decades as potential solid state laser hosts,[171–184] with recently renewed interest focusing on SL and RL in the context of radiation dosimetry.[2,185–194] Luminescence activators reported in the literature include a wide range of divalent and trivalent transition metal and lanthanide cations in a similarly wide range of fluoroperovskites.

Given the large variety of cations found in perovskite type crystals, it is not surprising that some diversity in structure is observed. A precursory indication of the likely structure of a given perovskite can be obtained from the Goldschmidt tolerance factor, t_G, defined in equation 2.33. As applied to fluoroperovskites, r_A and r_B are the ionic radii of the A and B site cations, and r_F that of the fluorine anion. For $0.9 < t_G < 1$ the structure is usually cubic, with the A site 12-fold fluorine co-ordinated and the B site 6-fold. An example of a cubic fluoroperovskite, $KMgF_3$, is illustrated in figure 2.6f. For $0.7 < t_G < 0.9$ the lattice distorts in order to contract and accommodate a relatively small A site cation, rotating the BF_6 octahedra and so reducing the symmetry of the A site. If $t_G > 1$, hexagonal variants occur in which the BF_6 octahedra have common faces. For $t_G < 0.7$ a trigonal lattice is possible. This interpretation of t_G assumes purely ionic bonding in the use of ionic radii and so has useful predictive power only for highly ionic crystals.[195]

$$t_G = \frac{r_A + r_F}{\sqrt{2}(r_B + r_F)} \tag{2.33}$$

Luminescence is often activated in fluoroperovskites by doping with luminescent species, typically rare earth and transition metal ions. Generally, the site of substitution will be that with the best matched ionic radii.[173,196] Rare earth dopants are therefore expected to integrate on the A site, the nature of which is often of little consequence, particularly for the lanthanides due to the weak interaction of the $4f$ valence electrons with the immediate crystal environment.[48] As the rare earth ions are almost always of higher valence than the host A cation, some form of charge compensation is expected. This may be realised as cation vacancies,[177,197] interstitial fluorine anions,[184,198] or integration of contaminants such as O^{2-} on anion sites.[199] Mismatched valence may also act to limit the achievable dopant concentration.[2]

Transition metals will typically be found on the B site. It is usual for the octahedral symmetry of this site to remain largely undistorted for the cubic, orthorhombic, and hexagonal perovskite structures mentioned above. Degeneracy of the two e_g and three t_{2g} levels is thus largely maintained

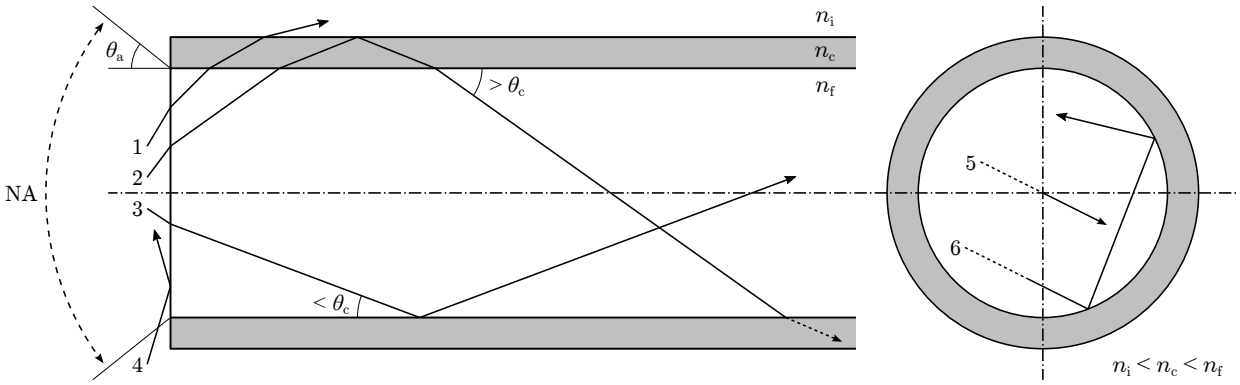

Figure 2.7: Geometric optics description of light in optical fibres. Illustrated modes of propagation are (1) radiated, (2) cladding, (3) guided, (4) rejected, (5) meridional, and (6) skew. The fibre NA defines the acceptance angle, θ_a, within which incident light will result in guided modes. This is determined by the refractive indices of the fibre core, n_f, cladding, n_c, and incident medium, n_i.

for transition metals on this site. Given the place held by the fluorine ligand in the spectro-chemical series, B site transition metal dopants will usually form high spin complexes with relatively small crystal field splitting energies.[38,49]

2.4 Fibre Coupled Dosimetry

Use of optical fibres in radiation dosimetry dates back several decades, to the initial reports of fibre mounted BC-400 scintillators for radiotherapy dosimetry.[164,165] The optical fibre itself has also been used as a dosimeter, exploiting both the luminescence of radiation induced colour centres[200] and the TSL properties[201] of fused silica (SiO_2) optics. Radiotherapy applications benefit from the remote nature of fibre optic dosimetry and the potential for physically small sensitive volumes, and so the role of the optical fibre is limited to the transport of light. This section will address some of the practical aspects of implementing fibre coupled dosimeters.

Nominal optical and radiometric data for a range of materials employed in experimental FCD hardware is presented in figure 2.8. Materials employed by more conventional radiotherapy dosimetry technologies are also included for comparison. This nominal data was compiled from literature to inform the design of prototype hardware and the interpretation of experimental results. None of the actual samples used in this work, many of which require additional trace impurities to activate luminescence, are directly represented.

2.4.1 Fibre Optics

Optical fibres are flexible light guiding structures of arbitrary length, fabricated most often from silica glass or polymer with diameters ranging from microns to millimetres. The most common geometry is a cylindrical core concentric to an optical cladding of lower refractive index, with the majority of the cross-sectional area in larger diameter fibres allotted to the core.[202] Optical fibres are manufactured by heating and drawing a solid preform with the required refractive index profile into a thread of the desired diameter. Diameters down to 2 μm are routinely made in this fashion.[203,204]

For optical fibres with core diameters many times larger than the wavelengths involved, propagation of light along the fibre is well described by geometric optics. The critical angle, θ_c (see

figure 2.7), for total internal reflection at the boundary of the core and cladding materials implies a cone within which light will be captured at the face of a fibre and propagated. This cone can be described by an acceptance angle, θ_a, but is usually quantified in terms of numerical aperture (NA), defined in equation 2.34. NA is a measure of light gathering power dictated in this context by relative refractive indices, specifically that of the fibre core, n_{f}, fibre cladding, n_{c}, and the incident medium n_{i}. It provides little if any indication of the expected divergence of light emitted at the distal end of the optical fibre.[203, 205]

$$\mathrm{NA} = \frac{n_{\mathrm{f}}}{n_{\mathrm{i}}}\sqrt{n_{\mathrm{f}}^2 - n_{\mathrm{c}}^2} = \frac{n_{\mathrm{f}}}{n_{\mathrm{i}}}\sin\theta_{\mathrm{a}} \tag{2.34}$$

There are multiple propagation modes which satisfy the conditions for total internal reflection, each with a different path length and transit time, thus photons launched coincident in time will disperse during propagation over any appreciable distance. Higher modes are those propagating at angles closer to θ_{c}, and cladding modes those slightly in excess of θ_{c} but which are refracted sufficiently to be reflected from the interface of the outer cladding surface. For fibres with cylindrical symmetry, modes may also be described as meridional if propagating in a plane through the fibre axis, otherwise as skew modes,[204, 206] see figure 2.7.

When fibre diameters are on the order of the wavelength of light transmitted, the wave nature of light can no longer be neglected and the optical fibre is better described as a dielectric waveguide. In this context, the lowest order modes propagating parallel to the fibre axis are transverse electromagnetic (TEM), meridional modes may be either transverse electric (TE) or transverse magnetic (TM), and skew propagation requires hybrid modes. For telecommunications applications, where maximising bandwidth is crucial, core diameter is reduced to less than 10 μm for infrared wavelengths, eliminating all but the fundamental TEM_{00} mode and so preventing intermodal dispersion.[203] It is also typical of telecommunications grade fibre, single or multi-mode, to have low NA as this precludes launching of higher order modes.[202]

FCD systems employ optical fibres simply as light pipes, for which multi mode fibres with more convenient NA and diameter are preferred. Bandwidth is relatively unimportant, but maintaining low signal loss requires some care in the management of fibre interfaces. Equation 2.35 defines the insertion loss, in dB, encountered when fibres of mismatched diameter are directly coupled. Loss is only experienced when area of the source fibre core face, A_1, is larger than that of the receiving fibre, A_2.[204]

$$\alpha = 10\log\left(\frac{A_1}{A_2}\right) \quad A_1 > A_2 \tag{2.35}$$

When coupling between a fibre of larger numerical aperture, NA_1, to a lower, NA_2, a range of higher order guided modes supported in the source fibre will become cladding and radiative modes in the receiving fibre. The minimum loss in this scenario may be calculated using equation 2.36. As is the case for diameter mismatch, such losses are only experienced in one direction of propagation. A similar mechanism of loss may occur at the interface between the optical fibre and remote dosimeter material. Refractive indices of the materials commonly used in fibre optics and the materials described in § 2.3 are illustrated in figure 2.8a.

$$\alpha = 10\log\left(\frac{\mathrm{NA}_1}{\mathrm{NA}_2}\right)^2 \quad \mathrm{NA}_1 > \mathrm{NA}_2 \tag{2.36}$$

Lateral misalignment reduces the area of core face overlap, with the resulting loss approximated for a small misalignment, δ, in fibres of identical diameter, d, using equation 2.37. Misalignment results in losses for light propagating in both directions. Insertion loss due to angular misalignment is negligible for angles up to a few degrees.[204]

$$\alpha = 10 \log \left(\frac{1}{1 - 4\delta/(\pi d)} \right) \quad \delta \ll d \tag{2.37}$$

Other sources of loss at fibre couplings include conversion to unguided modes following scattering from poorly polished end faces or with excessive bending radius, and return loss due to back reflection when a small air gap exists between abutted fibre faces. For large diameter fibres, the elimination of air gaps by maintaining high pressure contact is not feasible.[202, 204] For operation at visible wavelengths the air in the gap can instead be displaced with an index matching gel or liquid.

Modern glass optical fibre is fabricated from fused silica[vii] and has been refined to near the theoretical performance limits[202, 206] in response to the needs of the telecommunications industry. Both single-mode and multi-mode fibres are widely available with either graded or stepped refractive index profiles, obtained by doping with phosphorous, germanium, boron, or fluorine, enabling a selection of NA. In larger diameters, bending radius and flexibility becomes limited.[202] Where larger NA is desired polymer clad silica fibres may be used, for which the silica attenuation is realised at visible and ultraviolet wavelengths and some influence of the polymer absorption peaks must be tolerated in the infrared.[204]

Attenuation in silica optics is primarily attributed to electronic absorptions, molecular vibrations, and Rayleigh scattering. Losses intrinsic to silica itself include a fundamental absorption edge in the ultraviolet at energies approaching the band gap near 8 eV,[207] absorptions from molecular vibration in the infrared near 9 μm, and microscopic defects which promote broad spectrum scattering losses. Being an amorphous substance, the band gap of fused silica glass is not sharply defined[208] and contributes to electronic absorption even at near ultraviolet wavelengths. The sum of harmonics from the molecular absorption result in a rise in attenuation at wavelengths beyond 1.6 μm, and so a global minimum occurs in attenuation near 1.55 μm, where Rayleigh scattering dominates. Attenuation in this window can be as low as 0.2 dB/km for single-mode fibre,[206] or about 15 dB/km in polymer clad silica optics.[209]

Extrinsic losses due to metal impurities are low in modern silica optics for which a hydrogen-oxygen flame is often used to heat the preform. Trace water contamination occurs instead, for which the corresponding molecular OH^- absorption occurs at 2.73 μm, with harmonics at 1.39 μm, 1.24 μm, and 950 nm. These are carefully controlled in low OH fibre intended for use at infrared wavelengths, and permitted where improved ultraviolet performance is preferred.[202] Differences in absorption for low OH and high OH silica are shown in figure 2.8b.

The polymer of choice for modern plastic fibre optics is PMMA, with PST and polycarbonate based fibres exhibiting higher scattering loss and vulnerability to atmospheric moisture. In this material, optical absorption at short wavelengths occurs following electronic transitions between the molecular orbitals of covalent bonds, particularly the C=O double bond,[218, 219] while infrared and visible wavelength loss is largely due to vibration of C–H bonds.[220] Water molecules may be absorbed in humid environments leading to additional near infrared losses.[218] Transparency

[vii] Fused silica is synthetically derived in order to attain higher purity than would usually be possible with the mineral derived fused quartz. Both terms refer to amorphous silicon dioxide.[82]

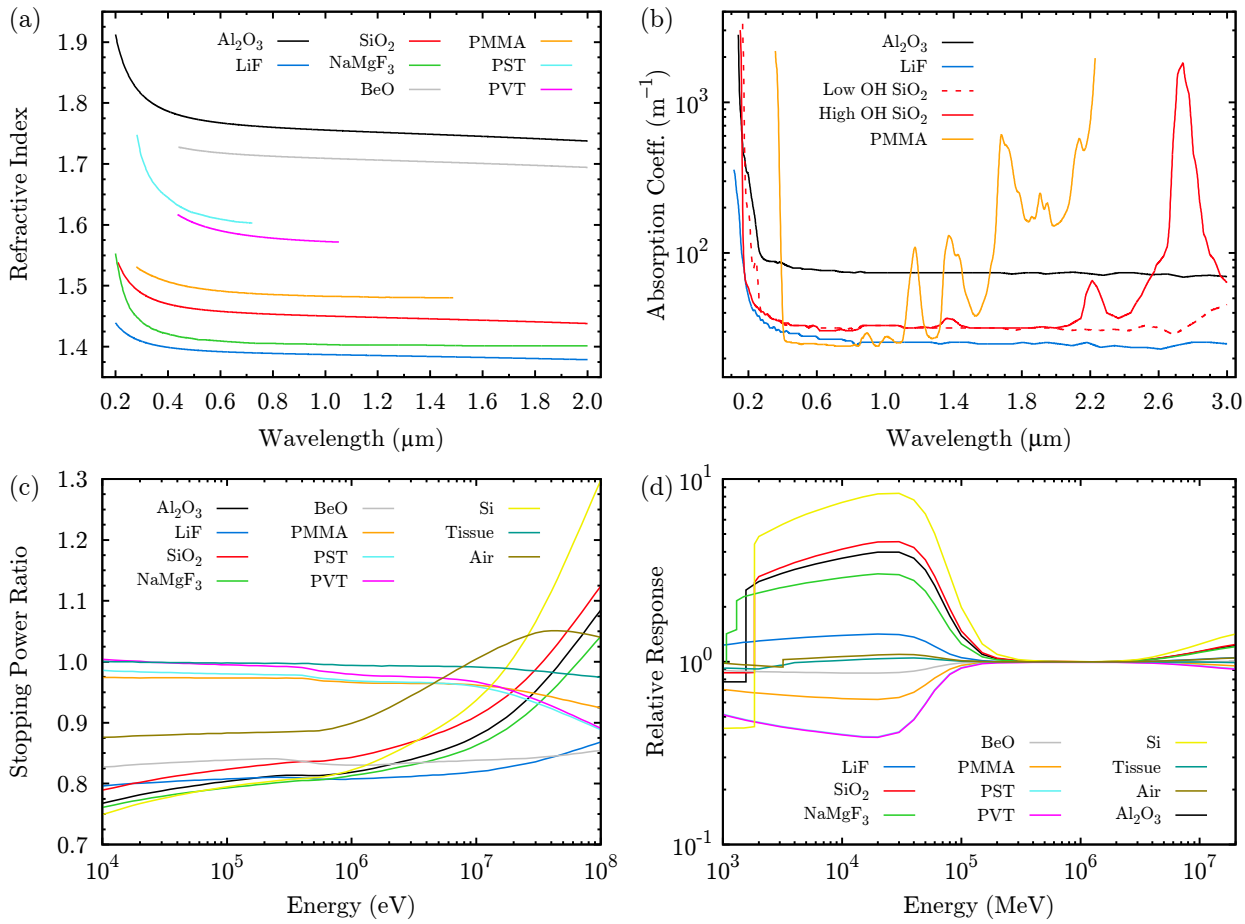

Figure 2.8: Properties of optical and dosimetry materials of interest for FCD systems, sourced from published literature,[90,207,208,210–216] the NIST x-ray mass attenuation coefficient tables,[20] and electron stopping power and range tables.[217] Includes wavelength dependence of (a) refractive index, and (b) absorption coefficient, and spectrally resolved (c) stopping power ratios, and (d) relative energy dependence. Both (c) and (d) are relative to liquid water at standard temperature and pressure, with (d) calculated using equation 2.18 for E_0 equal to the average emission of ^{60}Co. Data is given for pure materials, properties of active dosimeter materials may vary slightly due to the presence of impurities required for the activation of luminescence.

recovers at wavelengths on the order of 10^{-3} metres.[204]

Plastic fibres are typically highly dispersive due to the inability to create a sufficiently smooth core to cladding interface with relatively large polymer molecules. Attenuation minima occur in windows at 520 nm, 570 nm, and 650 nm, between the PMMA absorption peaks, with the lowest attenuation of approximately 85 dB/km at 570 nm.[204,221] The use of perfluorinated PMMA can theoretically reduce attenuation to levels typical of silica fibre, but attenuation better than 25 dB/km at the most optimal wavelengths, 850 nm to 1300 nm, has not yet been achieved.[204]

Cladding of plastic fibres is typically fluorinated polymer, for which attenuation is on the order of 10^4 dB/km, effectively absorbing cladding modes over short distances. High order modes also present additional opportunities for absorption of the evanescent wave which extends into the cladding at each reflection, resulting in a mode dependent attenuation which is not observed in silica.[222] Typical PMMA fibre with fluorinated cladding has NA near 0.5, which can only be modified through use of different polymers. For example, polycarbonate optical fibre which has a NA closer to 0.9.[204]

While the optical performance of polymer fibres is generally poor compared to silica, the use of plastics realise clear practical advantages in terms of cost, mechanical robustness, radiation

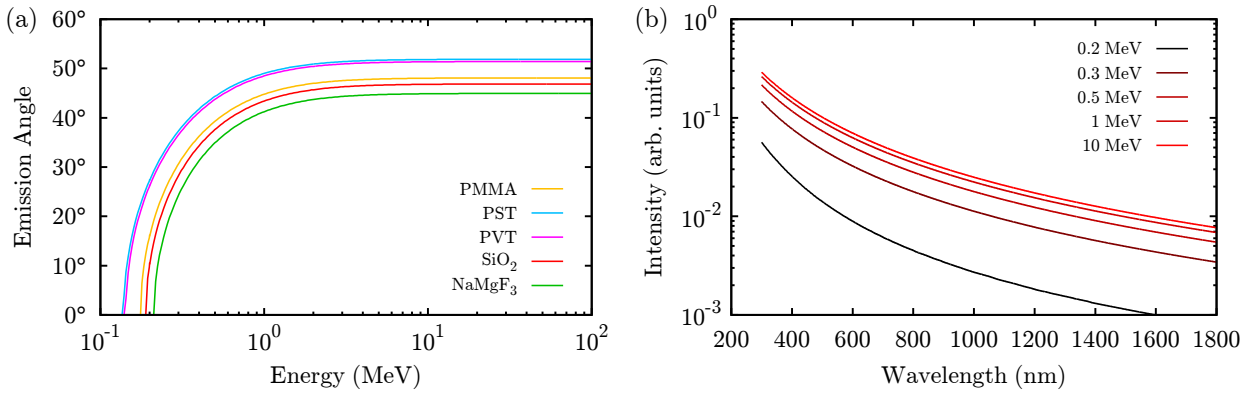

Figure 2.9: Influence of electron relativistic energy on Čerenkov (a) emission angle and (b) spectral intensity, as calculated with equations 2.38a and 2.38c respectively. Curves in (a) are for the refractive index of the indicated material at 500 nm. The threshold energies predicted by relation 2.38b are reflected in the 0° energies. Spectra plotted in (b) include the wavelength dependent refractive index data for PMMA shown in figure 2.8a.

tolerance, and relative ease of termination.

2.4.2 The Čerenkov Problem

Čerenkov photons are generated where the phase velocity of charged particles exceeds the speed of light in a dielectric medium. Emission occurs at an angle of θ with respect to the particle trajectory,[223] dictated by the refractive index of the dielectric, n, and the relativistic phase velocity of the charged particle, $\beta = v_p/c$, as per equation 2.38a. As θ is only defined for $\beta \geq 1/n$, a minimum kinetic energy for Čerenkov emission can be readily derived from the definition of total relativistic energy.[33] When this condition (relation 2.38b for electrons) is met a conical wavefront results, the apex of which is coincident with the supraluminal charge.[224] The spectral distribution is wide, covering the entirety of the visible spectrum with a theoretical λ^{-2} dependence. Spectral intensity can be calculated using the Frank-Tamm equation[224,225] (equation 2.38c), in which α is the fine structure constant.

$$\text{(a)}\ \cos\theta = \frac{1}{n\beta} \qquad \text{(b)}\ E \geq m_e c^2 \left(\frac{n}{\sqrt{n^2-1}} - 1 \right) \qquad \text{(c)}\ \frac{dN^2}{dx\,d\lambda} = \left(1 - \frac{1}{\beta^2 n^2} \right) \frac{2\pi\alpha}{\lambda^2} \tag{2.38}$$

Applying the above to either silica or PMMA fibre optics, it is found that electrons with kinetic energy in excess of approximately 170 keV will generate Čerenkov photons in these media, as seen in figure 2.9a. All penetrating x-ray and γ-ray radiations employed in radiotherapy generate a substantial fluence of secondary electron radiations at energies in excess of this threshold. As it is impossible to avoid exposure of the fibre optics in any practical FCD, a stem signal of Čerenkov photons must be contended with. This is observed experimentally, along with a small contribution from autofluorescence.[85,226,227] The fluorescence component has been reported to be more substantial in low OH than in high OH silica optics, and lower still for PMMA fibres.[228]

This stem signal is not trivial to suppress. Peak intensity Čerenkov emissions are well aligned in wavelength with the optimal sensitivity window of quartz or glass faced photomultipliers[227,229] and also the emission spectra of many RL and scintillator materials.[35] Furthermore, the directionality of the Čerenkov emission coupled with the criteria for guided modes in fibre optics gives rise to

strong angular dependence of the detected stem signal. The captured fraction of Čerenkov photons can be minimised by reducing the core diameter and NA of the readout fibre optic. This also reduces the efficiency of light collection from the active dosimeter element and so is unlikely to result in a net gain in signal to noise ratio (SNR).[230] Instead the refractive index of the dosimeter, n_{i} in equation 2.34, might be adjusted to increase θ_{a} and so also the collected light from the active volume. In practice this means employing different luminescence materials.

Various methods of suppressing the Čerenkov stem signal have been explored. These include, in approximate order of inefficacy, subtraction of the signal in an additional parallel fibre with no coupled dosimeter,[231–233] simple chromatic filtering,[85,234] use of air core fibres for the irradiated segment,[233,235,236] temporal discrimination in pulsed radiations exploiting the prompt (10^{-10} second) nature of Čerenkov emissions,[237–239] and spectral discrimination exploiting the approximate spectral constancy of the Čerenkov component.[240–242]

Due to the broad spectrum nature of Čerenkov emissions, simple chromatic filtering can only hope to improve the ratio of useful to background signal. While dual fibre subtraction can be effective if implemented with care, it is only reliable for static irradiation geometries. At this time, chromatic discrimination appears the preferred method although it is not without limitations. As the stem signal is a superposition of fluorescence and Čerenkov light, the ratio of which varies with beam energy and irradiation geometry, it is not strictly spectrally invariant as assumed. The resulting error depends on the conditions of calibration and use.[243]

Temporal discrimination is most effective when employed with RL detectors like α-Al_2O_3:C with longer lived emissions, but has also been demonstrated using the BC-444 type plastic scintillator.[101,237] This method is incompatible with the fast emissions from the remainder of the BC-*XXX* series scintillators,[66] and so organic plastic scintillators with longer lived emissions are actively sought specifically for this purpose.[69,238]

The air core fibre approach has been reported sufficient for the collection of usable beam characterisation measurements,[236] despite not addressing Čerenkov generated in the fibre train beyond the air core segment or dosimeter volume itself. While this approach appears effective in improving the Čerenkov to scintillation ratio, it requires two optical interfaces between air and higher refractive indices, which gives rise to back reflection loss. A twisted pair fibre has been proposed to compensate for Čerenkov photons generated beyond the air core segment by radiation scattered out of field.[244]

A much less explored possibility lies in the use of near infrared emitting dosimeter materials, for which equation 2.38c would imply a much more favourable Čerenkov to signal ratio. Feasibility of this approach has been recently demonstrated using the single line emission of Yb^{3+} doped into SiO_2 optical fibres.[245]

2.4.3 Optical Design Constraints

Prototype FCD systems appear in the literature utilising α-Al_2O_3:C,[114,121,246] BeO,[247–249] organic plastic scintillators,[164,231] scintillating polymer optical fibres,[250,251] $NaMgF_3$,[194] and rare earth doped SiO_2.[245,252] These are all implemented as some variation on the simplified schematic of a basic FCD system shown in figure 2.10.

The basic concept entails a sample of luminescent material coupled to the distal end of an optical fibre, where it can be safely exposed to ionising radiation without exposing the readout equipment or operator. A portion of the light emitted during irradiation is captured in the fibre

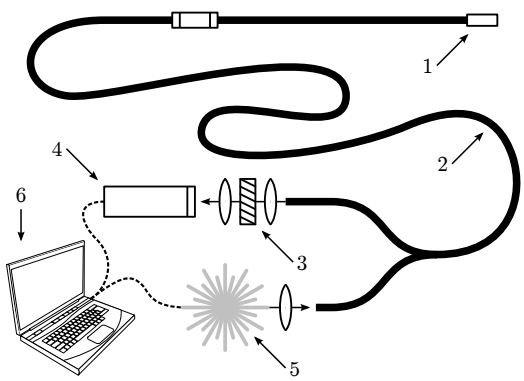

Figure 2.10: Diagram of a basic fibre coupled dosimeter, indicating key components required for both RL and OSL data acquisition in a radiotherapy dosimetry context. These include (1) active dosimeter element, (2) transmission fibre optic, (3) optical filters, (4) detector system, (5) light source, and (6) computer or suitable electronics to coordinate operation of (4) and (5).

optic and transported to the detection hardware, with 15 to 20 metres required to traverse the shielding maze of a typical radiotherapy treatment vault. Stimulation light for OSL measurements may also be delivered along the same optical fibre. Regardless of the material used for the active dosimeter element, care must be taken in the optical design of FCD equipment. Optical efficiency in particular is one of the principle factors dictating the achievable SNR, which directly impacts on measurement uncertainty.[253]

When detecting low levels of light SNR can be calculated using equation 2.39, in which ϕ is the optical photon fluence under measurement, η the detector quantum efficiency, t the integration period, s_d and s_r the variance in thermal dark signal and readout noise respectively, and N the number of averaged measurements.[254,255] For large signal with respect to s_d and s_r the calculation can be reduced to ratio of the arithmetic mean, μ, to the standard deviation, σ.

$$\mathrm{SNR} = \frac{\sqrt{N}\phi\eta t}{\sqrt{\phi\eta t + s_\mathrm{d} t + s_\mathrm{r}}} \simeq \frac{\sqrt{N}\mu}{\sigma} \tag{2.39}$$

In noise limited systems it is typical to seek gains in SNR by increasing N, or in some cases t. The direct relationship between SNR and uncertainty can be seen in the large signal limit, where it approximates the reciprocal of unexpanded type A uncertainty. Note that this expression implicitly assumes Poisson counting statistics, in that the term $\phi\eta t$ appears in both the numerator representing the mean signal value, and in the denominator representing the signal variance, which is shot noise.

Most, if not all, fibre coupled dosimeter prototypes appearing in the literature to date employ a luminescence material sample butt-coupled to a transmission fibre of comparable dimensions. If the luminescence emission is isotropic, the coupling efficiency is dictated largely by numerical aperture and can be readily estimated from solid angle which falls within the cone defined by the fibre acceptance angle. Collection efficiency at this point is typically the most significant limitation on optical performance,[205] with little scope in practice for optimisation through manipulation of refractive indices.

Optical absorption is primarily of concern for materials used in transmission optics. While modern fibre optics are achieving close to theoretical performance limits, the realised attenuation length is invariably less favourable than the attenuation coefficient of the core or cladding materials in isolation. The data presented in figure 2.8b is for the raw materials.

The performance of available detector technologies must also be considered. For luminescence emissions in the blue and ultraviolet region, high performance photo-multipliers may be employed and the ultimate in sensitivity achieved by employing single photon counting methods.[256] Of the

wide spectrum supported by available fibre optic technology, this region is also the most afflicted by the difficulties associated from Čerenkov radiation. Radiation damage effects, particularly those associated with colour centre absorptions, are also expected to be most severe in this region.[78,257]

In the near infrared, small area Si photodiodes are useful out to about 1 μm, while InGaAs photodiodes can be pushed to approximately 2 μm, beyond which thermal dark currents likely become prohibitive for FCD applications. Peltier cooled units provide a useful compromise between poor room temperature performance and the impracticality of cryogenic coolants. Excessive cooling results in a substantial shift in the long wavelength limit of semiconductor detectors to higher energies.[258]

2.4.4 Dosimetric Design Constraints

Electron stopping powers are presented in figure 2.8c as ratios to water, as they would be applied to Bragg-Gray or Spencer-Attix cavity theory. Equations 2.15 and 2.23 can in principle be used to formulate corrections for the energy dependence of a given dosimeter, but in practice such corrections are only applicable for a given energy fluence spectrum. This approach is useful for reference dosimetry but cannot be applied under a wider range of irradiation conditions. Even if $\Psi_{\mathrm{E}}(E)$ can be adequately determined, for example via Monte Carlo methods, the conditions for the application of cavity theory must also be met. Favoured materials are those for which such corrections would be small, thus minimising the influence of the experimental uncertainty associated with the limited knowledge of $\Psi_{\mathrm{E}}(E)$.

The energy dependence data shown in figure 2.8d is referenced to the mean decay energy of ^{60}Co, this being more well defined than an arbitrary nominal radiotherapy x-ray quality. The relative performance of one material versus another is evident but this does not necessarily translate directly to many of the more interesting usage scenarios in radiotherapy. For example, the material with the largest photoelectric enhancement of those shown in figure 2.8d, silicon, can be used under limited conditions for small field dosimetry in radiotherapy.[12,14,29]

While considerable attention is inevitably given to the radiological properties of active dosimeter materials, those of any substances in close proximity should also be considered. For the collection fibre placed in direct contact with the active dosimeter, polymer optics are favoured. If non-tissue equivalent materials are employed in the construction of the detector itself, at minimum the impact on system energy and angular response must be carefully considered.[259]

2.4.5 Radioluminescence and Scintillation Detectors

At present, there exist a range of luminescence materials believed suitable for realising clinical FCD systems. These can be broadly categorised as either organic plastic scintillators or inorganic materials exhibiting radioluminescence, both of which have been researched to fill essentially the same roles in radiotherapy. Both are readily miniaturised[65,236,260] and have demonstrated potential for novel *in vivo* applications in brachytherapy.[114,231,246,261]

As described in § 2.2.7, sensitivity of an RL dosimeter is dependent on the population of trapped charge in the material, and therefore dependent on previously absorbed dose.[65] While this effect can be mitigated by a suitable priming irradiation, the primed state is potentially degraded by thermal fading.[35,66] If significant low temperature TSL occurs, the temporal resolution and temperature dependence of the system will also be degraded. Organic plastic scintillators are

effectively exempted from such complications by their lack of active charge trapping sites.[70]

The longer emission lifetimes typical of RL dosimeters may be exploited to suppress Čerenkov stem signal.[237–239] Rapid decay (10^{-9} second) of luminescence is a common characteristic of plastic scintillator detectors,[66,69,238] precluding this solution to the Čerenkov problem for all but perhaps BC-444. This is not strictly a disadvantage as a short emission lifetime potentially allows dosimetry of individual pulses of radiation delivered from medical linear accelerators.[250]

Plastic scintillator detectors are relatively innocuous in biological terms and thus well suited for *in vivo* dosimetry. Inorganic luminescence materials encompass a larger range of chemical elements and some of the compounds investigated for their luminescent properties are known toxins and carcinogens.[35] This does not immediately preclude medical applications with sealed FCD constructions, but may limit use as *in vivo* dosimeters. Unlike plastic scintillators, inorganic materials in which luminescence arises from impurity doping can attain a considerably wider range of emission wavelengths and lifetimes. This affords a much higher degree of scope for the exploration of solutions to practical difficulties, including the Čerenkov problem.

Organic scintillator materials have a distinct advantage for applications highly sensitive to deviations from water equivalence in the dosimeter itself. Mass and electron density of these materials differs from that of water by only a few percent, and with a similar atomic composition the transport of charged radiation is not expected to be perturbed significantly between the dosimeter and a surrounding water equivalent medium.[164,165,230] Inorganic RL detectors studied to date for medical applications have acceptable but higher effective atomic numbers[2,35] and intrinsically different structure and atomic composition to either water or tissue.[32]

2.5 Summary

The supporting theoretical concepts and practical aspects of fibre coupled dosimetry have been explored in this chapter. An introduction to the relevant radiotherapy and luminescence physics has been given, selected existing solid state dosimetry materials introduced, and many practical engineering aspects of fibre coupled dosimeters have been discussed.

Chapter 3

Experimental Methods

Details of equipment and experimental techniques are given in this chapter. This is divided into the materials fabrication and characterisation work performed in the research laboratories of Victoria University and Callaghan Innovation, and the radiotherapy evaluation of both materials and dosimeter systems undertaken at Wellington Regional Hospital. Development of the prototype dosimeter hardware, which represents a significant volume of work in itself, is covered separately in chapter 5.

3.1 Sample Preparation

Samples denoted J*YYMMNN*[i] were fabricated as part of this study, while the fluoroperovskite samples denoted AE*XXXXX* were prepared prior to this work for use with the Mk-II dosimeter prototype. The non-tissue equivalent crystal $RbMgF_3$ was also included in this study to provide additional comparative data in the evaluation of energy dependence.

3.1.1 Neighbourite

The focus of this work is the fluoroperovskite $NaMgF_3$, which occurs naturally as the mineral neighbourite.[86] The structure of this crystal is derived from the ideal cubic perovskite structure (see figure 2.6f) by rotation of the MgF_6 octahedra by 17.9° at room temperature about the [111] axis.[262] This results in the primitive orthorhombic unit cell containing four formula units illustrated in figure 3.1a. Bonding in the MgF_6 complex is highly ionic, while the character of bonds in the NaF_8 polyhedra is mixed.[216] Fluorine co-ordination of the *A* site is reduced to 8 and the Na^+ cation displaced by 0.47 Å in the plane of the *a* and *b* axes from the centre of the NaF_8 polyhedron.[262] These distortions are consistent with the value of 0.87 calculated for t_G using standard ionic radii[141] for Mg^{2+} and Na^+ with co-ordination numbers 6 and 8 respectively. The space group is *Pbnm*.

The described structure is weakly temperature dependent, with the unit cell contracting by approximately 3 pm along *a* and *c* and less than 1 pm in *b* between 300 K and 50 K. No phase transitions occur below or in the vicinity of room temperature,[262] while tetragonal and cubic phases are reported above 1030 K and 1170 K respectively.[86] Despite the distortion of the $NaMgF_3$ unit cell, the MgF_6 octahedra largely retain their symmetry with the six Mg−F bond lengths differing by less than 1 pm at room temperature. At 300 K the lattice parameters reported in the literature[262] are $a = 5.3622$ Å, $b = 5.4885$ Å, and $c = 7.6694$ Å.

[i]Samples identified by year *YY* and month *MM* of fabrication, plus a sequence number *NN*.

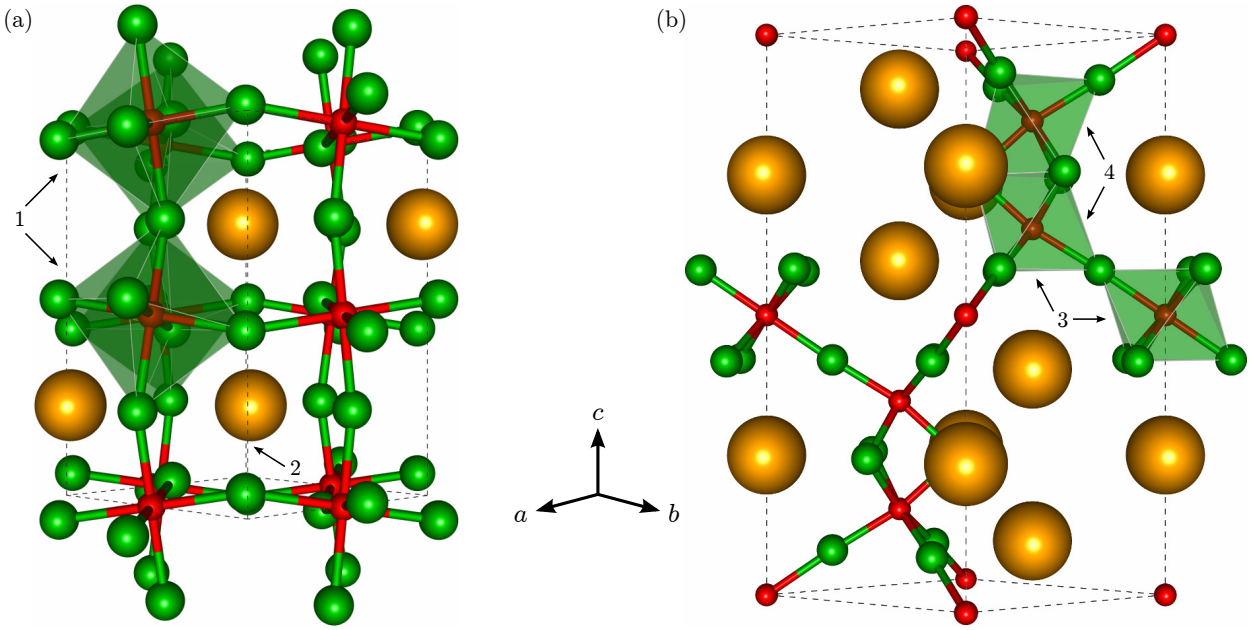

Figure 3.1: Orthorhombic unit cells for (a) pseudo-cubic $NaMgF_3$ and (b) hexagonal $RbMgF_3$, with the Na^+ and Rb^+ cations (A site) in orange, Mg^{2+} cations (B site) in red, and F^- anions in green. Tilting of the MgF_6 octahedra (1) and displacement of the Na^+ cation (2) are illustrated for $NaMgF_3$, as are the inequivalent corner sharing (3) and face sharing (4) MgF_6 octahedra of $RbMgF_3$. *Structure graphics generated using VESTA*[113].

$NaMgF_3$ is a insulator with a band gap of 5.9 eV,[216] and so can facilitate the types of luminescence described in § 2.2.6 and § 2.2.7. It has been previously identified as a viable host for luminescent species with radiological properties suitable for applications in radiotherapy and personal dosimetry.[2] Optically, $NaMgF_3$ is relatively well suited for fibre optic dosimetry, with reasonable transparency attainable over short optical depths (see figure 3.3g) and a refractive index approximately matched to the most common fibre optic core materials, PMMA and SiO_2 (see figure 2.8a). It does not exhibit significant birefringence.[86]

A heavier fluoroperovskite, $RbMgF_3$, was also included in the study to provide additional comparative data. With a t_G value of 1.05 due to the relatively large Rb^+ cation, this material takes on a hexagonal perovskite lattice with six formula units in the unit cell and space group $P6_3mmc$.[263] Two distinct MgF_6 sites result, one with common corners and one with common faces,[2,192] see figure 3.1b.

3.1.2 Luminescence Ion Selection

While the anion defects which give rise to luminescence in α-Al_2O_3:C, BeO, and LiF do occur in $NaMgF_3$, at least following irradiation,[78,265] luminescence in this material is widely attributable to valence electron transitions of deliberately introduced impurity cations. These impurities may reside on either of the perovskite A or B sites and are present in relatively small amounts, occupying at most a few percent of available cation sites. Thus the host contributes the vast majority of the material bulk and so dominates the physical and radiological properties. Luminescence characteristics may to some extent be tailored to a given application by selection of appropriate dopants.

In possessing two cation sites of contrasting radii, $NaMgF_3$ can readily integrate a wide range of luminescent transition metal and rare earth ions, of which many have previously been investigated

for this host,[55,184,264,266–273] although largely in contexts other than radiation dosimetry. As the observed luminescence in many cases involves intraconfigurational transitions, lifetimes on the order of milliseconds are typical. In the case of selected divalent rare earths, $4f \leftrightarrow 5d$ transitions with lifetimes several orders of magnitude shorter also occur. A range of emission energies are possible, from the near ultraviolet to the near infrared.

Desirable emission properties are dictated foremost by limitations in optical materials and available detector technologies, as discussed in § 2.4.3. There are three regions of interest for this study: 300–500 nm, 700–1000 nm, and 1500–1800 nm. At 300–500 nm the sensitivity and low noise of photo-multipliers is an indisputable advantage, provided a method of suppressing the Čerenkov background can be found. At 700–1000 nm, a reduction in the Čerenkov background is expected and emissions become well matched to the peak sensitivity of uncompensated Si photodiodes, whilst remaining within the low attenuation window of polymer optics (see figure 2.8b). Further into the near infrared, polymer optics and photo-multipliers are no longer viable but a substantial reduction in the captured Čerenkov fraction and freedom from colour centre absorptions is anticipated. All silica fibre optics have excellent attenuation properties in the region of 1500 nm, while beyond 1800 nm thermal noise in semiconductor detectors can pose a significant challenge.

Luminescence activators were chosen primarily with emission in these spectral regions in mind. Intense blue and near ultraviolet emissions[55,187] are expected from Yb^{2+} and Eu^{2+}, red emis-

	Dopant	C (%)	TTP	Z_{eff}	λ_{em} (nm)	Δ (nm)	τ (ms)
†AE00327	MnF_2	0.2	1	31	573	60	90
AE00519	EuF_3	0.1	2	12	360	1.5	0.8
†AE00562	EuF_3	0.2	1	31	358	3.0	2
AE01020	MnF_2	0.5	3	11	599	70	120
J140202	EuF_3	0.2	4	13	360	1.5	0.8
J140301	MnF_2	0.5	5	11	599	70	120
J140302	PrF_3	0.2	5	13	1070	20	0.07
J140303	EuF_3	0.1	6	12	360	1.5	0.8
J140304	ErF_3	0.5	6	17	1530	70	0.9
J140305	YbF_3	0.5	6	18	415	80	0.1
J140306	NiF_2	‡0.5	6	11	1620	300	0.1
J140307	SmF_3	0.5	6	16	697	2	10
J140308	CrF_3	‡0.8	6	11	745	100	0.2
J140401	NdF_3	0.6	5	16	1055	30	0.08
J140501	—	—	5	10	—	—	—
J140601	DyF_3	0.7	5	17	1005	20	2
J140801	MnF_2	0.5	5	11	599	70	120
J150401	NiF_2	‡5.0	7	12	1620	300	0.1
J150402	NiF_2	‡1.0	7	11	1620	300	0.1
J150501	—	—	7	10	—	—	—
J150502	SmF_3	1.0	7	18	697	2	10

Table 3.1: Summary of all samples investigated in this work, with $RbMgF_3$ samples marked†, else $NaMgF_3$. Reported dopant concentrations reflect the molar fractions of the dopant fluoride introduced during sample preparation, which is known to be an overestimate where marked‡. The listed furnace temperature profiles are illustrated in figure 3.2. Z_{eff} values are calculated using equation 2.17 with $n = 3.5$ and include the dopant at the indicated molar fraction. Spectral and lifetime data is tabulated for the primary emission of interest, which is generally the most intense. All figures are derived from this work, except lifetime data for the EuF_3 and YbF_3 doped materials which was sourced from the literature.[2,264]

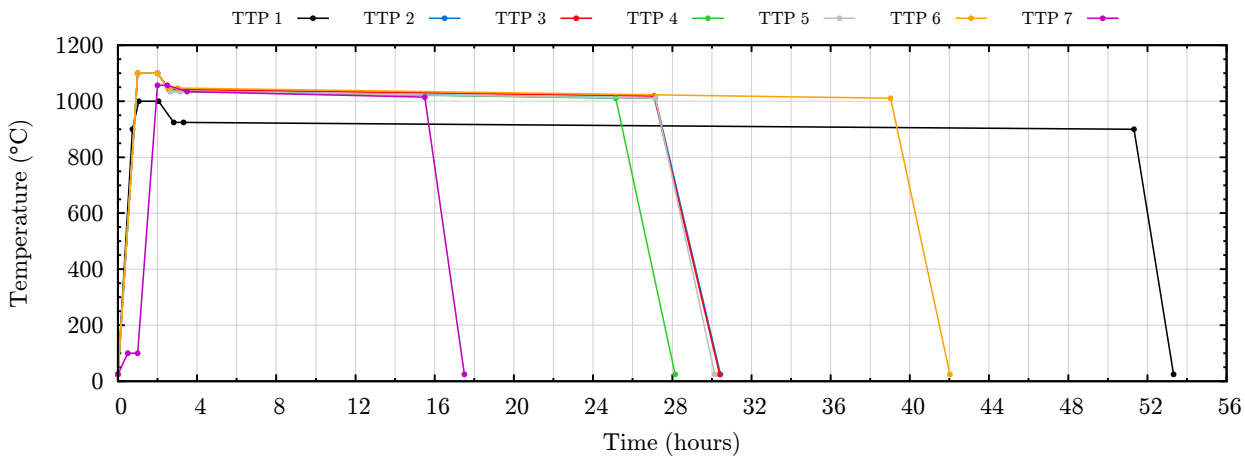

Figure 3.2: Time-temperature profiles programmed into the induction furnace. TTP 1 accommodates the lower melting point of $RbMgF_3$, while TTP 2 through TTP 5 as used for fabricating $NaMgF_3$ are essentially the same within the temperature uncertainty. TTP 6 is an extended run with a slower cooling rate. A short preheat at 100 °C is the most important feature of TTP 7.

sions[79,267] from Sm^{2+}, Sm^{3+}, Eu^{3+}, Yb^{3+} and Cr^{3+}, and both visible and near infrared emissions[48,272] from Ni^{2+} and many of the remaining trivalent lanthanide series. Those ultimately selected for study in $NaMgF_3$ are listed in table 3.1.

At approximately 600 nm, the Mn^{2+} emission in $NaMgF_3$ falls into a gap between the optimal sensitivity of fast photomultipliers and the longer wavelength region where semiconductor detectors are potentially useful in addressing the Čerenkov problem. This ion was included as it is unique with respect to the dopants listed in table 3.1, in that it emits in a single band from the lowest excited electronic state. Non-radiative population of this state from higher levels implies a high luminescence efficiency, and while the emission wavelength may not be optimal for the goals of this study it is by no means unviable from a technical standpoint.

3.1.3 Crystal Fabrication

All fluoroperovskite samples were prepared by a slow cooling method. Precursor materials were powdered and mixed in stoichiometric quantities and deposited in vitreous carbon crucibles for heating. The crucibles was then transferred to an induction furnace where the temperature was raised above the melting point NaF. After a short holding period, the melt was cooled through the melting point of $NaMgF_3$ (1030 °C)[274] over the course of 12 to 36 hours, resulting in the formation of transparent polycrystalline samples.

Only 'optical grade' NaF and MgF_2 of at least 99.9% purity were used, while fluorides used as dopants were not held to this standard as only trace quantities were required. Samples were prepared in a atmosphere of zero grade argon with water and oxygen content maintained below 1 ppm and 10 ppm respectively. Raw materials were stored under the same conditions.

The induction furnace consisted of a graphite susceptor which supports the crucible sealed in a vertical quartz tube. The susceptor and crucible were heated by eddy currents induced in the susceptor by an RF coil. Prior to heating the tube was purged with zero grade argon for a minimum of 30 minutes and positive pressure maintained until the furnace was returned to room temperature. An electronic process controller supplied with feedback from a thermocouple in contact with the susceptor was used to create a well defined time-temperature profile (TTP).

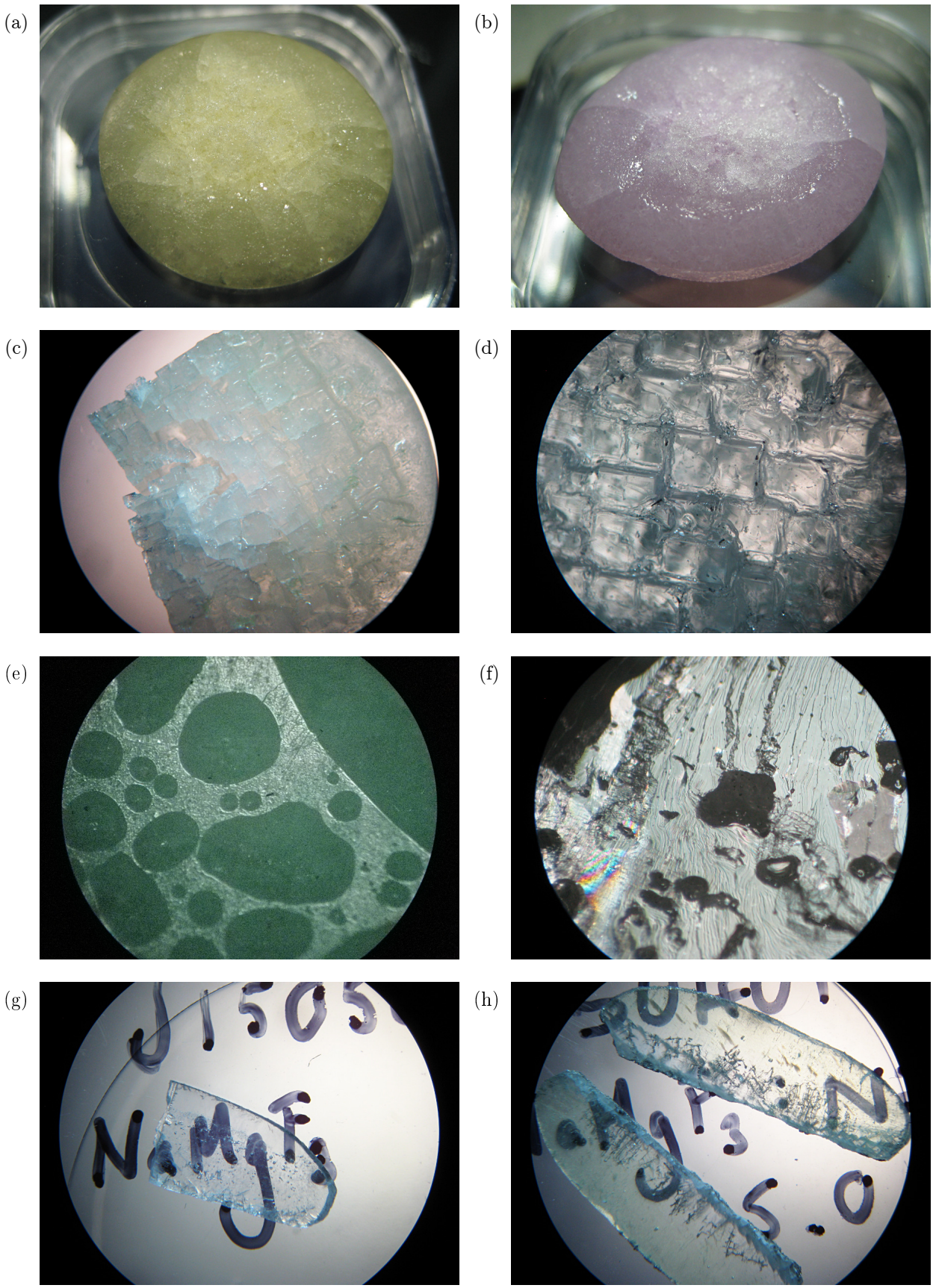

Figure 3.3: Photographs of crystal samples, illustrating dopant colouration for (a) J140307 ($NaMgF_3$:Sm) and (b) J140401 ($NaMgF_3$:Nd). Macroscopic lattice features as seen in a few samples are shown for (c) J140302 ($NaMgF_3$:Pr) and (d) J150402 ($NaMgF_3$:Ni). (e) Pockets formed by bubbles of gas trapped under the cooling melt are depicted for sample J140801 ($NaMgF_3$:Mn). (f) Enlarged detail of a fracture face in sample J140308 ($NaMgF_3$:Cr). Cut and polished pieces of (g) J150501 (undoped $NaMgF_3$) and (h) J150401 (heavily doped $NaMgF_3$:Ni) are included to illustrate achievable levels of transparency.

Some experimentation with the furnace TTP was undertaken in an attempt to improve consistency in crystal quality. Interpretation of the outcome of TTP adjustments was confounded somewhat by varied effects of the different dopants, but the most marked improvement was attributed to a 100 °C preheat, see TTP 7 in figure 3.2. This is expected to release moisture potentially acquired during the transfer to the furnace from the controlled environment under which samples were prepared. The precise rate of cooling through the melting point of $NaMgF_3$ appears relatively unimportant.

In a subset of samples, unused precursor material was found encapsulated in clumps up to a few millimetres in size. This was presumed to be MgF_2, of which the melting point is in the region of 1260 °C, higher than that attained by the furnace. This problem appears exacerbated by TTP 7 which achieves an even lower maximum temperature. Some dopants with still higher melting points, such as NiF_2 which is reported in the range of 1280 °C to 1430 °C,[275,276] instead retained deposits of the dopant precursor.

For samples J140501 and J140801 large cavities formed in the base of the sample, highly suggestive of trapped gas during cooling and crystal formation. This is illustrated in figure 3.3e. Smaller gas bubbles were observed in all samples of sufficient quality to cut and polish, and likely remained unrevealed in many others. All samples doped with either chromium or nickel crystallised with either or both excess dopant precursor or precipitated metal visible, see figure 3.3h. The reason for this remains unclear.

Despite the difficulties described above, as volumes on the order of cubic millimetres are sought for fibre mounting, even relatively poor quality samples can render usable dosimeter elements. Sample quality at both extremes of dopant concentration are shown in figures 3.3g and 3.3h after cutting and polishing to a thickness of approximately 1 mm.

3.2 Materials Characterisation

Materials characterisation was undertaken on bulk crystal samples in isolation, free from the influence of the readout systems and optics required of a fibre coupled dosimeter system (see figure 2.10). All samples fabricated were subject to x-ray diffraction, photoluminescence, and radioluminescence investigations. These initial measurements were used to identify those with potential utility in a fibre coupled system, which were then further investigated with thermoluminescence spectroscopy, optical absorption, and magnetisation studies as appropriate.

3.2.1 Irradiation of Samples

Most of the materials characterisation work described in the remainder of this section regards the response to, or the effects of, exposure to ionisation radiation. The majority of exposures were made using a Philips PW1730 x-ray generator retired from an obsolete powder diffractometer and fitted with a tungsten anode x-ray tube. All exposures were made at 40 kVp and 40 mA, with a 0.9 mm aluminium filter at the exit port. At the distances used for radioluminescence and thermoluminescence measurements a dose rate of 1.0 ± 0.5 Gy/s was measured using TLD-100.

For the study of radiation induced defect absorptions, higher energies were desired in order to provide a more uniform dose than achievable with 40 kVp x-rays. A Gammacell 300 Elan blood irradiator was used instead, in which samples were exposed to a ^{137}Cs line source with a nominal activity of 48 TBq.[277] A sample carrier for the Shimadzu UV-2100 spectrophotometer

was fabricated from black ABS plastic. For irradiation, the sample and carrier were sealed with a thin layer of polyethylene film, sandwiched in a paraffin wax mould, and inserted in a standard 50 mL polypropylene centrifuge vial. With secondary electron ranges on the order of the sample thickness[217] air gaps in the region of the sample may influence dose uniformity. This was addressed by fitting a plastic plug to the clear aperture in the sample holder and displacing air between the paraffin and polyethylene film with a water based ultrasound gel. Dose rate to TLD-100 at the sample location was 5.7 ± 1.8 Gy/min.

Irradiation in megavoltage x-rays was also undertaken, using the same geometries and dosimetry described in § 3.3.

3.2.2 X-ray Diffraction

Many of the key concepts of x-ray diffraction are concisely encapsulated in Bragg's law, given in equation 3.1 below. In this formula λ is the incident x-ray wavelength, n a positive integer, and d_{hkl} the spacing of the lattice plane (h, k, l) giving rise to x-ray diffracted intensity observed at angle θ.

$$n\lambda = 2d_{hkl} \sin\theta \tag{3.1}$$

Diffraction peaks are observed when the reflections from a lattice plane[ii] entail integer multiples of wavelength in additional path length.[33] As the crystal lattice comprises a highly regular structure in which said plane repeats many times, a very large number of reflections occur resulting in narrow diffraction peaks of measurable intensity. Readily observable diffractions occur for small n, and so optimal λ is on the order of d_{hkl}. This corresponds to x-rays in the keV regime, for which x-ray interactions with matter only involve atomic electrons, forming an image of electron density from which the locations of lattice atoms are inferred.[278,279]

Equation 3.1 only provides a geometric relationship between the lattice plane spacing and the angular position of the observed reflections. It follows that the values of θ for which diffraction is observed provide information regarding the unit cell shape and size, but from these angles alone little can be deduced regarding the atoms contained therein. This information is extracted from the relative intensities of each reflection, with the three most intense usually being sufficient to uniquely identify a known substance.[279]

Quantitative analysis requires an approximately monochromatic source of x-rays, in this case obtained by filtering of the characteristic x-rays from copper with a thin nickel foil.[279] The resulting spectrum is dominated by the $K\alpha_1$ and $K\alpha_2$ characteristic emissions of copper, of which reflections involving the latter were eliminated during post processing. Thus for the purposes of analysis, λ is assumed equal to Cu-$K\alpha_1$ at 1.5406 Å.

Given that this work is concerned essentially with a single substance, the structure of which has long since been solved,[86,262,280] diffraction measurements were required simply to confirm phase purity. All samples used were polycrystalline and so powder diffraction measurements were made, using a PANalytical X'Pert PRO powder diffractometer. This unit integrates a rotating sample stage, theta-theta goniometer, copper x-ray tube, and a Medipix2 based photon counting detector, all operated under computer control.

[ii] Lattice planes and their 'reflections' in x-ray diffraction patterns are theoretical constructs, not direct analogies to geometric optics.

Samples were ground to fine powder and loaded into plastic carrier discs, defining a cylindrical sample volume with diameter and height of 18 mm and 2 mm respectively. The height of this volume is effectively infinite for the x-rays energies involved. Diffraction data was collected at a resolution of approximately 0.01° over periods of up to 16 hours in order to clearly resolve numerous weaker reflections in the measurement range of 20° through 90° in 2θ. The beam was masked to width of 10 mm and height of 1° as defined at the goniometer focus and the sample rotated to mitigate preferred orientation effects.

Experimental data was processed using the PANalytical X'Pert HighScore+ software, with which the approximation of the Voigt function given below in equation 3.2 was fitted to the measured intensity. This expression is simply a linear combination of the Gaussian and Lorentzian functions in θ. The relative weight γ_n, position θ_n, and FWHM Δ_n, of the n^{th} reflection are treated as free parameters and the full pattern fitted to a summation over n. As low angle reflections are often subtly asymmetric, Δ_n was fitted independently above and below θ_n and the mean value reported. This fit includes peaks arising from Cu-$K\alpha_2$ x-rays which were then stripped, their positions readily inferred using equation 3.1. A broad background very weakly varying with θ was fitted using piecewise polynomials and subtracted during the fitting process.

$$I_n(\theta) = \frac{2\gamma_n}{\pi\Delta_n}\left[1 + 4\left(\frac{\theta-\theta_n}{\Delta_n}\right)^2\right]^{-1} + (\gamma_n - 1)\sqrt{\frac{4\ln 2}{\pi\Delta_n^2}}\exp\left[-4\ln 2\left(\frac{\theta-\theta_n}{\Delta_n}\right)^2\right] \tag{3.2}$$

As shown in figure 3.1a, the MgF_6 octahedra in the neighbourite unit cell are rotated, which gives rise to numerous super-lattice reflections[280] and so a diffraction pattern sporting the better part of 100 peaks over $2\theta \in [20, 90]°$. This renders traditional analytical indexing methods[279,281] somewhat intractable and so the fitted intensity was auto-indexed using the TREOR[282] method as implemented by HighScore+. The unit cell volume and lattice parameters were then refined using the free software UnitCell.[283]

3.2.3 Photoluminescence Spectroscopy

PL spectra were measured using the Horiba Fluorolog spectrofluorometer illustrated in figure 3.4. This instrument is equipped with a xenon discharge light source providing excitation across visible and near ultraviolet wavelengths, dual monochromators, and both photomultiplier and semiconductor detectors. The multi-alkali photocathode of the Hamamatsu R928P photomultiplier is sensitive from 185 nm to 900 nm[284] and was operated at 950 V in single photon counting mode. A semiconductor reference detector installed near the exit port of the excitation monochromator was used to monitor the excitation intensity and correct for changes in excitation intensity with both time and wavelength. The system response was fully spectrally corrected for the excitation range of 240 nm to 850 nm.

Near infrared emissions were measured using the IGA-020-E-LN7 and IGA2.2-010-E-LN7 cryogenic photoreceivers attached to the Horiba iHR320 spectrometer. This system consists of liquid nitrogen dewars used to cool each InGaAs photodiode, which is in turn DC coupled to a transimpedance preamplifier. When cooled to 77 K the spectral range of each detector covers approximately 800 nm to 1550 nm and 1300 nm to 2500 nm respectively, with spectral sensitivity corrections applied in software. The dark current of these detectors is significantly higher than that of the photomultiplier.

Both emission and excitation spectra were acquired for unpolished bulk crystals by fixing either

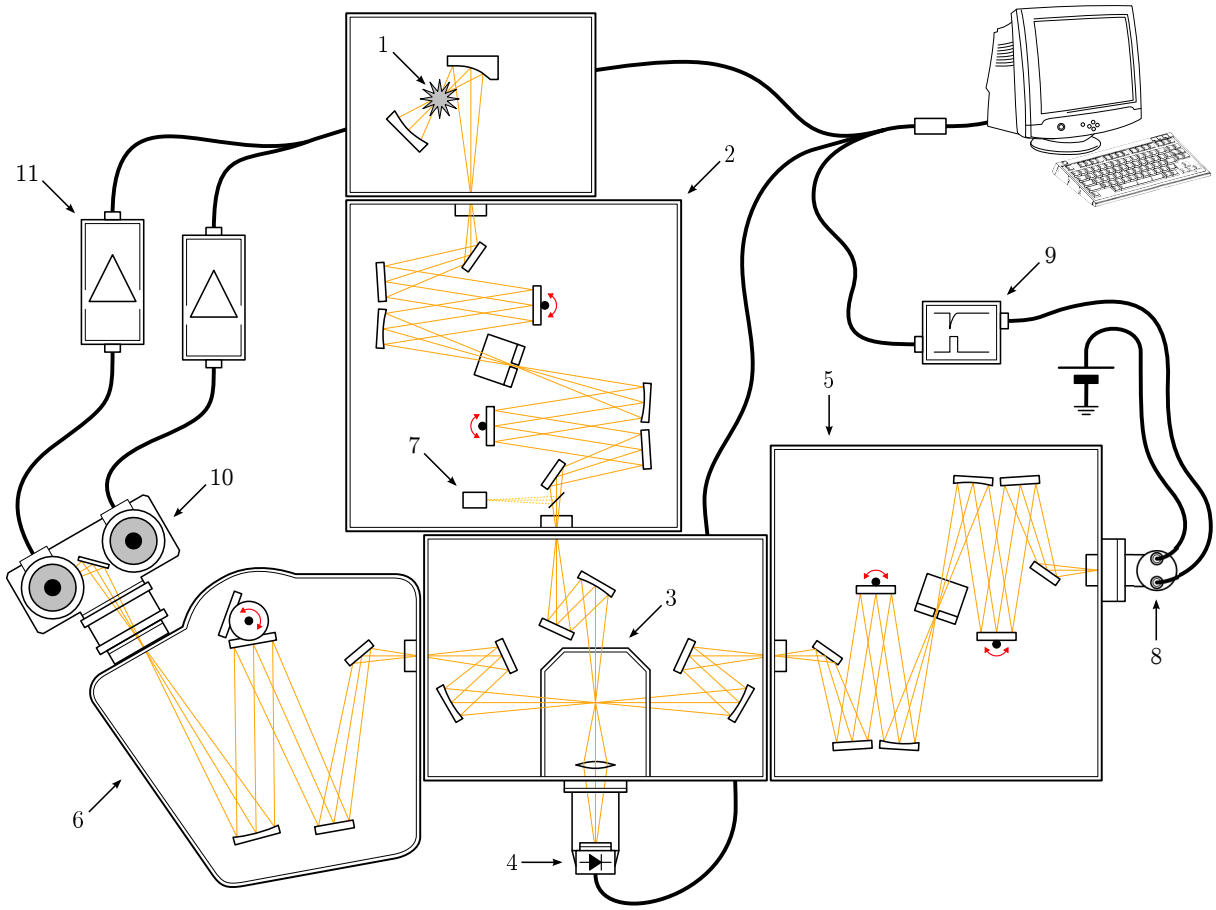

Figure 3.4: Diagram of the Horiba Fluorolog spectrofluorometer used for measurement of photoluminescence spectra and lifetimes, with optical paths shown in orange and mechanical motions in red. Labelled optical components are (1) 450 W xenon discharge lamp, (2) dual grating excitation monochromator, (3) sample chamber, (4) pulsed LED source, (5) dual grating UV-VIS emission monochromator, and (6) iHR320 spectrometer serving as a single grating VIS-NIR monochromator. Detector and data acquisition hardware includes (7) semiconductor excitation intensity monitor, (8) Hamamatsu R928P photomultiplier, (9) photon counting discriminator, (10) cooled InGaAs photodiodes, and (11) transimpedance preamplifiers. *Adapted from the Horiba Fluorolog spectrofluorometer documentation.*[285]

the emission or excitation monochromator and scanning the other. Crystals were mounted on a solid sample carrier the surface of which was oriented at 30° to the excitation source, presenting a larger area of the sample from the perspective of the emission monochromator optics. Long pass filters were frequently used on the emission monochromator, and bandpass filters on the excitation source were occasionally required when extending emission spectra to longer wavelengths. Where used, these are noted on the plotted data presented in chapter 4.

3.2.4 Photoluminescence Lifetimes

Lifetime data was also measured using the Horiba Fluorolog spectrofluorometer depicted in figure 3.4. Luminescence was excited with pulsed LED diode sources with centre wavelengths of 356 nm, 375 nm, or 465 nm, chosen as appropriate for the sample under investigation. The relatively wide bandwidths of these sources, 16 nm, 12 nm, and 25 nm respectively, necessitated the use of long pass filters on the emission monochromator for most measurements. These are identified on the plotted data in chapter 4 if used.

The spectrofluorometer was configured to generate an excitation pulse followed a fixed acquisi-

tion period during which counts were binned by the time elapsed since the most recent excitation. A decay curve was built up by repeating this cycle until sufficient counts were obtained for robust fitting. The excitation pulse duration for all samples was 1 ms, this being the minimum achievable in the described acquisition mode. For the relatively long lifetimes of the $d \rightarrow d$ and $f \rightarrow f$ emissions of the investigated dopants it was not necessary to assess or attempt to deconvolve the instrument response, which is several orders of magnitude faster.

Decay curves were fitted with single or double exponentials if possible, else a stretched exponential fit was attempted. The stretched exponential expression is given in equation 3.3, where I_0 is the emission intensity upon removal of the excitation source, τ a nominal decay lifetime, and β the stretch factor. β is constrained to the interval $[0, 1]$, with single exponential decay recovered for $\beta = 1$. The physical interpretation of intermediate values of β is discussed in chapter 4, as and where this type of fit is applied.

$$I(t) = I_0 \exp\left(\frac{t^\beta}{\tau}\right) \tag{3.3}$$

For fits other than single exponential, an effective lifetime $\langle\tau\rangle$ was determined by numerical evaluation of equation 3.4, in which $I(t)$ is the fitted decay of luminescence intensity.[286] This expression yields the expectation value of for τ, provided $I(t)$ is a physically reasonable decay function such that the integrals will converge. For single exponential $I(t)$, $\langle\tau\rangle$ reduces to τ. Uncertainty in τ and β was extracted from the co-variance matrix calculated by the least squares solvers used for fitting, and uncertainty in $\langle\tau\rangle$ estimated by systematically perturbing the fitted parameters by their type A uncertainty to establish the worst case deviation. All stated uncertainties are expanded by a coverage factor of 2.

$$\langle\tau\rangle = \frac{\int_0^\infty tI(t)\,\mathrm{d}t}{\int_0^\infty I(t)\,\mathrm{d}t} \tag{3.4}$$

As for spectrally resolved measurements, uncut bulk crystals were measured, with the face of the sample carrier oriented at 30° to the excitation source. No ultraviolet sources were available and so it was not possible to probe the lifetimes of the $5d \rightarrow 4f$ emissions of Eu^{2+} and Yb^{2+}. Nor was the instrument capable of using the InGaAs photodiode detectors to acquire lifetime data for emissions beyond the 900 nm limit of the R928P photomultiplier.

3.2.5 Absorption Spectroscopy

Absorption spectra were measured in order to evaluate the impact of radiation induced colour centres and to assist in the interpretation of the luminescence Ni^{2+} in $NaMgF_3$, for which the spectral range of the arc lamp used for photoluminescence excitation studies was not sufficient. A $NaMgF_3$ sample containing Ni^{2+} at approximately 5% (J150401) was fabricated for this purpose. Two spectrophotometers were used, a Shimadzu UV-2100 (UV-VIS) and PerkinElmer Lambda 1050 (UV-VIS-NIR). In both cases, absorption measurements were taken with reference to air.

A diagram of the UV-2100 optics is shown in figure 3.5, illustrating a relatively simple instrument with a single grating Czerny-Turner monochromator, two light sources (tungsten halide and deuterium), and a chopper gating the reference and sample beam lines. Spectral range is 190 nm to 900 nm, with a preset switch between light sources occurring at 360 nm. Both beam paths are monitored by the same Hamamatsu R928 photomultiplier, the gain of which is actively regulated

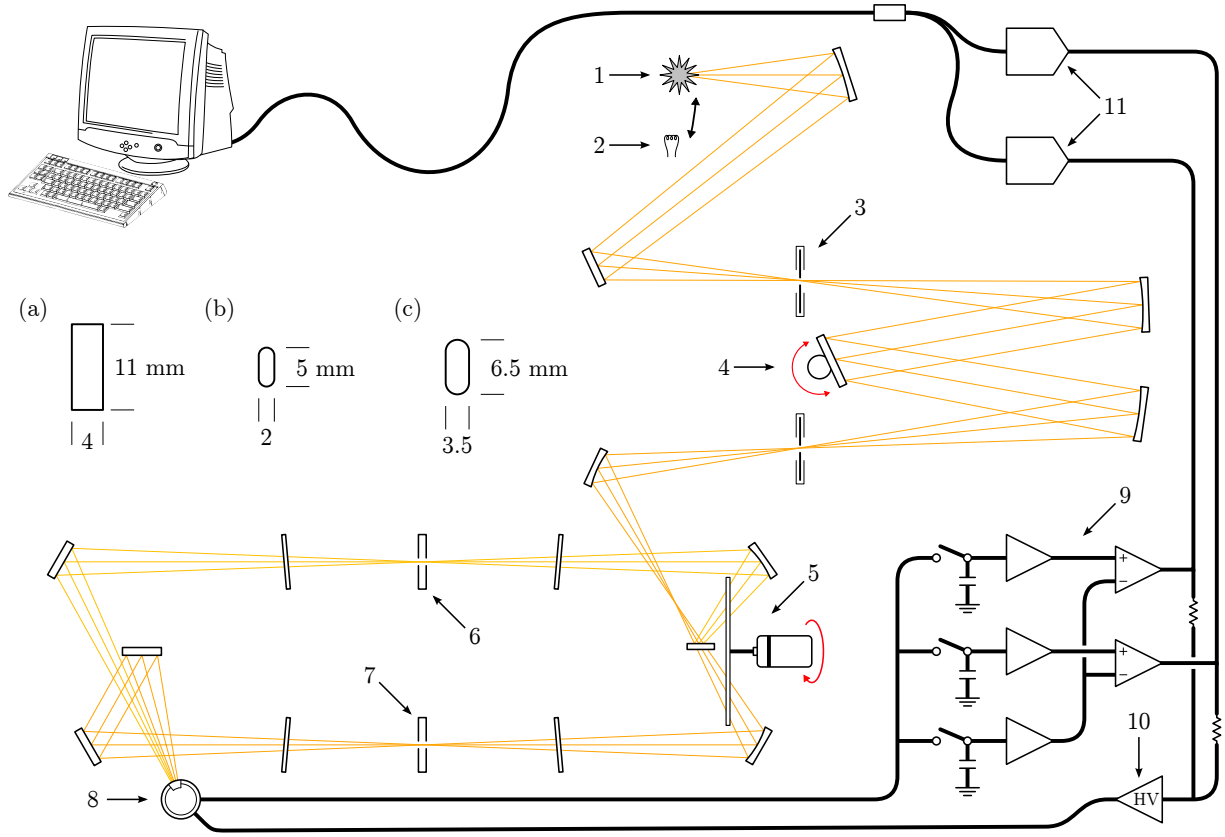

Figure 3.5: Schematic overview of Shimadzu UV-2100 UV-VIS spectrophotometer used for the majority of optical absorption measurements, with optical paths shown in orange and mechanical motions in red. Sources include (1) deuterium gas discharge and (2) incandescent tungsten-halide lamps, light from which is passed through the (3) slits and (4) diffraction grating of the Czerny-Turner monochromator. A (5) chopper is used to alternately illuminate the (6) reference and (7) sample beam paths, both of which are monitored by the (8) photomultiplier. The (9) readout electronics buffer the synchronously sampled signals, subtract dark current, and drive the (10) active gain control circuit and (11) analog to digital converters. Inset diagrams show the size and shape of (a) the light beam in cross-section for 2 nm slit width, (b) mask, and (c) sample mount clear aperture. *Adapted from the Shimadzu UV-2100 spectrophotometer documentation.*[287]

to compensate for changes in light source intensity. With the exception of the sample chamber and lamp housing, the instrument optics are hermetically isolated from the laboratory.

Prior to use in the study of radiation induced defect absorption in undoped $NaMgF_3$, which spanned several weeks, the short and long term repeatability of this instrument was assessed. For back-to-back acquisitions repeatability was established as 0.2% at 2σ across all wavelengths, increasing to 0.5% when the custom made sample carrier was removed and refitted. Day-to-day variation with respect to baseline was at most 1%, provided that an appropriate period was allowed for lamp intensity to stabilise before use. This level of performance is more than adequate given the level of dosimetric uncertainty associated with this experiment.

The Lambda 1050 is similar instrument fitted instead with three detectors to extend the measurement range into the near infrared. Transition between a multi-alkali photomultiplier and a thermoelectrically cooled InGaAs photodiode occurs at 860 nm, with gratings interchanged at the same wavelength. Tungsten halide and deuterium light sources are exchanged at 360 nm. The PbS photodetector intended for operation beyond 1800 nm was not used.

As the Lambda 1050 sample chamber was configured for cuvettes and slide mounted samples it was necessary to make holders for solid samples. These were fabricated by the SCPS workshop

from blackened sheet aluminium. In order to accommodate available sample sizes, these holders also masked the beam to the dimensions shown in figure 3.5c.

In preparation for absorption measurements, samples were cut to nominal thicknesses of 1 mm using a low speed circular diamond saw, then polished on alumina lapping discs. Polishing grit was reduced incrementally down to 3 μm. Surface and intrinsic defects remaining after polishing gave rise to a scattering background in the recorded absorption spectra, increasing markedly at shorter wavelengths. For samples where the absorption of interest was radiation induced, this background was removed by taking the difference of absorption spectra before and after irradiation. In the case of the Ni^{2+} absorption spectra, where the signal of interest arises from the dopant, the scattering background was fitted using a piecewise polynomial in the transmittance domain and subtracted after conversion back to absorption.

3.2.6 Thermoluminescence Spectroscopy

Stimulated luminescence as a function of temperature, or glow curves, provide information regarding the energy distribution and concentration of trapping defects after irradiation. Spectrally resolved TSL was measured for the $NaMgF_3$ samples used in the radiotherapy characterisation work reported in chapter 6, and for the subset of other samples which showed promise for fibre coupled dosimeter applications. These measurements were not attempted on samples which exhibited very low RL sensitivity as the equipment used could not accommodate extended integration periods.

Samples were ground to powder, mixed with silicone spray, and a thin layer of the resulting paste was painted on a 5×2.5 mm platinum resistance temperature detector (PT-100 RTD). This RTD was bonded to a second identical sensor which functioned as a heating element, forming a sample carrier with low thermal inertia, yet capable of reasonably precise temperature control and monitoring. The apparatus is illustrated in figure 3.6a and described in detail elsewhere.[288]

The unirradiated fluoroperovskite and silicon oil paste was first heated to approximately 700 K, evaporating most of the silicone oil and leaving a thin layer of crushed perovskite deposited on the sample carrier. Each sample was then held below room temperature and irradiated with unfiltered tungsten x-rays generated at 40 kVp and 40 mA. A low pressure flow of dry nitrogen gas passed through a copper coil immersed in liquid nitrogen was used to provide the required cooling. TSL emission was then recorded as the sample temperature was ramped at 1 K/s over a nominal range of 230 K through 700 K. These temperature limits are imposed by the temperature monitoring hardware plus a margin from the freezing and autoignition temperatures[289] of any residual silicone oil.

Prior to exposure of each sample, a full acquisition was made to capture the background of black body radiation detectable at elevated temperatures. This was subtracted from the sample TSL, correcting for both the spectrometer dark signal and black body background. The ceramic substrate of the RTD sensor also exhibits weak TSL, with a narrow emission at 690 nm and weak glow peaks at 0 °C and 150 °C. For most samples this was of negligible intensity and readily separable from the signal of interest.

Luminescence was detected using a USB2000+ Ocean Optics fibre optic spectrometer, which employs a fixed grating of 600 mm^{-1} and 400 nm blaze with a Sony ILX511B 2048 pixel charge coupled detector (CCD). With an input slit width of 200 μm, this instrument had sufficient sensitivity for most TSL measurements, but a limiting resolution of approximately 7.5 nm. CCD spectral

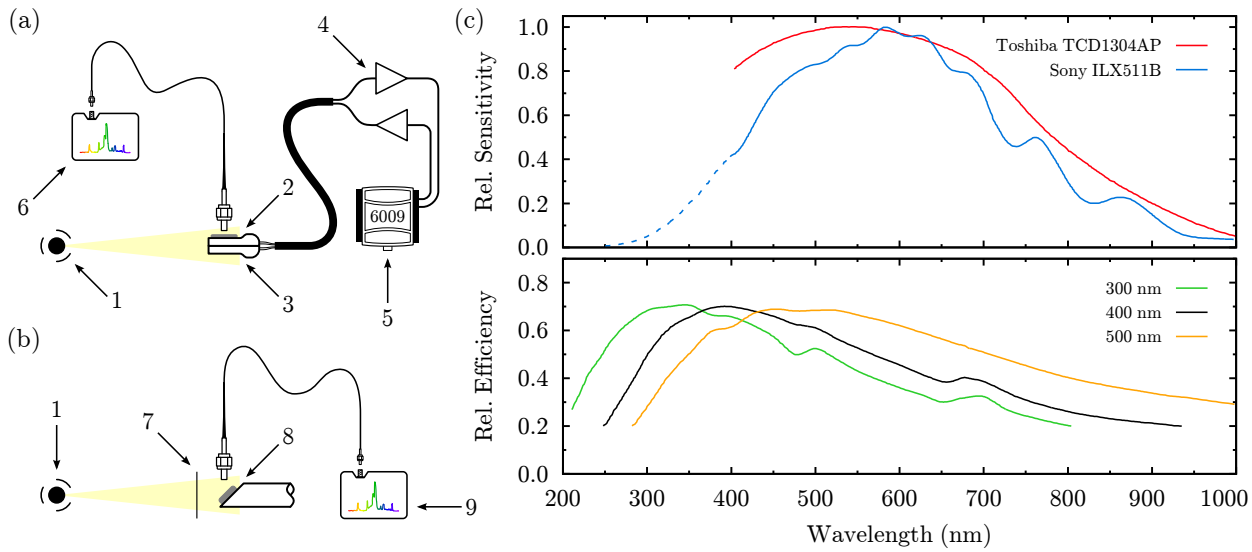

Figure 3.6: (a) Experimental setup for measurement of thermoluminescence, illustrating (1) x-ray source, (2) PT-100 temperature sensor, (3) heating element, (4) temperature controller supervised by (5) USB-6009 DAQ, and (6) USB2000+ fibre optic spectrometer. (b) A similar arrangement for the measurement of radioluminescence includes (7) 0.9 mm Al filter, (8) sample support, and (9) USB2000(+) or USB4000 fibre optic spectrometer. The detector spectral sensitivity and grating efficiencies for each spectrometer are shown in (c) as sourced from vendor documentation.[290–292] The dashed line indicates an independent measurement[293] of the ILX511B ultraviolet sensitivity.

sensitivity and grating efficiency, which dominate[iii] the wavelength dependence of the measurement system, are given in figure 3.6c. The combined response of the CCD and grating is most flat (±20%) in the region of 450 nm to 650 nm, outside of which some distortion of spectra occurs, particularly at shorter wavelengths. No corrections were applied.

The analytical expression for first order glow peak[294] given in equation 3.5 was used to fit individual glow peaks. In this expression, k is the Boltzmann constant in eV/K and T the sample temperature in K. Fitting parameters are the maximum observed TSL intensity, I_m, the temperature at which this occurs, T_m, and the activation of the corresponding trapping defect E_a. Generally all TSL emissions exhibit identical glow peaks, and so a single fit was made to the total integrated intensity unless otherwise stated.

$$I\left(T\right) = I_\mathrm{m} \exp\left[1 + \frac{E_\mathrm{a}}{kT}\frac{T-T_\mathrm{m}}{T_\mathrm{m}} - \frac{T^2}{T_\mathrm{m}^2}\exp\left(\frac{E_\mathrm{a}}{kT}\frac{T-T_\mathrm{m}}{T_\mathrm{m}}\right)\left(1-\frac{2kT}{E_\mathrm{a}}\right) - \frac{2kT_\mathrm{m}}{E_\mathrm{a}}\right] \tag{3.5}$$

For glow peaks with a more symmetric appearance, second order peaks were fitted using the analytical form given in equation 3.6 below.

$$I\left(T\right) = 4I_\mathrm{m}\exp\left(\frac{E_\mathrm{a}}{kT}\frac{T-T_\mathrm{m}}{T_\mathrm{m}}\right)\left[\frac{T^2}{T_\mathrm{m}^2}\left(1-\frac{2kT}{E_\mathrm{a}}\right)\exp\left(\frac{E_\mathrm{a}}{kT}\frac{T-T_\mathrm{m}}{T_\mathrm{m}}\right) + \frac{2kT_\mathrm{m}}{E_\mathrm{a}} + 1\right]^{-2} \tag{3.6}$$

3.2.7 Radioluminescence Spectroscopy

RL spectra were collected using very similar equipment as used for TSL measurements, see figure 3.6b. The same fibre optics were used, and for samples exhibiting broad emissions, also the same USB2000+ CCD spectrometer. For samples with narrow line emissions, an Ocean Optics

[iii] The silica optics used to couple light emitted from the sample to the spectrometer exhibit at most 1% loss across most of their usable range, with slightly reduced performance in the largely unutilised region of 200 nm.

USB4000 spectrometer was used instead. This device is built around the Toshiba TCD1304AP 3648 pixel CCD and uses a fixed 600 mm^{-1} grating with blaze at 300 nm. With entrance slit width fixed at 50 μm, a limiting resolution of about 2 nm was obtained with significantly reduced sensitivity. For the Nd and Yb dopants, an Ocean Optics USB2000 spectrometer was used, fitted with 200 μm slits and a 500 nm blaze grating. This third spectrometer is the predecessor to the USB2000+, employing the same CCD in conjunction with a lower resolution ADC, but was fitted with a grating usable out to 1030 nm.

In order to capture the effects of radiation damage, doses of at least 10 kGy were delivered at constant dose rate and the RL emission spectra recorded at intervals of 10 seconds. The Philips PW1730 x-ray generator was used as described in § 3.2.1, with total exposure times ranging from 3 to 6 hours. This produced datasets of several thousand spectra per sample.

Despite the lack of spectral correction, it was found the RL emissions could be reasonably modelled by a linear superposition of Gaussian and Lorentzian functions for band and line emissions respectively. The simplified analytical forms used, $\mathcal{G}(k)$ and $\mathcal{L}(k)$, are given below in equations 3.7a and 3.7b, in which the fitting parameters C_0, C_1, and C_2, set the peak height, position, and width respectively.

$$\text{(a) } \mathcal{G}(k) = C_0 \exp\left[-\left(\frac{k-C_1}{C_2}\right)^2\right] \qquad \text{(b) } \mathcal{L}(k) = C_0 \left[1+\left(\frac{k-C_1}{C_2}\right)^2\right]^{-1} \tag{3.7}$$

For each sample, a model function was created by assigning either $\mathcal{G}(k)$ or $\mathcal{L}(k)$ to each emission, and then fitting the the model to the entire time sequence of spectra using the Levenberg-Marquardt non-linear regression algorithm. C_0 was constrained to the positive real line, C_1 to within 1 nm of the initial solution, and C_2 allowed to vary by a factor of two. A scalar background term was used to account for background counts, the value of which was estimated by averaging range of data points in a region of the emission spectrum dominated by instrumental noise. In order to improve solution speed and ensure a smooth time evolution of the fitted model, the vector of parameter values from each fit was used as the initial guess for the subsequent spectrum. All data was fitted as a function of wavenumber.

This procedure allowed robust compensation for instrumental background drift and for the separation of overlapping emissions such that the dependence of each on time, and therefore dose, could be studied in more detail. Reliable fitting was achieved even for relatively weak emissions, in some cases for peaks with SNR approaching unity. The poorest fits occurred when using equation 3.7a to model emissions at higher energies, where the declining detector sensitivity illustrated in figure 3.6c caused asymmetric distortion of wider emission bands. Extraction of individual peak intensities was performed by integration of the corresponding $\mathcal{G}(k)$ or $\mathcal{L}(k)$ function with the fitted parameters for the peak in question.

For samples samples AE00519, AE01002, and J140306, RL emission spectra were captured at static temperatures between 220 K and 330 K after saturation to high doses. The apparatus described in § 3.2.6 was used to control temperature and spectra acquired using the OceanOptics USB2000+. Fitting was undertaken as described above but with relaxed constraints on changes in fitted centre energy, as this does in some cases exhibit shifts with irradiation temperature. At least three consistent emission spectra were acquired at each temperature to assess intensity changes due to absorbed dose dependency, and where this was found to be negligible the same data was then acquired for both positive and negative ΔT.

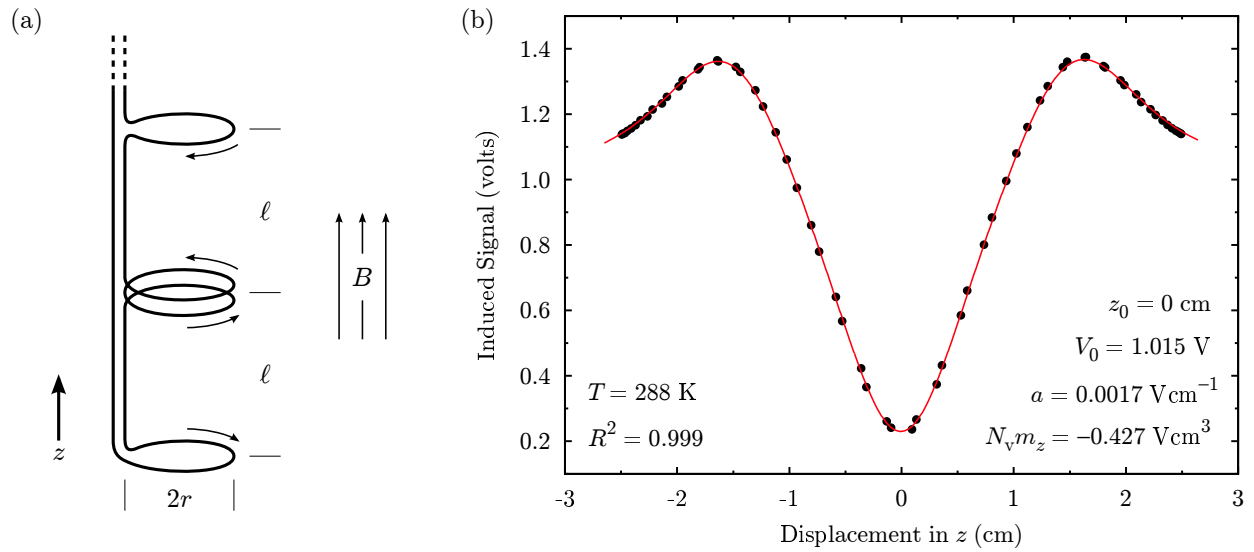

Figure 3.7: (a) Scale diagram of gradiometer pickup coils indicating orientation with respect z axis and external magnetic field B, baseline dimension ℓ, and coil radius r. The response of this specific gradiometer is illustrated in (b), including measured signal from irradiated sample J140307 near room temperature (black) and an example fit of the theoretical dipole function (red) given in equation 3.8. The fitted parameters are shown on the plot.

3.2.8 Magnetisation

The majority of the lanthanides possess unpaired electrons and so exhibit paramagnetism,[39,47] detectable even for low dopant concentrations against the weak diamagnetic background of the $NaMgF_3$ host. In some cases, this allows changes of valence in the rare earth activated samples to be probed by measurement of magnetic properties. A means to confirm valence conversions after exposure to ionising radiation is of interest as such changes may implicate the dopant site as a hole trap[192] in the charge kinetics model discussed in § 2.2.4.

A Quantum Design Magnetic Property Measurement System (MPMS) was used to measure magnetisation in samples J140307 ($NaMgF_3$:Sm) and J150501 ($NaMgF_3$) for $T \in [2, 300]$ K. The MPMS is a superconducting quantum interference device (SQUID) magnetometer employing a second order gradiometer through which samples were translated. Small signals induced by the dipole moment of the sample are inductively coupled to a DC SQUID cooled with liquid helium.[295]

The gradiometer pickup coils are depicted in figure 3.7, along with an example of a fitted point dipole response. It consists of single turns of superconducting wire with radius, r, of 0.97 cm and a baseline, ℓ, of 3.04 cm. The theoretical dipole response is given in equation 3.8 below, and is obtained by integrating the z component of the point dipole field over the area of each coil.[296]

$$V(z) = V_0 + \alpha z + N_v m_z (2\Omega_0 - \Omega_+ - \Omega_-) \tag{3.8}$$

In the above equation, V_0 and αz compensate for constant and linear measurement offset, N_v is the SQUID voltage calibration, and m_z the z component of the dipole moment of interest. The terms Ω_0, Ω_+, and Ω_- represent the signal induced in the gradiometer coils at zero, positive, and negative z offsets respectively, defined as follows.

$$\Omega_0 = \left[r^2 + (z + z_0)^2\right]^{-3/2} \tag{3.9}$$

$$\Omega_{\pm} = \left[r^2 + (z + z_0 \pm \ell)^2\right]^{-3/2} \tag{3.10}$$

While the peak amplitude of the dipole response is in principle sufficient to determine m_z, fitting to a known response function is a more robust approach.[297] Scan lengths of 5 cm were used in order to capture the three stationary points of the theoretical dipole response as shown in figure 3.7b. The sample was oscillated sinusoidally about the centre of the gradiometer, with each cycle sampling the illustrated response twice. Fitting of equation 3.8 was then used to reduce the dataset to m_z as a function of temperature, from which the volume susceptibility, χ, was deduced.

A magnetising field strength of 4.8×10^6 A/m was used, close to the operating limit of the superconducting solenoid,[295] in order to emphasise the signal arising from the dopant ions at the relatively low concentrations listed in table 3.1. The non-uniformity of this field over the 5 cm scan length used is near negligible, falling by 0.2% at ± 2.0 cm and 0.6% for the scan length extremes at ± 2.5 cm.[298] Samples were supported in lengths of plastic drinking straws, which are physically uniform over a length of many times ℓ. The second spatial derivative of the magnetisation in the support is therefore essentially zero, and so induces no significant signal in the gradiometer.[299]

Measured samples were fragments of the bulk crystal sized between 2 mm and 4 mm across, which is significant on the scale of the gradiometer and so not strictly the point dipole assumed in equation 3.8. Provided the sample is uniformly magnetised, the impact of finite sample size on the applicability of equation 3.8 depends on the sample geometry. Resulting error in the determined dipole moment is theoretically zero for spherical samples, about 0.1% for cubic samples, and becomes much more significant for more extreme cases like thin films oriented perpendicular to B.[296,297] The irregular crystal fragments used are considered a sufficient approximation of a cubic sample that the error is at most 1%. While correction factors for selected geometries are available in the literature,[300] given the irregularity of the sample fragments used the aforementioned maximum error was instead included in the reported experimental uncertainty for χ.

The majority of the lanthenide series exhibit Curie-Weiss paramagnetism, in some cases with a ferromagnetic phase at low temperatures.[301] Susceptibility for the paramagnetic phase is well described by equation 3.11 below, in which N is the number of ions, g the Landé g-factor, μ_{B} is the Bohr magneton, J the total angular momentum of the ground state, k the Boltzmann constant, T the temperature in K, and Θ the Weiss constant.

$$\chi = N\frac{g^2\mu_{\mathrm{B}}^2 J(J+1)}{3k\,(T-\Theta)} \tag{3.11}$$

The Landé g-factor was calculated as in equation 3.12 below,[302] using J as defined above, and the orbital and spin angular momenta, S and L from the relevant ground state spectroscopic term symbols (see § 2.2.1).

$$g = 1 + \frac{J(J+1) - L(L+1) + S(S+1)}{2J(J+1)} \tag{3.12}$$

For Curie-Weiss paramagnetism, J for the ground state alone is used under the assumption that the population of excited states is negligible. For the $4f^5$ and $4f^6$ configurations the ground and lower excited states constitute a multiplet with separation levels comparable to kT, and so equation 3.11 does not apply.[302–304] The paramegnetic susceptibility is instead described by the sum of contributions from each level of the multiplet, as in equation 3.13, which gives the susceptibility

for a Van-Vleck paramagnet. This form was used to model Sm^{2+}, Sm^{3+} and Eu^{3+}.

$$\chi = N\frac{\sum_J \left[\left(g^2\mu_B^2 J(J+1)/3kT\right)+\xi\right](2J+1)\,e^{-E_J/kT}}{\sum_J (2J+1)\,e^{-E_J/kT}} \tag{3.13}$$

The additional term ξ in the above is defined in equations 3.14 and 3.15 below, in which E_J is the energy of the excited level relative to the ground state. This term is ommitted from equation 3.11, where it is rendered negligible by the large difference between E_J and $E_{J\pm1}$.

$$\xi = \frac{\mu_B^2}{6(2J+1)}\left(\frac{F(J+1)}{E_{J+1}-E_J}-\frac{F(J)}{E_J-E_{J-1}}\right) \tag{3.14}$$

$$F(J) = \frac{1}{J}\Big[(S+L+1)^2-J^2\Big]\Big[J^2-(S-L)^2\Big] \tag{3.15}$$

As the $4f$ orbitals are relatively isolated from the crystal field, E_J can to a useful approximation be taken from the free ion energy levels.[305] In this work, the energies tabulated in chapter 4 were used, which are for the most part derived from experimental PL or RL spectra. The experimental susceptibility for sample J140307, χ_{Sm}, was fitted to the sum of the Van-Vleck susceptabilities for each valence of the samarium dopant, χ_{2+} and χ_{3+}, a Curie-Weiss susceptibility for both F–centres and contaminant Eu^{2+}, χ_F, and the temperature independent diamagnetic susceptibility of the host crystal, χ_0. The weighting fractions f_F, f_{2+}, and f_{3+}, and the diamagnetic background were used as fitting parameters.

$$\chi_{Sm} = f_F\chi_F + f_{2+}\chi_{2+} + f_{3+}\chi_{3+} + \chi_0 \tag{3.16}$$

The Van-Vleck terms χ_{2+} and χ_{3+} in equation 3.16 were calculated by evaluating equation 3.13 for all excited states in the multiplet.

3.3 Radiotherapy Characterisation

The remainder of this chapter will address the characterisation of radioluminescence response in clinical MV x-ray radiations. This was undertaken using the Mk-II prototype dosimeter described in § 5.1 and fibre coupled dosimeters fabricated from samples AE00327, AE00519, AE00562, and AE01020. As the Mk-II system lacked a reliable means of mitigating the substantial stem signal encountered at these x-ray energies, this work could not be extended to applications testing.

3.3.1 Medical Electron Accelerators

A simplified schematic of a modern medical electron accelerator, representative of the designs used in this work, is presented in figure 3.8. Electrons are accelerated by cyclic electric fields in a loaded waveguide and directed into a thick x-ray target. The resulting bremsstrahlung photon radiation is then flattened and collimated as appropriate for a given treatment or measurement. A standing wave is used for acceleration, with the nodal cavities located to the side of the beam path to reduce waveguide length. The entire beam transport system is gantry mounted and the patient positioned on a rotating treatment couch such that x-rays may be directed from almost any direction with respect to the treated anatomy. Secondary and tertiary collimation devices may also be rotated as a unit to provide flexibility in field shaping. The region of intersection of these couch, gantry,

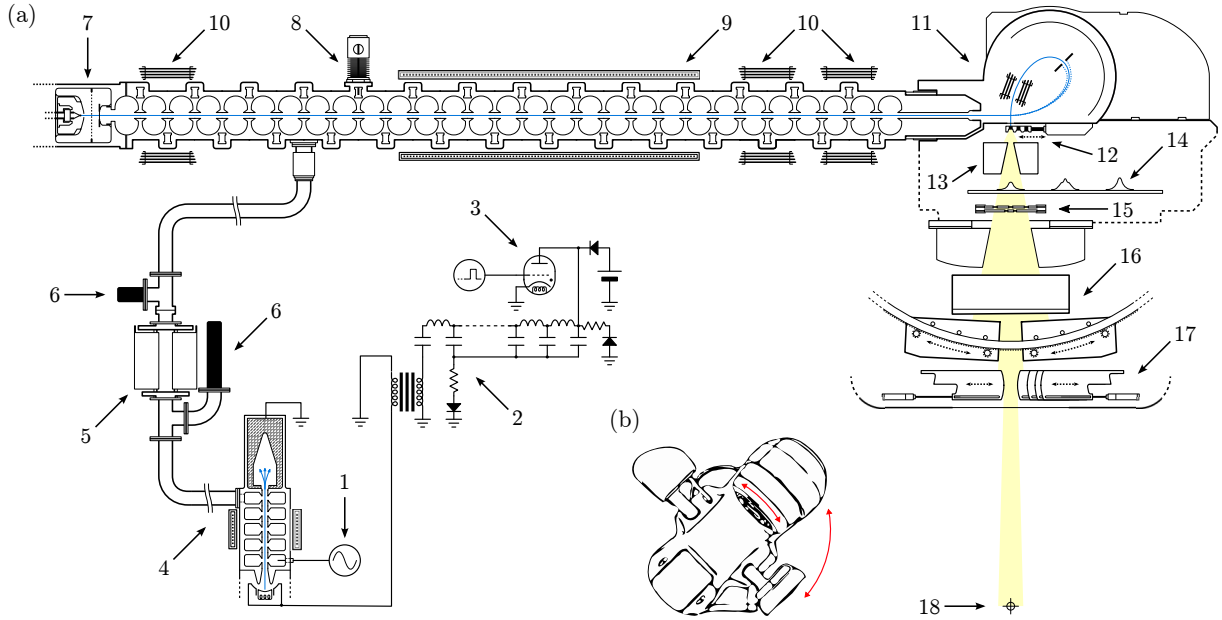

Figure 3.8: Schematic overview of (a) the medical electron accelerator type used in this work, including (b) illustration of gantry and collimation rotation axes (red). Key microwave power generation components are the (1) S band microwave source, (2) pulse forming network, (3) main thyratron, (4) klystron, (5) RF circulator, and (6) dummy loads. Components held under vacuum for electron beam transport (blue) include the (7) electron gun, (8) energy switch, (9) focusing solenoid, (10) steering coils, and (11) bending magnet. X-ray generation (yellow) and delivery is provided by the (12) x-ray target, (13) primary collimator, (14) flattening filters, (15) monitor chambers, (16) secondary collimators, and (17) tertiary collimation. Treatment isocentre (18) is 1 metre from the x-ray target. *Adapted from Varian TrueBeam technical drawings*.[306,307]

and collimator rotations is referred to as the mechanical isocentre.[12,308] The radiation isocentre is defined by the centre of symmetrical radiation fields under the same rotations.

To provide the cyclic electric field for acceleration, the waveguide is energised in the microwave S band, in the region of 2.85 GHz at instantaneous power levels on the order of MW. RF energy is provided by an inductor-capacitor pulse forming network (PFN), generating a low duty cycle[iv] pulse train at a nominal frequency of 360 Hz. The PFN is discharged by a thyratron, dumping the stored energy into a small klystron where it is modulated by the output of a low power microwave source. The klystron and accelerating structure are connected by a rectangular (TE_{01}) waveguide pressurised at two atmospheres with an SF_6 dielectric. A circulator is required to isolate the accelerator from the RF source, preventing back reflection of excess RF power into the klystron.[21,308,309]

Simultaneous with each microwave pulse, electrons are injected at approximately 100 keV into one end of the evacuated accelerating structure. Injection is gated by the potential applied to the electron gun grid, held several hundred volts negative with respect to the emitting cathode when no current is desired. Steering coils are positioned around the accelerator waveguide near the electron gun to trim alignment of the low energy electron beam and a pair of position steering coils are located towards the end of the acceleration path. These are used to deflect and re-align the beam, adjusting position but not angle prior to entry into the bending magnet. An axial focusing solenoid covers a large portion of the guide to minimise electron dispersal during acceleration.[21,306,307]

Dose rate for the static photon fields used in this work was controlled by servoing the electron gun pulse length to achieve the calibrated dose rate, with individual pulses gated to obtain lower

[iv] Actual duty cycle is subject to dose servo operation. Typical pulse widths are in the range of 5-10 μs.

pulse repetition rates. The servo used has a long time constant intended to deliver consistent dose per pulse for acquisition of images across multiple beam pulses.[310,311] Consistency of dose per pulse after beam generation stabilises was verified by monitoring the current flowing from the x-ray target to ground using an oscilloscope.

Following acceleration, an achromatic bending magnet rotates the high energy electron beam through 270°, allowing it to diverge while passing a water cooled energy selection slit prior to refocusing. Angle steering coils are positioned within the bending magnet, deflecting the beam during refocusing if necessary. A forward directed bremsstrahlung distribution is produced as the focused beam impinges on a thick x-ray target, and is selectively attenuated in a semi-conical flattening filter. The flattening filter produces a reasonably flat x-ray fluence across the useful angular spread of the x-ray field but also accentuates off-axis softening. The lowest atomic number attenuator that may be accommodated in the available space is used to minimise this effect. A tungsten primary collimator of conical cross section positioned between the target and flattening filter then defines the maximum field size.[12,21,308]

The fluence exiting the flattening filter traverses a pair of multi-sector transmission ionisation chambers which are used to integrate delivered dose and to provide feedback for active beam position and angle steering.[12,21] Each chamber contains a set of five symmetrical sectors used to continually assess the flatness and symmetry of the beam, while also providing redundant measurement of the accumulated dose. As the primary determinant of dose delivered to patients, the redundancy of the monitor chambers extends to independent cabling, power supplies, and integrating electronics.[306]

Below the monitor chambers, the x-ray field is collimated into rectangular shapes by large tungsten blocks, the secondary collimators, with curved trajectories to maintain optimal dose fall-off at the edges of all field sizes.[12,308] The tertiary multi-leaf collimator (MLC) positioned immediately before the mylar exit window was not used in this study.

The full length of the waveguide shown in figure 3.8a produces a nominal potential of 18 MV, with lower energies obtained by insertion of a conducting plunger into a side cavity, decoupling the distal cavities and rendering the remaining waveguide a drift tube. RF power levels may also be adjusted to achieve different energies. Each radiation quality produced requires a specific combination of x-ray target and flattening filter. The latter are held in a rotating carousel below the primary collimator.[21,308]

Two accelerators were used for the radiotherapy characterisation work described herein: a Clinac EX (serial number 2418) and a TrueBeam (serial number 1115), both manufactured by Varian Medical Systems. Matched x-ray radiations with NAP of 6 MV and 18 MV were available on both units with a maximum dose rate of 6 Gy/min at isocentre, and a 10 MV radiation was available only on unit 1115. This 10 MV radiation can also be delivered with the flattening filter replaced by a thinner uniform filter (10 MV FFF), producing a peaked dose profile with a central axis dose rate of 24 Gy/min.

Nominal energy spectra, dose profiles, and depth dose data are included in appendix A.

3.3.2 Ionisation Chamber Dosimetry

A number of measurements were made using commercial ionisation chambers, PTW type TW30012 (0.6 cm^3) for reference dosimetry, and types TW31014 (0.03 cm^3) and TW31015 (0.015 cm^3) for relative measurements. Reference dosimetry was performed prior to each experiment to precisely establish dose rate, which can otherwise vary from the nominal calibrated value by approximately

±1% from day to day and between treatment units. Relative dosimetry was performed using ionisation chambers to provide comparative data for investigations into energy dependence of the fibre coupled detectors.

For reference dosimetry, corrections for air temperature and pressure were made with equation 2.20. The effect of polarising voltage polarity was found to be negligible by application of equation 2.21 and so was left uncorrected. Charge recombination losses in air were corrected using equation 2.22 with the co-efficients $a_0 = 1.198$, $a_1 = -0.875$, $a_2 = 0.677$, for a polarising voltage ratio of $N = 3$. Radiation quality corrections for the type TW30012 chamber were obtained from TRS-398.[17]

Precision achieved for these measurements is at worst a few parts in one thousand,[312] with both ionisation chambers and modern medical accelerators being highly repeatable devices. Despite this, total uncertainty in absolute dose was as high as 1.7%. This figure includes the statements of uncertainty in instrument calibration provided by standards laboratories,[313] uncertainties in correction factors[17] and measurement of influence quantities, and the small departures from reference conditions possible within the mechanical tolerances of each treatment unit. For relative measurements, calibration and correction factor uncertainties are avoided and this is figure is reduced to approximately 0.6%.

No absolute dosimetry was possible for experiments involving ^{192}Ir radionuclide sources due to the small source-to-detector separations used.

3.3.3 Irradiation Geometries and Phantoms

Water and water equivalent phantoms were used for all characterisation measurements and priming irradiations, except for the initial exposures employing ^{192}Ir which were performed in air. Where necessary a MED-TEC liquid water phantom type MT-100-T was used, while for most 6 MV experiments CIRS plastic water slab phantoms (see figure 3.9a) were more convenient. Buildup and backscatter during priming was provided by decommissioned RMI solid water slabs (see figure 3.9b) to avoid unnecessary radiation damage to the plastic water used for routine dosimetry.

An RMI solid water slab was drilled to accommodate the dosimeter probes in both slab phantoms, and the correct location of the drilled cavity was verified radiographically. This slab was placed at depth d as indicated in figure 3.9b. Both the RMI and CIRS slabs present an area of 30×30 cm^2 perpendicular to the radiation field, limiting field sizes to 20×20 cm^2 as a margin of 5 cm is required to maintain full scatter conditions on the central beam axis.[17]

3.3.4 Priming

Previous research[186,187,190,191] has found the OSL dose response in both Mn^{2+} and Eu^{2+} activated fluoroperovskites to saturate at doses approaching 1 kGy, indicating that similarly large priming doses are required to obtain an RL sensitivity relatively independent of the absorbed dose history of a given dosimeter. This was initially attempted using an ^{192}Ir HDR brachytherapy source with nominal activity of 370 GBq.

Each dosimeter was mounted directly on 250 mm, 18 gauge, stainless steel brachytherapy needles for irradiation in air with a VariSource iX remote afterloader. This setup was radiographed using the HDR theatre C-arm with the afterloader dummy wire dwelled alongside the dosimeter in order to estimate the source-to-detector separation of 2 ± 1 mm. Further refinement of this separation

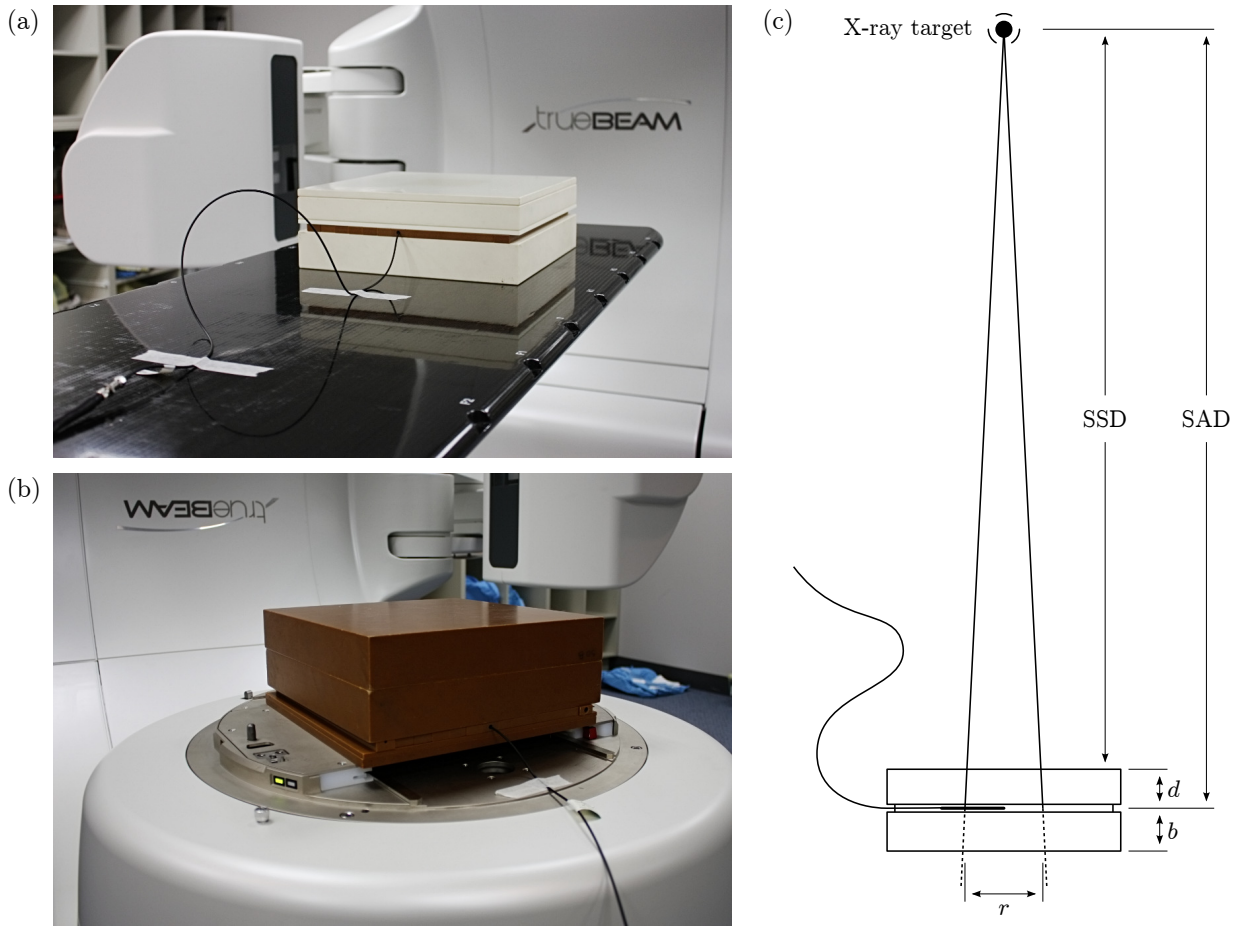

Figure 3.9: Photograph of fibre optic dosimeter probe fitted to water equivalent radiation phantoms in (a) reference geometry and (b) priming geometry. The setup depicted in (a) is optimised for reference dosimetry, while that in (b) is optimised for elevated dose rate. A scale diagram of an isocentric geometry is given in (c), in which SAD = SSD + d is fixed at 100 cm and the square field size r and depth of buildup d is varied. All irradiations were undertaken under this geometry.

was precluded by lateral movement in the active source wire and low image contrast with respect to the detector active volumes.

Dwell position was optimised by incrementally stepping the active wire past the dosimeter whilst monitoring the RL count rate for the expected peak in response. When combined with the difficulties of the TG-43 brachytherapy dose formalism at close range,[314] the large relative uncertainty on the imaged separation prevented meaningful estimation of the final priming dose. ^{192}Ir exposures thus served the sole purpose of preparing the dosimeters for initial RL investigations in megavoltage photon radiations.

Priming was eventually revisited in 6 MV photons on a decommissioned Varian Clinac 2100C/D (s/n 1027) and the unflattened 10 MV photon beam available on s/n 1115. In both cases, irradiation was undertaken in a non-isocentric, reduced SSD geometry for enhanced dose rate. The gantry was inverted and the dosimeter placed 2 cm deep in solid water resting on the collimation assembly, as pictured in figure 3.9b. Under these conditions the dose rate was 19.0 Gy/min and 74.7 Gy/min for 6 MV and unflattened 10 MV respectively, based on ionisation chamber measurements of dose rate at isocentre. The use of an unflattened photon beam allowed priming to be undertaken without excessive beam time, while providing an irradiation setup for which priming doses could be accurately determined.

3.3.5 Stem Signal

Čerenkov and fluorescence light originating in the transmission fibre was accounted for by subtraction of the observed signal in an identical dosimeter probe for which the active volume was absent, referred to herein as the inactive fibre. This fibre was substituted for the actual dosimeters in a given experimental setup and irradiation repeated for each filter used to evaluate the stem signal magnitude.

While this approach is entirely impractical for routine dosimetry, it is relatively simple to implement and was tenable due to the static nature of the characterisation measurements undertaken. Results obtained in this manner are subject to both the statistical uncertainty associated with the correction, and systematic error due to subtle geometric differences between exposure of the fluoroperovskite dosimeter and inactive fibre. Only the former was quantitatively accounted for.

3.3.6 Linearity

Linearity of dose rate response was established by measurement of RL signal at all six pulse repetition rates available, with nominal outputs of 1 to 6 Gy/min. This was then compared to dose rates determined by ionisation chamber dosimetry under the same geometry, for which the console beam timer was used to infer dose rate for integrated measurements. The RL signal at 6 Gy/min was also integrated for delivery of 1 Gy to 10 Gy, and the linearity of measurements of absorbed dose obtained in this manner established.

Dependence on dose per pulse was also investigated, again in an isocentric setup, but with dose rate reduced by the addition of water equivalent build up. As the detector is maintained at isocentre this essentially a direct measurement of TPR (see § 2.1.8), and so non-linearity may be expected if the detector has an energy dependence substantially removed from that of the TW30012 ionisation chamber used as a reference. The range of depths in plastic water used was 5 cm through to 35 cm, corresponding to doses per pulse between approximately 0.3 mGy and 0.08 mGy.

3.3.7 Temperature Dependence

The influence of temperature on RL sensitivity was investigated using a liquid water phantom and covered a range of approximately 15 °C to 50 °C in steps of 5 °C, encompassing both room and body temperature. In order to accurately position the flexible dosimeter probes at depth, all four were mounted with plastic cable ties alongside the inactive probe on a rigid perspex sheet 4.7 mm thick. This construction was then attached to the vertically travelling armature in the tank. Depth was zeroed at the water surface and dosimeters positioned isocentrically in a 10×10 cm^2 field at the 6 MV reference depth of 5 cm for all measurements.

Tap water at 60 °C was used to fill the tank to 20 cm, cooling to near the first measurement temperature of 50 °C during the initial tank setup on the treatment couch. The phantom was allowed to cool during measurements to 40 °C at which point tap water at room temperature, and eventually chilled water near 10 °C, was mixed into the phantom to achieve the desired temperatures. Approximately 30 minutes was allowed between measurement points for equilibrium between the phantom and the dosimeters to be established. Dosimeter depth, positioning in field, and SSD were verified prior to each measurement, as temperature changes while filling the phantom were observed to cause transient warping of the perspex mount. No adjustments to the couch height or dosimeter depth were made during data collection.

Each fluoroperovskite dosimeter was investigated in a separate measurement session in order to avoid the need to change optical filters during data collection. The accelerator dose rate was measured using a type TW30012 ionisation chamber in plastic water prior to filling the tank and upon completion of each experiment. Stem signal was measured for the entire temperature range while working with the $NaMgF_3$:Eu and $NaMgF_3$:Mn dosimeters and found to have no significant temperature dependence. Consequently, for the remaining dosimeters, stem signal was only measured before and after data collection over the full range of temperatures. In anticipation of a numerically small temperature dependency, the statistical significance of individual data points was strengthened by extending each irradiation to 2000 MU.

The test described above captures the temperature dependence of the entire dosimeter system, changes in which are generally more complex than a temperature driven scaling of RL emission intensity. Spectral changes in RL emission were investigated for the bulk crystals from which the fibre coupled samples were cut as part of the emission spectroscopy described in § 3.2.7, findings of which are reported in chapter 4. The influence of temperature on optical properties of the fibre train was established by literature review.[218,315–318]

3.3.8 Energy Response

Response to x-ray energies in the range of keV to MeV was probed by comparison to detectors with known energy response under irradiation conditions expected to change the incident radiation spectrum. Comparisons were made for each available x-ray radiation quality and for a range of depths and field sizes with 6 MV x-rays. The latter consisted of attempting to directly measure the ratio of TPR for d of 5 cm to 30 cm ($TPR_{30,5}$) for $r \in [3, 10, 20]$ cm, and $S_{c,p}$ at $d = 5$ cm.

As some of these measurements involved relatively small radiation fields, radiographic images were used to ensure that both the ionisation chamber effective point of measurement and fluoroperovskite crystal of each fibre coupled dosimeter was co-incident with the isocentre to within 1 mm. This was then verified by comparing response with the collimator positioned at 90° and 270°. Relative response for x-ray quality changes with d ranging from 5 cm to 35 cm was also collected at $r = 10$ cm while testing linearity with dose per pulse, as detailed in § 3.3.6.

While this approach does not provide a direct quantitative characterisation of energy dependence in the sense implied by equation 2.18 and figure 2.8d, it does provide practical experience with the dosimeters under test that can be more readily related to real usage scenarios. The method does rely heavily on accurate ionisation chamber dosimetry, which was repeated with both the TW31014 and TW31015 ionisation chambers (see § 3.3.2). While these chambers are specified[319] as suitable for measurements down to $r = 2$ cm, comparison to the $NaMgF_3$:Mn fluoroperovskite was only made for $r > 3$ cm, for which lateral electronic equilibrium is maintained for 6 MV (see equation 2.24). Where applicable, ionisation chamber data was also checked for gross error against nominal data tables for the accelerator used.

These measurements were undertaken for each of the $NaMgF_3$:Eu, $NaMgF_3$:Mn, $RbMgF_3$:Eu, and $RbMgF_3$:Mn dosimeters, except for measurement of $S_{c,p}$ for which only $NaMgF_3$:Mn was used. Additional comparative data was measured using a PTW type TW60012 electron dosimetry diode, a silicon detector which is often used in the harder radiation qualities of small MV x-ray fields but known to over-respond for $r \geq 10$ cm.[319]

3.4 Summary

A detailed account of experimental methods and apparatus has been presented in this chapter, encompassing both the materials science undertaken at Victoria University of Wellington and the radiotherapy characterisation at Wellington Regional Hospital. The remaining chapters address primarily the experimental findings and their interpretation.

Chapter 4

Materials Characterisation

The experimental data obtained from characterisation of bulk crystal samples is presented in this chapter. For most samples, powder diffraction, photoluminescence spectra, and radioluminescence spectra are presented, supplemented by spectrally resolved thermoluminescence glow curves, optical absorption spectra, and magnetisation measurements where applicable. A relatively large number of luminescence ions doped into $NaMgF_3$ were investigated and the results presented herein were used to select a smaller subset of these for further investigation.

Statement of Uncertainty in Reported Energy Levels

For each dopant investigated a tabulated energy level scheme is reported in this chapter, but these tables do not contain explicit statements of uncertainty in reported energy levels. This was ultimately a pragmatic decision in the face of a large quantity of data obtained with widely variable sources of uncertainty. The reader is advised to refer at first to the associated figures for guidance on how well defined an energy level might be, and to place more emphasis on PL spectroscopy and absorption data over RL spectra, the latter being obtained without corrections for instrument spectral sensitivity.

Levels identified from optical absorption or PL excitation data (tabulated as AB or EX) can be regarded as most precise, spectral widths aside. The specified instrumental accuracy for absorption data is 0.1 nm at visible (± 10 cm^{-1}) and ultraviolet (± 22 cm^{-1}) wavelengths and 0.3 nm in the near infrared (± 5 cm^{-1}). For PL excitation and emission these figures are similar at 0.5 nm at visible (± 40 cm^{-1}) and ultraviolet (± 110 cm^{-1}) wavelengths, and 0.2 nm (± 4 cm^{-1}) for near infrared measurements. Spectral resolution and repeatability for these instruments is typically better than 0.1 nm and so aforementioned wavelength accuracies represent potential systematic error expected to dominate the total uncertainty.

The CCD based spectrometers used for RL spectroscopy are instead resolution limited but ought to have have excellent energy reproducibility. Lack of viable corrections for spectral sensitivity introduces systematic error in energies determined from centre wavelengths, which might be estimated by examination of the response data presented in figure 3.6c. Wide band emissions near the limits of the wavelength range are most effected with errors in excess of 1 nm, perhaps significantly so, possible in these regions.

Energy levels identified from the emission spectrum (tabulated as EM) are reported as an average of all assigned emissions across the available PL and RL data, with each given equal weighting. RL peaks are isolated by fitting (see § 3.2.7) while PL peaks are reported as the observed centre wavelength as most peaks are either of narrow width or measured in isolation. For wide band emissions in PL data the centre wavelength was in most cases found by localised quadratic fitting. In cases where small splitting of a $4f$ free ion level is observed, the reported energy is again the average of all observed peaks with equal weighting. This leads to occasional minor inconsistencies such as an transition to the ground state reported with emission

energy a few cm^{-1} higher than the reported energy for the excited state. Again, the reader is referred to the spectral data presented in the figures, where such situations can be readily identified.

For a few samples, an energy level is reported which could not be resolved and assigned from absorption or excitation measurements but is implied by additional emissions observed under x-ray excitation. Such levels are assigned energy by reference to the NIST Atomic Spectra Database (ASD), Dieke diagram, or calculated with aid of the relevant Tanabe-Sugano diagram (tabulated as AS, DD, and TS respectively). Significant uncertainty is involved here, perhaps on the order of 100 cm^{-1} to 1000 cm^{-1} as the ASD and Dieke diagram represent free ion levels while the Tanabe-Sugano diagram arguably has insufficient free parameters to fully describe the influence of the crystal field on d orbitals. The select few energies tabulated as AS or DD take no account of the influence of the crystal field, and so have only been reported against rare earth dopants for which the error arising from this can reasonably expected to be small.

As a final note, the assignment of an unambiguous spectroscopic term label is not always possible for certain rare earth ions with a high density of states at optical energies. Where multiple labels are appropriate or are reported in relevant literature, multiple labels may be tabulated herein against a single spectral feature. These are listed in order of decreasing 'purity' in terms of the leading percentages given for the free ion levels in the NIST Atomic Spectra Database.[320]

Presentation of Spectral and Diffraction Data

For each sample reported in this chapter the x-ray diffraction and spectral data (PL, RL, TSL, and absorption) is presented with a common figure format which will be detailed here once. The first example is figure 4.3 on page 70, and the first example containing TSL data is figure 4.6 on page 77. In each of these figures, an XRD pattern is displayed in a vertically reduced layout, and the reference pattern plotted inverted with compressed dynamic range to ensure visibility of low intensity reflections. Lines in the reference pattern which are absent from the experimental data are marked with red arrows. Spurious low intensity peaks which are consistent with a plausible contaminant are similarly marked in green, and those which remain unexplained in blue. Plausible contaminants are limited to NaF, MgF_2, and the dopant listed in table 3.1 for the sample in question. Logarithmic scaling is used as well resolved reflections range in intensity by a factor of about 10^3, while the inset plot used to illustrate the fitted diffractogram linearly represents intensity.

PL spectra are normalised and the emission spectra plotted always in red. Where possible, assigned transitions are labelled on the plot, but otherwise can be identified with reference to the fitted RL data and the tabulated energy levels. Emission and excitation wavelengths are indicated in the legend, along with the SCHOTT designation[i] of any filters fitted to the emission monochromator. If used, excitation filters are indicated in the figure caption. Fitted RL spectra are plotted for a single snapshot at the indicated time during the high dose irradiations. For samples with relatively few RL emission peaks the time evolution of intensity for each may be displayed adjacent to the RL spectra in the same figure, while for more complex emission spectra this is shown in a separate figure with correlated colours in either case. RL intensity as a function of time is calculated as the intensity under the fitted peak, and so relative heights may not correspond to those in the spectrum. There is no deliberate correspondence of plot colours between PL and RL spectra.

Where available, TSL data is illustrated in a map of T against λ, with selected emission spectra plotted at the temperatures indicated by the dashed lines of the same colour across the map. Glow peaks fitted to equations 3.5 and 3.6 are shown in the plot immediately below the map, and unless otherwise stated, represent the intensity integrated under the entire emission spectrum to emulate non-spectrally resolved TSL as is more commonly reported in the literature. As most samples exhibit a wide range in intensity of TSL peaks, more so than may be visible in the colour map, the fitted glow peaks are plotted logarithmically, while the emission spectra are plotted linearly.

[i] These filters are widely used, nominal transmittance can be obtained from the vendor literature.[321]

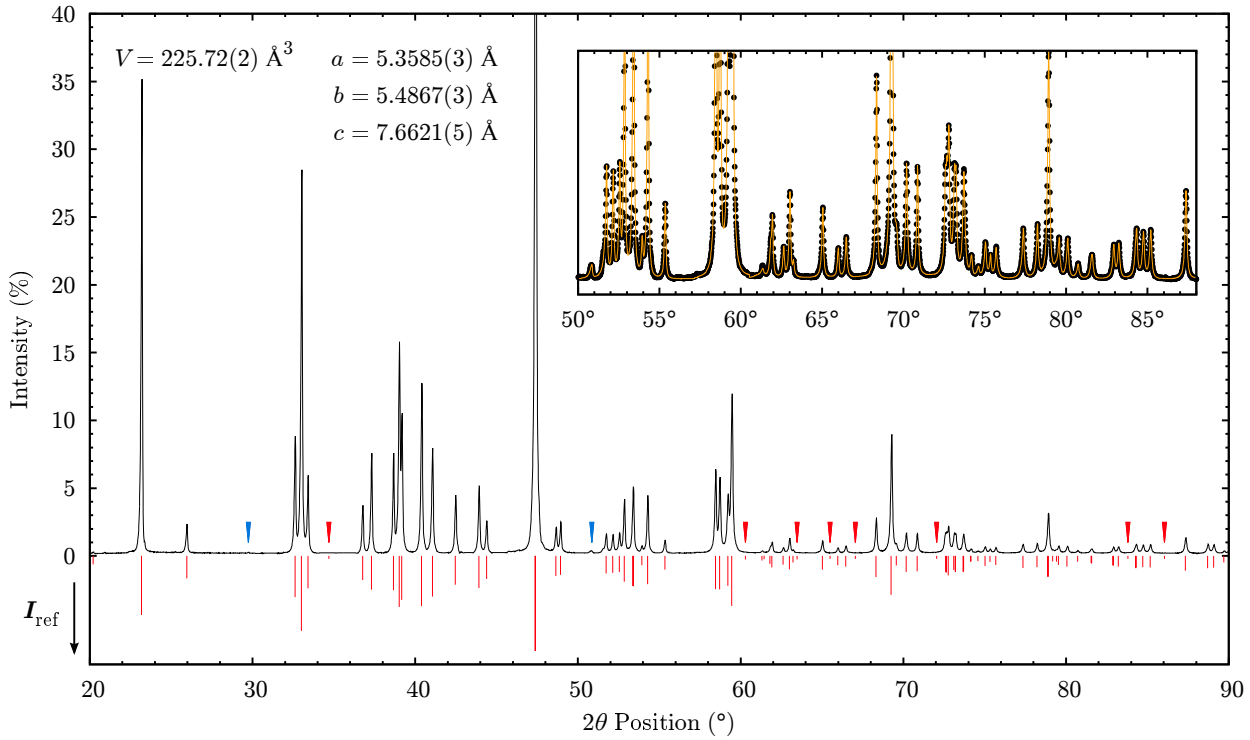

Figure 4.1: XRD pattern (black) for undoped $NaMgF_3$ (J150501) compared to reference data (red), with arrowhead markers indicating observed peaks absent from the reference pattern (blue) and unobserved peaks listed in the reference pattern (red). Unit cell volume and lattice parameters are given in the top left. Inset axes illustrate fitting, with experimental data plotted with point markers (black) and overlaid by fits (orange). Note that the dynamic range of the reference pattern has been compressed to ensure low intensity lines are visible.

4.1 Undoped $NaMgF_3$

Experimental data on the host crystal is presented first in this section as the results are pertinent to those obtained for activated samples. It should be noted that 'undoped' in this case might be better stated as 'nominally undoped', in that low level contamination with a range of the dopants listed in table 3.1 is inevitable as both samples J140501 and J150501 were necessarily prepared in the same glove-box using crucibles used for previous samples. As for several other samples, Eu^{2+} in particular was detected, despite not being intentionally introduced during preparation.

4.1.1 Diffraction Data

Powder diffraction data measured on sample J150501 is presented in figure 4.1, with the fit of experimental data to equation 3.2 illustrated in the inset plot. A total of 87 reflections are observed for $2\theta \in [20, 90]°$, with the majority of high angle reflections being of low intensity. 85 of these are indexed as reflections in the $NaMgF_3$ unit cell, while the two weak reflections marked in blue remain unexplained. To aid the presentation of data with such high dynamic range, the range of intensities in the reference pattern in figure 4.1 has been compressed and the most intense measured reflection near 47° has been cropped. All relative intensities are listed in table 4.1.

A literature reference pattern for $NaMgF_3$ was derived from the average of the peak positions and intensities for 7 patterns from the powder diffraction file: ICDD codes 01-076-6195[262], 04-015-9359[280], 04-015-9360[280], 04-015-3234[262], 04-011-9877[322], 04-012-1614[323], and 04-012-1616[323]. These represent all the 'starred' and 'indexed' patterns in the database for $NaMgF_3$ measured at standard temperature and pressure. Peaks with intensity below 1% appearing in only one of these references were excluded. This literature sourced reference pattern is plotted in red in figure 4.1 and is listed in table 4.1. Uncertainties in

the reference given in the table represent the statistical variation in these patterns for a confidence interval of 0.95. This pattern is used as a reference in the evaluation of the diffraction data for all samples in the study.

Peak intensities and positions derived from the integrated area and θ_n values of each fitted peak are also listed in table 4.1. The positions of all indexed peaks can be seen to agree with the listed reference values within the uncertainty bounds of each, and so accordingly the refined unit cell parameters and volume given in figure 4.1 are also in agreement with the reference pattern. A relatively consistent residual in 2θ averaging at $+0.03°$ is observed, suggesting a small systematic error. This level of error is reasonably attributable to instrument calibration and alignment in both the measured and reference data[ii].

Differences in intensities between the reference and measured patterns are broadly comparable, sufficiently so that there can be little doubt the structure is the same despite the intensity differences in many peaks exceeding experimental uncertainties. After normalisation, intensity of the three most significant reflections (at approximately 23°, 33°, and 47°) is poorly correlated, and so the measured intensities shown in table 4.1 were instead scaled to minimise residuals across the entire pattern in the least squares sense. Differences in intensity intensities can in part be attributed to the line nature of the instrument used, which does not integrate the entire Debye ring.

4.1.2 Radiation Induced Absorption

A marked increase in optical absorption was observed in undoped $NaMgF_3$ following exposure to ionising radiation, explored herein for doses on the order of 100 Gy and above. The primary absorption occurs at approximately 34500 cm^{-1} (295 nm) with lower intensity absorption peaks at 24400 cm^{-1} (410 nm), 20100 cm^{-1} (497 nm), and 15100 cm^{-1} (662 nm), observed for both samples J140501 (figure 4.2a) and J150501 (figure 4.2b) exposed to 40 kVp x-rays and ^{137}Cs γ-rays respectively. All samples were visibly yellow after irradiation. Absorption in sample J150501 was measured over a wider wavelength range than presented in figure 4.2b, but no change in absorption was observed from the low energy limit plotted here, at 11000 cm^{-1}, down to the experimental limit near 5500 cm^{-1}.

These absorptions are attributed to the creation of F–centres (34500 cm^{-1}), F_2–centres (24400 cm^{-1}), and possibly also F_3–centres (20100 cm^{-1} and 15100 cm^{-1}). The latter are designated F_3 and F_3' in figure 4.2, there being multiple spatial arrangements possible for more than two adjacent fluorine vacancies. These assignments are largely consistent with a previous study[78] of colour centre formation in $NaMgF_3$.

Individual absorption peaks isolated by fitting are depicted in the inset plots of figures 4.2a and 4.2b. It is clear that for both samples the principal peak mentioned above actually consists of a number of peaks, of which only the component near 34500 cm^{-1} is attributed to F–centres. Additional components appear at 30100 cm^{-1} (332 nm) in sample J150501, and in the region of 40000 cm^{-1} for both samples. These extra peaks are required to achieve a reasonable fit with Gaussians alone, along with a weaker absorption above 45000 cm^{-1} which is not fully resolved within the energy range of the spectrophotometer (dashed curves in figure 4.2 inset plots).

It is clear that the dose response of these components is sufficiently different that they cannot be attributed to the same defect. In particular the 30100 cm^{-1} in sample J150501 can be seen, even without fitting, to have a more rapid response and lower saturation dose. Absorptions at energies above that of the F–centre peak in both samples are possibly due to H–centres,[78] while the 30100 cm^{-1} peak observed for sample J150501 remains unidentified.

A measure of confidence in the assignments of given above can be found in their relative dose response. It is well established, at least for the alkali halides,[324] that an equilibrium condition $F_2 \leftrightarrow 2F$ exists during irradiation. This is reflected in the relative intensity of the absorption bands, in that $[F_2] \propto [F]^2$, where $[F]$ and $[F_2]$ are the absorption intensities for the F–centre and F_2–centre bands respectively. This is illustrated for both samples in figure 4.2c, where absorption is measured by integrating the fitted peaks. This data could

[ii]For comparison, the highest quality designations awarded in the powder diffraction file, 'starred' and 'indexed', require error in 2θ to be less than 0.03° and 0.06° respectively.

				Position (°)			Intensity (%)		
No.	h	k	l	Meas.	Ref.	Diff.	Meas.	Ref.	Diff.
1	1	0	1	20.23(3)	20.20(1)	0.03	0.1(1)	0.8(3)	−0.7
2	0	0	2	23.21(3)	23.18(2)	0.03	46.1(1)	39(4)	7.1
3	1	1	0	23.21(3)	23.18(1)	0.03	46.1(1)	38(4)	8.1
4	1	1	1	25.98(3)	25.96(1)	0.02	3.8(1)	5.6(3)	−1.9
5	0	2	0	32.63(3)	32.61(2)	0.02	10.9(1)	18.7(9)	−7.8
6	1	1	2	33.04(3)	33.01(2)	0.03	43.8(1)	62(4)	−18.2
7	2	0	0	33.43(3)	33.40(2)	0.03	8.6(1)	11.7(8)	−3.1
8	0	2	1	—	34.70(3)	—	—	0.1(0)	—
9	1	2	0	36.79(3)	36.77(2)	0.02	5.0(1)	6.4(2)	−1.4
10	2	1	0	37.33(3)	37.31(2)	0.02	11.5(1)	12.5(7)	−1.0
11	1	2	1	38.68(3)	38.66(2)	0.02	9.6(1)	13.0(6)	−3.4
12	1	0	3	39.03(3)	39.01(2)	0.02	27.3(1)	29(2)	−1.7
13	2	1	1	39.19(3)	39.18(2)	0.01	11.9(1)	21(2)	−9.1
14	0	2	2	40.41(3)	40.39(2)	0.02	20.3(1)	28(1)	−7.7
15	2	0	2	41.07(3)	41.06(2)	0.01	13.1(1)	18.2(8)	−5.1
16	1	1	3	42.49(3)	42.47(2)	0.02	7.3(1)	9.3(7)	−2.0
17	1	2	2	43.94(3)	43.92(2)	0.02	8.2(1)	11.5(5)	−3.3
18	2	1	2	44.41(3)	44.38(3)	0.03	4.1(1)	5.8(4)	−1.7
19	0	0	4	47.42(3)	47.38(3)	0.04	151.8(1)	100.0(0)	51.8
20	2	2	0	47.42(3)	47.38(3)	0.04	151.8(1)	100.0(0)	51.8
21	0	2	3	48.67(3)	48.64(2)	0.03	3.7(1)	4.5(4)	−0.8
22	2	2	1	48.95(3)	48.93(3)	0.02	4.0(1)	3.9(2)	0.1
23	1	2	3	51.76(3)	51.73(2)	0.03	3.1(1)	3.4(3)	−0.3
24	2	1	3	52.16(3)	52.14(3)	0.02	2.4(1)	3.2(2)	−0.8
25	3	0	1	52.57(3)	52.55(4)	0.02	2.3(1)	2.8(3)	−0.5
26	1	3	0	52.87(3)	52.84(3)	0.03	6.6(1)	7.3(7)	−0.7
27	1	1	4	53.41(3)	53.38(3)	0.03	9.1(1)	10(1)	−0.9
28	2	2	2	53.41(3)	53.38(3)	0.03	9.1(1)	10(1)	−0.9
29	3	1	0	53.94(3)	53.92(4)	0.02	0.7(1)	0.9(2)	−0.2
30	1	3	1	54.30(3)	54.28(3)	0.02	7.3(1)	8.8(6)	−1.5
31	3	1	1	55.36(3)	55.34(4)	0.02	1.7(1)	2.1(2)	−0.4
32	1	3	2	58.47(3)	58.45(3)	0.02	10.6(1)	12.2(6)	−1.6
33	0	2	4	58.74(3)	58.71(3)	0.03	9.6(1)	12(1)	−2.4
34	2	0	4	59.23(3)	59.21(3)	0.02	8.5(1)	9.9(9)	−1.4
35	3	1	2	59.48(3)	59.46(4)	0.02	22.1(1)	28(1)	−5.9
36	2	2	3	—	60.30(3)	—	—	0.1(0)	—
37	2	3	0	61.34(3)	61.31(3)	0.03	0.3(1)	0.2(0)	0.1
38	1	2	4	61.43(3)	61.44(3)	−0.01	0.2(2)	0.1(0)	0.1
39	2	1	4	61.84(4)	61.80(3)	0.04	0.8(2)	0.7(0)	0.1
40	3	2	0	61.95(3)	61.92(4)	0.03	1.2(1)	1.5(1)	−0.3
41	2	3	1	62.64(3)	62.62(3)	0.02	0.7(1)	0.9(0)	−0.2
42	1	0	5	63.03(3)	62.99(3)	0.04	2.1(1)	2.0(3)	0.1
43	3	2	1	63.23(3)	63.22(4)	0.01	0.3(1)	0.5(3)	−0.2
44	3	0	3	—	63.47(4)	—	—	0.1(0)	—
45	1	3	3	65.05(3)	65.01(3)	0.04	1.8(1)	2.0(3)	−0.2
46	1	1	5	—	65.49(6)	—	—	0.1(0)	—
47	3	1	3	66.00(3)	65.97(4)	0.03	0.7(1)	1.0(1)	−0.3
48	2	3	2	66.48(3)	66.46(4)	0.02	1.1(1)	1.2(1)	−0.1
49	3	2	2	—	67.05(4)	—	—	0.1(0)	—
50	0	4	0	68.35(3)	68.32(4)	0.03	4.6(1)	4.9(5)	−0.3
51	2	2	4	69.29(3)	69.25(4)	0.04	17.1(1)	17(1)	0.1
52	0	4	1	69.57(4)	69.56(5)	0.01	0.7(2)	1.0(2)	−0.3
53	4	0	0	70.19(4)	70.17(6)	0.02	3.2(1)	2.9(4)	0.3
54	1	4	0	70.87(4)	70.84(4)	0.03	2.7(1)	2.6(2)	0.1
55	1	4	1	—	72.05(4)	—	—	0.1(0)	—
56	4	1	0	72.58(4)	72.60(6)	−0.02	2.4(1)	2.9(8)	−0.5
57	2	3	3	72.67(4)	72.64(5)	0.03	1.4(1)	3.1(6)	−1.7
58	1	2	5	72.79(4)	72.75(4)	0.04	3.4(1)	4.2(5)	−0.8
59	2	1	5	73.14(4)	73.09(4)	0.05	2.4(2)	2.2(2)	0.2
60	0	4	2	73.23(4)	73.20(5)	0.03	2.1(1)	2.8(5)	−0.7
61	3	2	3	73.23(4)	73.20(4)	0.03	2.1(1)	2.8(4)	−0.7
62	1	3	4	73.71(4)	73.68(5)	0.03	3.5(2)	2.9(5)	0.6
63	4	1	1	73.71(4)	73.70(8)	0.01	3.5(2)	2.6(7)	0.9
64	0	0	6	74.19(4)	74.14(5)	0.05	0.5(1)	0.3(1)	0.2
65	3	3	0	74.19(4)	74.14(4)	0.05	0.5(1)	0.4(1)	0.1
66	3	1	4	74.62(4)	74.57(5)	0.05	0.3(2)	0.3(1)	0.0
67	4	0	2	75.04(4)	75.02(6)	0.02	1.1(2)	1.1(2)	0.0
68	3	3	1	75.35(4)	75.32(5)	0.03	0.6(1)	0.4(1)	0.2
69	1	4	2	75.69(4)	75.67(4)	0.02	1.0(2)	0.9(1)	0.1
70	4	1	2	77.37(4)	77.34(6)	0.03	1.6(2)	1.6(2)	0.0
71	2	4	0	78.24(4)	78.21(5)	0.03	1.5(1)	1.4(2)	0.1
72	1	1	6	78.93(4)	78.89(5)	0.04	6.5(1)	4.8(8)	1.7
73	3	3	2	78.93(4)	78.89(4)	0.04	6.5(1)	4.9(7)	1.6
74	0	4	3	79.21(3)	79.17(4)	0.04	0.1(1)	0.7(9)	−0.6
75	2	4	1	79.41(3)	79.40(7)	0.01	0.1(1)	0.3(1)	−0.2
76	4	2	0	79.58(4)	79.54(6)	0.04	1.7(2)	0.9(2)	0.8
77	2	2	5	80.10(4)	80.06(4)	0.04	1.3(2)	1.2(2)	0.1
78	4	2	1	80.74(4)	80.71(6)	0.03	0.5(2)	0.4(1)	0.1
79	3	2	4	81.55(4)	81.55(3)	0.00	0.4(2)	0.6(1)	−0.2
80	1	4	3	81.59(4)	81.58(5)	0.01	0.5(2)	0.7(1)	−0.1
81	2	4	2	82.93(4)	82.90(6)	0.03	1.0(2)	1.0(2)	0.0
82	3	0	5	82.93(4)	82.89(5)	0.04	1.0(2)	1.0(2)	0.0
83	4	1	3	83.24(4)	83.21(6)	0.03	1.1(2)	1.2(2)	−0.1
84	2	0	6	—	83.80(7)	—	—	0.1(0)	—
85	1	3	5	84.33(4)	84.30(5)	0.03	1.7(2)	1.5(3)	0.2
86	4	2	2	84.33(4)	84.28(5)	0.05	1.7(2)	1.7(2)	0.0
87	3	3	3	84.75(4)	84.72(5)	0.03	1.5(2)	1.4(3)	0.1
88	3	1	5	85.20(4)	85.16(5)	0.04	1.6(2)	1.4(2)	0.2
89	2	1	6	—	86.05(5)	—	—	0.1(0)	—
90	0	4	4	87.37(4)	87.33(5)	0.04	2.7(2)	2.4(4)	0.3
91	2	4	3	88.74(4)	88.70(5)	0.04	1.5(2)	1.7(3)	−0.2
92	4	0	4	89.10(3)	89.07(6)	0.03	1.5(2)	1.5(3)	0.0
93	1	4	4	89.72(3)	89.70(5)	0.02	0.6(3)	0.5(1)	0.1

Table 4.1: Summary of XRD data for undoped $NaMgF_3$ (J150501).

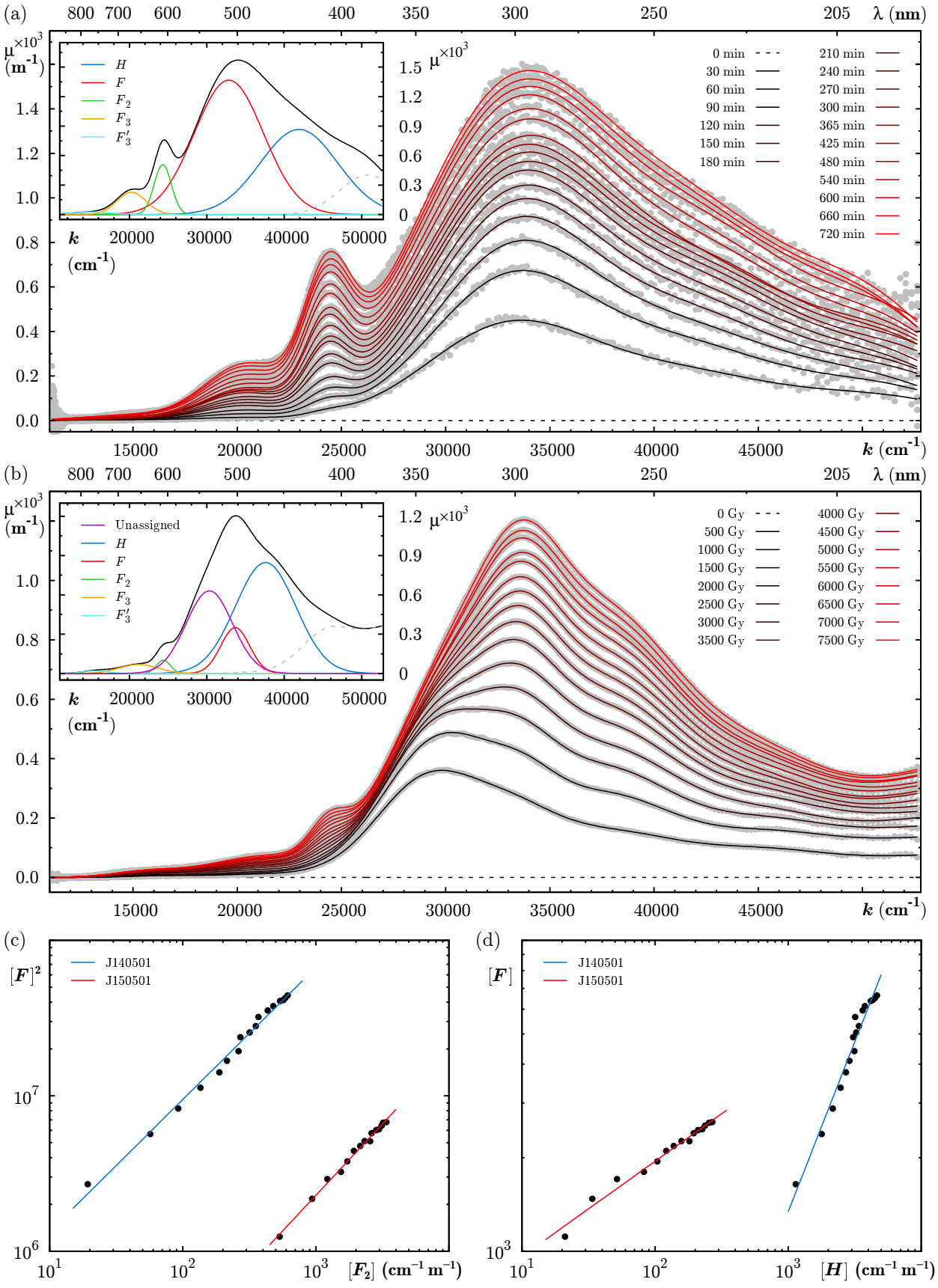

Figure 4.2: Radiation induced absorption in undoped $NaMgF_3$ as observed for exposure of samples (a) J140501 and (b) J150501 to 40 kVp x-rays and ^{137}Cs respectively, with individual fitted peaks and their assignments shown for the highest dose level in each inset plot. Baseline absorption prior to irradiation has been subtracted. Equilibrium between defect populations is illustrated between (c) F–centres and F_2–centres, and between (d) H–centres and F–centres, in terms of the integrated intensity of fitted peaks.

in principle be converted to absolute concentrations using equation 2.32, but this has not been attempted here for lack of an independent experimental estimation of the oscillator strength in $NaMgF_3$ for each of these centres.

Similarly, the equilibrium $H \leftrightarrow F$ almost certainly exists at least during irradiation, implying that one might also expect to find $[F] \propto [H]$. Figure 4.2d would appear to confirm this, but is must be acknowledged that there is considerably more uncertainty in fitting as these two peaks are not distinctly resolved at room temperature. This is reflected in the discrepancy in fitted location of the H–centre absorption peak between samples J140501 and J150501. It could be argued that in figure 4.2a there is no distinct absorption at energies higher than the F–centre band and that resolving an H–band absorption in this region is no more than an artifact of use of Gaussian functions. The assignment of the higher energy absorptions to H–centre defects is therefore tentative at best.

Differences between radiation induced absorption spectra in samples J140501 and J150501 are a product of inter-sample variation and dose rate effects. The absorption peak at 30100 cm^{-1} observed in sample J150501 is absent from sample J140501, and so conceivably may be an impurity. Of all the dopants studied, broad absorption or PL excitation at this energy was only observed for $NaMgF_3$:Sm (see figure 4.19b), although it is doubtful that trace contamination would give rise to the observed magnitude of absorption. The tendency toward saturation of the 30100 cm^{-1} absorption, while the F–centre band continues to grow, implies this absorption is associated with a defect capable of trapping charge for periods of days at room temperature, and which is present in relatively low concentrations. Apart from this anomalous absorption peak observed in sample J150501, these findings are broadly consistent with existing literature.[78,324]

For $n = 1.44$ (see figure 2.8a) and rough estimates from figure 4.2 of μ_{max} at 10 cm^{-1} and Δ at 1 eV, equation 2.32 yields an F–centre concentration on the order of 10^{17} cm^{-3}. This is assuming an oscillator strength for the absorption of 0.9, which is a reasonable assumption for alkali halide systems,[325] but may or may not apply to $NaMgF_3$. The resulting F–centre concentration is at best a first order approximation, but was used with some success in the models applied in § 4.8 and § 4.10.

4.2 $NaMgF_3$:Cr

Doping $NaMgF_3$ with CrF_3 produces weak near infrared luminescence, appearing as a broad emission band bordering the visible spectrum at 750 nm. The bandwidth is characteristic of a $3d$ intraconfigurational transition and the resolved energy levels are consistent with the Cr^{3+} ion being subject to an octahedral crystal field. This implies integration on the B site as would be expected for the relatively small ionic radii[141] of Cr^{3+} (0.615 Å). Relatively poor efficiency is attributed to low solubility of the dopant at the temperatures attained by TTP6 (see figure 3.2), which is evident in the coating of CrF_3 remaining on the surface of the fabricated sample. Only one sample (J140308) was characterised.

4.2.1 Diffraction Data

Powder diffraction data for sample J140308 is compared to the reference pattern in figure 4.3a, from which 9 low intensity peaks are absent from the experimental data, with 7 of these being the same as those not observed for sample J150501 (figure 4.1). The pattern is otherwise well matched in terms of peak positions, with an average residual of $+0.038°$ ($\sigma = 0.014°$) across all indexed peaks. A total of 20 additional reflections were observed, all below 0.3% intensity. Only one of these can be assigned to the dopant CrF_3 (ICCD 04-005-4253[326]) with any certainty. Others are aligned with plausible contaminants, particularly MgF_2.

While sample J140308 is clearly not pure, the diffraction data indicates the bulk of the sample comprises the orthorhombic phase of $NaMgF_3$.

4.2.2 Cr^{3+} Luminescence

PL excitation for this sample exhibits three broad bands centred at 15038 cm^{-1} (665 nm), 22624 cm^{-1} (442 nm), and 34483 cm^{-1} (290 nm). These energies can be reconciled with the Tanabe-Sugano diagram

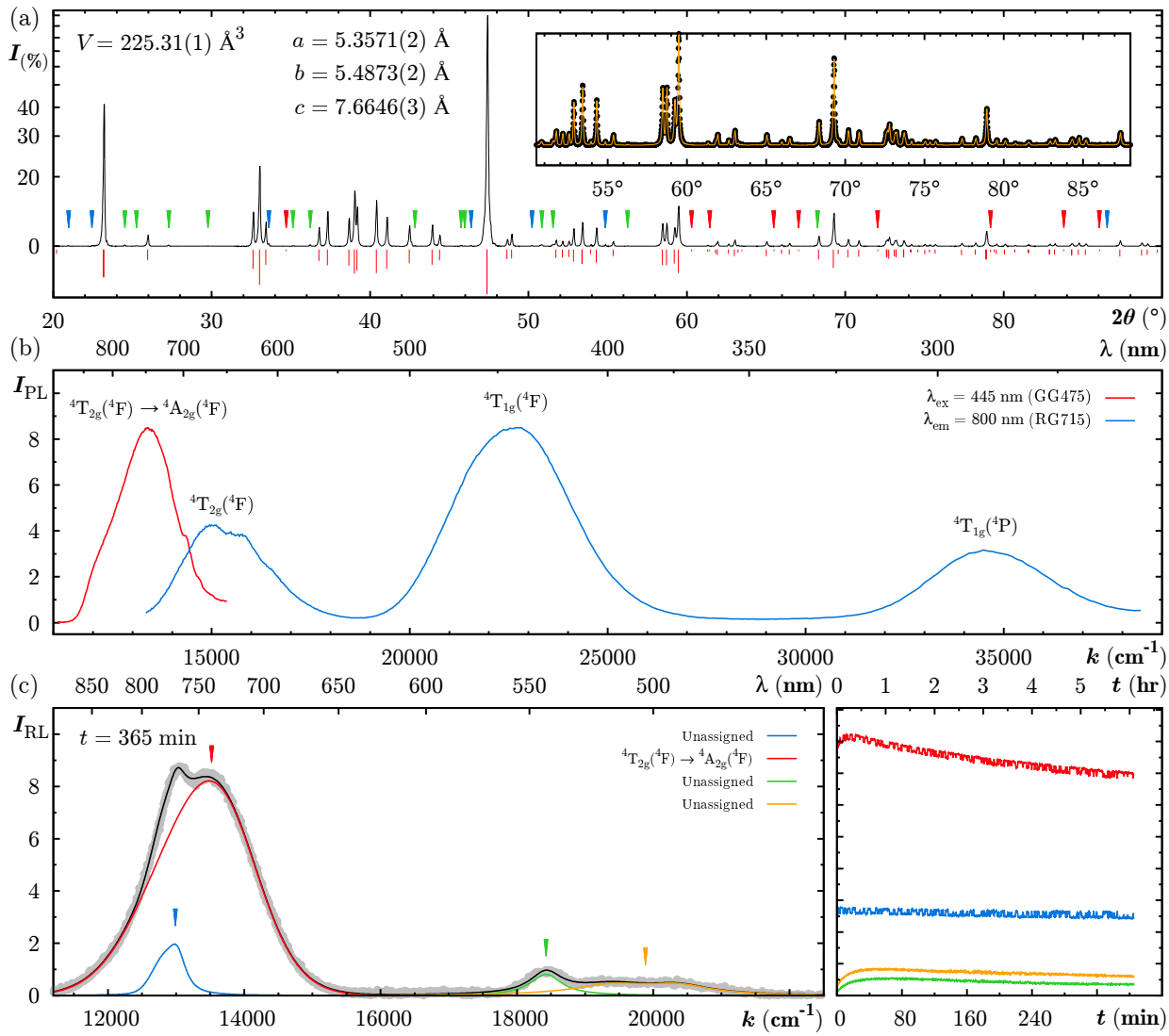

Figure 4.3: Basic characterisation measurements for $NaMgF_3$:Cr (J140308), including (a) XRD pattern, (b) photoluminescence spectra, and (c) fitted radioluminescence spectra. In (a), the experimental data is plotted (black) and the pseudo-Voigt fit (orange) illustrated in the inset, with markers over peaks which are missing from the reference pattern (red), explained by contaminants (green), and unexplained (blue). Markers in (c) are coloured to match the legend and the adjacent plot depicting the time dependence of each RL emission.

for the $3d^3$ configuration with $10Dq$ of 15038 cm^{-1} and Racah B parameter of 848 cm^{-1}. In this way, each of these excitations were assigned to transitions from the ground state, $^4A_{2g}(^4F)$, to the states $^4T_{2g}(^4F)$, $^4T_{1g}(^4F)$, and $^4T_{1g}(^4P)$, in order of increasing energy. The energies of the numerous other states within this configuration were then estimated from the Tanabe-Sugano diagram, but transitions from the ground state to these levels are all spin forbidden, and none were observed.

The broad emission observed at 13387 cm^{-1} (747 nm) in the PL and 13459 cm^{-1} (743 nm) in the RL is attributed to relaxation from the first excited state of the Cr^{3+} ion, $^4T_{2g}(^4F)$, to the ground state. The stokes shift is approximately 1600 cm^{-1}, with a bandwidth of about 100 nm in both the PL and RL emission, typical of an intraconfigurational transition within the $3d$ orbitals of a transition metal ion. A discrepancy of 4 nm between PL and RL is within the limits of uncertainty in fitting for the RL emission. Additional structure observed in the form of a narrower peak at 13057 cm^{-1} (766 nm) remains unassigned (see figure 4.3b). This unassigned peak appears essentially dose independent, which would indicate it does not arise from the Cr^{3+} ion.

Intensity of PL emission from sample J140308 was insufficient for an accurate lifetime measurement. Attempts at measuring the decay of the $^4T_{2g}(^4F) \rightarrow {}^4A_{2g}(^4F)$ emission (not illustrated) indicate an approx-

imate lower bound of 150 μs.

Intensity of the $^4T_{2g}(^4F) \rightarrow {}^4A_{2g}(^4F)$ emission in the RL spectra is initially enhanced, peaking after approximately 30 minutes of exposure followed by persistent decay. This shape can be explained by the presence of two competing processes with different time constants[iii], one which rapidly causes inflation of emission intensity, but saturates at relatively small doses, and another which causes gradual reduction in intensity, but saturates at much higher doses. In the simplest model, these processes are the filling of charge traps, which leads to higher luminescence efficiency, and the creation of colour centres which reduces the number of RL photons which are not self-absorbed. Similar time and dose dependence is observed in the RL emission of most materials reported in this chapter, and is explored quantitatively for samples J140306 and J140307 in § 4.8.2 and § 4.10.3 respectively.

4.2.3 Discussion

The Cr^{3+} ion produces luminescence in the region of the visible spectrum where silicon photodiodes are the most effective detectors, but at an energy slightly too high for optimal efficiency. The emission wavelength remains within the viable range for use of polymer optics. While absolute intensity comparisons between any of the samples reported herein has not been attempted, the long integration times required to acquire the luminescence data presented in figure 4.3 indicate a low luminescence efficiency for the one sample fabricated. This is no surprise as a significant portion of the 0.8% molar fraction of CrF_3 introduced to the sample melt remained deposited on the sample surface once cooled. While the melting point of CrF_3, which is reported variably[82, 327, 328] but may be as high as 1420 °C, is above the temperature attained during fabrication. This is also so for many dopants which were satisfactorily integrated. Thus it appears that CrF_3 in particular has low solubility in $NaMgF_3$.

If $NaMgF_3$:Cr can be fabricated with a higher Cr^{3+} content, perhaps via a different method of crystal growth or by doping with $CrCl_3$ which has a much lower melting point,[327] it may well have merit for fibre coupled dosimetry applications. Any preference given to $NaMgF_3$:Cr in terms of emission energy is also shared by $NaMgF_3$:Sm, which appears much easier to fabricated using the techniques employed in this study.

There is currently no intention to pursue $NaMgF_3$:Cr as a material for fibre coupled dosimetry.

[iii] A very similar curve shape is seen for PDD as a function of depth (d) in a homogeneous medium, in which the inflationary process for small d is the buildup of a secondary charged particle fluence, and the deflationary process for large d is absorption of the primary photon fluence.

State	Energy (cm^{-1})	Method	Emissions	Energy (cm^{-1})
$^4T_{1g}(^4P)$	34483	EX	—	—
$^2T_{1g}(^2H)$	33076	TS	—	—
$^2T_{2g}(^2H)$	32420	TS	—	—
$^2A_{1g}(^2G)$	29879	TS	—	—
$^2T_{2g}(^2G)$	25377	TS	—	—
$^4T_{1g}(^4F)$	22624	EX	—	—
$^2T_{1g}(^2G)$	18275	TS	—	—
$^2E_{1g}(^2G)$	17489	TS	—	—
$^4T_{2g}(^4F)$	15038	EX	$^4T_{2g}(^4F) \rightarrow {}^4A_{2g}(^4F)$	13423
$^4A_{2g}(^4F)$	0	—	—	—

Table 4.2: Summary of energy levels for Cr^{3+} in $NaMgF_3$ and emissions observed for sample J140308. Energies were assigned with reference to excitation spectra (EX) and the Tanabe-Sugano diagram (TS) of the $3d^3$ configuration for those intermediate levels not observed due to the spin forbidden nature of the transition.

4.3 $NaMgF_3$:Dy

When doped with DyF_3, $NaMgF_3$ exhibits luminescence with emissions occurring in narrow structured bands in the visible and near infrared. The luminescent species is without doubt Dy^{3+}, and is assumed to substitute for Na^+ on the A site on the basis of ionic radius (1.03 Å). The lower energy emissions are weak and widely scattered below approximately 12000 cm^{-1}, an unfavourable situation for the intended applications. Only one sample (J140601) was characterised.

4.3.1 Diffraction Data

The diffractogram for sample J140601 is shown in figure 4.4a, in which the orthorhombic phase of $NaMgF_3$ is clearly identified, albeit with a few spurious reflections of relatively low intensity. Those observed only for sample J140601 occur at 24.31°, 27.85°, 46.63°, 67.51°, and 86.79°, representing the highest intensity peaks which occur in ICDD pattern 00-032-0352,[329] strongly suggesting residual DyF_3. The reflection at 86.79° lies beyond the reported range in 2θ for this pattern, while those at 24.31° and 27.85° have residuals in 2θ of about 0.2°. This is several times larger than required for a confident match based on so few peaks, but are assigned nonetheless in the absence of any tenable alternate explanations. Pattern 00-032-0352 represents the only DyF_3 diffraction data measured at standard temperature and pressure obtained in a search of the PDF by chemical composition.

An additional 14 very weak reflections were observed which do not feature in the reference pattern listed in table 4.1. These are common to most of the samples investigated and so will be addressed later in § 4.14.1.

4.3.2 Dy^{3+} Luminescence

PL emission spectra measured for sample J140601 excited at 350 nm can be seen in figure 4.4b. In comparing with existing literature[330–335] all emissions can be assigned to known transitions within the $4f^9$ configuration of the Dy^{3+} ion. The most intense peaks are at 20886 cm^{-1} (479 nm), 17441 cm^{-1} (573 nm), 11962 cm^{-1} (836 nm) and 10095 cm^{-1} (991 nm), which are assigned to $^4F_{9/2} \rightarrow {}^6H_J$, for $J = (15/2, 13/2, 7/2)$, and $^6H_{5/2} \rightarrow {}^6H_{15/2}$ transitions respectively. The lowest energy emission observed occurs at 6667 cm^{-1} (1500 nm) and is attributed to the $^6H_{5/2} \rightarrow {}^6H_{13/2}$ transition. Lower energy emissions are expected between the first few excited states, but these could not be measured due to the band gap cut-off of the detector used, which precludes measurement beyond approximately 1550 nm.

Excitation is also shown in figure 4.4b as measured when monitoring the $^6H_{5/2} \rightarrow {}^6H_{15/2}$ emission, revealing all the known Dy^{3+} states between 20000 cm^{-1} and 40000 cm^{-1}. A summary is given in table 4.3 along with the observed PL and RL emissions. The ^6H_J and ^6F_J multiplets, which all lie in relative isolation at energies below 20000 cm^{-1}, are all relatively 'pure' states with leading percentages of at least 90% for the indicated term.[330,334] Reasonable estimates of their energies were derived from the PL emission spectra in most cases. As reported elsewhere,[320] the $^6F_{1/2}$ level is not observed.

Above 20000 cm^{-1} the Dy^{3+} states are increasingly closely spaced with substantial mixing of states, rendering assignments ambiguous and in some cases perhaps meaningless. The indicated terms for these levels have been obtained with reference to literature[330,331] for Dy^{3+} in other crystal systems, and should not be taken as unique, or even reliable, labels. Due to this narrow spacing of these levels, relaxation is largely non-radiative until the first substantial energy differential at $^4F_{9/2}$, from which the majority of the observed emissions originate. The assignment of the weak $^4I_{15/2} \rightarrow {}^6H_{15/2}$ at 22075 cm^{-1} is not unique, in that it can be accounted for by other energy differentials within the reported levels.

The RL spectra from sample J140601 is plotted in figure 4.4c. Emissions at 20717 cm^{-1} (483 nm), 17514 cm^{-1} (571 nm), 15146 cm^{-1} (660 nm), 14674 cm^{-1} (681 nm), and 13318 cm^{-1} (751 nm) were also seen in the PL data, and are similarly assigned. Differences in relative intensity between these four emissions with respect to the PL emission intensities are due to the combined spectral response of the silicon CCD sensor (see figure 3.6c) and transmittance of the silica fibre optics used, neither of which were corrected (see § 3.2.7). Changes in RL intensity as the irradiation progresses can be explained in terms of trap

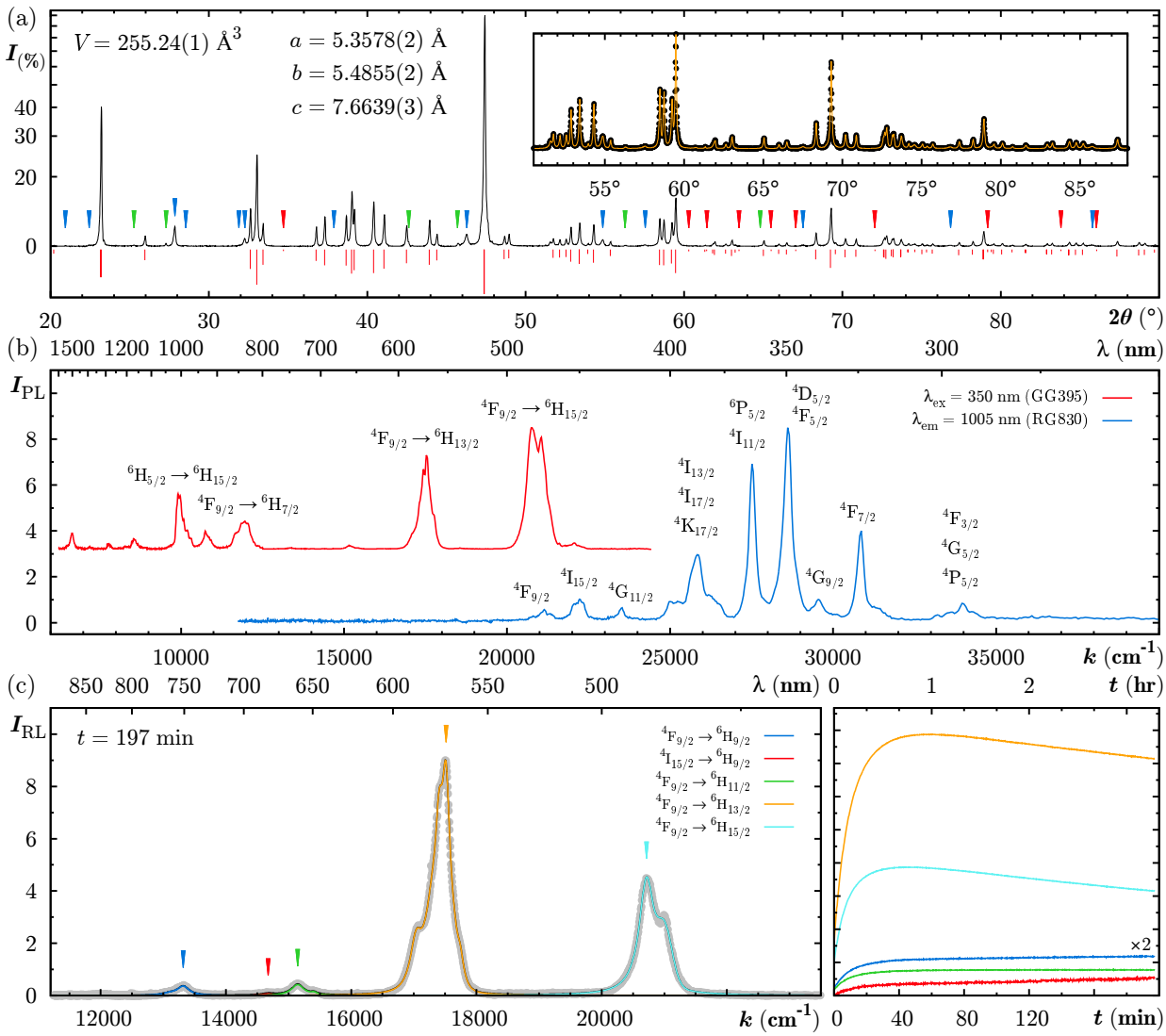

Figure 4.4: Basic characterisation measurements for $NaMgF_3$:Dy (J140601), including (a) XRD pattern, (b) photoluminescence spectra, and (c) fitted radioluminescence spectra. In (a), the experimental data is plotted (black) and the pseudo-Voigt fit (orange) illustrated in the inset, with markers over peaks which are missing from the reference pattern (red), explained by contaminants (green), and unexplained (blue). Markers in (c) are coloured to match the legend and the adjacent plot depicting the time dependence of each RL emission.

filling and radiation induced absorptions, as discussed in § 4.2.2. The degree of downturn at high doses for different emission energies is qualitatively consistent with the energy dependence of the colour centre absorption spectrum in figure 4.2. Only those emissions overlapping the colour centre absorption bands at visible wavelengths exhibit significant reduction in intensity with absorbed dose, while the lower intensity near infrared RL emissions appear essentially uninfluenced.

Decay of the 20886 cm^{-1} (479 nm) and 17441 cm^{-1} (573 nm) PL emissions from $NaMgF_3$:Dy are depicted in figure 4.5. These were excited using a broadband LED source centred at 28090 cm^{-1} (356 nm). Both of these emissions are parity forbidden and hence the observed long PL lifetimes are expected. Stretched exponential fits using equation 3.3 are illustrated, with the fitted values for τ and β shown on the figure. The effective lifetime, $\langle\tau\rangle$, as calculated with equation 3.4, is 1.93 ± 0.05 ms for both emissions. The origin of the stretched exponential behaviour is not immediately clear, but is often taken to indicate a distribution of lifetimes, both radiative and non-radiative, due to an inherent structural disorder.[336] In the case of $NaMgF_3$:Dy this may indicate a distribution of non-radiative decay centres, perhaps due to a range of inequivalent dopant sites arising from impurities, for which there is ample evidence in the diffraction data, and charge compensation defects.

4.3.3 Discussion

As shown in figure 4.5, the optical emissions from $NaMgF_3$:Dy are relatively long lived due to the parity forbidden nature of the $f \rightarrow f$ transitions involved. The measured effective lifetime of 1.93 ± 0.05 ms is well suited for temporal gating of stem signal in fibre coupled dosimeter applications, at least if used with Varian electron accelerators which typically generate radiation in x-ray pulses at several hundred Hz with a duty cycle well below 1%. While it was not possible to measure the lifetime of the near infrared emissions, it is plausible that at least those lower energy emissions deriving from the same excited state will have a similarly useful lifetime.

The Dy^{3+} ion possess a complex distribution of states between which excitation energy decays non-

State	Energy (cm^{-1})	Method	Emissions	Energy (cm^{-1})
$^4F_{3/2}$, $^4G_{5/2}$, $^4P_{5/2}$	33985	EX	—	—
$^4G_{7/2}$	31447	EX	—	—
$^4F_{7/2}$	30840	EX	—	—
$^6P_{3/2}$	30053	EX	—	—
$^4G_{9/2}$	29455	EX	—	—
$^4D_{5/2}$, $^4F_{5/2}$	28613	EX	—	—
$^4I_{11/2}$, $^6P_{5/2}$	27510	EX	—	—
$^4M_{19/2}$	26369	EX	—	—
$^4I_{13/2}$, $^4I_{17/2}$, $^4K_{17/2}$	25578	EX	—	—
$^4M_{21/2}$	25000	EX	—	—
$^4G_{11/2}$	23516	EX	—	—
$^4I_{15/2}$	22268	EX	$^4I_{15/2} \rightarrow {}^6H_{15/2}$	22075
			$^4I_{15/2} \rightarrow {}^6H_{9/2}$	14668
$^4F_{9/2}$	21051	EX	$^4F_{9/2} \rightarrow {}^6H_{15/2}$	20886
			$^4F_{9/2} \rightarrow {}^6H_{13/2}$	17441
			$^4F_{9/2} \rightarrow {}^6H_{11/2}$	15234
			$^4F_{9/2} \rightarrow {}^6H_{9/2}$	13528
			$^4F_{9/2} \rightarrow {}^6H_{5/2}$	10741
			$^4F_{9/2} \rightarrow {}^6F_{9/2}$	11962
			$^4F_{9/2} \rightarrow {}^6H_{7/2}$	11669
			$^4F_{9/2} \rightarrow {}^6F_{5/2}$	8562
$^6F_{3/2}$	13060	AS	—	—
$^6F_{5/2}$	12489	EM	—	—
$^6F_{7/2}$	10870	AS	—	—
$^6H_{5/2}$	10095	EM	$^6H_{5/2} \rightarrow {}^6H_{15/2}$	10095
			$^6H_{5/2} \rightarrow {}^6H_{13/2}$	6662
$^6H_{7/2}$	9382	EM	—	—
$^6F_{9/2}$	9089	EM	—	—
$^6F_{11/2}$	8000	DD	—	—
$^6H_{9/2}$	7799	EM	$^6H_{9/2} \rightarrow {}^6H_{15/2}$	7799
$^6H_{11/2}$	5899	EM	—	—
$^6H_{13/2}$	3433	EM	—	—
$^6H_{15/2}$	0	—	—	—[333]

Table 4.3: Summary of energy levels for Dy^{3+} in $NaMgF_3$ and emissions observed for sample J140601. The average emissions energies are tabulated for transitions observed in both PL and RL. States above about 22500 cm^{-1} are increasingly impure and the assignments less certain. Energies were determined with reference to the reported excitation spectrum (EX), emission spectrum (EM), with free ion levels from the Dieke diagram[48] (DD), and the NIST atomic spectra database[320] (AS) included where the level is expected but could not be isolated in the PL or RL spectra.

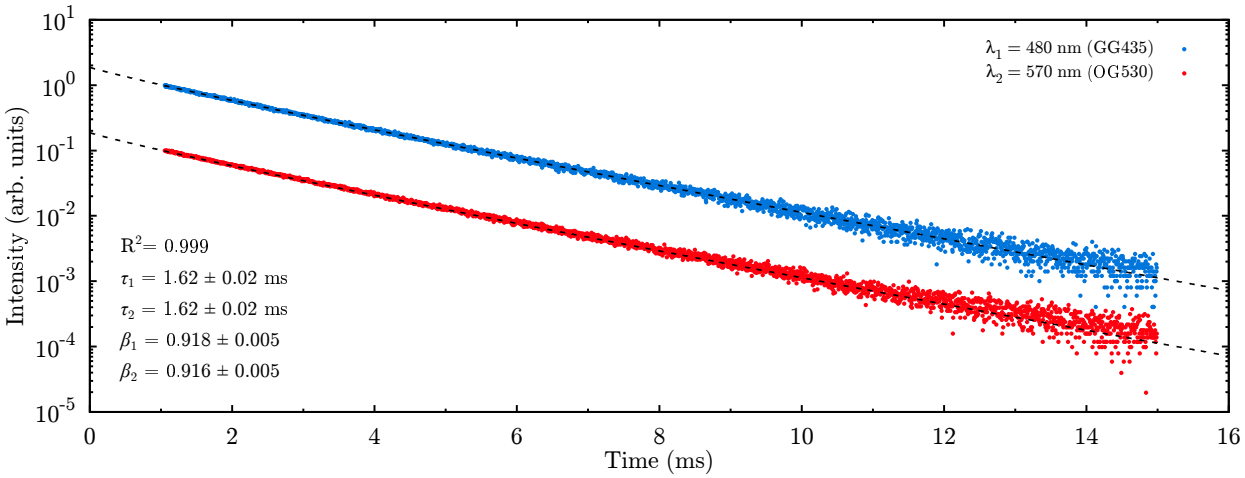

Figure 4.5: Decay of the $^4F_{9/2} \rightarrow {}^6H_J$ PL emissions for $J = (13/2, 15/2)$ in $NaMgF_3$:Dy (sample J140601) excited at 28090 cm^{-1}. Highly significant fits are illustrated for both decays, using stretched exponentials with the indicated parameters. Both emissions were found to have the same lifetime within the experimental uncertainty.

radiatively towards a large difference at the $^4F_{9/2}$ level, from which radiative emission occurs. This arrangement is favourable in that a broad range of excitation energies can lead to the observed emission, but the energy of the $^4F_{9/2}$ is too high to produce the desired near infrared emissions. These instead arise from transitions between the many lower excited states, while the majority of the emitted energy is released at visible wavelengths by relaxations of the $^4F_{9/2}$ level to the ground and first excited states. These visible emissions might be applied for RL dosimetry, but with no advantage over the band emissions of Mn^{2+} or Ni^{2+} discussed later in this chapter, while incurring the radiological disadvantages of a high atomic number dopant.

There is currently no intention to pursue $NaMgF_3$:Dy as a material for fibre coupled dosimetry.

4.4 $NaMgF_3$:Er

The luminescence activated upon doping $NaMgF_3$ with ErF_3 is qualitatively similar to that observed with DyF_3, with narrow structured emissions in the visible and near infrared characteristic of Er^{3+}. Unlike with $NaMgF_3$:Dy, the primary near infrared emission occurs near 1500 nm, which is well positioned to take advantage of the low attenuation in silica fibre optics whilst minimising the fraction of detected Čerenkov signal in high energy radiations. A significant portion of the excitation is unfortunately also emitted as visible light. The ionic radius of Er^{3+} is 1.00 Å under 8-fold co-ordination and 0.89 Å under 6-fold co-ordination, and so the preferred cation site is ambiguous in this regard. This is of little consequence as only $4f$ intraconfigurational transition are observed, the interpretation of which is possible without consideration of the crystal field. Only one sample was characterised (J140304).

4.4.1 Diffraction Data

The diffraction pattern for sample J140304 (see figure 4.6a) unambiguously identifies $NaMgF_3$ as the dominant phase in the sample, with significant additional reflections located at 28.13°, 32.19°, 33.36°, 46.77°, 47.64°, and 55.48°. The most intense of these are in reasonable agreement with the expected positions of the [111] and [301] reflections of ErF_3 as seen in ICDD pattern 04-012-5525.[337] However plausible the presence of ErF_3 might be this does not constitute a certain assignment, particularly while the other spurious lines remain unexplained. As with all samples, MgF_2 was identified.

EuF_3 was also checked for given that significant Eu^{2+} contamination was in evidence in the PL emission. None was observed in the diffraction data.

4.4.2 Er^{3+} Luminescence

PL emission from $NaMgF_3$:Er is plotted in figure 4.6b, after fitting and subtracting a broad tail from the $4f^6\left[^7F_0\right]5d(E_{1g}) \rightarrow {}^8S_{7/2}$ band emission of contaminant Eu^{2+}. The remaining structured emissions are all attributable to transitions within the $4f^{11}$ configuration of Er^{3+}. As excited at 27778 cm^{-1} (360 nm), the near infrared emissions were assigned to the transitions ${}^4S_{3/2} \rightarrow {}^4I_{11/2}$ at 8188 cm^{-1} (1221 nm) and ${}^4S_{3/2} \rightarrow {}^4I_{13/2}$ at 11826 cm^{-1} (846 nm), then from each to the ground state, ${}^4I_{15/2}$, with emission at 10128 cm^{-1} (987 nm) and approximately 6500 cm^{-1} (1550 nm). Visible emissions are assigned to the transitions from each of the states ${}^2H_{11/2}$, ${}^4S_{3/2}$, and ${}^4F_{9/2}$, to the ground state, with emitted energies of 19053 cm^{-1} (525 nm), 18337 cm^{-1} (545 nm), and 15218 cm^{-1} (657 nm) respectively. These assignments are consistent with the literature for Er^{3+} as observed in a number of different hosts,[176,338,339] including neighbourite.[268,340] The energy levels are summarised in table 4.4.

Close inspection of the PL emission reveals most of the line groupings have a common structure. Specifically, those groups near, 10000 $^{-1}$, 15500 cm^{-1}, 18000 cm^{-1}, and 19000 cm^{-1} have remarkably similar character and all terminate at the ground state, ${}^4I_{15/2}$, which is thus assumed to be the dominant source of the observed pattern. Using the peak positions observed in the PL emission and the peak centres from the fitted RL emission (see § 3.2.7), it can be deduced that the ground state is split into a minimum of four components at $-195(4)$ cm^{-1}, $-72(10)$ cm^{-1}, $+50(10)$ cm^{-1}, and $+201(24)$ cm^{-1} relative to their arithmetic mean. The values in brackets represent the spread across all examined peaks at 1σ. This may be a consequence of crystal field splitting or evidence for multiple sites brought about by varied charge compensation mechanisms. Excitation peaks are well correlated with the known energy levels[46,48,320] of Er^{3+} with centre energies, as seen in the PL spectra, shifted by up to 250 cm^{-1} to higher energies with respect to the free ion states.

The PL decays detected for the ${}^2H_{11/2} \rightarrow {}^4I_{15/2}$ and ${}^4S_{3/2} \rightarrow {}^4I_{15/2}$ emissions after 26670 cm^{-1} (375 nm) pulsed excitation can be seen in figure 4.7. Two peaks have been isolated for each of these transitions at the wavelengths indicated on the figure. These decays could not be fitted to a single exponential and so were fitted using the stretched exponential expression in equation 3.3. As described in § 4.3.2, the stretched exponential can be interpreted to indicate structural disorder in the region of the dopant site. In the case of $NaMgF_3$:Er such disorder may be due to a range of charge compensation defects. Both adjacent A site vacancies and H-centre defects are likely compensation mechanisms and have been shown to occur in a similar material,[198] $KMgF_3$:Eu^{3+}. Vacancy–Er^{3+} pairs, or clusters thereof, would perturb the local crystal field and so be expected to result in more than one distinct emission lifetime. Effective lifetimes calculated with equation 3.4 were 0.83 ± 0.02 ms, 0.83 ± 0.01 ms, 0.82 ± 0.01 ms, and 0.82 ± 0.02 ms for the 519 nm, 539 nm, 543 nm, and 551 nm emissions respectively. The lifetime of the ${}^2H_{11/2}$ and ${}^4S_{3/2}$ states are therefore identical within experimental uncertainty, and as these represent both spin allowed and forbidden transitions within the $4f^{11}$ configuration it would seem reasonable to expect that the remaining observed emissions have similar lifetimes.

RL emission measured during high dose x-ray irradiation of $NaMgF_3$:Er can be seen in figure 4.6c. Four peaks at 11824 cm^{-1} (846 nm), 15188 cm^{-1} (658 nm), 18386 cm^{-1} (544 nm), and 19020 cm^{-1} (526 nm) are also seen in the PL emissions (see figure 4.6b). A number of additional RL emissions were observed that are absent from the PL emission which originate from levels above the PL excitation energy of 27780 cm^{-1}. Specifically, from the ${}^2P_{3/2}$ level relaxing to ${}^2H_{11/2}$, ${}^4S_{3/2}$, ${}^4F_{9/2}$, ${}^4I_{11/2}$, ${}^4I_{13/2}$, and the ground state. The corresponding emission energies are listed in table 4.4. A broad emission of low intensity occurs near 20000 cm^{-1}, exhibiting bandwidth and time dependence inconsistent with any of the observed transitions within the $4f^{11}$ configuration. An emission of similar energy and character is also seen in samples J140307 ($NaMgF_3$:Sm) and J140308 ($NaMgF_3$:Cr), and so is considered unlikely to originate from the Er^{3+} site. A similar band emission in the RL of $NaMgF_3$:Er has been previously attributed to exciton luminescence, but was not reported at room temperature.[268]

Time dependence of fitted RL intensity was similar to that presented for $NaMgF_3$:Cr and $NaMgF_3$:Dy, and is not presented for $NaMgF_3$:Er as the qualitative interpretation is identical and no quantitative analysis was attempted for this sample.

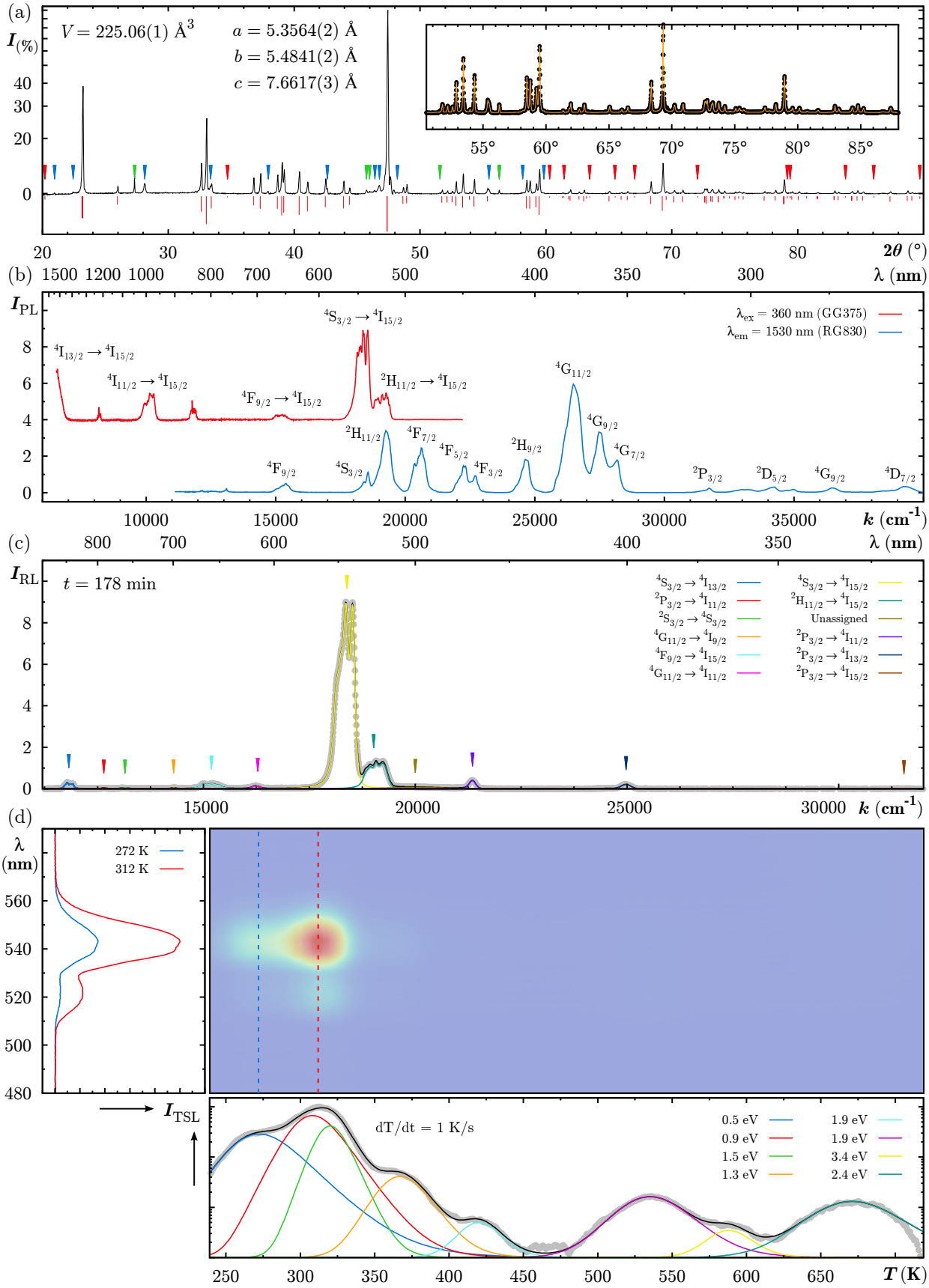

Figure 4.6: Basic characterisation measurements for $NaMgF_3$:Er (J140304), including (a) XRD pattern, (b) photoluminescence spectra, (c) fitted radioluminescence spectra, and (d) thermoluminescence emission spectra with fitted glow curves. In (a), the experimental data is plotted (black) and the pseudo-Voigt fit (orange) illustrated in the inset, with markers over peaks which are missing from the reference pattern (red), explained by contaminants (green), and unexplained (blue). Markers in (c) are coloured to match the legend. Activation energies for each of the fitted second order glow peaks in (d) are given on the subplot.

Sample J140304 exhibited strong room temperature TSL, with distinct second order glow peaks at 272 ± 1 K, 308 ± 2 K, 327 ± 2 K, and considerably weaker peaks at 367 ± 1 K, 420 ± 2 K, 535 ± 10 K, 588 ± 1 K, and 671 ± 1 K. The emission spectra and glow peaks are shown in figure 4.6d for the $^4S_{3/2} \rightarrow {}^4I_{15/2}$ and $^2H_{11/2} \rightarrow {}^4I_{15/2}$ emissions. These two emissions were fitted using the analytical approximation for second order thermoluminescence given in equation 3.6. Fits using equation 3.5 for first order kinetics did not produce satisfactory results, particularly for the higher temperature peaks, which seen in isolation appear symmetric in T. It can be seen in figure 4.6d that the TSL can be fitted with 8 distinct glow peaks, the fitted activation energies for which are listed on the plot.

All the peaks observed in the RL emission spectrum are present in the TSL emission spectrum on the principal glow peak near 312 K, although all but the $^4S_{3/2} \rightarrow {}^4I_{15/2}$ and $^2H_{11/2} \rightarrow {}^4I_{15/2}$ are extremely faint and have been excluded from the spectra shown in figure 4.6d. The intensity of the $^2H_{11/2} \rightarrow {}^4I_{15/2}$ emission relative to the $^4S_{3/2} \rightarrow {}^4I_{15/2}$ emission increases with rising temperature, becoming approximately equal for the faint glow peaks at and above 535 K. This may reflect temperature dependence of the emission efficiency. Additional weak TL was observed at 700 nm, with faint glow peaks at 270 K and 420 K. As mentioned in § 3.2.6 this is known to arise from the platinum heating element of the measurement apparatus.[288]

State	Energy (cm^{-1})	Method	Emissions	Energy (cm^{-1})
$^4D_{7/2}$	39293	EX	—	—
$^4G_{9/2}$	36496	EX	—	—
$^2D_{5/2}$	34695	EX	—	—
$^2D_{7/2}$	34247	EX	—	—
$^2K_{13/2}$	33113	EX	—	—
$^2P_{3/2}$	31746	EX	$^2P_{3/2} \rightarrow {}^4I_{15/2}$	31532
			$^2P_{3/2} \rightarrow {}^4I_{13/2}$	24766
			$^2P_{3/2} \rightarrow {}^4I_{11/2}$	21257
			$^2P_{3/2} \rightarrow {}^4S_{3/2}$	13150
			$^2P_{3/2} \rightarrow {}^2H_{11/2}$	12650
			$^2P_{3/2} \rightarrow {}^4F_{3/2}$	8929
$^4G_{7/2}$	28169	EX	—	—
$^2K_{15/2}$	27586	EX	—	—
$^4G_{9/2}$	27473	EX	—	—
$^4G_{11/2}$	26490	EX	$^4G_{11/2} \rightarrow {}^4I_{11/2}$	16259
			$^4G_{11/2} \rightarrow {}^4I_{9/2}$	16259
$^2H_{9/2}$	24631	EX	—	—
$^4F_{3/2}$	22701	EX	—	—
$^4F_{5/2}$	22272	EX	—	—
$^4F_{7/2}$	20619	EX	—	—
$^2H_{11/2}$	19249	EX	$^2H_{11/2} \rightarrow {}^4I_{15/2}$	19037
$^4S_{3/2}$	18570	EX	$^4S_{3/2} \rightarrow {}^4I_{15/2}$	18364
			$^4S_{3/2} \rightarrow {}^4I_{13/2}$	11826
			$^4S_{3/2} \rightarrow {}^4I_{11/2}$	8188
$^4F_{9/2}$	15396	EX	$^4F_{9/2} \rightarrow {}^4I_{15/2}$	15203
$^4I_{9/2}$	12350	AS	—	—
$^4I_{11/2}$	10128	EM	$^4I_{11/2} \rightarrow {}^4I_{15/2}$	10128
$^4I_{13/2}$	6575	EM	$^4I_{13/2} \rightarrow {}^4I_{15/2}$	6575
$^4I_{15/2}$	0	—	—	—

Table 4.4: Summary of energy levels for Er^{3+} in $NaMgF_3$ and emissions observed for sample J140304. The average emissions energies are tabulated for transitions observed in both PL and RL. Energies were determined with reference to the reported excitation spectrum (EX), emission spectrum (EM), with free ion levels from the NIST atomic spectra database[320] (AS) included where the level is expected but could not be isolated in the PL spectra.

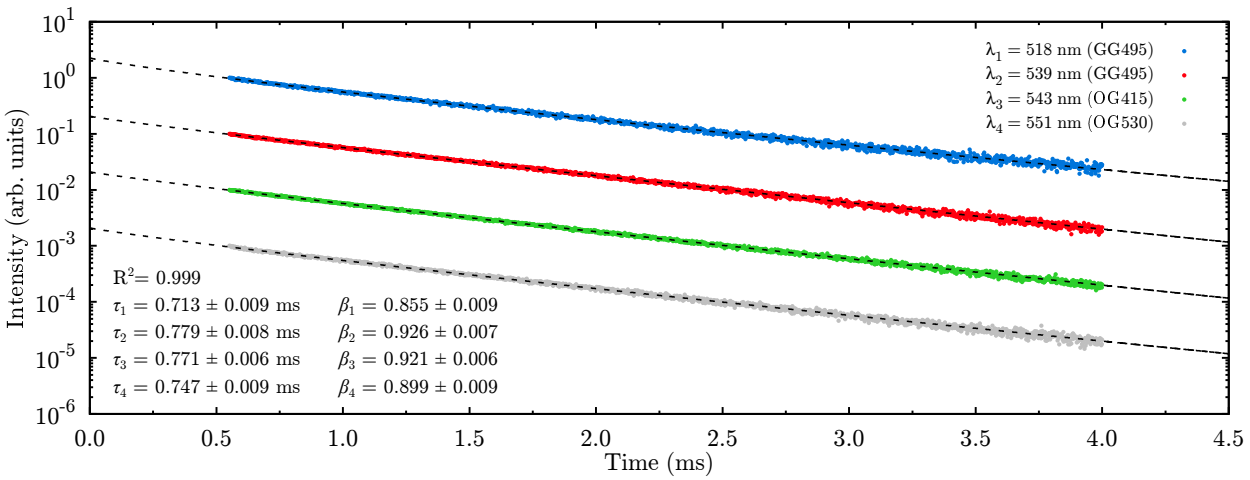

Figure 4.7: Decay of the $^2H_{11/2} \rightarrow {}^4I_{15/2}$ (518 nm and 539 nm) and $^4S_{3/2} \rightarrow {}^4I_{15/2}$ (543 nm and 551 nm) emissions for sample J140304 excited at 26667 cm^{-1} (375 nm). Highly significant fits are illustrated for all decays, using stretched exponentials with the indicated parameters. Both emissions were found to have the same effective lifetime within the experimental uncertainty.

It was observed that during repeated cycles of x-ray exposure, TSL readout, and thermal annealing, that the intensity of TSL per unit time of exposure to x-rays increased. This is indicative of the presence of deep or nearly disconnected traps,[116] that are also seen in other fluoroperovskites.[341] These trap have energies which are not accessible at the maximum attainable annealing temperature of 720 K. In samples previously unirradiated, the higher temperature glow peaks are considerably more intense, and the 535 K peak is increased to approximately half the intensity of the primary low temperature peaks when irradiation occurs at room temperature. The mechanism for quenching of this glow peak for irradiation at lower temperatures is not known.

4.4.3 Discussion

While $NaMgF_3$:Er produces near infrared emissions, one of which is located in the desired region of 1500-1800 nm, the most intense emissions occur in the visible range between 500 nm and 600 nm. As discussed in § 3.1.2, this region of the visible spectrum is least favoured by the optical detector technologies available for the dosimeter prototypes used in this work. Significant room temperature TSL was also observed, and primarily for this reason, $NaMgF_3$:Er has not been further pursued.

4.5 $NaMgF_3$:Eu

All of the luminescence species investigated herein are known to occur in more than one oxidation state, yet most only exhibit evidence of a single optically active valence when residing on either cation site in $NaMgF_3$, regardless of the oxidation number occurring in the dopant fluoride. $NaMgF_3$:Eu appears as an exception to this trend, with both Eu^{2+} and Eu^{3+} were observed when EuF_3 is used as a dopant. Luminescence of the trivalent ion appears much weaker, although this does not directly reflect relative concentrations as the divalent emission is dominated by an intraconfigurational transition with a much higher oscillator strength. Circumstantial evidence for conversion from Eu^{2+} to Eu^{3+} with exposure to ionising radiation is seen the time dependence of the RL emission spectrum, which would implicate the dopant ion as a hole trapping site. This has also been suggested on the basis of magnetisation measurements[192] for $RbMgF_3$:Eu, a finding which was not corroborated by this study as the dopant concentrations used were too high for the anticipated change in magnetisation to be experimentally observable. As with many rare earths dopants, the ionic radii of both Eu^{2+} (1.25 Å) and Eu^{3+} (1.07 Å) favour integration on the *A* site.

Sample AE00519 was used in the radiotherapy characterisation work detailed in chapter 6.

4.5.1 Diffraction Data

Diffraction data for sample J140202 is illustrated in figure 4.8a, clearly reflecting the reference pattern. Residual MgF_2 is clearly identified and a number of additional low intensity reflections occur which are also observed for other samples in this study, but are absent from the reference pattern. Weak reflections at 25.19° and 86.82° are observed only for sample J140202, which are insufficient in number to assign with confidence but are not consistent with any of the principal reflections of the EuF_3 dopant. The same 9 reference peaks are absent from the experimental data.

4.5.2 Eu^{2+} Luminescence

In the PL spectra shown in figure 4.8b an intense Eu^{2+} emission is depicted, comprising a sharp line emission at 27739 cm^{-1} (361 nm) with narrow side bands of lower intensity all superimposed on a broad band emission. The line emission arises from the $^6P_{7/2} \rightarrow {}^8S_{7/2}$ relaxation within the $4f^7$ configuration, while the weaker lines at 27435 cm^{-1} and 28169 cm^{-1} are consistent with transitions from the adjacent ^6P_J levels, for $J = (3/2, 5/2)$.

Intensity of the ^6P_J emissions is significantly greater than in other hosts, which is in part due to the absence of intermediate levels, and so minimal non-radiative relaxation[342] occurs, but mostly due to the proximity of the e_g splitting of the lowest lying $5d$ state.[2,192] This level is labelled herein as $4f^6\left[{}^7F_0\right]5d(E_{1g})$ and appears in the PL excitation peaking at 29586 cm^{-1} (338 nm). The energy of this state exceeds the energy of the highest $^6P_{5/2}$ level by only 0.17 eV, allowing efficient thermal population of the ^6P_J multiplet from the more readily excited $5d$ levels. As can be seen in figure 4.8b, the interconfigurational transition $5d(E_{1g}) \rightarrow {}^8S_{7/2}$ is centred near 26500 cm^{-1} in the PL emission, with a Stokes shift of approximately 2900 cm^{-1}. Weak excitation into the $^6P_{5/2}$ and $^6P_{7/2}$ levels is also observed, with excitation intensity well over an order of magnitude less than for the $5d$ states. The excitation spectra measured on the $4f$ line and $5d$ band emissions are identical.

It was not possible to measure the lifetime of either Eu^{2+} emission for lack of a suitable ultraviolet LED source. These have been reported elsewhere as sub-millisecond mixed exponential decays. Both the lifetime and the intensity of the $5d(E_{1g}) \rightarrow {}^8S_{7/2}$ emission exhibit significant temperature dependence.[2]

The same Eu^{2+} transitions are seen in the RL emission spectrum shown in figure 4.8c, and are dominant above approximately 25000 cm^{-1}. An anomalous emission occurs near 22500 cm^{-1} which cannot be explained within the energy scheme presented in table 4.5. The evolution of this emission with absorbed dose is markedly different from the europium peaks occurring at shorter wavelengths, strongly suggesting it does not arise from the Eu^{2+} site. It is not seen in the PL emission, and so it was not possible to obtain an excitation spectra or lifetime data which might have otherwise shed more light on the nature of the responsible defect. The colour centre absorptions detailed in § 4.1.2 have a pronounced influence on the detectable Eu^{2+} RL intensity, which declines significantly at higher absorbed doses as a result.

Temperature dependence of RL emission is illustrated in figure 4.9a, in which it can be seen that the $5d(E_{1g}) \rightarrow {}^8S_{7/2}$ and the $^6P_J \rightarrow {}^8S_{7/2}$ emissions have positive and negative temperature co-efficients re-

State	Energy (cm^{-1})	Method	Emissions	Energy (cm^{-1})
$4f^6\left[{}^7F_0\right]5d\,(T_{2g})$	36232	EX	—	—
$4f^6\left[{}^7F_0\right]5d\,(E_{1g})$	29586	EX	$4f^6\left[{}^7F_0\right]5d\,(E_{1g}) \rightarrow 4f^7\left[{}^8S_{7/2}\right]$	26498
$^6P_{5/2}$	28169	EM	$^6P_{5/2} \rightarrow {}^8S_{7/2}$	28134
$^6P_{7/2}$	27739	EM	$^6P_{7/2} \rightarrow {}^8S_{7/2}$	27716
$^6P_{3/2}$	27435	EM	$^6P_{3/2} \rightarrow {}^8S_{7/2}$	27365
$^8S_{7/2}$	0	—	—	—

Table 4.5: Summary of energy levels for Eu^{2+} in $NaMgF_3$ and emissions observed for samples AE00519 and J140202. The average emissions energies are tabulated for transitions observed in both PL and RL. Energies were determined with reference to the reported excitation spectrum (EX) and emission spectrum (EM).

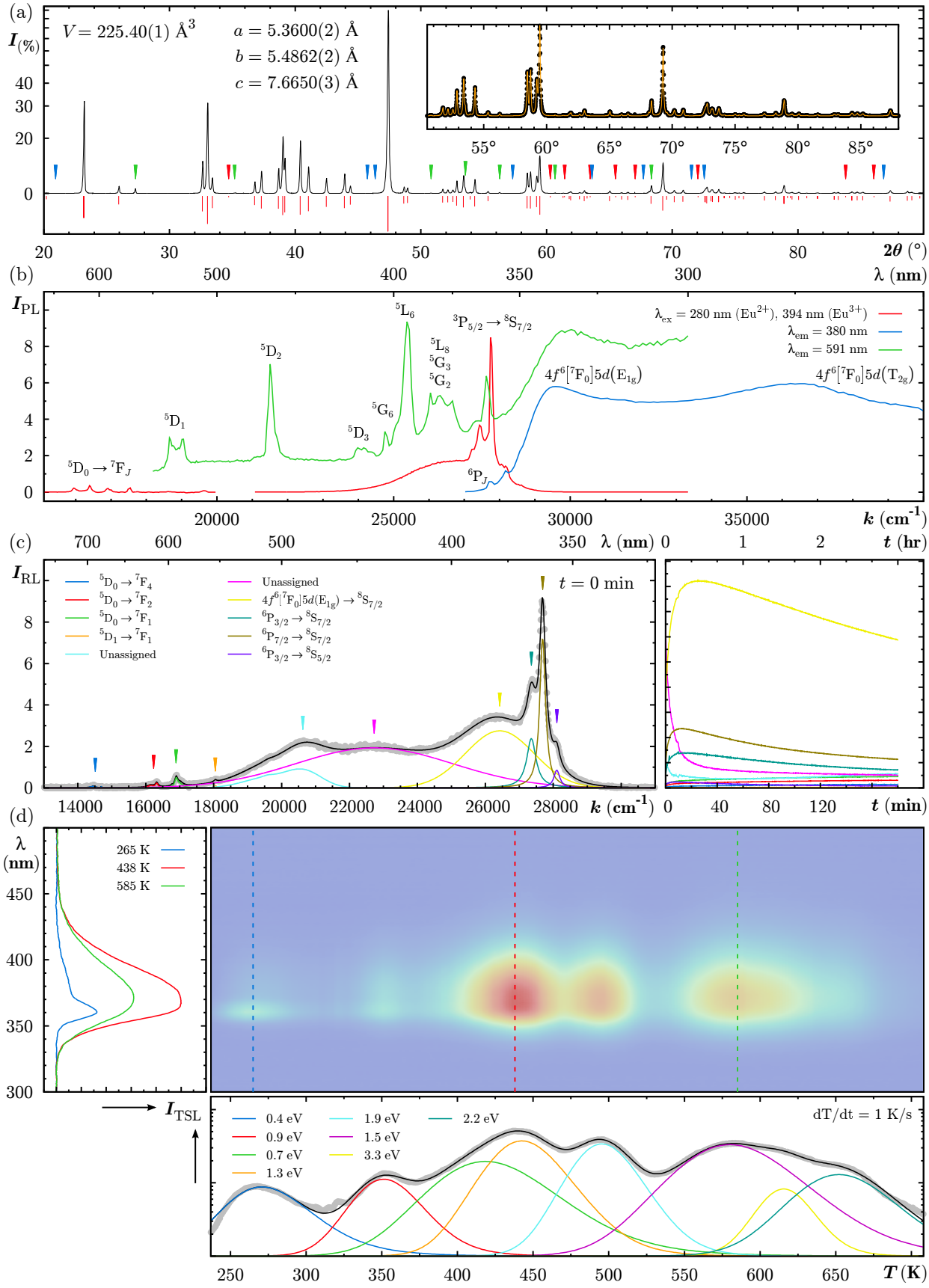

Figure 4.8: Basic characterisation measurements for $NaMgF_3$:Eu, including (a) XRD pattern (J140202), (b) photoluminescence spectra (AE00519), (c) fitted radioluminescence spectra (AE00519), and (d) thermoluminescence emission spectra with fitted glow curves (J140202). In (a), the experimental data is plotted (black) and the pseudo-Voigt fit (orange) illustrated in the inset, with markers over peaks which are missing from the reference pattern (red), explained by contaminants (green), and unexplained (blue). Markers in (c) are coloured to match the legend. Activation energies for the glow peaks in (d) are given on the subplot.

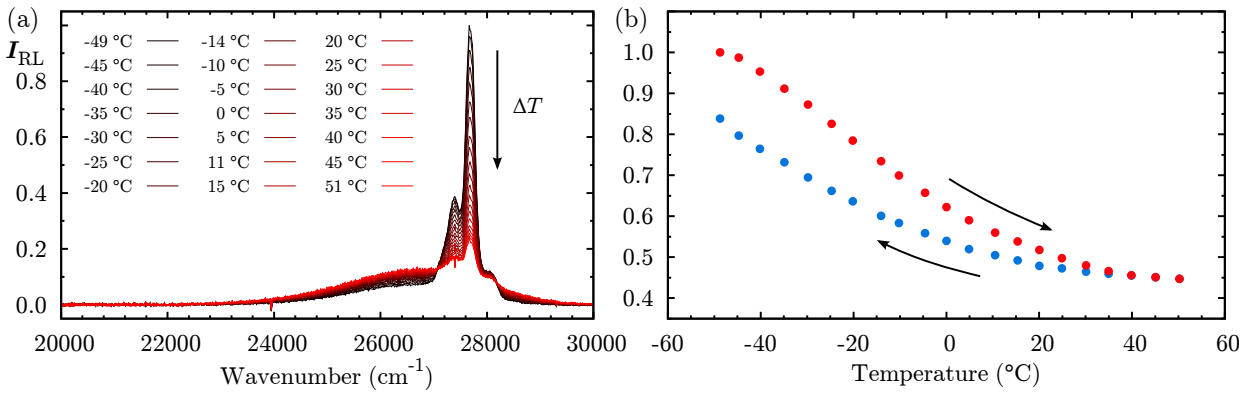

Figure 4.9: Temperature dependence of RL (a) emission spectrum and (b) integrated intensity of the fitted $^6P_J \rightarrow {}^8S_{7/2}$ emission. The $4f^6\left[{}^7F_0\right]5d\,(E_{1g}) \rightarrow 4f^7\left[{}^8S_{7/2}\right]$ emission temperature dependence is approximately the inverse, as can be seen in (a). Arrows marked on (b) indicate the direction of temperature cycling, with response measured under positive ΔT plotted in red and that measured while lowering the sample temperature back to the starting point in blue.

spectively, although neither is strictly linear. Substantial temperature dependence for an emission arising from a d orbital is not unusual,[39] and the complementary response of the line emission is consistent with the aforementioned thermal population of the ^6P_J states from the lowest lying $5d$ level. At temperatures where the $5d(E_{1g}) \rightarrow {}^8S_{7/2}$ emission is more efficient, the population available to drive the $^6P_J \rightarrow {}^8S_{7/2}$ emission is correspondingly reduced. This interpretation is supported by the relative temperature independence of the total integrated intensity of both the band and line emissions, which varies by less than 3% over the temperature range investigated.

In figure 4.9b the relative temperature response of the $^6P_J \rightarrow {}^8S_{7/2}$, isolated by fitting as described in § 3.2.7, is shown for the full thermal cycle. The initial intensity is not recovered after returning the sample to the initial temperature as a non-negligible dose is necessarily delivered, resulting in colour centre formation and a reduction in the detected RL intensity.

TSL glow curves are dominated by Eu^{2+} luminescence, as shown in figure 4.8d. Second order glow peaks are fitted with peak temperatures at 270 ± 1 K, 351 ± 1 K, 418 ± 17 K, 442 ± 1 K, 580 ± 1 K, 616 ± 1 K, and 652 ± 2 K, with the corresponding activation energies shown in the figure. Stated uncertainty for the fitted peak temperatures indicate type A uncertainty in the fitting parameters and do not encompass systematic errors in temperature (see § 3.2.6). The inflated uncertainty in the broader 418 K peak reflects that, unlike the remaining fits, it does not correspond to an isolated peak. That the most prominent experimental glow peak requires two overlapping second order peaks to describe it could represent two traps of similar depth, but it could also indicate experimental artifact or model inadequacies.

4.5.3 Eu^{3+} Luminescence

PL emission from Eu^{3+} arises from optical transitions between the ^5D_J and ^7F_J levels of the Eu^{3+} ion, with a structured emission spectra observed across the red to infrared wavelengths.[343] Transitions observed in the PL originate only from the $^5D_0$ state, while in the RL weak peaks consistent with the energy differential between the $^5D_1$ and ^7F_J levels are also observed. In the PL excitation, the lower lying ^5D_J levels are well resolved, with assignments becoming increasingly ambiguous at higher energies, a situation similar that described for Dy^{3+} in § 4.3.2. No emission from the higher levels of the $4f^6$ configuration were observed, likely these decay non-radiatively to the ^5D_J levels.[40,343] In the ultraviolet, Eu^{2+} excitation is observed even for the emission wavelength of 591 nm shown in figure 4.8b, attesting to the extremely low intensity of the Eu^{3+} emission relative to that observed in the same sample from Eu^{2+}.

The full TSL emission spectra (not shown) is comparable to the RL spectrum in that extremely weak Eu^{3+} is also resolved.

4.5.4 Discussion

The position of the $4f^6\left[^7\mathrm{F}_0\right]5d\,(\mathrm{E}_{1\mathrm{g}})$ level is serendipitous and so some consideration of why is warranted. In $KMgF_3$ this state lies at higher energy, promoting emission from the $^6\mathrm{I}_J$ multiplet in a similar fashion to that described for $NaMgF_3$ herein.[342] Unlike $NaMgF_3$, this host possesses the prototypical perovskite structure (see figure 2.6f) and the Eu^{2+} dopant site retains both high symmetry and high fluorine co-ordination number, and so splitting of the $5d$ orbitals is minimal. In $NaMgF_3$, the nature of the A site is somewhat more complex. The distortion illustrated in figure 3.1a reduces it in both symmetry and size, hence the $5d$ orbitals are further split and the E_{1g} component of the lowest is reduced in energy. Note also that the distortion renders the A site non-centrosymmetric, and so the $f \rightarrow f$ transitions for rare earth ions on this site become induced electric dipole in nature,[40] forbidden by neither parity of spin selection rules.

The near ultraviolet energy is advantageous if coupled with highly sensitive detector systems employing photomultipliers operated as single photon counters. Such sensitive readout systems are required where low doses are of interested, such as in TSL or OSL dosimetry systems designed for personal or environmental dosimetry. In fibre coupled dosimetry applications, where the materials are inevitably exposed to high doses, colour centre absorption occurring at the emission wavelength presents an undesired complication. The Čerenkov component of the stem signal encountered at external beam radiotherapy x-ray energies is also most significant at these shorter wavelengths. Despite the attraction of a relatively efficient and narrow emission, $NaMgF_3$:Eu is consequently not ideal for use as a fibre coupled dosimeter if operated for real-time dosimetry during irradiation. OSL is possible by stimulating in the tail of the F–centre absorption, at energies below that of the $^6\mathrm{P}_J \rightarrow {}^8\mathrm{S}_{7/2}$ emissions.

While the presence of weak Eu^{3+} luminescence is of little interest for RL dosimetry applications, the relative intensity of selected $^5\mathrm{D}_0 \rightarrow {}^7\mathrm{F}_J$ transitions can be used to infer the symmetry of the site on which Eu^{3+} resides.[40] Specifically, the electric dipole character of the $^5\mathrm{D}_0 \rightarrow {}^7\mathrm{F}_2$ transition renders it sensitive

State	Energy (cm^{-1})	Method	Emissions	Energy (cm^{-1})
$^5\mathrm{D}_4$	27701	EX	—	—
$^5\mathrm{L}_8$	26667	EX	—	—
$^5\mathrm{G}_2$	26316	EX	—	—
$^5\mathrm{G}_3$	25974	EX	—	—
$^5\mathrm{L}_6$	25381	EX	—	—
$^5\mathrm{G}_6$	25063	EX	—	—
$^5\mathrm{D}_3$	23981	EX	—	—
$^5\mathrm{D}_2$	21505	EX	$^5\mathrm{D}_2 \rightarrow {}^7\mathrm{F}_3$	19642
$^5\mathrm{D}_1$	18870	EX	$^5\mathrm{D}_1 \rightarrow {}^7\mathrm{F}_1$	18083
$^5\mathrm{D}_0$	17544	EM	$^5\mathrm{D}_0 \rightarrow {}^7\mathrm{F}_4$	14511
			$^5\mathrm{D}_0 \rightarrow {}^7\mathrm{F}_2$	16197
			$^5\mathrm{D}_0 \rightarrow {}^7\mathrm{F}_1$	16983
			$^5\mathrm{D}_0 \rightarrow {}^7\mathrm{F}_0$	17544
$^7\mathrm{F}_6$	4940	AS	—	—
$^7\mathrm{F}_5$	3910	AS	—	—
$^7\mathrm{F}_4$	3114	EM	—	—
$^7\mathrm{F}_3$	1859	EM	—	—
$^7\mathrm{F}_2$	1373	EM	—	—
$^7\mathrm{F}_1$	580	EM	—	—
$^7\mathrm{F}_0$	0	—	—	—

Table 4.6: Summary of energy levels for Eu^{3+} in $NaMgF_3$ and emissions observed for samples AE00519 and J140202. The average emissions energies are tabulated for transitions observed in both PL and RL. Energies were determined with reference to the reported excitation spectrum (EX), emission spectrum (EM), with free ion levels from the NIST atomic spectra database[320] (AS) included where the level is expected but could not be isolated in the PL or RL spectra.

to the symmetry of the crystal field, while the $^5D_0 \rightarrow {}^7F_1$ transition is magnetic dipole in nature and thus relatively insensitive to the crystalline environment. In addition, if Eu^{3+} resides on a site with a centre of inversion, the $^5D_0 \rightarrow {}^7F_0$ emission is typically suppressed.[40,199] In the $NaMgF_3$:Eu samples studied, the $^5D_0 \rightarrow {}^7F_2$ to $^5D_0 \rightarrow {}^7F_1$ emission intensities are approximately equal and the $^5D_0 \rightarrow {}^7F_0$ emission is observed with intensity on the same order of magnitude. These observations are consistent with Eu^{3+} on the *A* site of $NaMgF_3$, the distorted and non-centrosymmetric nature of which is detailed in § 3.1.1.

The broad emission bands in the region of 15000 cm^{-1} to 20000^{-1} remain unexplained, but are more likely to be defect luminescence than arise from the dopant. This assignment is made tentatively on the basis of an RL time dependence inconsistent with both the known Eu^{2+} and Eu^{3+} emissions, but might be confirmed through systematic examination of samples with varied dopant concentration. The impact of this emission for fibre coupled dosimetry applications can be mitigated through the use of narrow pass-band interference filters, as was the approach taken in this work.

As with $NaMgF_3$:Er, room temperature luminescence is observed, although in this case the dominant glow peak lies well above room temperature at 442 K. The 351 K peak represents a trap sufficiently close to room temperature to impact temperature dependency of RL, consistent with the observation of TSL 'afterglow' upon cessation of high dose irradiations. It should be noted that the presence of a $5d \rightarrow 4f$ emission will also have an impact on temperature dependency, as will the thermally driven population of the ^6P_J states which drives the high intensity line emission discussed above.

4.6 $NaMgF_3$:Mn

As discussed in § 3.1.2, the emission from $NaMgF_3$:Mn falls into a region of the visible spectrum where high performance photomultipliers are borderline unviable, but the Čerenkov component of optical stem effects and the impact of colour centre absorptions are still significant. This is somewhat compensated by the high sensitivity of the material and so it has been included nonetheless. Manganese can take on a wide range of oxidation states but in $NaMgF_3$ only the Mn^{2+} ion is observed when probed optically. Mn^{2+} appears to substitute isoelectronically on the *B* site. This is expected in terms of ionic radius (0.83 Å) for the 6-fold fluorine co-ordination of this site and is consistent with the observed arrangement of energy levels measured in the PL excitation.

Sample AE01020 was used in the radiotherapy characterisation work detailed in chapter 6.

4.6.1 Diffraction Data

Figure 4.10a compares the XRD pattern for sample J140301 with the reference pattern in table 4.1. The same peaks are missing from the reference pattern as observed for all samples discussed so far, but the data otherwise closely reflects the reference pattern for orthorhombic $NaMgF_3$. The experimental pattern contains the same additional low intensity peaks as are observed in the majority of samples on which XRD measurements were made, as well as the usual reflections reasonably attributable to MgF_2. Beyond this, no unexplained features were present and no evidence of residual MnF_2 dopant was observed.

4.6.2 Mn^{2+} Luminescence

PL emission and excitation spectra are depicted in figure 4.10b. In $NaMgF_3$, manganese forms an high-spin octahedral MnF_6 complex for which the splitting of the 3*d* orbitals occurs as discussed in § 2.2.2 and is well described by the relevant Tanabe-Sugano diagram. As the site is octahedral, the t_{2g} states are of lower energy and it is from one of these, $^4T_{1g}(^4G)$, that the observed emission occurs. In the PL emission spectrum, this $^4T_{1g}(^4G) \rightarrow {}^6A_{1g}(^6S)$ transition is seen at 17010 cm^{-1} (588 nm) with a stokes shift of approximately 1900 cm^{-1}. In the PL excitation a number of levels split from the ^4D, ^4G, and ^4P free ion states are resolved between 15000 cm^{-1} and 30000 cm^{-1}. The energies of these states are listed in table 4.7 and are consistent with a splitting of $10Dq$ at 9256 cm^{-1} and Racah *B* parameter of 783 cm^{-1}, based on the experimental energies of the lowest two terms. The strong coupling of these 3*d* states to the crystal

lattice results in non-radiative relaxation from all higher excited states, with emission observed only from the $^4T_{1g}(^4G)$ level.[175,189,273]

The emission at 20144 cm^{-1} (496 nm) is also attributed to the $^4T_{1g}(^4G) \rightarrow {}^6A_{1g}S$ emission, but instead for Mn^{2+} residing on a highly distorted B site,[79] although the exact mechanism of distortion remains unclear. This is consistent with the changes to the excitation spectrum for this peak, which exhibits features corresponding only to those states which are relatively independent of the crystal field: $^4A_{1g}(^4G)$, $^4E_{1g}(^4G)$, and $^4E_{1g}(^4D)$. Substantially increased intensity and a reduction in lifetime for this emission would be expected for a site sufficiently distorted so as to loose inversion symmetry, both of which are observed experimentally. Glow curves also differ between the two emission peaks. It is likely that the fraction of sites exhibiting this distortion is relatively small and that the increased PL intensity reflects an allowed transition, but this cannot even be estimated without knowledge of the specific nature of the distortion. Emission from the distorted site is also observed in nano-particle $NaMgF_3$:Mn, but only under optical excitation.[79]

Emission lifetimes were found to differ between the 17010 cm^{-1} and 20144 cm^{-1} bands, being dominated by single exponential components with τ of 67 ± 6 ms and 12.6 ± 0.5 ms respectively. A shorter 0.7 ± 0.2 ms component is also observed in both. These lifetimes are difficult to separate reliably and were modelled herein using a double-exponential fit with a constant background term, shown fitted to the experimental data in figure 4.12. The first decay term in all cases is the sub-millisecond component (τ_1) while the second decay term models in turn both of the longer components detected at 500 nm or 550 nm (τ_2), and 600 nm or 650 nm (τ_3). The stated uncertainties reflect the range of the fitted lifetimes for all emission wavelengths.

The RL emission spectra (see figure 4.10c) is comparably simple, with the same two band emissions observed arising from the $^4T_{1g}(^4G) \rightarrow {}^6A_{1g}(^6S)$ transition on the perovskite B site and the distorted variation thereof. The higher energy emission attributed to the distorted site exhibits a smaller increase in intensity with dose and saturates earlier in time, both suggesting a lower concentration of the site giving rise to the emission. The change in intensity for the distorted site emission is approximately a factor of 3, while the lower energy emission for the undistorted site undergoes a 10-fold increase in intensity, both over 2 hours of exposure. A very weak third band emission was recorded at 13106 cm^{-1} (763 nm), is not seen in the PL, and exhibits a time dependence inconsistent with those assigned to Mn^{2+}. It is therefore considered unlikely that this is Mn^{2+} luminescence.

Changes in the RL emission spectra were observed as a function of temperature, with a reduction in the relative intensity of the higher energy band emission with increasing T, and a progressive shift to higher emission energies in both bands. Changes in intensity are anticipated, but could not be experimentally

State	Energy (cm^{-1})	Method	Emissions	Energy (cm^{-1})
$^4A_{1g}(^4F)$	38085	TS	—	—
$^4T_{1g}(^4P)$	37037	TS	—	—
$^2A_{1g}(^2I)$	36464	TS	—	—
$^2E_{1g}(^2I)$	33433	TS	—	—
$^4E_{1g}(^4D)$	30581	EX	—	—
$^2A_{2g}(^2I)$	30396	TS	—	—
$^4T_{2g}(^4D)$	28217	EX	—	—
$^4A_{1g}(^4G)$, $^4E_{1g}(^4G)$	25381	EX	—	—
$^2T_{2g}(^2I)$	23975	TS	—	—
$^4T_{2g}(^4G)$	22779	EX	—	—
$^4T_{1g}(^4G)$	18382	EX	$^4T_{1g}(^4G) \rightarrow {}^6A_{1g}(^6S)$	20144
			$^4T_{1g}(^4G) \rightarrow {}^6A_{1g}(^6S)$	17010
$^6A_{1g}(^6S)$	0	—	—	—-

Table 4.7: Summary of energy levels for Mn^{2+} in $NaMgF_3$ and emissions observed for samples AE01020. The average emissions energies are tabulated for transitions observed in both PL and RL. Energies were determined with reference to the reported excitation spectrum (EX) and the Tanabe-Sugano diagram (TS) for the $3d^5$ configuration for those intermediate levels not observed.

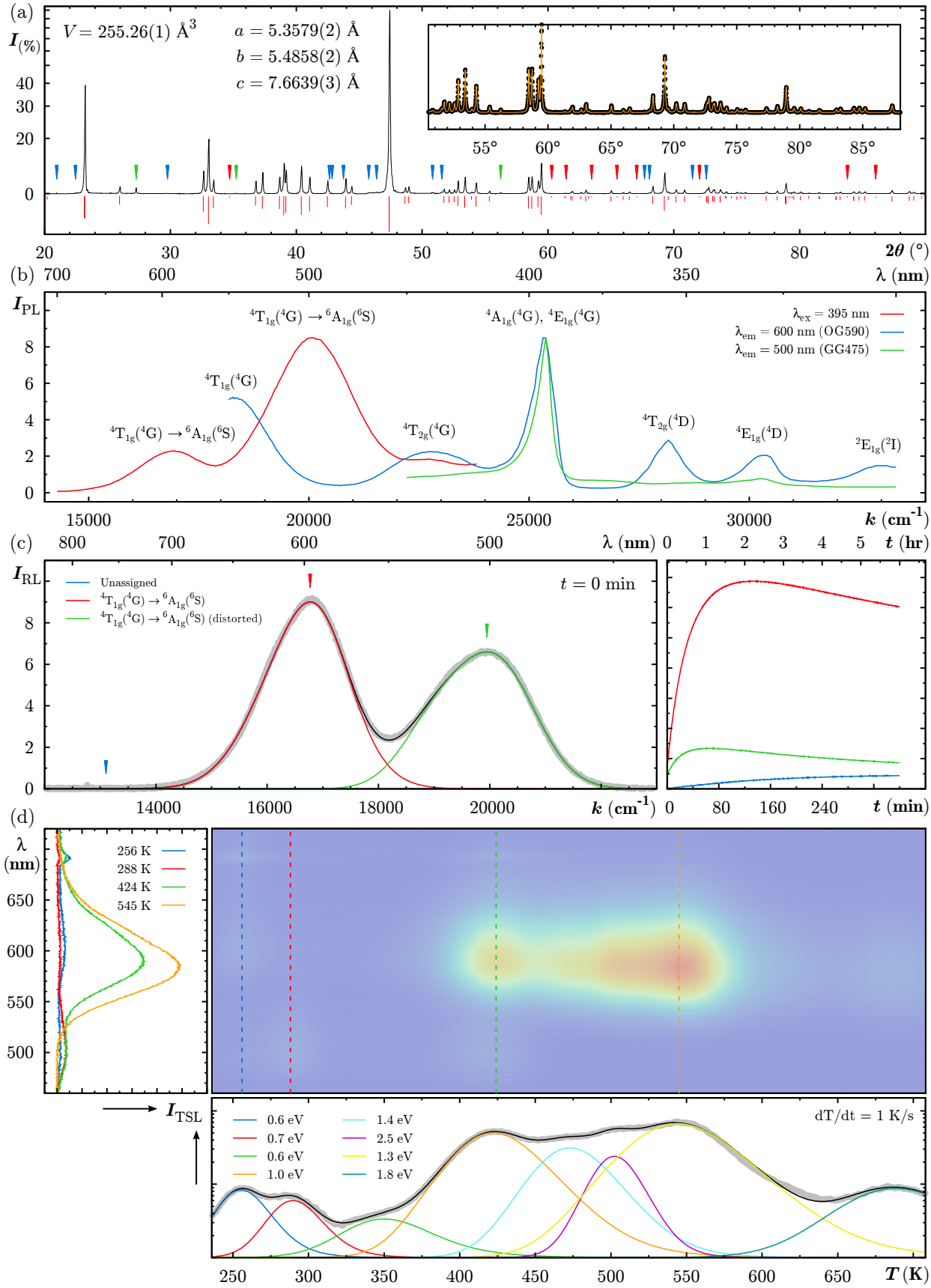

Figure 4.10: Basic characterisation measurements for $NaMgF_3$:Mn, including (a) XRD pattern (J140301), (b) photoluminescence spectra (AE01020), (c) fitted radioluminescence spectra (AE01020), and (d) thermoluminescence emission spectra with fitted glow curves (J140301). In (a), the experimental data is plotted (black) and the pseudo-Voigt fit (orange) illustrated in the inset, with markers over peaks which are missing from the reference pattern (red), explained by contaminants (green), and unexplained (blue). Markers in (c) are coloured to match the legend. Activation energies for the glow peaks in (d) are given on the subplot.

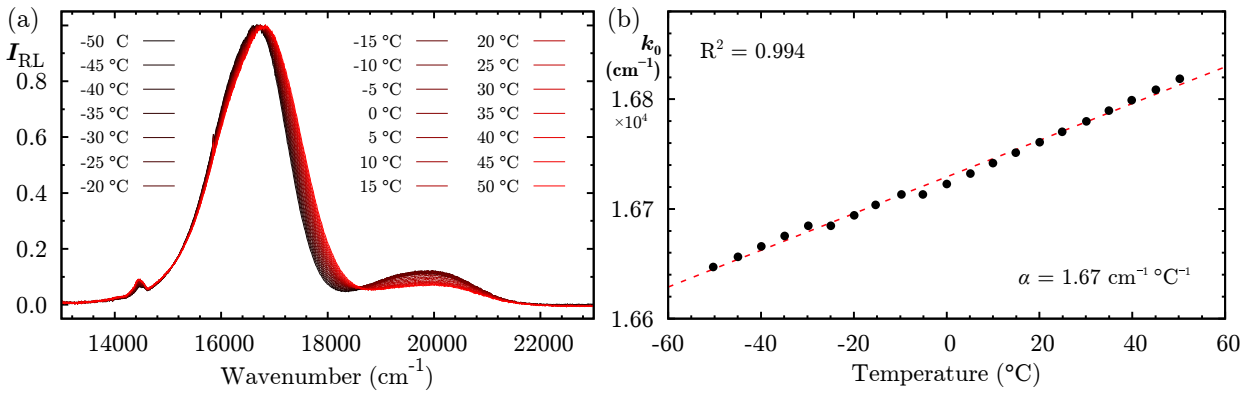

Figure 4.11: Temperature dependence of (a) RL emission and (b) the energy of peak RL emission intensity for the $^4T_{1g}(^4G) \rightarrow {}^6A_{1g}(^6S)$ transition. The latter is linear over the investigated range with the temperature co-efficient given on the figure. The narrow emission near 14400 cm^{-1} is luminescence from the ceramic in the sample carrier, as described in § 3.2.6.

separated from the TSL response, and so the temperature dependent spectra presented in figure 4.11a are normalised to the peak intensity. The energy of fitted peak emission intensity is plotted as a function of temperature in figure 4.11b along with a statistically significant fit giving a dependency of +1.67 cm^{-1} °C^{-1}. It is tempting to explain this in terms of a reduction in $10Dq$ driven by lattice expansion as a function of temperature, but bond lengths in first co-ordination sphere of the B site are almost completely independent of temperature for the investigated conditions.[262]

Glow curves and TSL emission spectra are illustrated in figure 4.10d. Glow peaks with second order kinetics are fitted with peak temperatures of 255 ± 1 K, 290 ± 2 K, 350 ± 4 K, 422 ± 1 K, 473 ± 1 K, 503 ± 1 K, 544 ± 1 K, and 688 ± 1 K. The corresponding activation energies are shown on the figure. All peaks are significant, in the sense that the omission of any results in a poor fit using either first or second order kinetics. The use of 4 glow peaks to fit the TSL intensity between 400 K and 600 K is justified by the unrealistically low activation energy which results if a fit is attempted with 3 peaks. Emission spectra shown at 256 K, 424 K, and 545 K reveal a systematic shift in the peak emission energy with temperature, increasing at slightly less than 2 cm^{-1} per K. This is consistent with the temperature dependence of the energy of peak intensity in the RL emission shown in figure 4.11.

The glow curve illustrated in figure 4.10d is integrated over both of the $^4T_{1g}(^4G) \rightarrow {}^6A_{1g}(^6S)$ emissions, although that of the undistorted site clearly dominates, at least for the principle glow peaks between 400 K and 600 K. Careful inspection of the emission spectra reveals that the distorted site emission exhibits a markedly different glow curve, with only two peaks. One is the 290 K glow peak to which the undistorted site makes little if any contribution, and the other is co-incident with the 422 K peak. These differences implicate the Mn^{2+} sites as charge traps[iv], though by no means the sole traps in the system. TSL measured on sample AE01020 (not shown) from room temperature through 620 K exhibits glow peaks with similar, but not identical, peak temperature and relative intensities.

4.6.3 Discussion

The observed Mn^{2+} luminescence is unique within this study, in that the emission occurs almost exclusively from a single transition between the first excited state and the ground state. Under x-ray excitation, population of higher excited states almost certainly occurs but is followed by non-radiative relaxation to the first excited state,[2] enhancing the observed emission. The material therefore appears one of the most efficient of those included in the study. Although this has not been established directly via absolute spectra measurements, it is supported through experience with sample AE01020 reported in chapter 6.

[iv]If the Mn^{2+} site does not participate in the trapping process then charge carriers released from other traps would require some manner of 'sorting' mechanism in order to recombine selectively on the distorted and undistorted sites at a given temperature.

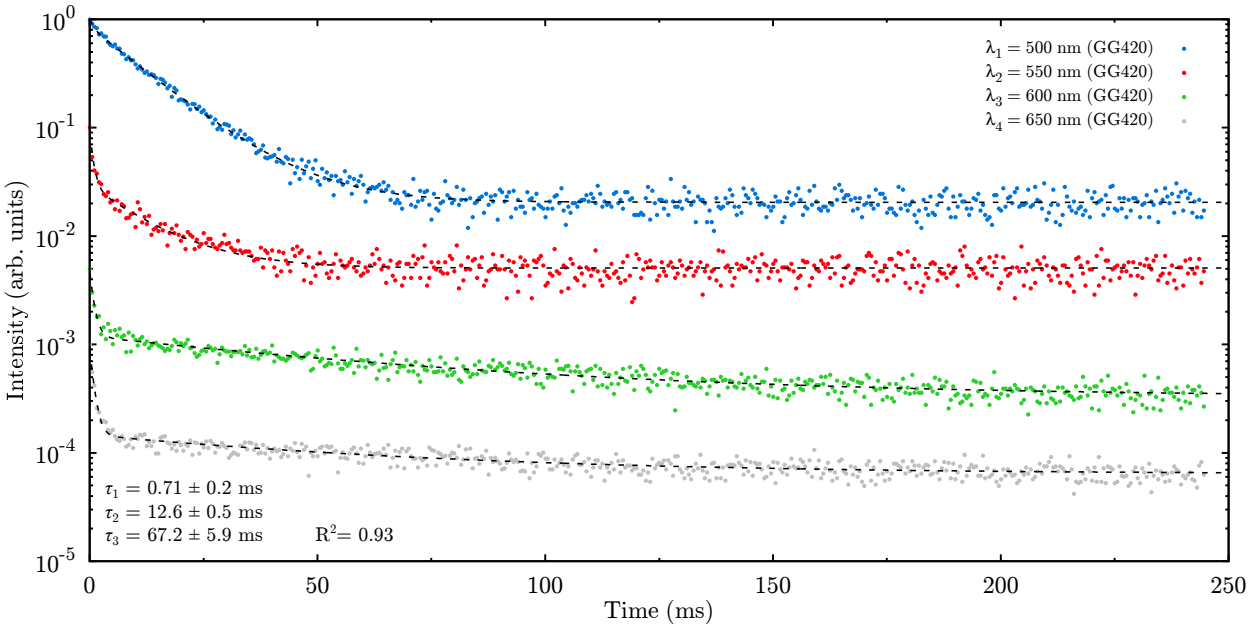

Figure 4.12: Decay of the $^4T_{1g}(^4G) \rightarrow {}^6A_{1g}(^6S)$ emission from sample AE01020 as excited at 26667 cm^{-1} (375 nm). In comparing disparate lifetimes the background level counts have been included in both the figure and the fitted model, which consists of the 3 distinct lifetimes stated on the figure.

At approximately 600 nm, the peak emission wavelength falls outside the criteria outlined in § 3.1.2 but nonetheless remains of interest in light of the above. As one of the lighter transition metal dopants, an advantage also exists in the comparatively minimal perturbation of the radiological properties of the host crystal. This permits a higher dopant fraction and perhaps even higher sensitivity.

Use as an OSL dosimeter would be problematic, as the PL excitation overlaps much of the *F*-centre absorption band, and so stimulating OSL emission would be expected to also produce a substantial PL background.

4.7 $NaMgF_3$:Nd

Nd^{3+} is known to yield near infrared emissions from the $^4F_{3/2} \rightarrow {}^4I_J$ transitions in perovskite hosts. It was included in this study on the basis of reported emission wavelengths in the literature.[344,345] While the aforementioned emissions were observed, the intensity of both PL and RL was very low, likely due to limited solubility of the NdF_3 dopant. Only one sample (J140401) was characterised.

4.7.1 Diffraction Data

All reflections listed for the $NaMgF_3$ reference pattern listed in table 4.1 are present except for the 8 low intensity peaks absent from all samples. In addition, the [110], [101], [210], and [220] reflections of MgF_2 are observed, as is almost every reflection listed at over 5% intensity for the dopant, NdF_3, ICDD pattern 04-006-8285.[346] A number of additional low intensity peaks are observed which are not part of the literature sourced reference pattern, but are seen in all other samples in the study. Unexplained reflections with intensity below 1% at 27.17°, 45.12°, and 57.51° are observed only in this sample, as marked in figure 4.13a.

4.7.2 Nd^{3+} Luminescence

Figure 4.13b illustrates the PL emission and excitation from $NaMgF_3$:Nd. Excitation peaks are relatively well correlated with the energy levels of the free Nd^{3+} ion, with unambiguous assignments possible for the states between $^4F_{5/2}$ and $^2P_{3/2}$ inclusive, detected at 12655 cm^{-1} and 26420 cm^{-1} respectively. Assignment of excitation peaks has been made with less confidence up to an energy of 31104 cm^{-1}. Very weak excitation

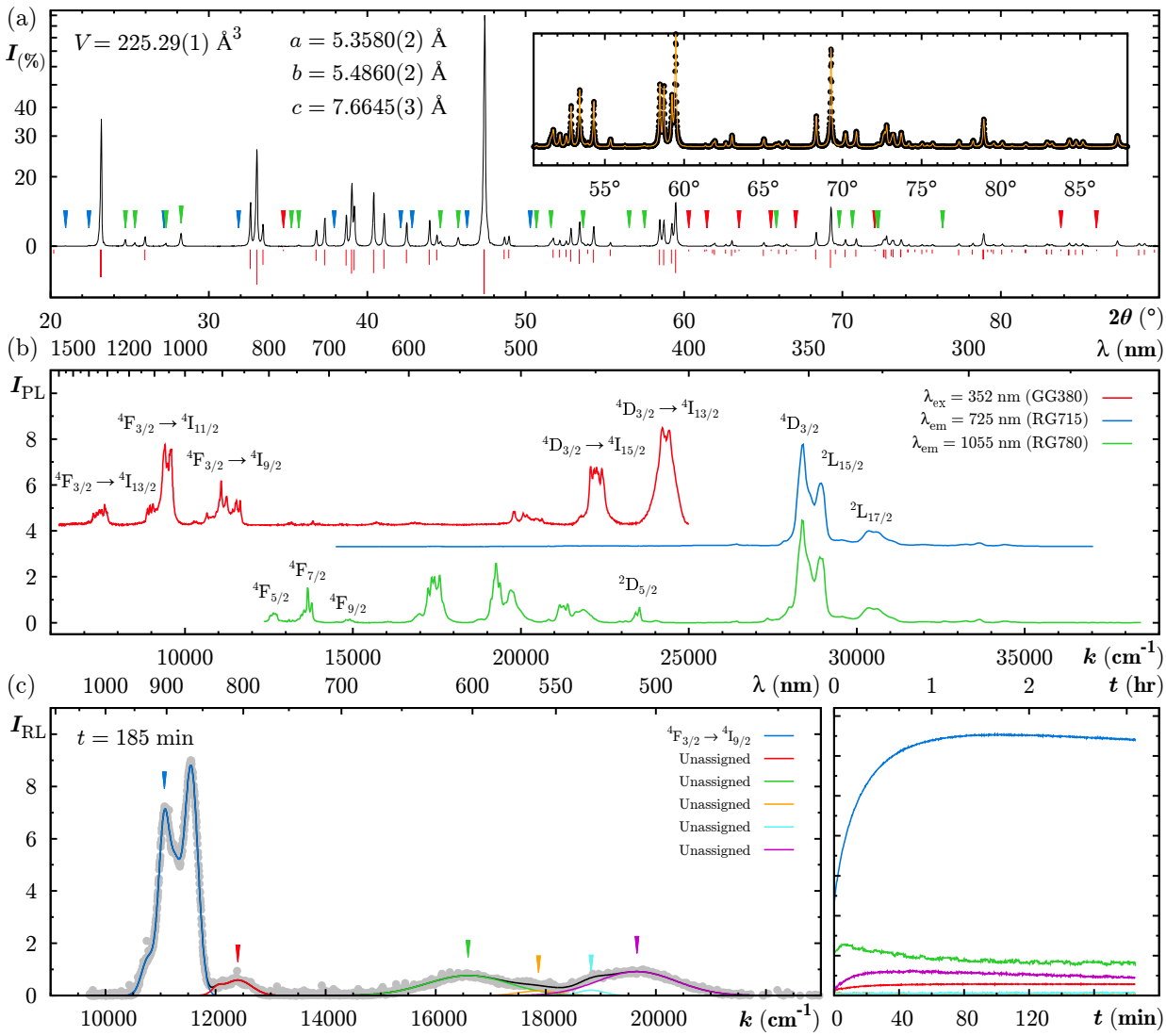

Figure 4.13: Basic characterisation measurements for $NaMgF_3$:Nd (J140401), including (a) XRD pattern, (b) photoluminescence spectra, and (c) fitted radioluminescence spectra. In (a), the experimental data is plotted (black) and the pseudo-Voigt fit (orange) illustrated in the inset, with markers over peaks which are missing from the reference pattern (red), explained by contaminants (green), and unexplained (blue). Markers in (c) are coloured to match the legend the adjacent plot illustrating the time dependence of each RL emission. A U-360 filter was used on excitation mono while measuring PL emission.

peaks were observed at 14535 cm^{-1}, 18797 cm^{-1}, 24038 cm^{-1}, 27360 cm^{-1} and 29586 cm^{-1} which could not be unambiguously assigned to a known state in the $4f^3$ configuration. Excitation into the states below $^4D_{3/2}$ was not observed for emissions energies above 13793 cm^{-1} (725 nm), confirming that the near infrared emissions arise from transitions between the lower energy states.

At visible wavelengths, PL emission was only observed with significant intensity at 24311 cm^{-1} (414 nm) and 22311 cm^{-1} (448 nm). There exist multiple transitions with the observed energy differential, but these have been assigned as $^4D_{3/2} \rightarrow {}^4I_{13/2}$ and $^4D_{3/2} \rightarrow {}^4I_{15/2}$ respectively. The relative intensity of these two emissions implicates a spin allowed transition, in which case each should have origin in the ^4D_J multiplet. The $^4D_{3/2}$ state is thus considered the most likely candidate as it lacks any levels immediately lower in energy to which a non-radiative pathway might be preferred. Weaker PL emissions up to two orders of magnitude lower in intensity were recorded between 13175 cm^{-1} (759 nm) and 20631 cm^{-1} (485 nm), for which the complexity of the Nd^{3+} energy levels precludes unambiguous assignments. PL emission lifetime was measured at less than 1 ms but could not be reliably fitted due to the low emission intensities.

Further into the near infrared, groupings of line emissions at 11635 cm^{-1} (860 nm) to 10272 cm^{-1} (974 nm), 9597 cm^{-1} (1042 nm) to 9355 cm^{-1} (1069 nm), 9132 cm^{-1} (1095 nm) to 8857 cm^{-1} (1129 nm),

and at 7683 cm^{-1} (1302 nm) to 7281 cm^{-1} (1374 nm), were detected. The mean wavelengths of each of these groupings are in agreement with the energy of $^4F_{3/2} \rightarrow {}^4I_J$ transitions, for $J = (9/2, 11/2, 13/2)$, and the transition $^4F_{9/2} \rightarrow {}^4I_{15/2}$, as listed in table 4.8. A further possible emission near 5200 cm^{-1} (1923 nm), arising from a $^4F_{3/2} \rightarrow {}^4I_{15/2}$ transition was not observed in this study. The reported near infrared emissions are consistent with infrared luminescence from Nd^{3+} seen in other hosts.[344,345]

A very weak RL emission spectrum was measured with low resolution, capturing little more than the $^4F_{3/2} \rightarrow {}^4I_{9/2}$ emission in the region of 11000 cm^{-1}, as can be seen in figure 4.13c. It was not possible to determine the origin of the broad peaks above 15000 cm^{-1}. Integrated RL intensities are plotted in figure 4.13c for each emission isolated by fitting. The initial increase in the $^4F_{3/2} \rightarrow {}^4I_{9/2}$ emission intensity can be accounted for in the charge transport and trapping model discussed in § 2.2.4, while similar dynamics are observed for the unassigned emissions observed near 12200 cm^{-1} (820 nm) and 19700 cm^{-1} (508 nm). On the basis of these similarities, it is likely that these two unassigned emissions also arise from Nd^{3+}, with the latter also apparent in the PL emission spectrum. The time evolution of the emission near 16800 cm^{-1} (595 nm) is anomalous and the origin of this peak remains unclear.

4.7.3 Discussion

While $NaMgF_3$:Nd does exhibit infrared emissions in the range of 1000 nm to 1500 nm which would be of interest for dosimetry applications, the intensity under both selective optical excitation and high dose

State	Energy (cm^{-1})	Method	Emissions	Energy (cm^{-1})
$^2L_{17/2}$	31104	EX	—	—
$^4D_{7/2}$	30465	EX	—	—
$^2L_{15/2}$	28902	EX	—	—
$^4D_{5/2}$, $^2I_{11/2}$	28369	EX	—	—
$^4D_{3/2}$	28011	EX	$^4D_{3/2} \rightarrow {}^4I_{15/2}$	22171
			$^4D_{3/2} \rightarrow {}^4I_{13/2}$	24311
$^2P_{3/2}$	26420	EX	—	—
$^2D_{5/2}$	23474	EX	—	—
$^2P_{1/2}$	23029	EX	—	—
$^4G_{11/2}$, $^4K_{15/2}$	21917	EX	—	—
$^4G_{9/2}$, $^2D_{3/2}$	21166	EX	—	—
$^2G_{9/2}$	19704	EX	—	—
$^4G_{7/2}$	19256	EX	—	—
$^4G_{5/2}$, $^2G_{7/2}$	17327	EX	—	—
$^2H_{11/2}$	16052	EX	$^2H_{11/2} \rightarrow {}^4I_{15/2}$	10304
			$^2H_{11/2} \rightarrow {}^4I_{13/2}$	12216
			$^2H_{11/2} \rightarrow {}^4I_{9/2}$	15805
$^4F_{9/2}$	14900	EX	$^4F_{9/2} \rightarrow {}^4I_{15/2}$	8977
$^4F_{7/2}$, $^4S_{3/2}$	13611	EX	—	—
$^4F_{5/2}$, $^2H_{11/2}$	12655	EX	—	—
$^4F_{3/2}$	11156	EM	$^4F_{3/2} \rightarrow {}^4I_{13/2}$	7527
			$^4F_{3/2} \rightarrow {}^4I_{11/2}$	9475
			$^4F_{3/2} \rightarrow {}^4I_{9/2}$	11156
$^4I_{15/2}$	5923	EM	—	—
$^4I_{13/2}$	3625	EM	—	—
$^4I_{11/2}$	1678	EM	—	—
$^4I_{9/2}$	0	—	—	—

Table 4.8: Summary of energy levels for Nd^{3+} in $NaMgF_3$ and emissions observed for sample J140401. The average emissions energies are tabulated for transitions observed in both PL and RL. Energies were determined with reference to the reported excitation spectrum (EX) and emission spectrum (EM).

rate x-ray excitation is low enough as to present a challenge for the reported spectroscopy. It is therefore considered unlikely that this material will produce viable RL intensity at infrared wavelengths for dosimetry applications.

4.8 $NaMgF_3$:Ni

Doping with NiF_2 produces perhaps one of the most promising materials of those investigated. The observed luminescent species is Ni^{2+}, which emits broadly in the infrared at wavelengths relatively well aligned with available detector technologies and the theoretical optimum transmission of silica fibres (see § 2.4.1). As a transition metal, the dopant integrates on the B site and has a less detrimental impact on the radiological properties of the bulk crystal than do the rare earth elements. No significant TSL was observed.

Three $NaMgF_3$:Ni samples were made (J140306, J150401, and J150402) with most of the characterisation measurements reported for sample J140306. Sample J150401 was fabricated specifically to facilitate absorption measurements to complement the PL excitation data.

4.8.1 Diffraction Data

The diffraction data for sample J140306 suggests the least structurally compromised sample in the study. All reflections observed were either indexed to orthorhombic $NaMgF_3$, the MgF_2 precursor, or belong to the selection of additional low intensity reflections common to all samples. That no signal attributable to the dopant was observed is surprising as clearly NiF_2 did not completely dissociate in the crystal melt, being found in isolated pockets in the sample. A very small quantity of metallic precipitate was also visible in the base of the sample.

XRD measurements were also made on sample J150401 (not shown), for which the much larger dopant fraction was associated with a larger quantity of macroscopic metal visible in the crystal. This can be seen in figure 3.3h. Nickel was evident in the diffraction pattern for this sample, with the [111] and [220] reflections of the cubic lattice of metallic nickel observed at 44.515° and 76.379°. An additional peak near 51.8° is expected from those listed in ICDD pattern 04-010-6148,[347] but appears to overlap the [123] reflection of $NaMgF_3$, which is correspondingly enhanced in the data for sample J150401. The metallic precipitate is thus almost certainly nickel.

While several dopants posed difficulties in obtaining full dissolution of the dopant precursor fluoride, $NaMgF_3$:Ni was the only material in which the metallic form of the dopant was encountered as a product of the fabrication process. In the case of sample J150401 which was doped with 5% NiF_2, the $NaMgF_3$ produced would be expected to be magnesium deficient, with nickel ions being precipitated in metallic form in preference to integrating on the perovskite B site. No evidence of this is observed in the XRD for this sample, which might be due to loss of NaF to evapouration in the crystal melt. This would be consistent with white deposits found on the crucible lid for many samples and with NaF having the lowest melting point of all the precursor chemicals. $NaMgF_3$:Ni with dopant concentration up to 5% is reported in the literature,[272] and so presumably the technique can be refined or an alternative method found.

4.8.2 Ni^{2+} Luminescence

Optical absorption in the $NaMgF_3$:Ni sample prepared with 5% NiF_2 (J150401) can be seen in figure 4.14b, in which the absorption coefficient is plotted in m^{-1}. Three distinct peaks are observed at energies that correspond to the Ni^{2+} spin allowed transitions from the ground state to the $^3T_{2g}(^3F)$, $^3T_{1g}(^3F)$, and $^3T_{1g}(^3P)$ energy levels, at 7716 cm^{-1} (1296 nm), 13228 cm^{-1} (756 nm), and 24631 cm^{-1} (406 nm) respectively. These findings are in good agreement with previously reported data on $NaMgF_3$:Ni at a similar dopant concentration.[272] Using the energy of these spin allowed absorptions, an estimation of the crystal field splitting energy $10Dq$ at 7850 cm^{-1} and the Racah parameter B of 925 cm^{-1} was made with reference to the Tanabe-Sugano diagram for the $3d^8$ configuration in an octahedral complex. These values are calculated under the assumption that Ni^{2+} prefers the B site on the basis of ionic radii. Weaker absorptions can be seen at 15541 cm^{-1}

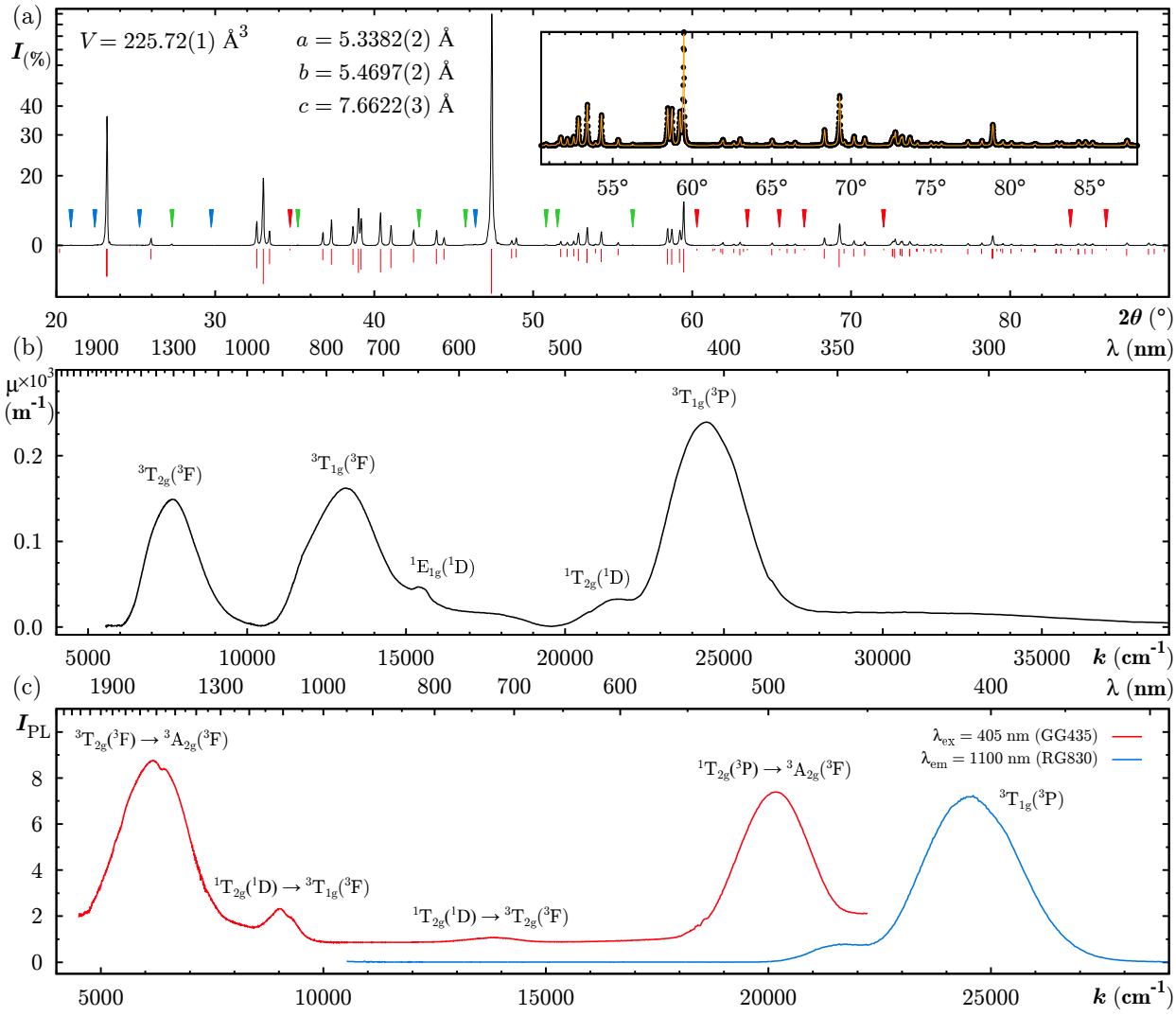

Figure 4.14: Basic characterisation measurements for $NaMgF_3$:Ni, including (a) XRD pattern (J140306), (b) absorption spectrum (J150401), and (c) photoluminescence spectra (J140306). In (a), the experimental data is plotted (black) and the pseudo-Voigt fit (orange) illustrated in the inset, with markers over peaks which are missing from the reference pattern (red), explained by contaminants (green), and unexplained (blue).

(644 nm) and 21650 cm^{-1} (436 nm) that are consistent with the calculated energies of the $^1E_{1g}(^1D)$ and $^1T_{2g}(^1D)$ levels. The complete energy level scheme is sumarised in table 4.9. An additional weaker and broad absorption appears at approximately 18000 cm^{-1} which is not consistent with the known energies of the Ni^{2+} ion, while a similarly weak broad absorption in the region of 32000 cm^{-1} may be attributable to F–centres.

The PL excitation spectra from the $NaMgF_3$:Ni sample is shown in figure 4.14c, and consists of two overlapping bands at 24510 cm^{-1} and 21510 cm^{-1}. These bands appear closely correlated with the absorption data and so are assigned similarly. Identical PL excitation spectra were measured for each of the reported band emissions at 20121 cm^{-1} (497 nm), 13292 cm^{-1} (752 nm), 9143 cm^{-1} (1094 nm), and 6302 cm^{-1} (1587 nm), as is expected because all these emissions derive ultimately from the same excited state. The 20121 cm^{-1}, 13292 cm^{-1}, and 6302 cm^{-1} emission bands can be assigned to $^1T_{2g}(^1P) \rightarrow {}^3A_{2g}(^3F)$, $^1T_{2g}(^1D) \rightarrow {}^3T_{2g}(^3F)$, and $^3T_{2g}(^3F) \rightarrow {}^3A_{2g}(^3F)$ transitions within the $3d^8$ configuration of the NiF_6 complex. These assignments reflect those made in other reports on Ni^{2+} in hosts with octahedral dopant sites.[272,348–350] It is tempting to assign the 20121 cm^{-1} emission to the spin allowed $^3T_{1g}(^3P) \rightarrow {}^3A_{2g}(^3F)$ transition on the basis of relative intensity, but the assignment given in table 4.9 is more consistent with the size of the energy gap below the $^1T_{2g}(^1D)$ and $^3T_{1g}(^3P)$ levels. The high intensity of this assigned spin

forbidden transition could be explained in a similar manner to the enhancement of the $^6P_J \rightarrow {}^8S_{7/2}$ emission in $NaMgF_3$:Eu, by the proximity of a more highly populated state at an immediately higher energy (see § 4.5.2). The weak emission at 9143 cm^{-1} was assigned to the transition $^1T_{2g}(^1D) \rightarrow {}^3T_{1g}(^3F)$, although the subsequent spin allowed relaxation from $^3T_{1g}(^3F)$ to the ground state was notably absent.

PL decay from the $^1T_{2g}(^1P) \rightarrow {}^3A_{2g}(^3F)$ and $^1T_{2g}(^1D) \rightarrow {}^3T_{2g}(^3F)$ emissions after 26670 cm^{-1} (375 nm) pulsed excitation are plotted in figure 4.15. It was not possible to fit the PL lifetime data to a single exponential, and so each decay was fitted to the stretched exponential function given in equation 3.3. The higher energy emission was fitted with an effective lifetime (equation 3.4) of 142 ± 4 μs and the lower energy emission at 161 ± 6 μs. Stated uncertainties represent statistical uncertainty in the fitting process, and do not include the systematic error arising from the dark counts included in acquisition of the lifetime data for the 13292 cm^{-1} emission, which is almost two orders of magnitude lower in intensity. The effect of this is to artificially extend the fitted decay, and so it is relatively certain that both these emissions have a lifetime closer to that measured for the $^1T_{2g}(^1P) \rightarrow {}^3A_{2g}(^3F)$ transition. The fitted values of τ and β leading to the reported effective lifetimes are given in figure 4.15.

For all but the highest energy emission, each band consists of two overlapping peaks separated by approximately 250 cm^{-1} where there is only one energy level theoretically expected. This is suggestive of a second inequivalent B site, perhaps similar to that postulated to explain the dual emission bands observed with $NaMgF_3$:Mn. That the PL emission decay data can also be fitted with a double exponential would support this hypothesis, but it is considered unlikely as the double emission is not observed in the higher energy RL emissions. The decision to fit either a double or stretched exponential does not significantly alter the reported values of $\langle\tau\rangle$ as calculated using equation 3.4.

When irradiated at room temperature no TSL was observed between 310 K and 710 K above the background noise of the CCD spectrometer, even if irradiated to doses in excess of 3 kGy. When irradiated

State	Energy (cm^{-1})	Method	Emissions	Energy (cm^{-1})
$^1A_{1g}(^1S)$	61921	TS	$^1A_{1g}(^1S) \rightarrow {}^1T_{2g}(^1G)$	22795
			$^1A_{1g}(^1S) \rightarrow {}^1E_{1g}(^1G)$	23535
			$^1A_{1g}(^1S) \rightarrow {}^1T_{1g}(^1G)$	27824
			$^1A_{1g}(^1S) \rightarrow {}^1A_{1g}(^1G)$	30093
			$^1A_{1g}(^1S) \rightarrow {}^3T_{2g}(^3P)$	30713
			$^1A_{1g}(^1S) \rightarrow {}^1T_{1g}(^1D)$	32165
			$^1A_{1g}(^1S) \rightarrow {}^1E_{1g}(^1D)$	34423
			$^1A_{1g}(^1S) \rightarrow {}^3T_{1g}(^3F)$	39365
			$^1A_{1g}(^1S) \rightarrow {}^3T_{2g}(^3F)$	42699
$^1T_{2g}(^1G)$	33785	TS	—	—
$^1E_{1g}(^1G)$	33335	TS	—	—
$^1T_{1g}(^1G)$	27664	TS	—	—
$^1A_{1g}(^1G)$	24442	TS	—	—
$^3T_{1g}(^3P)$	24631	AB	—	—
$^1T_{2g}(^1D)$	22918	TS	$^1T_{2g}(^1D) \rightarrow {}^3T_{1g}(^3F)$	9143
			$^1T_{2g}(^1D) \rightarrow {}^3T_{2g}(^3F)$	13292
			$^1T_{2g}(^1D) \rightarrow {}^3A_{2g}(^3F)$	20060
$^1E_{1g}(^1D)$	15517	TS	—	—
$^3T_{1g}(^3F)$	13228	AB	—	—
$^3T_{2g}(^3F)$	7716	AB	$^3T_{2g}(^3F) \rightarrow {}^3A_{2g}(^3F)$	6302
$^3A_{2g}(^3F)$	0	—	—	—

Table 4.9: Summary of energy levels for Ni^{2+} in $NaMgF_3$ and emissions observed for sample J140306. The average emission energies are tabulated for transitions observed in both PL and RL. Energies were determined with reference to the reported absorption spectrum (AB) and the Tanabe-Sugano diagram (TS) of the $3d^8$ configuration.

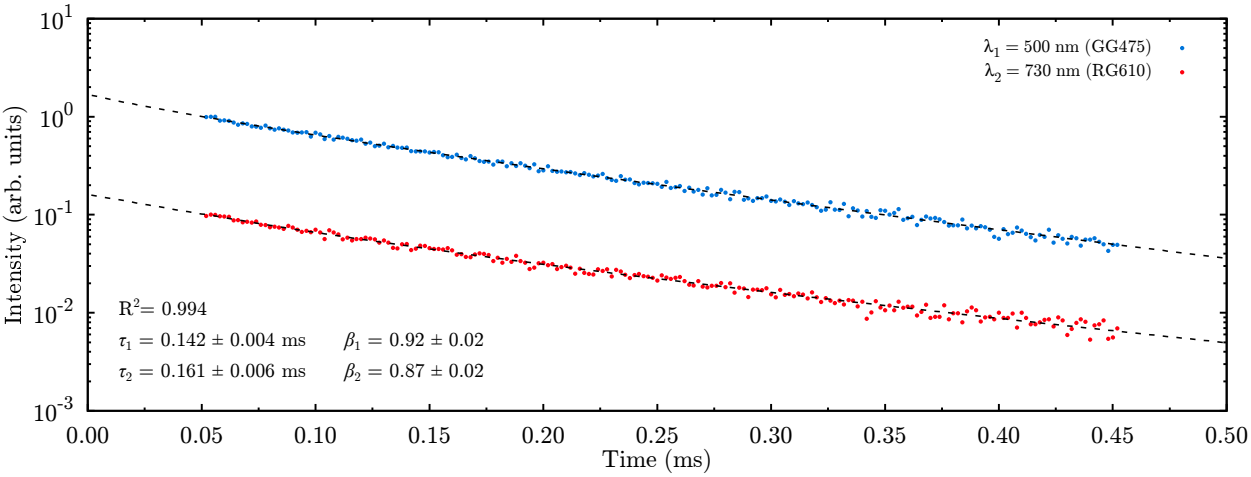

Figure 4.15: Decay of $^1T_{2g}(^1D) \rightarrow {}^3A_{2g}(^3F)$ (blue) and $^1T_{2g}(^1F) \rightarrow {}^3A_{2g}(^3F)$ emissions for sample J140306 excited at 26667 cm^{-1} (375 nm) and 21505 cm^{-1} (465 nm). Fits are illustrated for both decays, using stretched exponentials with the indicated parameters. The spin forbidden emission at 730 nm is of sufficiently low intensity that the background of dark counts has slightly inflated the measured lifetime, which is expected to more closely match that measured at 500 nm.

to similarly high doses while held below room temperature at 230 K an extremely weak glow peak, SNR of approximately 3, was observed at 300 K at an emission energy consistent with the $^1T_{2g}(^1P) \rightarrow {}^3T_{2g}(^3F)$ transition, which dominates the PL and RL spectrum. No additional glow peaks were observed up to 710 K. This data is not presented graphically as the poor SNR results in integrated intensity which cannot be reliably fitted. For each of these measurements the expected low level background TSL signal from the ceramic carrier of the heating element (see § 3.2.6) and black body radiation were observed, and so the lack of TSL from $NaMgF_3$:Ni is not attributed to experimental error. A lack of significant TSL is consistent with the very low level of room temperature 'afterglow' observed after irradiation to high doses during RL spectroscopy.

A number of additional emissions were observed when excited with x-rays, seen at 16610 cm^{-1} and above 20000 cm^{-1} in figure 4.16a, along with the 20121 cm^{-1} and 13292 cm^{-1} emissions of Ni^{2+} observed in the PL emission spectrum. The transition energies of the extra peaks could not be reconciled with the $3d^7$ configuration of Ni^{3+}, or with any plausible contaminant species. It is most likely that these emissions derive from the $^1A_{1g}(^1S)$ level of Ni^{2+}, which was calculated to lie at 61921 cm^{-1}, well beyond the range of optical excitation sources available for PL spectroscopy. As it was not possible to obtain data describing the $^1A_{1g}(^1S) \leftarrow {}^3A_{2g}(^3F)$ absorption[v], no theoretical estimate of the Stokes shifts for these emissions could be attempted and so assignments remain uncertain. Despite this, tentative assignments can been made for relaxation from $^1A_{1g}(^1S)$ to $^1T_{1g}(^1G)$, $^1A_{1g}(^1G)$, $^3T_{2g}(^3P)$, and $^1T_{1g}(^1D)$, based on their pattern of energies and the expected lower relative intensity of the spin forbidden $^1A_{1g}(^1S) \rightarrow {}^3T_{2g}(^3P)$ transition. Collectively, these features are considered unlikely to coincidentally support such assignments.

Between $^1A_{1g}(^1S)$ and $^1T_{1g}(^1G)$ resides the $^1T_{2g}(^1G)$ and $^1E_{1g}(^1G)$ levels, the energy separation of which is very small and essentially independent of $10Dq$, and thus the two heavily overlapped emission bands between 20000 cm^{-1} and 25000 cm^{-1} can subsequently be assigned as $^1A_{1g}(^1S) \rightarrow {}^1T_{2g}(^1G)$ and $^1A_{1g}(^1S) \rightarrow {}^1E_{1g}(^1G)$. That no emissions are observed from any of the aforementioned end states to lower energy levels is consistent with their small relative separation, which would be expected to support non-radiative relaxation down to at least $^1T_{2g}(^1D)$, from which the emissions observed in the PL spectrum occur. This leaves relaxation from $^1A_{1g}(^1S)$ to the first three excited states listed in table 4.9 as candidates for the emissions observed at 34423 cm^{-1}, 39365 cm^{-1}, and 42699 cm^{-1}, with a presumed relaxation from $^1A_{1g}(^1S)$ to the ground state above the captured energy range. These last three assignments would require

[v]Even had suitable equipment been available, the wavelengths at which this absorption would be expected to occur lie beyond the fundamental absorption edge of $NaMgF_3$ for the band gap energy given in § 3.1.1.

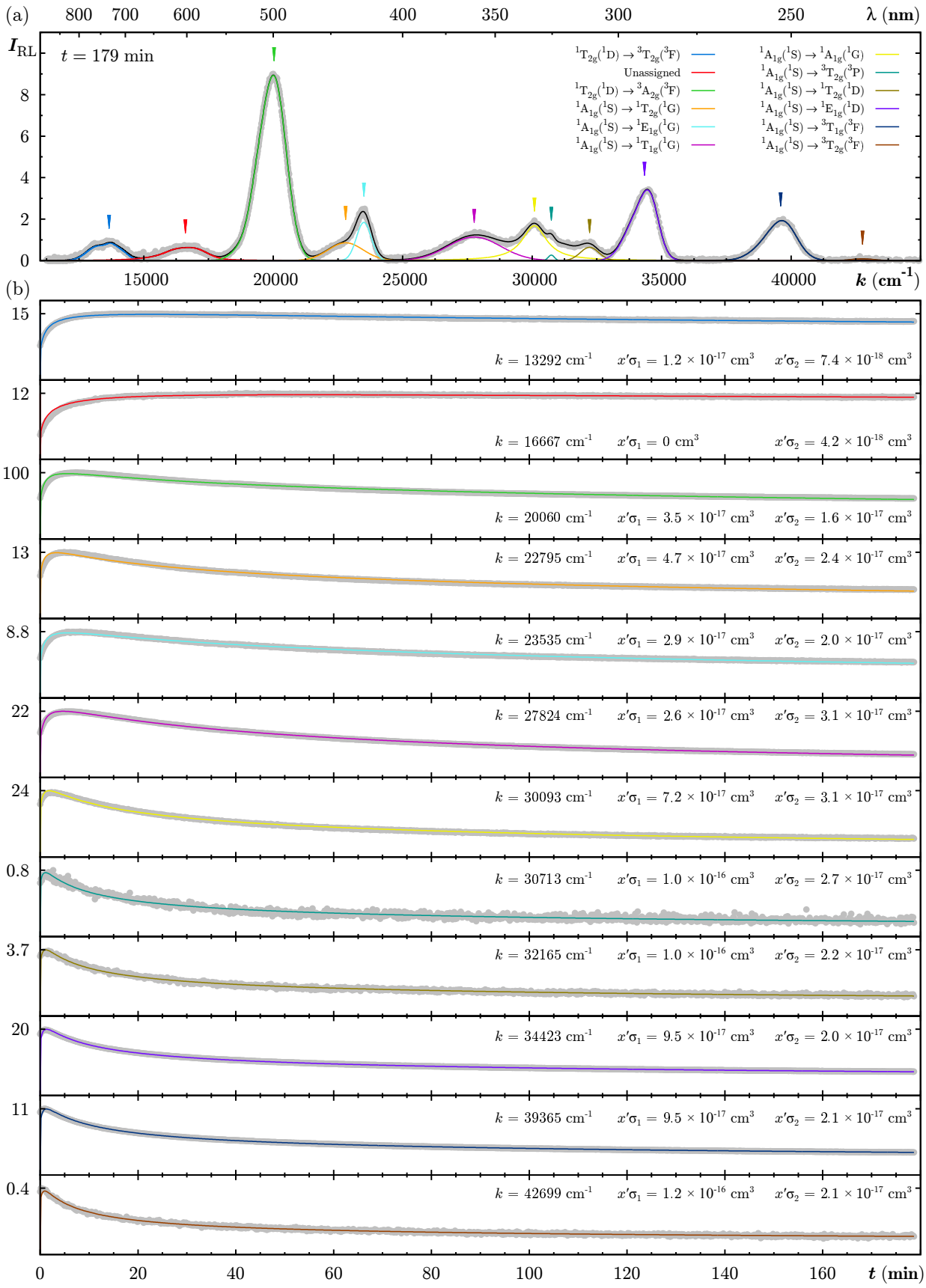

Figure 4.16: (a) Fitted RL emission spectrum for $NaMgF_3$:Ni (J140306), and (b) changes in intensity with time for each peak. Time dependence is fitted to the model described by equations 4.1 to 4.5 with parameters $\Gamma = 10^{14}$ cm^{-3} Gy^{-1}, $\Phi = 1$ Gy s^{-1}, $A_1^m = 10^{-8}$ cm^3 s^{-1}, $A_1^n = 2.9\times10^{-8}$ cm^3 s^{-1}, $A_2^n = 2.0\times10^{-24}$ cm^6 s^{-1}, $A_{12}^n = 2.8 \times 10^{-5}$ s^{-1}, $A_1^{mn} = 8.6 \times 10^{-7}$ cm^{-3} s^{-1}, $M_1 = 2.0 \times 10^{19}$ cm^{-3}, and $N_{12} = 1.3 \times 10^{17}$ cm^{-3}. Charge carrier concentrations at $t = 0$ are zero, except for $m_1(0) = 1.8 \times 10^{15}$ cm^{-3}.

perhaps unusually large Stokes shifts, approaching 13000 cm^{-1} for $^1A_{1g}(^1S) \rightarrow {}^3T_{2g}(^3F)$. While similarly large Stokes shifts are observed in other inorganics, for example $Bi_4Ge_3O_{12}$[351] at approximately 14000 cm^{-1}, no reports of shifts of this magnitude with a $NaMgF_3$ were found in the literature. Alternatively, as the calculated energy of the $^1A_{1g}(^1S)$ state of approximately 7.7 eV exceeds the band gap of $NaMgF_3$, these emissions may be explained as originating instead from valence band states.

Also shown in figure 4.16b are the changes in intensity of each fitted emission as absorbed dose is accumulated. Each emission exhibits a dose dependence consistent with the expected interplay between increased luminescence efficiency as charge carrier traps are saturated, and the optical absorptions of colour centres detailed in § 4.1.2. As $NaMgF_3$:Ni emits across most of the visible spectrum, the impact of colour centres is particularly evident in the more pronounced downturn for those higher energy peaks which overlap the F–centre absorption. The basic single trap and single luminescence centre model described in § 2.2.4 was extended to substantiate this interpretation by including the influence of colour centre absorptions on the observed RL intensity and fitting it to the experimental data. This extended model is given in equations 4.1 through 4.5 below, using the same nomenclature as in § 2.2.4.

$$\frac{\mathrm{d}n_\mathrm{c}}{\mathrm{d}t} = \Gamma\dot{\Phi} - n_\mathrm{c}A_1^n\left(N_{12} - n_1 - n_2\right) - n_1 n_\mathrm{c}A_2^n\left(N_{12} - n_1 - n_2\right) - n_\mathrm{c}m_1A_1^{mn} \tag{4.1}$$

$$\frac{\mathrm{d}m_\mathrm{v}}{\mathrm{d}t} = \Gamma\dot{\Phi} - m_\mathrm{v}A_1^m\left(M_1 - m_1\right) \tag{4.2}$$

$$\frac{\mathrm{d}n_1}{\mathrm{d}t} = n_\mathrm{c}A_1^n\left(N_{12} - n_1 - n_2\right) - n_1 n_\mathrm{c}A_2^n\left(N_{12} - n_1 - n_2\right) - 2n_1A_{12}^n \tag{4.3}$$

$$\frac{\mathrm{d}n_2}{\mathrm{d}t} = n_1 n_\mathrm{c}A_2^n\left(N_{12} - n_i - n_2\right) + n_1A_{12}^n \tag{4.4}$$

$$\frac{\mathrm{d}m_1}{\mathrm{d}t} = m_\mathrm{v}A_1^m\left(M_1 - m_1\right) - n_\mathrm{c}m_1A_1^{mn} \tag{4.5}$$

Observed radioluminescence intensity is then taken as proportional to the recombination of conduction band electrons with trapped holes, as in § 2.2.4, with optical absorption dictated by the population of n_1 and n_2 as modelled by the Beer-Lambert law. This is described by equation 4.6 below, in which x' is an effective optical path length specific to the sample geometry, and σ_1 and σ_2 the optical absorption cross-sections of the colour centres represented by n_1 and n_2 respectively.

$$I_{\mathrm{RL,Ni}} \propto n_\mathrm{c}m_1 \exp\left(-x'\sigma_1 n_1\right)\exp\left(-x'\sigma_2 n_2\right) \tag{4.6}$$

As x' cannot be experimentally quantified, the free parameters for fitting are the implied constant of proportionality, and the product terms $x'\sigma_1$ and $x'\sigma_2$. All other parameters in the model were adjusted for approximate optimality and then fixed during fitting (see figure 4.16). $\dot{\Phi}$ was measured with TLD dosimetry (see § 3.2.1), N_{12} estimated using equation 2.32 and absorption data in figure 4.2a, M_1 from the dopant concentration given for sample J140306 in table 3.1, while Γ and selected trapping and recombination probabilities were estimated with reference to the literature.[54] A non-zero value of $m_1(0)$ is used to provide the observed non-zero $I_{\mathrm{RL,Ni}}(0)$, although this is not the only physically plausible means by which this might be achieved[vi].

The value obtained for N_{12}, at 1.3×10^{17} cm^{-3}, is not physically unreasonable, implying that only one in 5×10^5 anion sites need be vacant to facilitate a model which neglects F–centre creation as a second order effect. The small numerical value of A_2^n does not indicate a negligible term as it acts on both the n_c and n_1 populations, while the comparatively large value for A_{12}^n supports amalgamation as the dominant mechanism by which F_2–centres are formed, over creation *in situ*. This large value for A_{12}^n is also consistent with the apparent equilibrium between the F–centre and F_2–centre populations reported for alkali halides,[324] and

[vi]The model might be extended with a term for direct radio-excitation of the Ni^{2+} centre, but it was decided to instead minimise the number of fitting parameters.

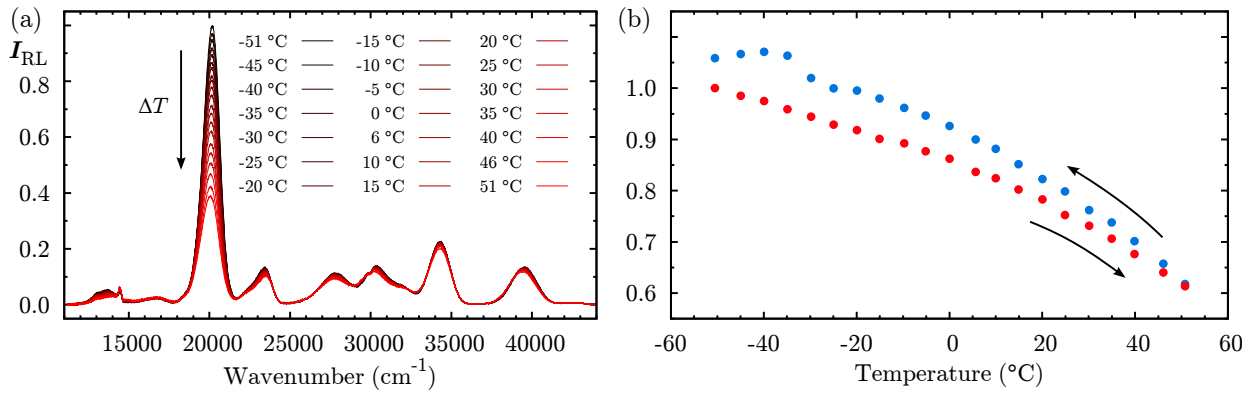

Figure 4.17: Temperature dependence of (a) RL emission spectrum and (b) integrated intensity, the latter of which is dominated by the changes in the intensity of the $^1T_{2g}(^1D) \rightarrow {}^3A_{2g}(^3F)$ emission near 20000 cm^{-1}. Arrows marked on (b) indicate the direction of temperature cycling, with response measured under positive ΔT plotted in red and that measured while lowering the sample temperature back to the starting point in blue.

observed for sample J140501. With slightly different trapping probabilities, the population dynamics of n_1 and n_2 can be fitted to the absorption data depicted in figure 4.2a (not shown).

Temperature dependence of the RL emission spectrum is shown in figure 4.17, where it can be seen that the dominant feature is significant reduction in the $^1T_{2g}(^1D) \rightarrow {}^3A_{2g}(^3F)$ emission at elevated temperature. In the absence of complications from room temperature TSL these spectra were not normalised. As for $NaMgF_3$:Mn, small shifts in emission energy and intensity are observed for all the other emissions assigned to transitions with the $3d^8$ configuration. As the change in intensity of the $^1T_{2g}(^1D) \rightarrow {}^3A_{2g}(^3F)$ emission with temperature is so much larger than that observed for all other emissions, it is considered more likely attributable to an as yet unidentified mechanism of thermal quenching rather than intrinsic temperature dependence. The presence of a non-radiative recombination centre with an excited state in the region of the calculated energy for the $^1T_{2g}(^1D)$ level (22918 cm^{-1}) could explain the observed quenching, although no independent evidence for such exists in the available experimental data. As no significant TSL was observed, the failure to return to the initial intensity after the temperature cycle illustrated in figure 4.17b is attributed to emission spectra changes due to radiation damage. If the temperature of sample J140306 is cycled rapidly between −50 °C and +50 °C such that the dose delivered between extremes of temperature is minimised, then repeatable RL intensities are observed.

Close inspection of the temperature dependent RL emission spectra shown in figure 4.17a reveal that the weak band emission near 16500 cm^{-1}, unassigned in figure 4.16a, is essentially temperature independent. This emission is also anomalous in terms of dependency on absorbed dose, appearing largely unaffected by the colour centre absorptions which cause reduction in observed intensity for the emissions of immediately higher and lower energies: $^1T_{2g}(^1D) \rightarrow {}^3T_{2g}(^3F)$ and $^1T_{2g}(^1D) \rightarrow {}^3A_{2g}(^3F)$. That the $x'\sigma_1$ term is not required to model this peak, while it is required to model all other observed emissions, reflects this difference. On the basis of the above, the unassigned 16550 cm^{-1} is considered unlikely to arise from the Ni^{2+} dopant.

4.8.3 Discussion

The low energy near infrared emission from the $^3T_{2g}(^3F)$ state occurs in a region of the optical spectrum which is not only potentially advantageous in the mitigation of Čerenkov stem effects in radiotherapy applications, but is also relatively well aligned with the windows of optimum attenuation in silica fibre optics at 1550 nm. Attenuation of silica fibre at these wavelengths can theoretically be as low as 0.3 dB/km,[202] albeit higher for polymer clad silica optics of large diameter and numerical aperture. This can be exploited to reduce signal attenuation and hence reduce measurement uncertainty in radiotherapy applications, where several tens of metres of fibre optics are necessary to traverse shielding mazes in typical treatment vaults.

The observed emission lifetime in the region of 150 μs is probably sufficiently long to allow temporal

gating of prompt stem signal in radiotherapy applications involving pulsed radiations. However, for the duty cycle and pulse repetition frequencies typical of the accelerators used in this work (see § 3.3.1) lifetimes substantially below 1 ms may place unrealistic bandwidth requirements on the optical acquisition system. The chromatic discrimination approach to suppressing stem signal might be preferable for $NaMgF_3$:Ni, and if applied to the $^3T_{2g}(^3F) \rightarrow {}^3A_{2g}(^3F)$ emission would not be subject to the additional uncertainty incurred by the fluorescent component when implemented with PMMA optics.[243]

Quenching of the $^1T_{2g}(^1D) \rightarrow {}^3A_{2g}(^3F)$ emission at molar concentrations above those of the crystals employed in this study has been reported for Ni^{2+} in other fluoroperovskite hosts,[348] where it is attributed to cross relaxation between dopant ions. Quenching via this mechanism is not possible for emission from the $^3T_{2g}(^3F)$ state due to the lack of any intermediate energy levels. This would suggest that the luminescence efficiency at near infrared wavelengths may scale more favourably with dopant concentration, but this has not been investigated in detail herein.

Temperature dependency is manageable, and in the absence of any significant TSL is also quite reproducible. If the substantial intensity dependence on temperature observed for the $^1T_{2g}(^1D) \rightarrow {}^3A_{2g}(^3F)$ emission is due to thermal quenching as proposed, then it is possible that the infrared emission of most interest, $^3T_{2g}(^3F) \rightarrow {}^3A_{2g}(^3F)$, might also exhibit the minimal temperature dependence observed for the remainder of emissions assigned to Ni^{2+}. This has not yet been assessed.

The high dose behaviour of the $^3T_{2g}(^3F) \rightarrow {}^3A_{2g}(^3F)$ emission has not been discussed in this section as it could not be measured using the fibre optic spectrometers used to acquire the data presented in figure 4.16. This emission was monitored using a small area semiconductor up to a dose of approximately 30 kGy during testing of dosimeter prototype hardware and was found to be essentially free of the colour centre absorption effects reported here. After saturation, a dependence of sensitivity on absorbed dose on the order of 10^{-6} Gy^{-1} was observed, which is about as good as can be hoped for in any type of solid state dosimeter. See figure B.3 in appendix B for details.

4.9 $NaMgF_3$:Pr

Like many of the rare earth doped samples, $NaMgF_3$:Pr exhibits near infrared luminescence alongside a range of emission peaks at visible wavelengths. The latter dominates the emitted energy but is at best of secondary interest to this study. Sensitivity of the one sample fabricated (J140302) was poor, again due to low dopant solubility at the temperatures attained in the melt. As the material shows relatively little promise for fibre coupled dosimetry applications, only one sample was made.

4.9.1 Diffraction Data

A diffractogram for sample J140302 is shown in figure 4.18a, in which it can be seen that orthorhombic $NaMgF_3$ is the dominant phase. The presence of PrF_3 was also established with certainty, with almost all peaks listed in ICDD reference pattern 00-046-1167[352] of intensity greater than about 10% clearly resolved, except those co-incident with the expected reflections from $NaMgF_3$. As for all other samples, the most intense lines of MgF_2 were also observed, as were a small selection of very low intensity reflections observed in all samples, but absent from the $NaMgF_3$ reference pattern given in table 4.1. These are discussed further in § 4.14.1. The sole remaining unexplained feature was a weak reflection at 27.037° with intensity 0.5% that of the strongest reflection.

4.9.2 Pr^{3+} Luminescence

PL excitation and emission are depicted in figure 4.18b. Interpretation of the excitation spectrum is somewhat ambiguous, in that five distinct peaks are observed in the region of 22000 cm^{-1} where there is expected to be four energy levels of the free ion: $^1I_6$, $^3P_0$, $^3P_1$, and $^3P_2$. Assignments were made for energies that best reflect the observed emissions, but these may well be in error. The two excitation peaks near 17000 cm^{-1}

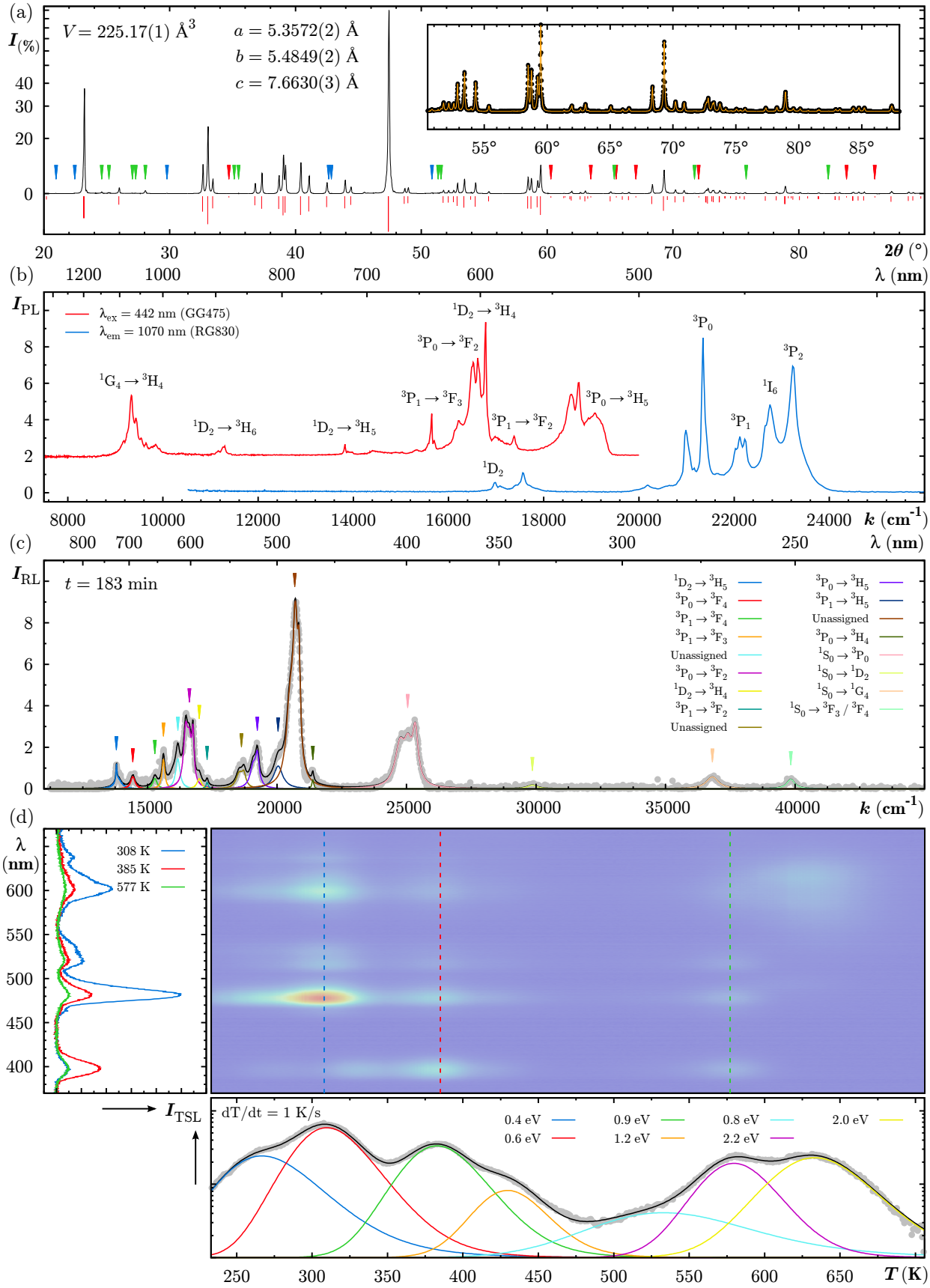

Figure 4.18: Basic characterisation measurements for $NaMgF_3$:Pr (J140302), including (a) XRD pattern, (b) photoluminescence spectra, (c) fitted radioluminescence spectra, and (d) thermoluminescence emission spectra with fitted glow curves. In (a), the experimental data is plotted (black) and the pseudo-Voigt fit (orange) illustrated in the inset, with markers over peaks which are missing from the reference pattern (red), explained by contaminants (green), and unexplained (blue). Markers in (c) are coloured to match the legend. Activation energies for each of the fitted second order glow peaks in (d) are given on the subplot.

to the $^1D_2$ level are the most consistent with the otherwise somewhat varied assignments made in the literature for neighbourite[271] and a range of other hosts.[353–355] A tentative energy level scheme is summarised in table 4.10. Under x-ray excitation, emissions are also observed from the $^1S_0$ level, which was located at approximately 46300 cm^{-1} based on the assignments shown in the fitted RL emission spectra. These emissions are shown in figure 4.18c.

A TSL map for sample J140302 after exposure to approximately 300 Gy is shown in figure 4.18d, depicting a relatively complex array of glow peaks which differ across the emission spectrum. As only one valence of the dopant ion was observed, these differences are possibly caused by the varied temperature dependence of each transition probability, which was not otherwise investigated for either the PL or RL emission. Second order glow peaks (equation 3.6) were fitted to the net intensity across all wavelengths at temperatures of 266 ± 1 K, 310 ± 1 K, 383 ± 1 K, 429 ± 2 K, 532 ± 21 K, 580 ± 1 K, and 633 ± 1 K, with the activation energies shown on the figure. The glow peak fitted at 532 K appears physically implausible, being very wide in temperature and exhibiting excess statistical uncertainty in T_m. This peak is required for a satisfactory fit of peak next highest in temperature, but otherwise does not represent a significant perturbation. The broad emission spectrum of the 633 K glow peak seen at the high temperature and long wavelength limit of the colour map in figure 4.18d is not characteristic of Pr^{3+}. It is seen also in sample J140301 ($NaMgF_3$:Mn) and J140304 ($NaMgF_3$:Er) when irradiated at room temperature. It may arise from the host crystal or the experimental apparatus.

4.9.3 Discussion

Of all the rare earth dopants investigated in this study, Pr^{3+} exhibits perhaps the largest degree of shifts and splitting in the free ion energy levels. This renders the assignment of many spectral features ambiguous, both within the data presented here and in the literature. If the energies given in table 4.10 are taken as approximately reliable, it could be reasonably expected that the near infrared emission peaking at 9437 cm^{-1}

State	Energy (cm^{-1})	Method	Emissions	Energy (cm^{-1})
$^1S_0$	46300	EM	$^1S_0 \rightarrow {}^1I_6, {}^3P_0$	25038
			$^1S_0 \rightarrow {}^1G_4$	36805
			$^1S_0 \rightarrow {}^3F_3, {}^3F_4$	39825
$^3P_2$	23229	EX	—	—
$^1I_6$	22753	EX	—	—
$^3P_1$	22124	EX	$^3P_1 \rightarrow {}^3H_5$	20040
$^3P_0$	21345	EX	$^3P_0 \rightarrow {}^3F_4$	14414
			$^3P_0 \rightarrow {}^3F_2$	16518
			$^3P_0 \rightarrow {}^3H_5$	19127
			$^3P_0 \rightarrow {}^3H_4$	21381
$^1D_2$	16978	EX	$^1D_2 \rightarrow {}^3F_4$	9872
			$^1D_2 \rightarrow {}^3H_5$	13812
			$^1D_2 \rightarrow {}^3H_4$	16986
$^1G_4$	9337	EM	$^1G_4 \rightarrow {}^3H_4$	9437
$^3F_4$	6855	EM	—	—
$^3F_3$	6475	EM	—	—
$^3F_2$	4747	EM	—	—
$^3H_6$	4403	EM	—	—
$^3H_5$	2261	EM	—	—
$^3H_4$	0	—	—	—

Table 4.10: Summary of energy levels for Pr^{3+} in $NaMgF_3$ and emissions observed for sample J140302. The average emissions energies are tabulated for transitions observed in both PL and RL. Energies were determined with reference to the reported excitation spectrum (EX) and emission spectrum (EM).

is not necessarily the lowest energy optical transition likely to occur with this dopant. A $^1G_4 \rightarrow {}^3H_5$ transition might reasonably be expected within the range of the spectrometer used, but was not observed.

The narrow emission in the region of 1100 nm observed with $NaMgF_3$:Pr could be useful in conjunction with selected types of small area Si photodiode detectors which exhibit peak sensitivity in this region. Were this the principal emission, this material might warrant further study within the scope of this work, but a greater fraction of the excitation energy appears to be released in the visible wavelength emissions. This emission energy is also slightly too low to be viable with polymer optics.

4.10 $NaMgF_3$:Sm

Luminescence of $NaMgF_3$:Sm has been previously reported,[266, 267, 356] but was included in this study both as a potential long wavelength emitter viable for use with polymer fibre optics, and because the luminescence ion is reported in $NaMgF_3$ as both divalent and trivalent. The presence of two optically active valences presents an opportunity to study a process less commonly observed in other samples, namely conversion between oxidation states during irradiation, which in the case of $NaMgF_3$:Sm can be investigated by optical and magnetic methods. While two valences are also seen in $NaMgF_3$:Eu and $NaMgF_3$:Yb, in the case of $NaMgF_3$:Sm both valences emit at similar energies and intensities, and so are less subject to uncertainty due to the effects of radiation induced colour centre absorptions.

Two samples were made, J140307 and J150502, only the first of which has been reported here. A fibre coupled section of J140307 of approximately 1 mm^3 was successfully used in many of the engineering tests for the point dosimeter prototype detailed in appendix B, and so is considered likely to possess sufficient sensitivity for radiotherapy applications.

4.10.1 Diffraction Data

Diffraction data for sample J140307 is presented in Figure 4.19a. Orthorhombic $NaMgF_3$ is by far dominant, with MgF_2 detectable as for all other samples, and also the [011], [101], [020], [112], and [040] reflections of SmF_3. These reflections for SmF_3 include many of the more prominent peaks in ICDD pattern 00-032-0981,[329] but not the 100% line, which at 27.327° overlaps with the [110] peak of MgF_2 and so is not separately resolved. Several remaining unexplained features occur at 28.703°, 38.036°, 46.768°, and 53.659°, all at approximately 0.1% the intensity of the most intense $NaMgF_3$ peak. An additional 13 reflections of similarly low intensity are observed, some at positions common to most other samples, yet are absent from the reference pattern.

A systematic offset in 2θ averaging at 0.137° was observed for sample J140307, seen for both peaks indexed to $NaMgF_3$ and the MgF_2 and SmF_3 contaminants. This was attributed to instrumental uncertainty, perhaps in the removal and refitting of the rotating sample stage. As this offset is an order of magnitude larger than observed for all other samples, it was was corrected for the purposes of unit cell refinement. This resulted in a change in the final lattice parameters on the order of 1 pm.

4.10.2 Sm^{2+} Luminescence

PL excitation was obtained separately for each valence by monitoring either the $^5D_0 \rightarrow {}^7F_1$ transition of Sm^{2+} at 14341 cm^{-1} (697 nm) or the $^4G_{5/2} \rightarrow {}^6H_{7/2}$ transition of Sm^{3+} at 16573 cm^{-1} (603 nm). Both are plotted in figure 4.19b. The Sm^{2+} excitation reflects at least two $5d \leftarrow 4f$ absorptions with some additional structure at low intensity, which does not correlate with the Sm^{3+} excitation peaks and so is likely attributable to transitions within the $4f^6$ configuration of Sm^{2+}. The lowest lying $4f^5\left[{}^6H_{5/2}\right]5d$ level is in the region of 24000 cm^{-1} for the free Sm^{2+} ion,[320, 357] and so would appear to be lowered by about 2000 cm^{-1} in $NaMgF_3$. This valence of samarium is isoelectronic to Eu^{3+} (see § 4.5.3), with a similarly high density of $4f^6$ levels at the excitation energies measured,[48] precluding unambiguous assignments. Only the energy of the $^5D_4$ state is tentatively included in table 4.11 on the basis of excitation features, with the remaining levels in the ^5D_J and ^7F_J multiplets inferred from the PL emission spectrum.

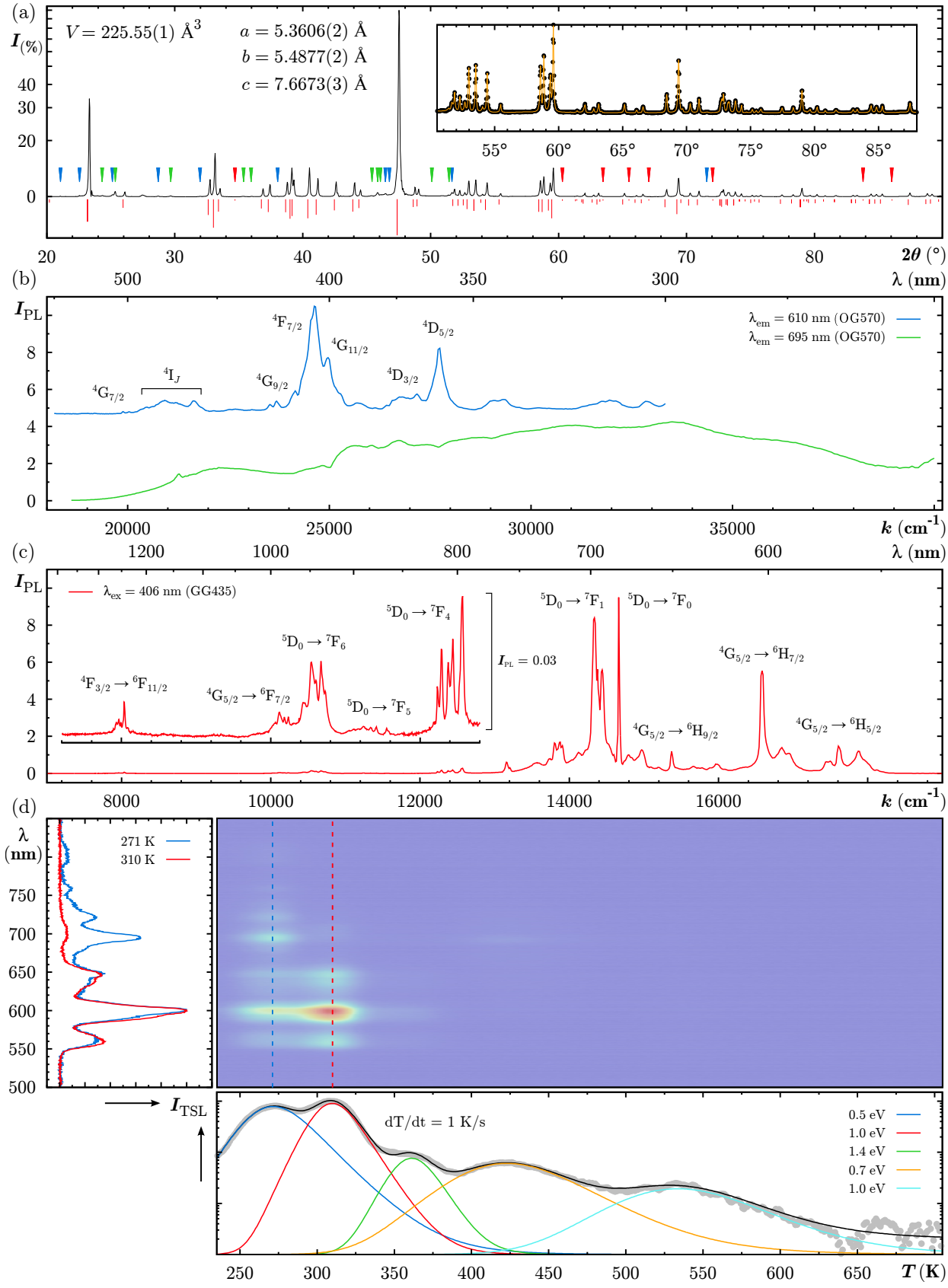

Figure 4.19: Basic characterisation measurements for $NaMgF_3$:Sm (J140307), including (a) XRD pattern, (b) PL excitation, (c) PL emission, and (d) TSL emission spectra with fitted glow curves. In (a), the experimental data is plotted (black) and the pseudo-Voigt fit (orange) illustrated in the inset, with markers over peaks which are missing from the reference pattern (red), explained by contaminants (green), and unexplained (blue). PL excitation in (b) is shown for both Sm^{2+} (green) and Sm^{3+} (blue), and PL emission (c) for both valences. Activation energies for each of the fitted second order glow peaks in (d) are given on the subplot.

Emission is plotted in figure 4.19c under excitation at 24631 cm^{-1} (406 nm), showing only peaks arising from the intraconfigurational transitions of both Sm^{2+} and Sm^{3+}. The Sm^{2+} spectrum dominates at energies between approximately 15000 cm^{-1} through 10500 cm^{-1}, with at least 10 line emissions resolved and assigned and a further three at higher energies overlapping the region dominated by Sm^{3+}. The most intense and well isolated Sm^{2+} emissions are labelled in figure 4.19c and the remainder listed in table 4.11. All observed transitions originate from the lower three levels of the ^5D_J multiplet, with many assignments supported by existing literature for the same host.[266,267,356] No direct radiative relaxation from the $5d$ states was observed in the measured energy range under excitation at 12631 cm^{-1}. The few emissions overlapping the Sm^{3+} emission are identified by the dependency of their intensity on absorbed dose under x-ray excitation, and can be assigned unambiguously within the energy level scheme in table 4.11, with discrepancies less than 200 cm^{-1}, under the assumption that optically observable Sm^{2+} emissions derive from the ^5D_J levels for $J = (0, 1, 2)$ only.

Decay of PL emissions was measured selectively for the more prominent emission lines, and collectively for those weaker groupings which appear in isolation. A number of lower intensity emissions were omitted as it was not possible to acquire lifetime data with sufficiently narrow monochromator slits to ensure that only the emission of interest was captured. All of the measured Sm^{2+} lifetimes were well described by single exponentials, for which the fitted lifetimes ranged from 10.3 ms to 11.0 ms with average lifetime of 10.7 ms. While similar, these lifetimes differ in excess of the expanded uncertainties stated in figure 4.20, including those measured for different lines within a group assigned to the same electronic transition. This suggests that the presence of multiple spectral features near the energy of a single free ion transition is perhaps a consequence of multiple sites, rather than crystal field induced structure from a homogeneous population of Sm^{2+} sites. Multiple Sm^{2+} sites are reported when Sm^{2+} is doped into $KMgF_3$, where it is also attributed

State	Energy (cm^{-1})	Method	Emissions	Energy (cm^{-1})
$^5D_4$	22662	EX	—	—
$^5D_3$	19844	LT	—	—
$^5D_2$	17873	EM	$^5D_2 \rightarrow {}^7F_5$	14771
			$^5D_2 \rightarrow {}^7F_2$	16869
			$^5D_2 \rightarrow {}^7F_0$	17860
$^5D_1$	15931	LT	$^5D_1 \rightarrow {}^7F_4$	13548
			$^5D_1 \rightarrow {}^7F_2$	14954
			$^5D_1 \rightarrow {}^7F_1$	15640
$^5D_0$	14631	EM	$^5D_0 \rightarrow {}^7F_6$	10622
			$^5D_0 \rightarrow {}^7F_5$	11464
			$^5D_0 \rightarrow {}^7F_4$	12370
			$^5D_0 \rightarrow {}^7F_3$	13167
			$^5D_0 \rightarrow {}^7F_2$	13830
			$^5D_0 \rightarrow {}^7F_1$	14341
			$^5D_0 \rightarrow {}^7F_0$	14627
$^7F_6$	4008	EM	—	—
$^7F_5$	3166	EM	—	—
$^7F_4$	2250	EM	—	—
$^7F_3$	1451	EM	—	—
$^7F_2$	799	EM	—	—
$^7F_1$	288	EM	—	—
$^7F_0$	0	—	—	—

Table 4.11: Summary of energy levels for Sm^{2+} in $NaMgF_3$ and emissions observed for this species in sample J140307. The average emissions energies are tabulated for transitions observed in both PL and RL. Energies were determined with reference to the reported excitation spectrum (EX), emission spectrum (EM), and theoretical free ion levels reported in the literature[320,358] (LT).

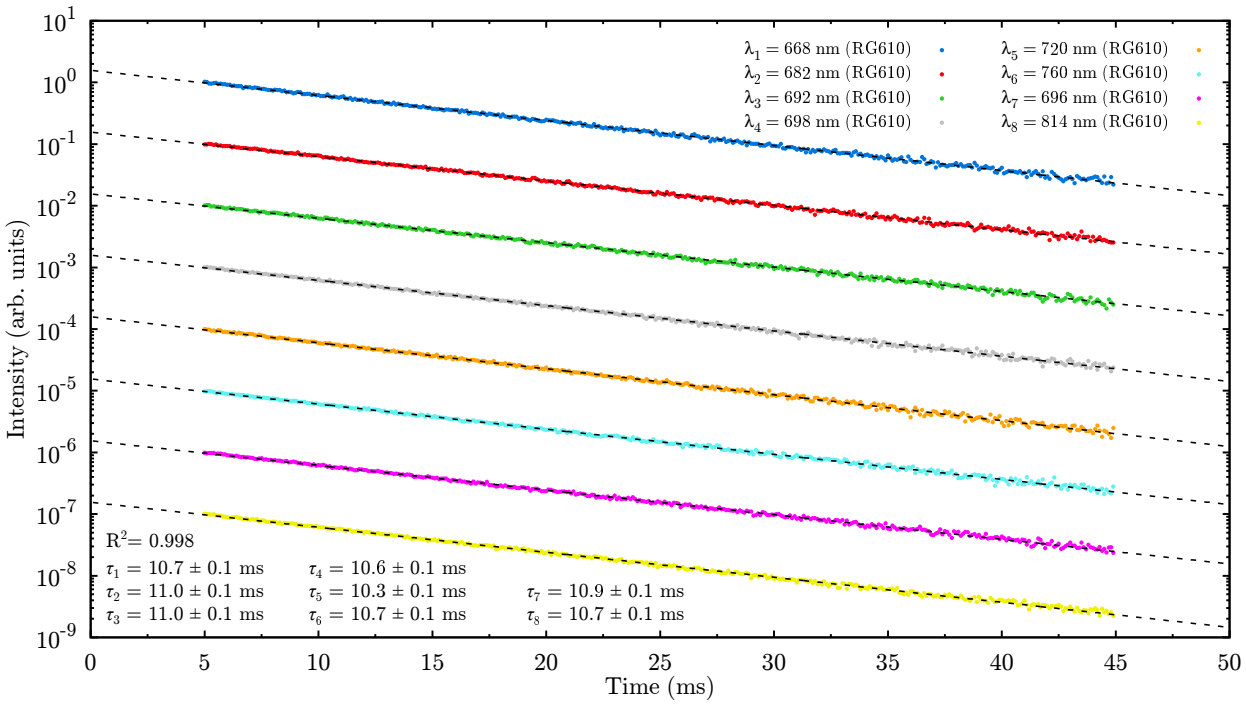

Figure 4.20: A representative set of single exponential fits to the PL emission decays observed for Sm^{2+} emissions. All are excited at 26667 nm^{-1} (375 nm) and measured with narrow emission monochromator slits. The $^5D_0 \rightarrow {}^7F_1$ is sampled twice at 682 nm and 692 nm, as is the $^5D_0 \rightarrow {}^7F_4$ emission at 796 nm and 814 nm.

to charge compensation defects on the basis of varied site symmetries implied from $^5D_0 \rightarrow {}^7F_J$ transition intensities.[359]

The majority of transitions observed in the PL emission spectrum are also seen in the RL emission, which is fitted in figure 4.21a. Initial dependence of intensity on absorbed dose for those peaks assigned as Sm^{2+} is markedly different from that typically observed, in that the intensity decreases immediately towards a steady state from which a slight growth occurs at higher doses. The more pronounced growth in RL intensity which dominates the response during the first kGy of dose in all other materials discussed so far, unexplained RL emissions aside, is also observed in $NaMgF_3$:Sm, but not for those emissions attributed to Sm^{2+}. This is illustrated in the upper 8 panes of figure 4.21b, from which the emissions $^5D_2 \rightarrow {}^7F_0$, $^5D_2 \rightarrow {}^7D_2$, and $^5D_1 \rightarrow {}^7F_1$ are omitted as their overlap with the Sm^{3+} emissions incurs unacceptable uncertainty in fitting for intensity.

A possible explanation for the different dependence on absorbed dose could be that the divalent ion is converted to a trivalent ion during irradiation, with the decline in the Sm^{2+} intensity then attributed to depletion of the divalent population. When such a valence conversion is built into a multi-trap model similar to that described in § 4.8.2, it is found that neither the non-zero steady state intensity nor the slight long term growth can be accommodated without the addition of extraneous, often non-physical, parameters. Furthermore, an increase in oxidation number is also inconsistent with reported valence conversion of samarium in other hosts,[360] where the opposite is reported. While valence conversion obviously must occur if the dopant site traps holes, this is not considered a plausible explanation for the experimental data for sample J140307. A simpler model which accounts for the observed dose dependence in terms of the relative concentration of each valence is explored in more detail in § 4.10.3.

TSL was observed primarily near room temperature, with second order peaks fitted at 271 ± 1 K, 310 ± 1 K, 361 ± 1 K, 422 ± 2 K, and 533 ± 7 K (see figure 4.19d). Of the higher temperature peaks, the one fitted at 422 K arises from the ceramic of the heating element, while at 533 K the emission is so weak that spectral features are no longer clearly resolved. The Sm^{2+} emission intensity is reduced significantly relative to that observed from Sm^{3+} between the two most intense glow-peaks at 271 K and 310 K. This could

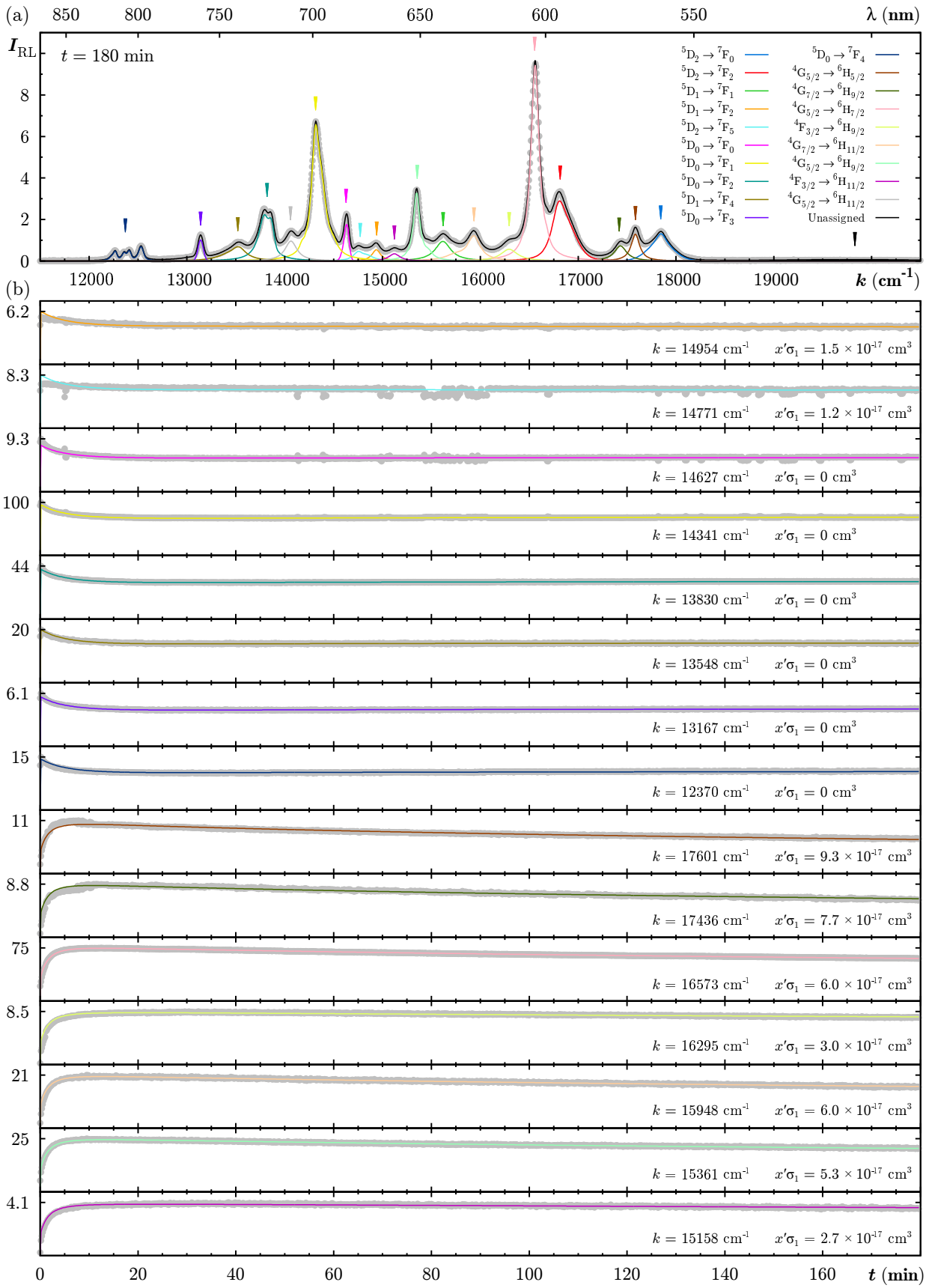

Figure 4.21: (a) Fitted RL emission spectrum for $NaMgF_3$:Sm (J140307), with changes in intensity with time for each peak assigned to (b) Sm^{2+} and (c) Sm^{3+} emissions. Time dependence is fitted to the model described by equations 4.7 to 4.11 with parameters $\Gamma = 10^{13}$ cm^{-3} Gy^{-1}, $\Phi = 1$ Gy s^{-1}, $A_1^m = 2.2 \times 10^{-8}$ cm^3 s^{-1}, $A_2^m = 1.1 \times 10^{-8}$ cm^3 s^{-1}, $A_1^n = 4.5 \times 10^{-9}$ cm^3 s^{-1}, $A_1^{mn} = 1.6 \times 10^{-6}$ cm^3 s^{-1}, $A_2^{mn} = 2.6 \times 10^{-6}$ s^{-1}, $M_1 = 4.5 \times 10^{18}$ cm^3, $M_2 = 1.8 \times 10^{19}$ cm^{-3}, and $N_1 = 1.1 \times 10^{17}$ cm^{-3}. Charge carrier concentrations at $t = 0$ are zero, except for $m_1(0)$ and $m_2(0)$ which are given in the text.

possibly be explained by attributing each of the two low temperature glow peaks to sites of different valence, but could equally well be an artifact of emission temperature dependence. The latter was not investigated for RL as performed for selected other samples as the presence of these low temperature glow peaks renders the interpretation such measurements precarious.

4.10.3 Sm^{3+} Luminescence

PL excitation for Sm^{3+} is depicted in figure 4.19b, illustrating well defined peaks, many of which can be assigned to transitions within the $4f^5$ configuration of Sm^{3+} with reference to literature for similar hosts.[361,362] Additional features in the excitation spectrum at 24155 cm^{-1}, 25707 cm^{-1}, and 29070 cm^{-1} are not tabulated herein, but are correlated with undesignated states in the Dieke diagram.[48] The ^6H_J levels are inferred from the PL emission spectrum while free ion energies for the ^6F_J multiplet, which lie below the range of the excitation source, were included to assist in assignment of emissions.

The majority of PL emissions observed at energies above 15000 cm^{-1} arise from Sm^{3+} transitions, with only the $^4G_{5/2} \rightarrow {}^6H_{11/2}$ emission overlapping the region dominated by Sm^{2+}. Two very weak groups of line emissions centred at 8014 cm^{-1} (1248 nm) and 10168 cm^{-1} (983 nm) are not seen when exciting Sm^{2+} at wavelengths between the various Sm^{3+} excitation peaks, and so are assigned as $^4F_{3/2} \rightarrow {}^6F_{11/2}$ and $^4G_{5/2} \rightarrow {}^4F_{7/2}$ respectively. These weak low energy emissions are shown enlarged in the inset of figure 4.19c. While no substantial shifts in the energy levels within $4f$ configurations of Sm^{2+} and Sm^{3+} are observed with respect to the free ion, for both valences the lower energy emissions exhibit significant and varied splitting. As suggested in the discussion of Sm^{2+} lifetime data in § 4.10.2, this is likely a result of multiple sites brought about by a range of possible charge compensation mechanisms, which can reasonably be expected when substituting rare earth ions on the monovalent Na^+ site.[55,184,359]

PL lifetime measurements were attempted for the $^4G_{5/2} \rightarrow {}^6H_{7/2}$ and $^4G_{5/2} \rightarrow {}^6H_{5/2}$ emissions of Sm^{3+} but these were found to have multiple components, at least one of which is attributed to contaminant europium. When fitting was attempted it was found that in addition to a short Eu^{2+} component, the decay was also distorted by a high background count resulting from the need to use narrow monochromator slits to isolate these emissions. Meaningful fitting was deemed impossible, but visual assessment places these Sm^{3+} lifetimes in the range of 5-10 ms, similar to that observed for Sm^{2+}.

The fitted RL emission spectra in figure 4.21a includes the majority of the Sm^{3+} emissions listed in table 4.12. Intensity evolution with absorbed dose is shown in the lower 7 panes of figure 4.21b, from which a low intensity defect emission near 20000 cm^{-1} and the $^4G_{5/2} \rightarrow {}^6H_{11/2}$ emission have been omitted, the latter due to the fitting uncertainty caused by overlap with the Sm^{2+} emissions. The response seen in the remaining Sm^{3+} emissions in this figure is typical of those observed in other materials, with initial growth attributed to trap filling followed by a slow decline in observed RL intensity due to colour centre absorptions. With all of the $NaMgF_3$:Sm emissions occurring at wavelengths longer than about 550 nm, the effect of colour centres as seen in figure 4.2 is expected to be small but non-negligible, and unlike as seen for $NaMgF_3$:Ni in § 4.8.2, should exhibit minimal spectral dependence. This is reflected in figure 4.21 in the relatively flat response at higher doses.

Equations 4.7 through 4.11 below describe a charge kinetics model similar to that introduced in § 2.2.4, but with an additional hole trap.

$$\frac{\mathrm{d}n_\mathrm{c}}{\mathrm{d}t} = \Gamma\dot{\Phi} - n_\mathrm{c}A_1^n\left(N_1 - n_1\right) - n_\mathrm{c}m_1A_1^{mn} - n_\mathrm{c}m_2A_2^{mn} \tag{4.7}$$

$$\frac{\mathrm{d}m_\mathrm{v}}{\mathrm{d}t} = \Gamma\dot{\Phi} - m_\mathrm{v}A_1^m\left(M_1 - m_1\right) - m_\mathrm{v}A_2^m\left(M_2 - m_2\right) \tag{4.8}$$

$$\frac{\mathrm{d}n_1}{\mathrm{d}t} = n_\mathrm{c}A_1^n\left(N_1 - n_1\right) \tag{4.9}$$

$$\frac{\mathrm{d}m_1}{\mathrm{d}t} = m_\mathrm{v}A_1^m\left(M_1 - m_1\right) - n_\mathrm{c}m_1A_1^{mn} \tag{4.10}$$

$$\frac{\mathrm{d}m_2}{\mathrm{d}t} = m_\mathrm{v} A_2^m \left(M_2 - m_2\right) - n_\mathrm{c} m_2 A_2^{mn} \tag{4.11}$$

Unlike in the model applied in § 4.8.2 for $NaMgF_3$:Ni, there is no interaction between any of the hole or electron traps. The anomalous dose dependence of the Sm^{2+} emission can be reproduced simply by imposing different hole trap concentrations, M_1 and M_2, and careful selection of the initial hole trap populations, $m_1(0)$ and $m_2(0)$. An immediate decrease in one of the hole trap populations occurs provided the recombination term $n_\mathrm{c} m_j A_j^{mn}$ is dominant at small t. This leads to the observed steady state at intermediate t as the depletion of this trap reduces the recombination rate towards an equilibrium with the corresponding hole trapping term $m_\mathrm{v} A_j^m (M_1 - m_1)$. If the latter term is large enough, it can dominate the response at large t and so produce the slow growth observed at higher absorbed doses.

State	Energy (cm^{-1})	Method	Emissions	Energy (cm^{-1})
$^4D_{5/2}$	27739	EX	—	—
$^4D_{3/2}$	27174	EX	—	—
$^4D_{1/2}$	26738	EX	—	—
$^4G_{11/2}$	24969	EX	—	—
$^4F_{7/2}$	24631	EX	—	—
$^6P_{5/2}$	23697	EX	—	—
$^4G_{9/2}$	23529	EX	—	—
$^4I_{13/2}$	21645	EX	—	—
$^4I_{11/2}$	20921	EX	—	—
$^4I_{9/2}$	20492	EX	—	—
$^4G_{7/2}$	20040	EX	$^4G_{7/2} \rightarrow {}^6H_{11/2}$	15948
			$^4G_{7/2} \rightarrow {}^6H_{9/2}$	17436
$^4F_{3/2}$	18939	EX	$^4F_{3/2} \rightarrow {}^6F_{11/2}$	8014
			$^4F_{3/2} \rightarrow {}^6H_{11/2}$	15158
			$^4F_{3/2} \rightarrow {}^6H_{9/2}$	16295
			$^4F_{3/2} \rightarrow {}^6H_{7/2}$	17498
$^4G_{5/2}$	17899	EX	$^4G_{5/2} \rightarrow {}^4F_{7/2}$	10168
			$^4G_{5/2} \rightarrow {}^6H_{11/2}$	14092
			$^4G_{5/2} \rightarrow {}^6H_{9/2}$	15361
			$^4G_{5/2} \rightarrow {}^6H_{7/2}$	16573
			$^4G_{5/2} \rightarrow {}^6H_{5/2}$	17601
$^6F_{11/2}$	10470	AS	—	—
$^6F_{9/2}$	9080	AS	—	—
$^6F_{7/2}$	7910	AS	—	—
$^6F_{5/2}$	7050	AS	—	—
$^6F_{3/2}$	6540	AS	—	—
$^6H_{13/2}$	6470	AS	—	—
$^6F_{1/2}$	6290	AS	—	—
$^6H_{13/2}$	4990	AS	—	—
$^6H_{11/2}$	3389	EM	—	—
$^6H_{9/2}$	2228	EM	—	—
$^6H_{7/2}$	930	EM	—	—
$^6H_{5/2}$	0	—	—	—

Table 4.12: Summary of energy levels for Sm^{3+} in $NaMgF_3$ and emissions observed for this species in sample J140307. The average emissions energies are tabulated for transitions observed in both PL and RL. Energies were determined with reference to the reported excitation spectrum (EX) and emission spectrum (EM), with free ion levels from the NIST atomic spectra database[320] (AS) included where the level is expected but could not be isolated in the PL or RL spectra.

The Sm^{3+} dose response is modelled in much the same fashion as in § 4.8.2. RL emission intensity for the Sm^{2+} and Sm^{3+} sites is independently dictated by the populations of m_1 and m_2 respectively, with the usual correction for colour centre absorptions driven by n_1, as per equations 4.12a and 4.12b below.

$$\text{(a) } I^{2+}_{\mathrm{RL,Sm}} \propto n_{\mathrm{c}} m_1 \exp\left(-x'\sigma_1 n_1\right) \qquad \text{(b) } I^{3+}_{\mathrm{RL,Sm}} \propto n_{\mathrm{c}} m_2 \exp\left(-x'\sigma_1 n_1\right) \tag{4.12}$$

This model was fitted to the experimental data by optimising on the implied constant of proportionality and the product $\sigma_1 n_1$, with all other parameters held constant at the values given in the caption of figure 4.21. While reasonable fixed values for the model parameters were found, it was not possible to fit both the Sm^{2+} and Sm^{3+} responses with identical initial conditions. For Sm^{2+} the initial hole trap populations used were $m_1(0) = 1.8 \times 10^{15}$ cm^{-3} and $m_2(0) = 1.3 \times 10^{15}$ cm^{-3}, and for Sm^{3+} $m_1(0) = 7.8 \times 10^{14}$ cm^{-3} and $m_2(0) = 2.0 \times 10^{14}$ cm^{-3}. If either of these is applied for both valencies, the qualitative behaviour of the system is retained, but acceptable fits for the other valence are not achieved. An exhaustive search of the parameter space for a solution which admits a common set of initial conditions is computationally prohibitive[vii], and so has not in this work been proven to not exist. If initial conditions satisfying the experimental data for both valences are in fact mutually exclusive, then the model must be considered incomplete.

Sm^{3+} emissions are observed in the TSL emission spectrum, as detailed in § 4.10.2.

4.10.4 Magnetisation

Volume susceptibility measured for sample J140307 is presented as a function of temperature in figure 4.22, both before and after exposure to x-ray doses similar to that delivered during the RL spectroscopy presented in figure 4.21. Due to the relatively low dopant concentration the diamagnetic influence of the host crystal is non-negligible and dominates at high temperatures. The observed temperature dependence does not obey the Curie-Weiss law (equation 3.11), but can be modelled as a combination of the Van-Vleck paramagnetic behaviour of both Sm^{2+} and Sm^{3+}. Both valences are described by equation 3.13, yet exhibit contrasting low temperature behaviour due to the different energies and momenta in the $^7\mathrm{F}_J$ and $^6\mathrm{H}_J$ multiplets which constitute the lowest lying excited states of each. Most significantly, the $^7\mathrm{F}_0$ ground state of the $4f^6$ configuration has $J = 0$, and so at lower temperatures equation 3.13 reduces to the constant value of $N\xi$ and the susceptibility plateaus out at a value dictated by equation 3.14. For the $^7\mathrm{F}_J$ levels determined from optical spectra for sample J140307, this occurs below approximately 50 K. Thus the experimental susceptibilities shown in figure 4.22 are clearly dominated by the Sm^{3+} which exhibits the observed divergence of χ at low T. Note that while Van-Vleck paramagnetism for the $4f^5$ configuration is qualitatively similar to Curie-Weiss magnetism, the vanishing susceptibility for $T \gg \Theta$ seen for the latter does not occur for Sm^{3+}. Equation 3.13 instead predicts a non-zero minima in the region of 400 K with slow recovery at higher T.

Equation 3.16 was fitted to data obtained for both irradiated and unirradiated pieces of sample J140307, using the energies listed in tables 4.11 and 4.12. In both cases it was found that f_F and Θ were awarded negligibly small values during the optimisation, indicating that the Curie-Weiss term is of no significance. The remaining parameters are reported on figures 4.22a and 4.22b. As fitted, the diamagnetic contribution of host crystal, χ_0, is the same before and after irradiation within the stated uncertainty, with an average volume susceptibility of 1.43×10^{-5}. This value is comparable with that published for other ionic crystals.[363] Errors in the correction for sample mass and differences in sample geometry and position within the magnetometer render direct comparison of the magnitude of susceptibility before and after irradiation difficult, but the ratio f_{3+}/f_{2+} is of some interest. Before irradiation this ratio is 4.2 in favour of Sm^{3+}, while after exposure it is reduced to 3.8, suggesting a conversion of Sm^{3+} to Sm^{2+}. This change is statistically significant in terms of fitting uncertainty and reflects the same type of conversion observed in other hosts.[360] A more convincing shift may be observed if the measurement were repeated on a more lightly doped sample. Of further note is that the ratio of Sm^{3+} to Sm^{2+} resulting from optimisation of the charge kinetics model reported in § 4.10.3, M_1/M_2, is remarkably similar in value, at 4.0. While this may be considered serendipitous and should not

[vii] If performed using consumer desktop computer hardware, as was done in this work.

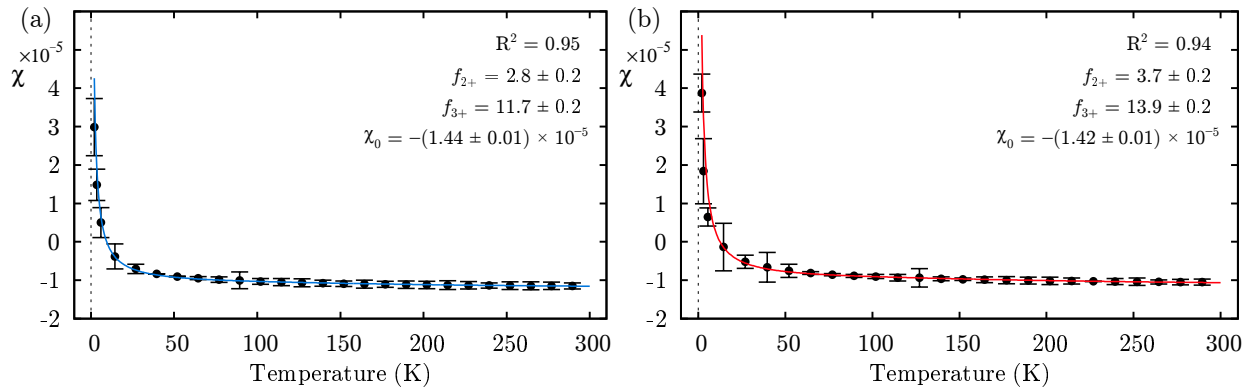

Figure 4.22: Volume susceptibility of $NaMgF_3$:Sm (J140307) as measured (a) before irradiation and (b) after a 40 kVp x-ray dose of approximately 10 kGy. Coloured curves represent a fit to equation 3.16 for Θ and f_F equal to zero and the remaining parameters as indicated on each plot. Experimental points are shown only at intervals of approximately 10 K for clarity. χ_0 is the diamagnetic volume susceptibility of the $NaMgF_3$ host as determined by fitting.

be taken as a robust quantitative result, the implication that sample J140307 contains a larger fraction of Sm^{3+} than Sm^{2+} is not unreasonable.

No significant change in magnetisation was observed in undoped $NaMgF_3$ (J150501) under the same experimental procedure, supporting the interpretation that the response exhibited in figure 4.22, including changes across irradiation, is attributable to the sample dopant. While F–centres created during irradiation also ought to be paramagnetic, their concentration as estimated using equation 2.31 is some two orders of magnitude lower than the total samarium content, and so does not significantly perturb the total magnetisation.

4.10.5 Discussion

$NaMgF_3$:Sm exhibits a highly structured and complex emission spectrum with most of the useful intensity in the range of 12000 cm^{-1} to 18000 cm^{-1}, corresponding to red and near infrared emissions relatively well aligned with the peaks sensitivity of typical Si photodiodes. The two most prominent transitions observed in the RL emission spectrum, $^4G_{5/2} \rightarrow {}^6H_{7/2}$ and $^5D_0 \rightarrow {}^7F_1$, are unambiguously assigned to different valences and so can potentially be exploited to determine dose since the last annealing. These emissions are observed in $NaMgF_3$ very close to 600 nm and 700 nm respectively, and so can be isolated with commercially available filters, for example the 600/14 nm and 700/13 nm interference bandpass filters from Semrock, Inc. Relative intensity of these two peaks could be interrogated under either x-ray excitation or using readily available 405 nm lasers. The latter would be essentially an RPL technique, the viability of which has been demonstrated for Sm^{2+}/Sm^{3+} combination in fluoroaluminate and fluorophosphate glasses for the purposes of x-ray imaging.[360] Pursuant to the above, it is also possible to selectively excite Sm^{2+} by targeting energies between the Sm^{3+} excitation peaks shown in figure 4.19b, although the inverse is not possible due to the broad nature of the $5d \leftarrow 4f$ excitations exhibited by Sm^{2+}.

As discussed in § 4.5.4, the $^5D_0 \rightarrow {}^7F_J$ transitions can be used to infer information about the symmetry of the Sm^{2+} site. Specifically, the strong presence of the $^5D_0 \rightarrow {}^7F_0$ transition (see figure 4.19c) indicates a non-centrosymmetric site. This implies either substitution on the A site, which is non-centrosymmetric in $NaMgF_3$, or perhaps on the B site with an adjacent charge compensation defect. The latter is considered unlikely on the basis of ionic radii and the lack of need for charge compensation in substitution of Sm^{2+} for Mg^{2+}. However, the ratio of the $^5D_0 \rightarrow {}^7F_1$ to $^5D_0 \rightarrow {}^7F_2$ intensity is inconsistent with that which might be expected for a low symmetry site.[40,359]

Emissions omitted from figure 4.21b, which are identified in § 4.10.2 and § 4.10.3, were fitted in the RL emission spectrum in order to identify the centre energies, but the resulting absorbed dose dependence of intensity was in all cases a combination of the two distinct behaviours modelled. This is because the spectral

fitting was undertaken primarily using the Lorentzian function given in equation 3.7b, which vanishes as the reciprocal of wavenumber with separation from C_1, rather than exponentially as does the Gaussian. More intensity is therefore shared with neighbouring peaks and so an Sm^{2+} peak cannot be reliably fitted for true intensity when closely surrounded by Sm^{3+} emission lines, and vice versa, at least using the methods employed herein. Omission of such peaks from the modelling does not change the physical interpretation of the $NaMgF_3$:Sm luminescence.

Taken at face value, the results of magnetisation measurements on sample J140307 would suggest that valence conversion is perhaps not as negligible as assumed in the charge kinetics model used in § 4.10.3 to describe the $NaMgF_3$:Sm dose dependency. Assuming the mechanism of conversion involves the Sm^{3+} capturing a conduction band electron into a valence band state, this could be described by introducing time dependence for M_1 and M_2. However, the physical significance of being able to fit this type of model to experimental data is arguably diminished with each additional free parameter. The gross features of the solutions to equations 4.7 through 4.11 are a consequence of the imbalance in M_1 and M_2, which will remain even if the model incorporates the implied transfer of about 10% of one population to the other.

4.11 $NaMgF_3$:Yb

$NaMgF_3$:Yb was included in the study in the hope of exploiting the simple energy level scheme of the $4f^{13}$ configuration to achieve a single narrow emission in the region of 1000 nm from the $^2F_{5/2} \rightarrow {}^2F_{7/2}$ transition, as has been achieved for other hosts.[245] While Yb^{2+} emissions from $NaMgF_3$:Yb have previously been reported,[55,264] little or no data for this host under x-ray excitation appears in the literature to date. Both Yb^{2+} and Yb^{3+} were observed in the one sample (J140305) fabricated.

4.11.1 Diffraction Data

In most regards the diffractogram for sample J140305 is typical of all samples in the study, a clear match for orthorhombic $NaMgF_3$ with trace MgF_2 and the same handful of additional unexplained low intensity reflections as seen in other samples. The YbF_3 dopant is not seen in the XRD pattern, nor is YbF_2, suggesting near complete integration of the 0.5% molar fraction introduced during preparation. A number of low intensity reflections which are not consistent with the reference patterns of either MgF_2, YbF_2, or YbF_3, nor seen in any other sample, remain unexplained. The position of these peaks are marked in blue in figure 4.23a.

4.11.2 Yb^{2+} Luminescence

The PL excitation and emission spectra for $NaMgF_3$:Yb are shown in figure 4.23b, in which only Yb^{2+} transitions are observed. Four broad peaks are clearly resolved in the excitation spectrum, which are assigned to $4f^{13}\left[{}^2F_{7/2}\right]5d \leftarrow 4f^{14}\left[{}^1S_0\right]$ interconfigurational transitions. Four free ion $5d$ states exist at comparable energies,[320] specifically $\left(\frac{7}{2},\frac{3}{2}\right)_J$ for $J = [2,3,4,5]$ in the parlance of Jj coupling[viii], but these cannot reasonably be assigned to the observed excitations in the absence of any definitive consideration of crystal field on the A site of $NaMgF_3$. This site is highly distorted, non-centrosymmetric, and a theoretical treatment of the resulting effect on the $5d$ orbitals is beyond the scope of this work. Accordingly, these levels have not been labelled in table 4.13 or figure 4.23b.

PL emission occurs in a single broad band centred at 24038 cm^{-1} (416 nm) which is asymmetric in wavenumber, but can be described by a superposition of two Gaussians centred at 23220 cm^{-1} (431 nm) and 24560 cm^{-1} (407 nm). The simplest interpretation of radiative relaxation from the lowest lying $5d$ state is

[viii] The notation $(J_0, j)_{J^*}$ describes the coupling of the total angular momentum of one configuration, J_0, with that of a single electron j in another, for a total momentum in the excited state of J. In this case, the promotion of an electron from the closed shell $4f^{14}$ configuration of Yb^{2+} to a $5d$ orbital leaves behind the ground state of the $4f^{13}$ configuration of Yb^{3+}, which has the term symbol $^2F_{7/2}$ under LS coupling. The lowest energy $5d$ electron has $j = 3/2$, and so the various possible couplings are denoted $\left(\frac{7}{2},\frac{3}{2}\right)_J$.

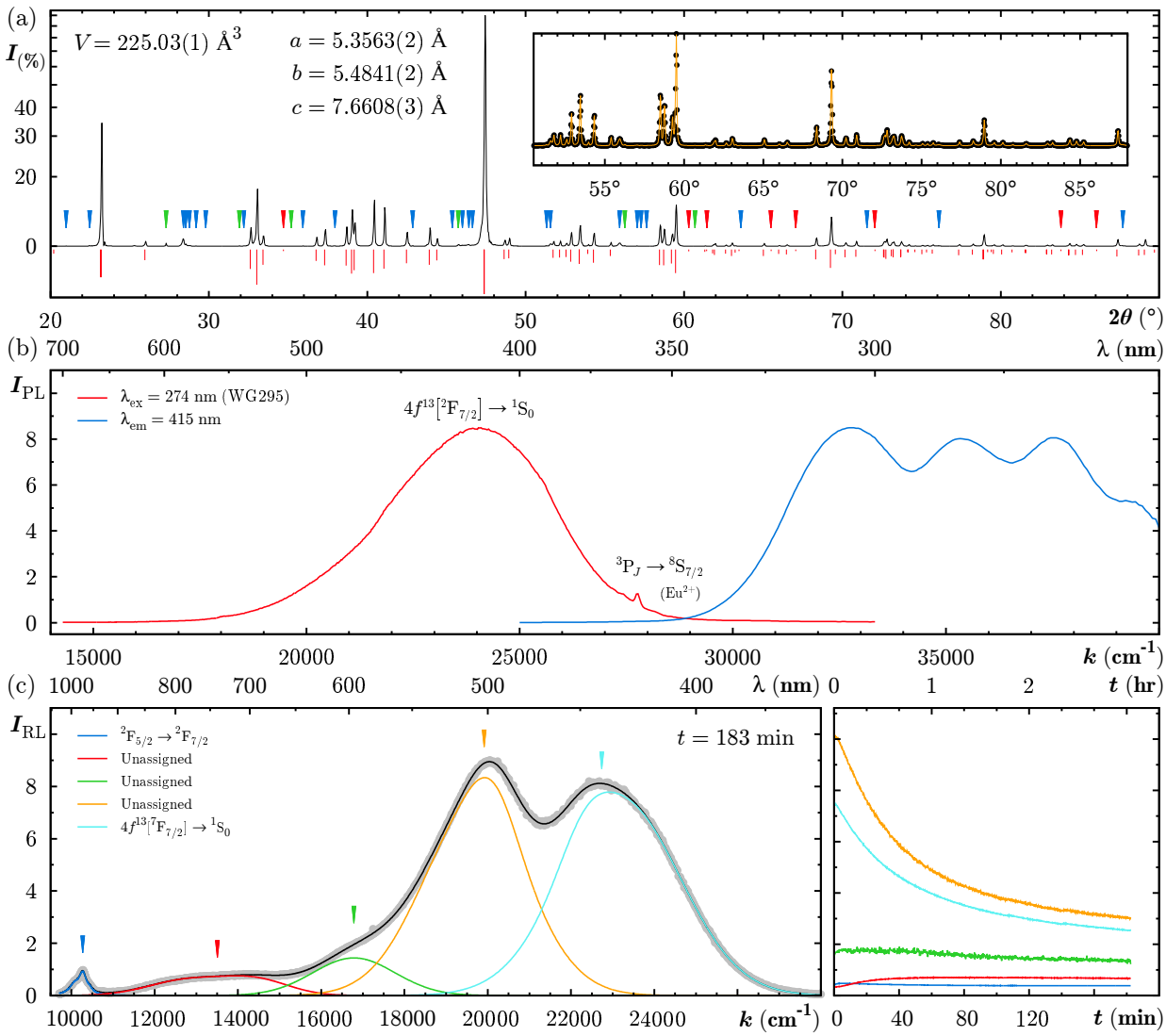

Figure 4.23: Basic characterisation measurements for $NaMgF_3$:Yb (J140305), including (a) XRD pattern, (b) photoluminescence spectra, and (c) fitted radioluminescence spectra. In (a), the experimental data is plotted (black) and the pseudo-Voigt fit (orange) illustrated in the inset, with markers over peaks which are missing from the reference pattern (red), explained by contaminants (green), and unexplained (blue). Markers in (c) are coloured to match the legend and the adjacent plot illustrating the time dependence of each RL emission.

excluded on the basis of a much larger Stokes shift than would be expected[364] from the systematic analysis of lanthanide luminescence in a range of inorganic hosts,[365] including $NaMgF_3$. The band emission depicted in figure 4.23b is instead thought to arise from either an intermediate impurity trapped exciton state,[55] or alternatively, from an intervalence charge transfer transition between paired Yb^{2+}–Yb^{3+} dopant sites.[366]

This same emission is observed in the radioluminescence emission shown in figure 4.23c, accompanied by at least three additional band emissions fitted at approximately 13500 cm^{-1} (740 nm), 16800 cm^{-1} (595 nm), and 19900 cm^{-1} (503 nm). The $^2F_{5/2} \rightarrow {}^2F_{7/2}$ emission of Yb^{3+} is also observed near 10270 cm^{-1} (974 nm). Evolution of intensity with absorbed dose for each emission is shown in the right hand axes of figure 4.23c, reflecting the usual energy dependent dynamics imposed by colour centre absorption, as observed across almost all materials reported herein. It is possible, despite the marked differences in response to accumulated dose, that the unassigned band emissions may also arise from the Yb^{2+} dopant site, perhaps from the delocalised bands to defect states or the 5*d* levels seen in the PL spectra.

If interpreted as exciton luminescence, the broad and asymmetric nature of the PL emission can be accounted for as two overlapping emissions deriving from the ground state and an excited state of the exciton, separated by approximately 1600 cm^{-1}. Near ultraviolet excitation is followed by non-radiative

relaxation to the excitonic states and then radiatively to the Yb^{2+} ground state $^1S_0$. This is substantiated experimentally by the observation that pulsed illumination at near infrared energies, which is expected to increase the population of the higher energy exciton state, enhances the higher energy component of the observed emission.[55]

The intervalence charge transfer interpretation assumes Yb^{2+} and Yb^{3+} are present in the host crystal predominantly in pairs. The process begins with an optical excitation from the Yb^{2+} ground state to the lowest lying e_g level of a $5d$ orbital, followed by a non-radiative charge transfer transition (Yb^{2+}–$Yb^{3+} \rightarrow Yb^{3+}$–$Yb^{2+}$) from the e_g state to a higher vibrational level of the $^2F_{5/2}$ excited state in the adjacent Yb^{3+} ion. Non-radiative relaxation down the $^2F_{5/2}$ vibrational levels ensues and is eventually followed by another optical excitation to a higher $5d$ level. From here the observable charge transfer emission occurs, to the ground state of the initial Yb^{2+} ion (Yb^{3+}–$Yb^{2+} \rightarrow Yb^{2+}$–$Yb^{3+}$). The large stokes shift arises from the relative displacement of each ion in the reaction co-ordinate. This is perhaps better illustrated with reference to the corresponding configurational co-ordinate diagram in the literature.[366] Near edge x-ray absorption fine structure spectroscopy has shown that the ratio of Yb^{3+} to Yb^{2+} sites in $NaMgF_3$:Yb is 1.8 ± 0.5 in favour of Yb^{2+} for crystals with similar nominal dopant concentrations.[367] This is sufficiently close to unity for Yb^{2+}–Yb^{3+} pairs to conceivably dominate the luminescence properties.

It was not possible to measure PL lifetimes as a suitable excitation source did not exist. Lifetimes on the order of milliseconds are reported in the literature at cryogenic temperatures,[55,264] but shorter at room temperature.

4.11.3 Yb^{3+} Luminescence

As the $4f^{13}$ configuration of the Yb^{3+} ion has only one excited state, no intraconfigurational transitions were observed in the PL spectra for this valence. This is because in the region of 10000 cm^{-1}, the $^2F_{5/2}$ level is beyond available excitation range. The emission would be expected to occur at approximately the same energy.

The $^2F_{5/2} \rightarrow {}^2F_{7/2}$ transition is clearly resolved in the RL emission spectrum, and might be estimated with reference to figure 3.6 to be of similar peak intensity to the Yb^{2+} emission if the instrument spectral response were corrected. This line emission is attributed to Yb^{3+} as the closed shell $4f^{14}$ configuration of Yb^{2+} admits no such intraconfigurational $4f$ transitions. Multiple Lorentzians are required to fit the emission, but no clear structure is resolved within the resolution limit of the CCD spectrometer. It was not possible to perform higher resolution measurements as the spectrometer used for other trivalent rare earths has a low energy limit of 11250 cm^{-1}. The centre energy for the fitted emission is 10261 cm^{-1} (975 nm), which is the best available estimate of the energy if the $^2F_{5/2}$ level in $NaMgF_3$. For completeness, the levels are summarised in table 4.14.

4.11.4 Discussion

At 400 nm, the broad emission from Yb^{2+} in $NaMgF_3$ is remarkably well aligned with the peak photosensitivity of bi-alkali (Sb-K-Cs) photocathodes typically found in photomultipliers designed for single photon

State	Energy (cm^{-1})	Method	Emissions	Energy (cm^{-1})
—	39370	EX	—	—
—	37594	EX	—	—
—	35336	EX	—	—
—	32787	EX	$4f^{13}\left[^2F_{7/2}\right]5d^1 + e^- \rightarrow 4f^{14}\left[^1S_0\right]$	24038
$^1S_0$	0	—	—	—

Table 4.13: Summary of energy levels for Yb^{2+} in $NaMgF_3$ and emissions observed for this species in sample J140305. The average emissions energies are tabulated for transitions observed in both PL and RL. Energies were determined with reference to the reported excitation spectrum (EX) and emission spectrum (EM).

counters. $NaMgF_3$:Yb might therefore have utility as an OSL phosphor. Unfortunately, the relatively high energy of this emission is less suited to fibre coupled dosimetry applications involving RL emissions as it overlaps both the F–centre absorption in the host and the highest Čerenkov radiation intensities expected at visible wavelengths.

Of all the materials covered in this chapter, $NaMgF_3$:Yb provides the only emission with near complete overlap to the $^3T_{1g}(^3P) \leftarrow {}^3A_{2g}(^3F)$ excitation of Ni^{2+}. It might potentially be used to sensitise $NaMgF_3$:Ni by radiative transfer of energy between Yb^{2+} and Ni^{2+} if very lightly co-doped. The additional rare earth dopant would likely have very little detriment in terms of radiological properties, if introduced at concentrations an order of magnitude lower than typical of the materials in this study.

The single Yb^{3+} emission has been exploited in SiO_2 as an emission in a relatively Čerenkov free region of the optical spectrum.[245] It might be argued that the wide band 1600 nm emission from $NaMgF_3$:Ni has more to offer in this regard, but the latter requires the use of silica fibre. ESKA GH4001 polymer optical fibre has a window of marginally viable attenuation at the Yb^{3+} emission wavelength, and so of all materials in this study $NaMgF_3$:Yb provides the lowest energy optical emission which is in any meaningful way compatible with polymer optics. significantly cheaper and easier to work with, but also a dosimetric advantage as the radiological properties of silica glass are less favourable.

4.12 $RbMgF_3$:Eu

$RbMgF_3$:Eu was included in this study for the sole purpose of providing comparative data for the evaluation of energy dependence in MV photon radiations. The material is severely water inequivalent regardless of the dopant fraction, with Z_{eff} of 31 and the corresponding relative energy response to photons inflated by at least one order of magnitude in the keV regime, with respect to $NaMgF_3$. Basic characterisation data is included here to provide context for results presented in chapter 6.

PL emission and excitation spectra for $RbMgF_3$:Eu are shown in figure 4.24a, in which the spectral features corresponding to $4f$ intraconfigurational transitions are comparable to those observed in $NaMgF_3$:Eu, and are assigned similarly. The interconfigurational $4f^6\left[{}^7F_0\right]5d(E_{1g}) \rightarrow {}^8S_{7/2}$ band emission is extremely weak when excited at 37000 cm^{-1}, but is seen in the RL emission near 25000 cm^{-1}. Differences in the relative intensity of the line and band emissions in $RbMgF_3$:Eu with respect to $NaMgF_3$:Eu arise from differences in the crystal field environment, which influences the energy difference between the lowest e_g splitting of the $5d$ levels and the ^6P_J multiplet.

In the RL emission shown in figure 4.24b, both the aforementioned Eu^{2+} luminescence and significant Eu^{3+} luminescence are observed. As was discussed in § 4.5.4, the relative intensities of the $^5D_0 \rightarrow {}^7F_J$ transitions can be used to infer information about the symmetries of the crystal field. In comparison to $NaMgF_3$:Eu, the relative magnitude of the $^5D_0 \rightarrow {}^7F_2$ and $^5D_0 \rightarrow {}^7F_1$ intensities are reversed and the $^5D_0 \rightarrow {}^7F_0$ emission is much more prominent in $RbMgF_3$:Eu. This suggests a higher symmetry site of integration than for $NaMgF_3$, but still one lacking an inversion centre. This is consistent with integration on either of the hexagonal perovskite A sites in $RbMgF_3$, both of which are of higher symmetry than the distorted A site in $NaMgF_3$.

For applications tolerant of the radiological properties of the $RbMgF_3$ host crystal, $RbMgF_3$:Eu is a potentially useful optical radiation detector. A high effective atomic number renders it of relatively high sensitivity, and the dominant emission arising from the ^6P_J has quite narrow spectral bandwidth.

State	Energy (cm^{-1})	Method	Emissions	Energy (cm^{-1})
$^2F_{5/2}$	10261	EM	$^2F_{5/2} \rightarrow {}^2F_{7/2}$	10261
$^2F_{7/2}$	0	—	—	—

Table 4.14: Summary of energy levels for Yb^{3+} in $NaMgF_3$ and emissions observed for this species in sample J140305. Energies are for transitions observed in the RL emission (EM) only.

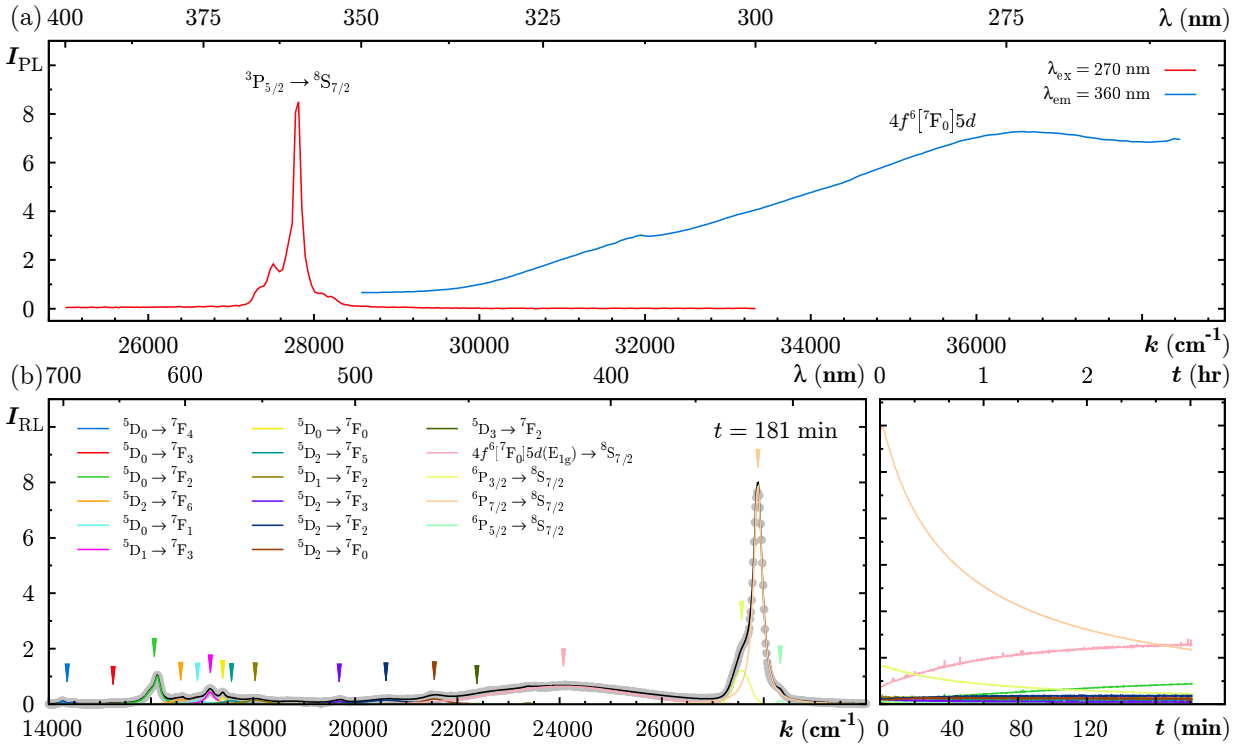

Figure 4.24: Basic characterisation measurements for $RbMgF_3$:Eu (AE00562), including (a) photoluminescence spectra and (b) fitted radioluminescence spectra. Markers in (b) are coloured to match the legend and the adjacent plot illustrating the dependence of each RL emission.

4.13 $RbMgF_3$:Mn

The PL and RL spectra for $RbMgF_3$:Mn are presented in figure 4.25. At the indicated excitation energy, a single emission band is observed with a centre energy about 100 cm^{-1} lower than for the lowest energy emission reported for $NaMgF_3$:Mn. Given the susceptibility of the 3*d* energy levels to the local crystal field, this similarity in emission energy is taken as strong evidence for integration on the *B* site in both hosts, the *A* sites of $NaMgF_3$ and $RbMgF_3$ being vastly dissimilar (see figure 3.1). The spectra shown in figure 4.25a are for one of two inequivalent *B* sites (see § 3.1.1 and figure 3.1b). If the PL emission is excited in the region of 405 nm rather than at 396 nm, then the $^4A_{1g}(^4G) \leftarrow {}^6A_{1g}(^6S)$ excitation occurs predominantly for the other *B* site and emission appears at an energy increased by the better part of 1000 cm^{-1}, as is reported elsewhere.[2, 193]

Excitation by x-rays is not site selective and so the RL emission band is the composite of these two emissions, as depicted in figure 4.25b. When fitted with Gaussian functions the lower energy emission is centred at 16880 cm^{-1}, more or less in agreement with the site selective PL emission at 16920 cm^{-1}, while the inequivalent *B* site emission was fitted at 17670 cm^{-1}. The relative intensities of these fitted emissions and their near identical response up to approximately 20 kGy, as shown in the right hand axes of figure 4.25b, might suggest comparable levels of site occupancy if a similar oscillator strength is assumed for each. Under this assumption, a tentative assignment of the emission at 17670 cm^{-1} to the corner sharing *B* site might be made simply on the basis of a lower emission intensity for half the number of these sites existing than of those sharing faces.[263] This emission energy is also consistent with that observed in $NaMgF_3$:Mn, where all MnF_6 octahedra are corner sharing. However, without any indication of the relative oscillator strengths this is speculative at best.

$RbMgF_3$:Mn was included for the same reasons as was $RbMgF_3$:Eu, to provide comparative data for evaluation of energy dependence of the $NaMgF_3$ based materials in MV x-ray radiations. The relevant data is presented in § 6.5. Similarly to $RbMgF_3$:Eu, it was found that the higher effective atomic number renders the material of much higher sensitivity than $NaMgF_3$:Mn.

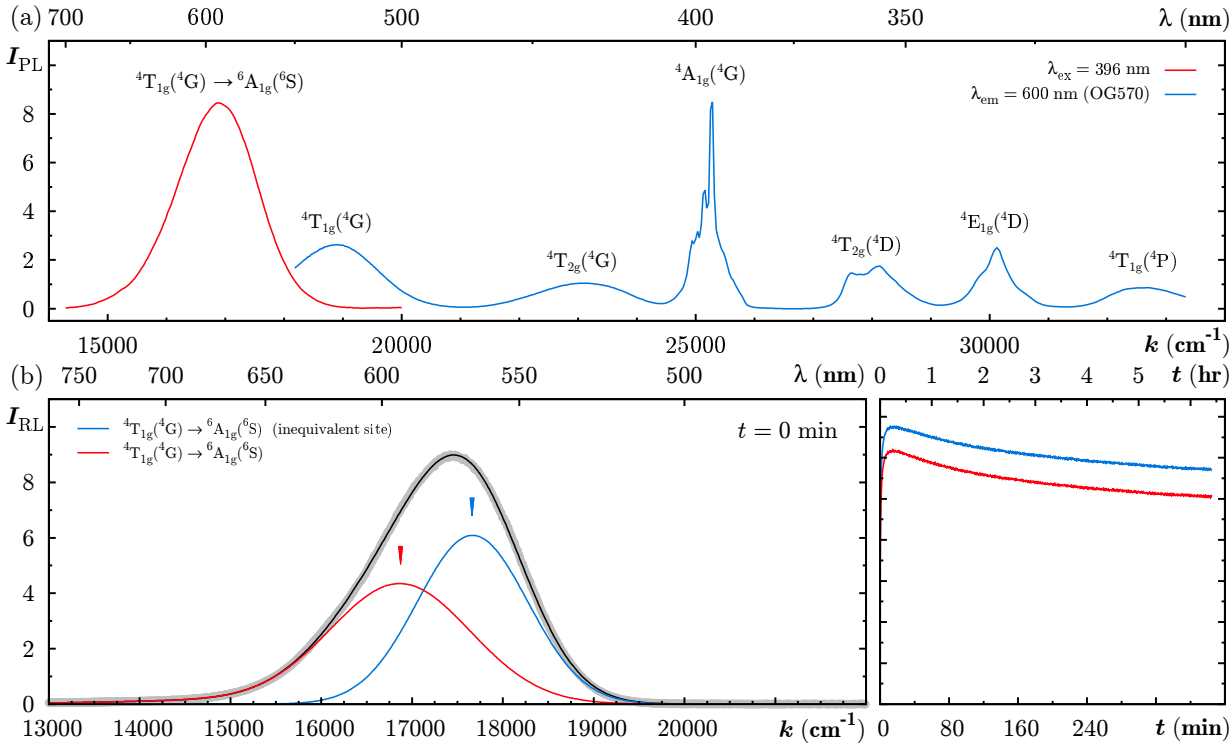

Figure 4.25: Basic characterisation measurements $RbMgF_3$:Mn (AE00327), including (a) photoluminescence spectra, and (b) fitted radioluminescence spectra. The latter depicts a single asymmetric band fitted by two Gaussians, representing the individual emissions of Mn^{2+} on each of the corner sharing and face sharing perovskite B sites depicted in figure 3.1b.

4.14 Common Experimental Findings

A small number of experimental features are common to all samples, regardless of dopant. These are briefly detailed in this section.

4.14.1 X-ray Diffraction

Of the numerous low intensity unassigned reflections reported in this chapter, a handful were seen at consistent positions in the majority of samples. These positions are 20.96°, 22.45°, 25.28°, 29.76°, 31.91°, 37.92°, 42.84°, 45.76°, 46.01°, 46.37°, 50.82°, 51.56°, and 72.60°. In addition, a consistent set of very low intensity reflections found in all the ICDD datasets included in the reference pattern were consistently absent from the experimental data for all samples. These are 34.70° [021], 60.30° [223], 63.47° [303], 65.49° [105], 67.05° [322], 72.05° [141], 83.80° [206], and 86.05° [216]. These discrepancies attest to minor phase impurity, albeit at a level which is unlikely to invalidate the interpretation of spectral data reported herein, and which does not unacceptably compromise the optical quality of most samples.

This is perhaps not surprising, given the difficulties in maintaining precise stoichiometry during sample preparation. In all samples, strong evidence for excess MgF_2 was seen, with many of the higher intensity reflections from ICDD patterns 00-041-1443 and 04-003-0647 discernible. An attempt was made to fabricate magnesium poor neighbourite, Na_2MgF_4, using the method described in § 3.1.3 in the hope that experimental diffraction data on such a sample might show some correlation with the aforementioned anomalous reflections. Only $NaMgF_3$ with excess NaF was obtained.

It is considered likely that the crystal fabrication techniques used here will not deliver much higher purity $NaMgF_3$, given the disparity in melting points of NaF, MgF_2, and the various dopant fluorides. A small quantity of white powder was found deposited on the crucible lid as each sample was removed from the furnace, suggesting vapour loss of some fraction of the precursor fluorides. This would imply the crystal melt is in contact with the vapour phase of at least one of the constituent compounds, a situation expected

to promote non-stoichiometry in the crystal produced.[368]

4.14.2 Thermoluminescence Glow Curves

Glow peaks observed consistently across the majority of samples for which TSL measurements were possible are those at temperatures of 267 ± 17 K, 305 ± 20 K, 357 ± 17 K, 422 ± 11 K, 536 ± 12 K. The uncertainties stated here represent the range of fitted T_{m} across all samples. They are considered in agreement within the limitations of the temperature control and monitoring of the experimental apparatus, in which the control system can only apply heat and is subject to different thermal inertia and cooling power for each sample.

That some glow peaks are specific to each sample while others are common across all samples would suggest that a number of different types of trapping defect are present. Glow curve features common to all samples can probably be attributed to the host, and some may correspond to the colour centres discussed in § 4.1.2. Those seen only in specific samples are presumably related to or promoted by the presence of the dopant ion. Variations in crystal fabrication conditions and technique may also play a role.

The intense room temperature TSL observed in $NaMgF_3$:Er, $NaMgF_3$:Pr, $NaMgF_3$:Sm, and to a less extend in $NaMgF_3$:Eu and $NaMgF_3$:Mn, is expected to exacerbate temperature dependence of RL intensity. This was observed to some extent for $NaMgF_3$:Mn, for which the RL intensity was found to depend not only on T, but also on $\mathrm{d}T/\mathrm{d}t$. Such behaviour is a barrier to applications in radiotherapy dosimetry, where measurements are performed at room or body temperature.

A significant reduction in low temperature glow peak intensity following sintering and rapid quenching has been demonstrated[187] for $NaMgF_3$:Eu. As inferred by the models presented in § 4.8.2 and § 4.10.3, the F–centre is thought to participate in electron trapping, and the shallow traps producing room temperature TSL are perhaps F–centre aggregations.[187] These would be expected to dissociate during sintering. The crystals to which this technique was applied were fabricated using the same slow cooling method, and so a similar technique might reasonably be attempted to reduce this difficulty in any such $NaMgF_3$ based sample. However, if the assignment of low temperature TSL peaks to F–centre aggregates is correct, the radiation induced absorption data presented in § 4.1.2 represents strong evidence that any gains would eventually be lost after further exposure to ionising radiation.

4.14.3 Anomalous Radioluminescence

The overwhelming majority of RL emission spectrum features were attributable to the dopant or a contaminant co-dopant, except for sample J140401 ($NaMgF_3$:Nd) in which a number of unexplained emissions were observed at visible wavelengths. A single common anomalous emission, a weak and broad band in the region of 500 nm, was observed for $NaMgF_3$:Cr, $NaMgF_3$:Er, $NaMgF_3$:Eu, $NaMgF_3$:Nd, and $NaMgF_3$:Sm, and may be present yet masked by the dopant emission in all other samples. The energy of this emission is probably too low to attribute to colour centre luminescence. No such emission was observed in the PL emission of any samples, and so no corresponding excitation spectrum or emission lifetime could be measured.

4.15 Summary

A substantial body of spectroscopic, magnetisation, and powder diffraction data has been presented in this chapter, constituting the basic experimental characterisation of 10 different luminescence species in $NaMgF_3$. This work has led to the selection of a small subset of these materials which merit further investigation, specifically $NaMgF_3$:Eu, $NaMgF_3$:Mn, $NaMgF_3$:Ni, and $NaMgF_3$:Sm, for the reasons discussed in § 4.5.4, § 4.6.3, § 4.8.3, and § 4.10.5 respectively. At the time of this materials characterisation work, some experience with both $NaMgF_3$:Eu and $NaMgF_3$:Mn was already available from the earlier MV x-ray characterisation, and the corresponding data presented in chapter 6 also supports this selection.

Chapter 5

Point Dosimeter Prototypes

The radiotherapy clinic is an environment somewhat removed from the laboratory, with research and development efforts accommodated after patient treatments, quality assurance checks, repairs, and preventative maintenance. A typical radiotherapy physics experiment is necessarily assembled, executed, and torn down within hours, with data analysis undertaken after the fact. Hardware which is portable, repeatable, quick to set up, and efficient to operate, is therefore a significant asset. The design of a practical fibre coupled dosimetry system is thus as much an undertaking in engineering and ergonomics as it is of science.

As indicated in section § 2.4, a fibre coupled dosimeter consists of both a suitable luminescent dosimeter material and an optical readout platform to support recording of the luminescence signal. While much emphasis is appropriately placed on the materials science and characterisation undertaken in this study, the design of the prototype dosimeter systems utilised is also due some attention. This chapter is dedicated to the substantial engineering efforts undertaken to realise these systems.

5.1 Mk-II Prototype

The system with which the majority of radiotherapy characterisation experiments have been undertaken will be referred to herein as the the Mk-II prototype, Mk-I being a proof of concept device which predates this work. Mk-II was conceived and assembled at the crown research institute Industrial Research Limited by the Radiation and Imaging Detection Group prior to the commencement of this study. A diagrammatic overview is given in figure 5.1d.

This system was eventually dismantled for components usable in the Mk-III prototype.

5.1.1 Detector and Readout System

The Mk-II prototype was built around a Hamamatsu H5783P photomultiplier module, a Hamamatsu C9744 photon counting unit, and the USB-6008 DAQ from National Instruments. The H5783P is a sealed module integrating a bi-alkali (Sb-K-Cs) photomultiplier head and a Cockcroft-Walton voltage multiplier circuit. It is operated from a low voltage DC power supply. The voltage multiplier is referenced from an external DC control voltage in the range of 250 mV to 900 mV which linearly sets the photocathode high potential. Transistors are used in the divider stages for dynodes nearest to the anode to minimise the impact of higher photocurrents on linearity.[256, 369] The photocathode quantum efficiency is shown in figure 5.1a.

This photomultiplier module was housed in a blackened alloy casing into one end of which the signal fibre was installed. An adjustable space exists for several 25 mm diameter circular filters between the fibre face and the photocathode. Filters were secured against the photomultiplier casing, which was allowed to move along the fibre axis when not retained by a grub screw. This arrangement was eventually discovered to have a significant detrimental impact on reproducibility of system sensitivity across filter exchange as the distance between the fibre exit face and the detector entrance window could not readily be reproduced.

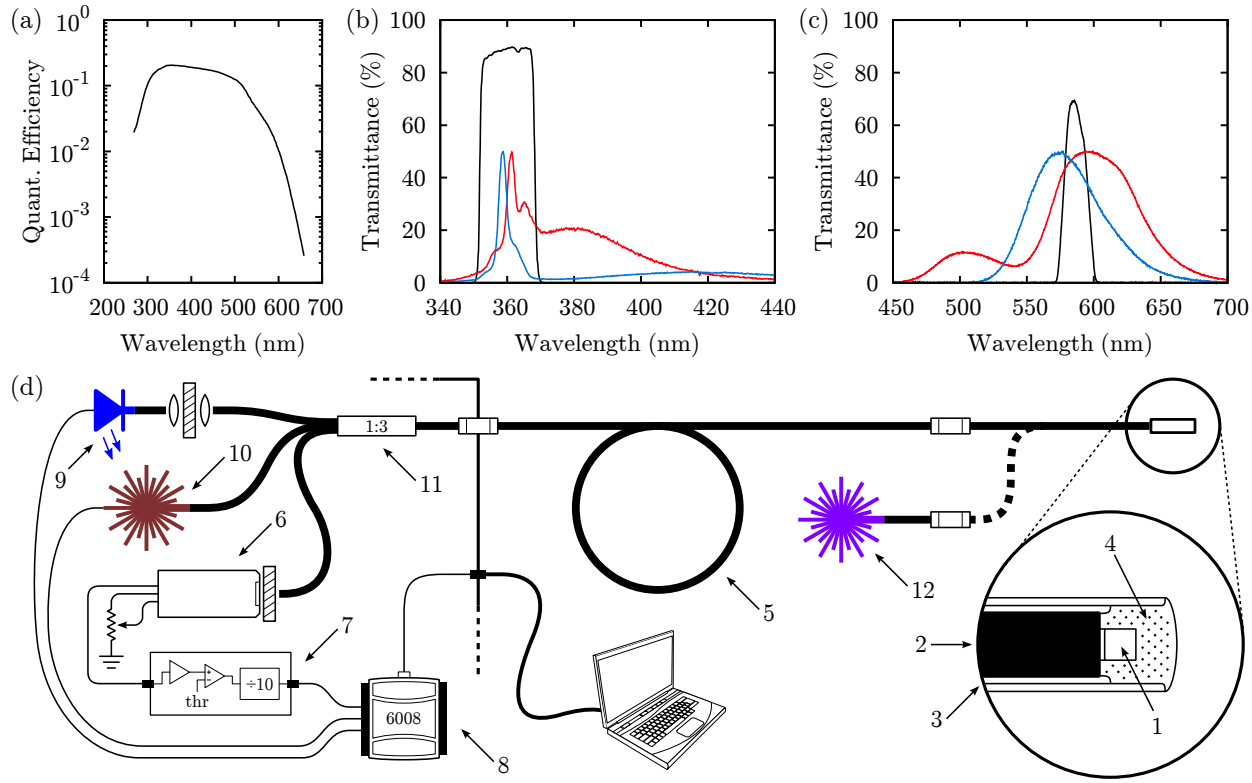

Figure 5.1: Optical characteristics of Mk-II prototype including (a) photocathode quantum efficiency, and the transmittance of (b) the 360/12 nm and (c) 590/20 nm band pass filters. A simplified schematic of the Mk-II system is shown in (d). Coloured curves in (b) and (c) are radioluminescence emission spectra of Eu^{2+} and Mn^{2+} respectively, as measured in the $NaMgF_3$ (red) and $RbMgF_3$ (blue) host crystals. Dosimeter probes consist of (1) the luminescent crystal glued to (2) polymer fibre optic, sealed with (3) heatshrink tubing and (4) epoxy resin mixed with graphite. The (5) silica extension fibre guides photons to (6) the photomultiplier, the signal from which is processed by the (7) photon counting discriminator and (8) USB-6008 DAQ. Integrated light sources include (9) a 470 nm LED and (10) a 980 nm fibre coupled laser, coupled to the fibre train by (11) a 1:3 splice. Rapid bleaching is achieved with (12) an external 405 nm laser.

360/12 nm and 590/20 nm band pass interference filters were used to isolate the Eu^{2+} and Mn^{2+} emissions respectively, somewhat improving the detected ratio of radioluminescence to Čerenkov photons. This type of filter typically possesses a remarkably well defined pass band, while maintaining stop band transmittance on the order of 10^{-5}, at least across the sensitive range of the photomultiplier used. The 360/12 nm filter is also transparent in the near infrared (not shown). Transmittance spectra for each filter in the region of the relevant emission are shown in figure 5.1.

The assembly of the photomultiplier and filter(s) was itself contained within a grounded aluminium enclosure providing a measure of electromagnetic screening from the remainder of the electronics. A multi-turn potentiometer was mounted on this screen to set the photomultiplier control voltage, nominally held at 800 mV for a gain of approximately 10^6. Exchange of filters was a somewhat involved task, requiring three different tools and the removal and refitting of up to 13 fasteners.

Discrimination was performed by the Hamamatsu C9744 photon counting unit. This is a self contained unit which employs a wide band video amplifier directly coupled to a high speed comparator, with emitter coupled logic used to achieve the required speeds in the digital back end. Prescaling by a factor of 10 was provided by this unit, reducing the speed of the output signal to count rates accommodated by the USB-6008 DAQ. Theoretical linearity of the counting system extended at least to 10^5 cps,[256] with a resolution and fundamental noise floor of 10 cps imposed by the prescaler. Typical mean dark count rates were in the region of 10–20 cps.

Data retrieval was managed by a LabView application which plotted time resolved data in real time and saved the sequence of samples to disk in text format.

Figure 5.2: Photograph of the Mk-II prototype with the built in 470 nm LED source in operation.

5.1.2 Dosimeter Probes and Optics

The active fluoroperovskite element of each dosimeter probe was a cut and polished cube of crystal 1 mm on a side. This was mounted at the tip of a short length of the now obsolete Mitsubishi ESKA EH4001 polymer optical fibre, core diameter of 980 μm. Samples AE00327 ($RbMgF_3$:Mn), AE00519 ($NaMgF_3$:Eu), AE00562 ($RbMgF_3$:Eu), and AE01020 ($NaMgF_3$:Mn) were used. Crystal and fibre were bonded using ethyl cyanoacrylate adhesive which cures with usable transparency to visible light[370] and has a nominal refractive index of in the range of 1.43 to 1.49,[371] intermediate to that of $NaMgF_3$ and the PMMA fibre core (see figure 2.8). To protect the mounted crystal the fibre tip was encased in heatshrink and the end filled with an opaque mixture of epoxy resin and graphite. An inactive probe for the quantification of stem signal was constructed in exactly the same manner except for the omission of the fluoroperovskite crystal. With the exception of the two fluoroperovskite samples containing rubidium, all of these materials used in the dosimeter probe construction are low atomic number compounds. These probes are referred to herein as the first generation dosimeter probes, as pictured in figure 5.3.

Between the dosimeter probe and the detector, 20 m of silica fibre were required to traverse the distance from the accelerator isocentre to the shielded control area where the prototype could be set up. Ideally, this fibre extension would be a continuous length with core diameter and NA matched to that of ESKA EH4001 in order to minimise insertion losses. In practice, four prefabricated 5 m patch leads of Thorlabs BFL37-600 polymer clad silica, NA of 0.37 and core diameter of 600 μm, were more easily obtained. As these patch leads were designed for use at infrared wavelengths it was necessary to jacket each in an additional layer of heatshrink to prevent pickup of ambient light.

To facilitate OSL experiments the Mk-II system was fitted with two light sources, a 470 nm LED and 980 nm fibre coupled laser. These sources were installed mid-2012 at Industrial Research Limited, at which time the ESKA EH4001 inactive fibre was lost and replaced with a comparable length of ESKA GH4001. Injection onto the transmission fibre was achieved using a four port polymer fibre splice permanently installed in the dosimeter. Losses due to this splice, mismatched NA and core diameter, additional SMA couplings,

Figure 5.3: Photograph of first generation dosimeters used in conjunction with the Mk-II prototype for radiotherapy characterisation measurements. Each consists of a length of ESKA EH4001 polymer optical fibre mounted with a 1 mm^3 sample of $NaMgF_3$:Eu, $NaMgF_3$:Mn, $RbMgF_3$:Eu, or $RbMgF_3$:Mn. The active tip is isolated from ambient light by a heatshrink wrap and and epoxy resin mixed with graphite, while the proximal end of the fibre optic is SMA terminated. Nominal outer diameter at the probe tip is 4 mm.

and the poor ultraviolet performance of polymer optics tally in excess of 20 dB between the active dosimeter element and the photomultiplier. Actual figures are given in table 5.1. This does not include scattering losses in the multiple air interfaces in the filter assembly. As most of these losses are incurred in both directions OSL measurements using the light sources built into the Mk-II prototype proved completely unviable.

An external 405 nm laser source was used when rapid bleaching was required.

5.1.3 Practical Limitations

While the Mk-II prototype facilitated a useful body of experimental work, the system was severely limited in two regards. Foremost, it was not designed with the use of high energy x-rays in mind and so lacked any real facility for Čerenkov background correction. Consequently, only static irradiation geometries could be accommodated. In addition, due to the significant optical inefficiencies listed in table 5.1, achieving the desired statistical uncertainty in RL measurements required exposures of up to 10 Gy. For experiments involving multiple exposures, cumulative dose therefore reached levels where the relative effects of radiation damage often had to be corrected, resulting in increased uncertainty.

Further difficulties included the necessity for partial disassembly to change filters, being limited to time series acquisitions at 1 Hz, the elevated noise floor due to prescaling of counts, and the relatively poor reliability of the LabView based software. Overall system sensitivity did not repeat well between setups, precluding any attempt at absolute dosimetry or system calibration.

These difficulties were the primarily driving force behind the decision to invest in a further development cycle and create a third prototype.

	Loss (dB)
Core diameter mismatch	4.3
NA mismatch	2.6
SMA couplings	5.0
Attenuation loss	4.0
Source injection splitter	8.2
Absorption in adhesive	0.5
Total	24.6

Table 5.1: Summary of theoretical optical losses in the Mk-II optical train when operated in RL mode. Core diameter and NA mismatch are calculated using equations 2.35 and 2.36, and SMA insertion loss taken at an optimistic nominal value of 1.0 dB per coupling. Splitter and attenuation loss is estimated using manufacturer nominal data[372,373] for 1 m of EH4001 and 20 m of BFL37-600 at 360 nm, the wavelength of the Eu^{2+} line emission. Optical absorption in cured ethyl cyanoacrylate is as reported in the literature[370] for a 100 μm bond thickness measured at 400 nm.

Figure 5.4: Photograph of the second generation dosimeter probes used during testing of the Mk-III. Like those depicted in figure 5.3, a 1 mm^3 fluoroperovskite sample was used and the tip encapsulated in epoxy resin mixed with graphic powder. However, the heatshrink wrap was omitted for a nominal outer diameter of 2.2 mm. The probes pictured here were fabricated using ESKA GH4001 polymer optics, suitable for emissions between approximately 300 nm and 850 nm. BFL48-1000 was obtained for testing dopants with longer wavelength emissions.

5.2 Mk-III Prototype

Two objectives were sought in the design of the Mk-III system: to address as many of the difficulties described in § 5.1.3 as possible and to provide a platform with which the longer wavelength emissions of the materials discussed in chapter 4 could be further explored. Development and testing progressed alongside the scientific aspects of this work, nearing completion at a late stage in the project.

As is apparent through comparison of figures 5.1 and 5.5, the Mk-III is a much more complex and ambitious system, the completion of which proved impossible within the available time frame. Development and testing was undertaken for most of the key subsystems, detailed appendix in B and the remainder of this chapter, but did not progress to the stage of trials in megavoltage x-rays. The prototype is pictured in figure 5.7.

5.2.1 Dosimeter Probe Construction

Dosimeter probes used in testing the Mk-III system were functionally comparable to the first generation probes described in § 5.1.2, but have a smaller outer diameter. They were constructed using ESKA GH4001 polymer optics and 1 mm^3 sample volumes, with the end overfilled using a similar mixture of epoxy resin and graphite powder. Once cured, this encapsulation was sanded back to the fibre jacket radius of 1.1 mm, resulting in a flush probe with a rounded tip, as pictured in figure 5.4. Dosimeters of this construction are referred to herein as second generation dosimeter probes.

For the purposes of initial testing probes were fabricated without end encapsulation or with the tip ground back to expose the dosimeter. This was necessary as most testing was undertaken using 40 kVp x-rays, which lack the penetrating power to deposit a useful level of dose within the sensitive volume of properly sealed probes.

5.2.2 Optical Fibre Train

The optics of the Mk-II and Mk-III systems are broadly similar, the architecture being dictated by the common goal of connecting a selection detectors and light sources to a single dosimeter probe. In the Mk-III, the largest source of loss listed in table 5.1, the polymer fibre optic splitter, was removed from the internal optics and additional SMA ports provided on the rear of the enclosure for light sources. This allows for greater flexibility in optical configurations, including those which eliminate the splitter entirely when not required.

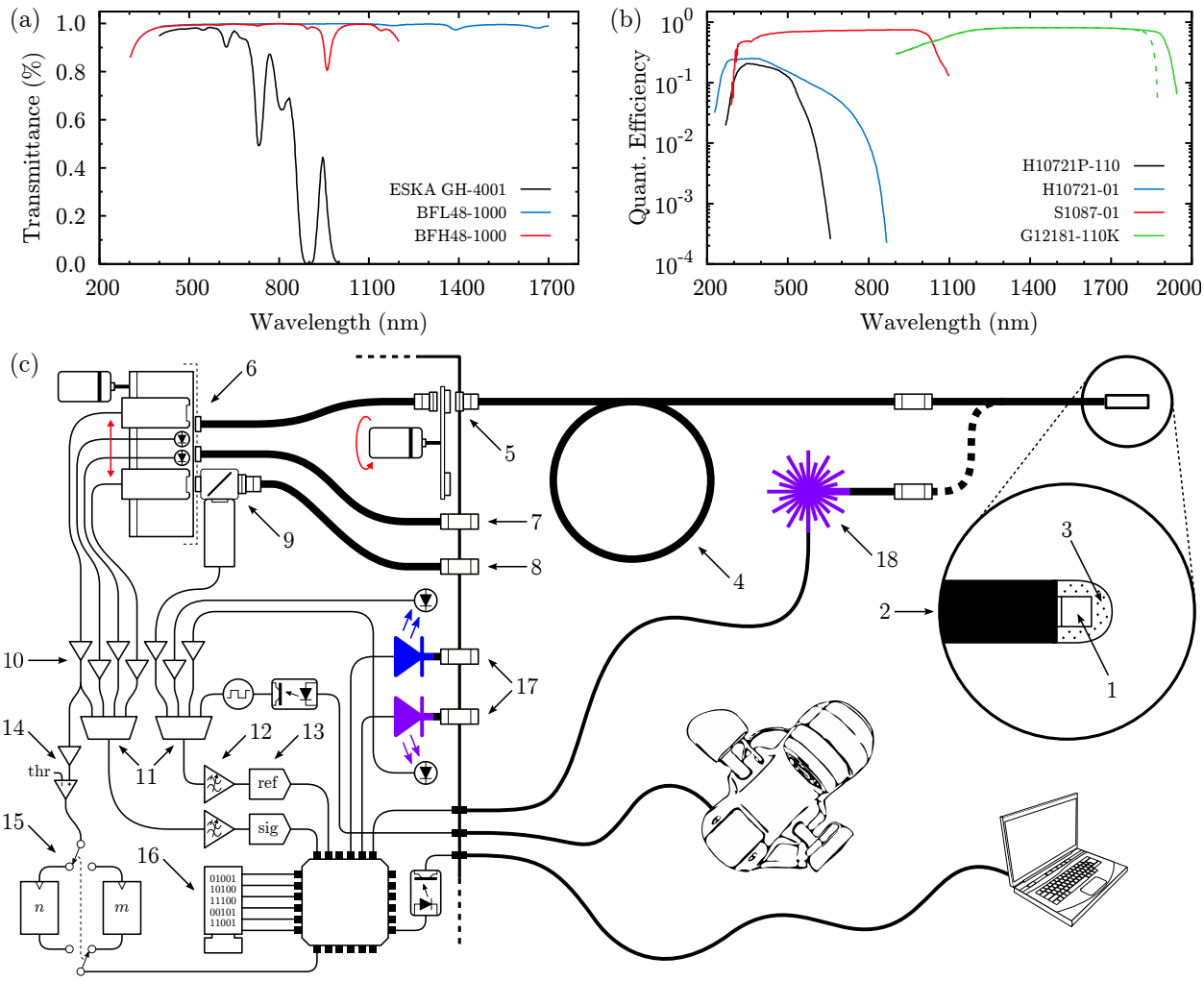

Figure 5.5: Optical characteristics of the Mk-III prototype including (a) transmittance of fibre optics used, and (b) detector quantum efficiencies. A simplified schematic overview of the system is shown in (c). Dosimeter probes consist of (1) the luminescent crystal bonded to (2) an optical fibre stem and encapsulated by (3) epoxy resin mixed with graphite. Luminescence is transported by (4) a silica extension fibre to (5) the filter carousel and (6) the detector array. Alternative routes for the luminescence signal include (7) a filter wheel bypass, and (8) a reference channel which delivers a portion of the light to (9) the reference photomultiplier. Electrical signal from photo-detectors drives (10) amplifier circuits, the output of which is routed via (11) analogue multiplexers and (12) anti-aliasing filters, to (13) a pair of synchronous analogue-to-digital converters. Signal from one of the photomultipliers may also be digitised using (14) the single photon discriminator and (15) high speed counters. Sampled data is stored in (16) buffer memory prior to readout. Light source include (17) monitored integrated LED light sources, and (18) an externally switched light source.

A continuous 20 m length of polymer clad silica fibre was used to transport luminescence emissions between the dosimeter probe and the detectors built into the prototype. Thorlabs BFL48-1000 and BFH48-1000 fibres were selected, both with NA of 0.48 and core diameter of 1000 μm. This fibre is well matched to ESKA GH4001 polymer optical fibre, which has NA of 0.50 and a core diameter at 980 μm, as can be readily achieved. Theoretical insertion loss is reduced from 9.9 dB to 0.5 dB, including the elimination of the three additional SMA couplings used to string patch leads together in the Mk-II system. These fibres are unfortunately notoriously difficult to work with and design around, due to the limited bending radius of 155 mm and a fluoropolymer buffer which cannot be stripped and so must be accommodated during termination.

Both the high OH (BFH48) and low OH (BFL48) variants of this fibre were obtained as neither is specified for operation at both extremes of the wavelength range to be accommodated (see figure 5.5a). With reference to the absorption co-efficient data given in figure 2.8b, it seems likely that the BFL48-1000 would suffice even in the near ultraviolet, and so this fibre was used for all optical interconnects permanently

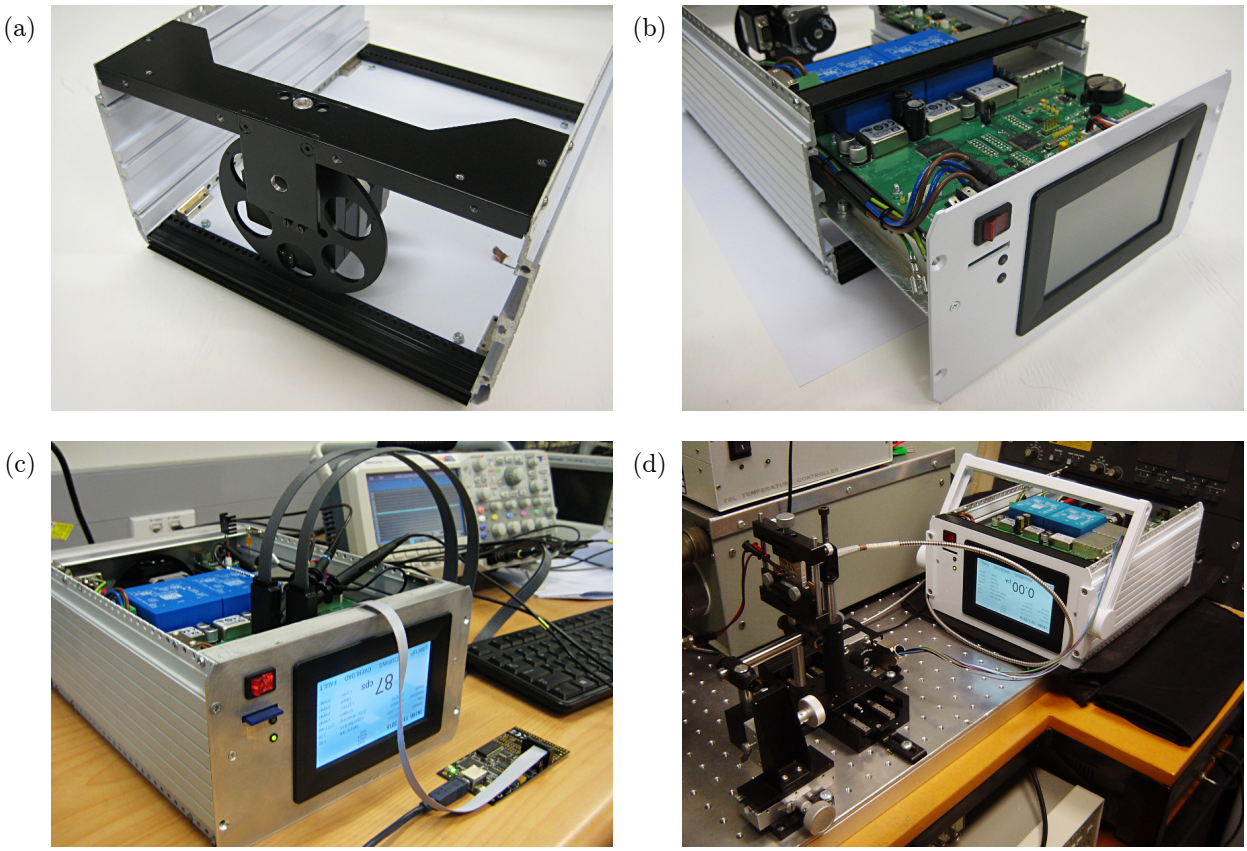

Figure 5.6: Selected photographs taken during development of the Mk-III prototype. These images depict (a) motorised filter wheel mounted on custom made alloy bracket, (b) ancillary electronics assembly being installed via the front of enclosure, (c) on-board computer attached to debugger and logic analyser during testing of buffer memory, and (d) testing of motorised components and detector optics in x-ray laboratory.

installed within the enclosure. For any portion of the fibre train exposed to radiation, the high OH variant may prove advantageous as BFH48 has been shown to exhibit a lesser magnitude of scintillation stem effect than BFL48.[228]

Six filters were housed in a rotating carousel between the proximal end of the transmission fibre and the detector array. The FRM 40-6-D25-HSM stepper motor driven filter wheel from OWIS GmbH was used, accommodating six 25 mm filters with positional accuracy better than 1°. An integrated hall effect sensor provided a positional reference from which the desired filter could be selected under software control.[374] A pair of small aspherical fused silica lenses were used to provide a collimated beam in which filters were positioned. Due to the large spot size presented by the 1000 μm optics, a loss up to 5.2 dB[i] was incurred when condensing the filtered light for injection into the upstream fibre. A bypass fibre was provided so that this loss need not be incurred if filters were not required.

5.2.3 Detector Array

The dopants listed in table 3.1 have emissions ranging from the near ultraviolet (Eu^{2+}, 360 nm) to the near infrared (Ni^{2+}, 1620 nm), for which no single detector technology is optimal. In order to cover this spectral range, four detectors were included in the design: the G12181-110K and S1087-01 semiconductor photodiodes and H10721P-110 and H10721-01 photomultiplier modules. All of these are manufactured by Hamamatsu Photonics.

The H10721P-110 photomultiplier module is the successor of the H5783P used in the Mk-II system, operating with a lower DC supply voltage but otherwise sporting the same form factor and what appears to be an identical photomultiplier head.[369,375] As seen in figure 5.1a, the Sb-K-Cs photocathode fitted

[i]This can be improved by using a smaller diameter fibre, measured at 2.2 dB for core diameter of 600 μm.

to these detectors is usable out to 650 nm, albeit with significantly impaired sensitivity beyond 550 nm. In conjunction with photon counting electronics, this detector delivers the highest sensitivity and dynamic range in the Mk-III system, despite having the lowest quantum efficiency. The H10721-01 module uses a multi-alkali (type S-20, Sb-Na-K-Cs) photomultiplier covering from 250 nm to 850 nm, but is not suitable for single photon counting.

In the near infrared, photomultiplier performance is comparatively poor and so solid state detectors were preferred, providing broadly comparable performance to infrared photocathodes at considerably less cost and physical size. Covering the visible and near infrared, the S1087-01 is a silicon PIN photodiode with an active area of 1.3×1.3 mm^2 and spectral sensitivity ranging from 320 nm to 1100 nm, peaking at 960 nm.[376] Operating further into the near infrared, the G12181-110K is an InGaAs PIN photodiode providing coverage out to 1950 nm, with a circular sensitive are of 1 mm diameter.[377] Both were operated in photovoltaic mode.

In the absence of reverse bias these photodiodes theoretically generate no dark current, but are still subject thermal noise. This can be modelled as Johnson current noise generated in a shunt resistance parallel with the photo-current source. The root mean square (RMS) magnitude of this noise current, $I_{j,\mathrm{rms}}$, is given by equation 5.1a in which B is the effective bandwidth in Hz, k the Boltzmann constant in J/K, T the junction temperature in K, and R_{sh} the shunt resistance in ohms.[378] R_{sh} is determined by measuring dark current at minimal reverse bias, typically 10 mV. It scales linearly with active area and is exponentially diminished by rising temperature.[258]

Under illumination, the generated photo-current from any of the aforementioned detectors exhibits shot noise, $I_{s,\mathrm{rms}}$. The RMS magnitude is given by equation 5.1b for the photo-current I in amperes, and bandwidth B in Hz, and elementary charge e in Coulombs.

$$\text{(a) } I_{j,\mathrm{rms}} = \sqrt{\frac{4BkT}{R_{\mathrm{sh}}}} \quad \text{(A)} \qquad \text{(b) } I_{s,\mathrm{rms}} = \sqrt{2BeI} \quad \text{(A)} \tag{5.1}$$

At room temperature the shunt resistance of the S1087-01 and G12181-110K photodiodes is approximately 250 GΩ and 5 MΩ respectively,[376,377] with corresponding $I_{j,\mathrm{rms}}$ of 0.3 fA and 57 fA for a bandwidth of 1 Hz. This low fundamental noise floor realised in photovoltaic operation together with the relatively high quantum efficiencies of these photodiodes can theoretically deliver comparable dynamic range to the photomultipliers. However, without the high levels of intrinsic gain provided by the electron multiplication process, the burden of realising this is instead placed on the preamplifier electronics. This is discussed further in § 5.2.4.

The elevated Johnson noise exhibited by the G12181-110K photodiode correlates with the smaller band gap of InGaAs required to achieve longer wavelength sensitivity. Selected devices in the G12181 series, including the G12181-110K, are provided with integrated Peltier coolers capable of lowering the junction temperature to at least 253 K, reducing $I_{j,\mathrm{rms}}$ by almost an order of magnitude. These devices were accommodated in the Mk-III design, despite being considerably bulkier, as they provide multiple means to improve SNR. Specifically, by reducing $I_{j,\mathrm{rms}}$ or increasing active area[ii] and cutoff wavelength for the same $I_{j,\mathrm{rms}}$. As cooling increases the band gap energy, the long wavelength limit of a given device is unfortunately reduced,[379] requiring accurate temperature control if the detected spectrum extends to lower energies. This was tested for Hamamatsu InGaAs photodiodes in conjunction with the $NaMgF_3$:Ni infrared emission, see appendix B.

As discussed in § 5.2.2, the Mk-III prototype contains no internal fibre splitters. The detectors described above were instead mounted side by side on a stepper motor driver linear stage, the LTM 60P-75 from OWIS GmbH, which aligned the desired device with the end face of the transmission fibre. An aluminium mount was designed to maintain precise alignment in the axis perpendicular to the motion of the linear stage. The mount also serves as a heat-sink for the Peltier cooled G12181-110K.

The LTM 60P-75 is specified for a bidirectional positional repeatability of 15 μm.[380] Misalignment on this scale is estimated using equation 2.37 to generate loss of at most 0.1 dB, and so theoretically imposes

[ii] R_{sh} scales more or less linearly with the sensitive area of a PIN photodiode.

Figure 5.7: Photograph of the Mk-III prototype.

a limitation on reproducibility at the level of 1–2%. With the motor controller programmed to always approach the target position from the same direction, optical reproducibility arising from positional error was measured at 0.6% (3σ) with the G12181-110K. The larger entrance window diameter of 8 mm featured by the photomultiplier modules does not demand such high positional accuracy of the linear stage.

An optical reference channel was provided by an additional H10721-01 photomultiplier module. This detector has a separate optical connection and was not mounted on the moving detector stage.

5.2.4 Acquisition and Readout System

A schematic overview of the Mk-III acquisition electronics is shown in figure 5.5c, illustrating the key components: analog front end, analog-to-digital converter (ADC), photon counting circuit, buffer memory, micro-controller unit, and a universal serial bus (USB) interface for communication with software running on a computer. The analog front end, ADC, and photon counter are physically separated in a shielded light-tight enclosure, and are referred to as the light-box electronics, while the remaining supporting hardware will be referred to as the ancillary electronics. This separation provides isolation for the sensitive light-box electronics from both external interference and from noisy ancillary components, such as stepper motor drivers.

At the dose rates of interest, the semiconductor detectors discussed in § 5.2.3 will typically yield photocurrents in the region of 10^{-12} A to 10^{-10} A when used in conjunction with the materials discussed in chapter 4. In order to be digitised, these small photocurrents must be converted linearly into a voltage mode signal and amplified to the level of a few volts, presenting a considerable challenge in the design of readout electronics. The photomultiplier tubes can be operated with internal gains of up to 10^7, with a corresponding reduction in gain required for the associated preamplifier.

Photocurrent from the S1087-01, G12180-110K, and H10721-01 detectors is fed directly into the virtual ground node of a transimpedance amplifier designed around a precision operational amplifier with very well controlled input bias current ($\sim 10^{-15}$ A). This permitted significant gain (10^9 was tested successfully) in

the first amplifier stage without generating unacceptable voltage offset.[378] After additional gain stages the voltage signal is applied to an analog multiplexer used to route the signal from any given photo detector onto the ADC. A switched capacitor filter prevents aliasing, with an adjustable corner frequency set by the firmware as appropriate for the programmed sample rate.

In order to accommodate photon counting operation, the signal from the H10721P-110 was first routed through a high speed preamplifier stage with relatively little gain. This stage employs an operational amplifier with a current feedback architecture, effecting current-to-voltage conversion while maintaining the wide bandwidth required to resolve individual photon pulses in the input photocurrent. At this point, the voltage mode signal is either buffered and routed to the ADC via an additional gain stage for acquisition under higher levels of illumination, or routed into an additional current feedback operation amplifier and to a high speed comparator. The comparator output drives a pair of 16-bit hardware counters, comprising a 4-bit high-speed synchronous counter cascaded with a 12-bit ripple counter. Only one counter operates at any given time while the other is gated off during readout, an arrangement which renders dead time negligible while enabling reliable readout of the ripple counter[iii].

Data from the ADC or photon counting system is buffered in on-board SRAM along with a 32-bit timestamp which denotes the time of capture since the start of acquisition, within the limits of precision imposed by the system clock (±16 ns). With 16 MB of buffer memory acquisition can run for approximately 2 minutes at the maximum sample rate of 10 kHz, to slightly over 2 weeks at the minimum sample rate of 1 Hz. The upper bound on sample rate of 10 kHz derives from both buffer memory limitations and the degradation in SNR incurred as the bandwidth of the transimpedance amplifier must also increase with sample rate. The use of a programmable anti-aliasing filter in the analogue signal pathway allows SNR to be recovered when high sample rates are not required.

Acquired data is retrieved via the USB interface by a Windows application and written to a text file. In order to avoid ground loops and the electrical noise that typically is incurred in sharing an electrical ground with a computer, the USB interface is implemented as a bus-powered USB-to-serial converter with the downstream serial port optically isolated from the on-board microprocessor.

5.2.5 Excitation Light Sources

Operation of three light sources is facilitated, two internal sources and a control signal for operating an external light source. Pulse width modulation (PWM) is used to program each source, with three adjustable parameters available: frequency, duty cycle, and linear ramp period. As can be seen in figure 5.5c, each of the built in light sources has a photodiode monitor with a dedicated reference channel which can be recorded simultaneously with the active detector, while an external light source can be monitored using the external optical reference channel. A frequency range of 1 Hz through to at least[iv] 10 KHz is supported, facilitating pulsed OSL studies[381] at lower frequencies and duty cycles while providing intensity control which is linear in optical power when operating at higher frequencies. A programmable linear ramp period is to facilitate linear modulated OSL[150,382] studies. Continuous wave OSL is achieved simply by setting the duty cycle to 100% and the frequency high. Both the built in light sources consist of a light emitting diode (LED) with a ball lens for coupling the light into optical fibres. Only one channel supports high power emitters.

While OSL is beyond the scope of this work, the inclusion of light sources increases the flexibility of the prototype, and by not coupling internal sources permanently into the optical train the insertion losses associated with injection are avoided when sources are not required. Of the more promising materials discussed in chapter 4, PL emission from both $NaMgF_3$:Ni and $NaMgF_3$:Sm can be efficiently excited by relatively cheap and compact 405 nm diode lasers. The inclusion of light sources in the design is therefore relevant also for RL applications, where an indication of the optical losses present for a given setup can be estimated, and perhaps corrected, by optically exciting the emission using a monitored light source. In the

[iii] The output of ripple counters is asynchronous, and so if read within one full chain propagation delay of the most recent count will return an inconsistent result.

[iv] Constrained to maintain resolution in duty cycle, can be higher if required for samples with shorter emission lifetimes.

case of the $^3T_{2g}(^3F) \rightarrow {}^3A_{2g}(^3S)$ emission of $NaMgF_3$:Ni, a typical InGaAs photodiode detector is completely insensitive to a 405 nm laser source suitable for efficient PL excitation. This has been demonstrated in appendix B.

5.2.6 Stem Signal Suppression

One of the major limitations of the Mk-II system noted in § 5.1.3 was a lack of means to suppress the Čerenkov and autofluorescence stem signal observed with fibre coupled dosimetry systems operated in MV x-rays. The Mk-III prototype has been designed to implement both temporal and spectral discrimination methods (see § 2.4.2), although neither has been properly tested at the time of this writing.

Temporal discrimination is to be facilitated by acquisition at sample rates well in excess of the accelerator pulse delivery rate, such that for an RL emission lifetime on the order of milliseconds only a small fraction of the converted samples will contain the prompt Čerenkov and autofluorescence. A monitor circuit consisting of an opto-isolator and D-type flip-flop was included, which generates a digital square wave with each edge corresponding to an x-ray pulse. This signal is acquired synchronously with the luminescence signal by routing it into the reference channel of the ADC, and can therefore be used to identify samples which contain prompt stem signal and so might then be discarded and interpolated. Testing of this target current monitor circuit is detailed in appendix B. It is possible that for the semiconductor detectors, higher gain requirements will translate into a bandwidth limitation in the analog front end, which precludes this in practice, but it should at least be possible to implement using photomultipliers in either current or photon counting mode.

Spectral discrimination as described in the literature[240–242] can be implemented by using, in principle, any of the four primary detectors in conjunction with the reference photomultiplier. Mechanical design has been undertaken to accommodate a small dichoric mirror to divert short wavelength luminescence to the reference photomultiplier while allowing the longer wavelengths to pass through to the light-box, see figure 5.5c. It would also be possible to implement an optically simpler arrangement in which the fibre train included an external splitter to illuminate both the reference photomultiplier and primary detector, but this arrangement has lower optically efficiency.

5.3 Summary

Two point dosimeter prototypes were involved in this work. The Mk-II system was used to perform the preliminary radiotherapy characterisation work reported in the following chapter, while the Mk-III system was developed to address the design limitations of the former. The Mk-III design was largely completed and tested (see appendix B) but has not yet been used to gather data at therapeutic x-ray energies.

Chapter 6

Radiotherapy Characterisation

This chapter details the experimental characterisation of a prototype dosimeter system in the radiation qualities of megavoltage external beam radiotherapy. The scope of this investigation was somewhat limited by the capabilities of the Mk-II system, foremost the lack of an effective means to suppress or isolate the optical stem signal. While much was learnt regarding $NaMgF_3$ in a fibre coupled dosimeter setting, no meaningful applications testing was possible as a result of this deficiency.

6.1 Dose History Dependence

Dependence of sensitivity on previously absorbed dose is one of the principal difficulties with inorganic radioluminescence dosimeters, second only to the Čerenkov problem. In the case of $NaMgF_3$ the two dominant causes are competition between trapping defects and recombination centres for delocalised charge carriers, and radiation damage to both the dosimeter and the optical train. The interaction of these processes has a relatively complex and non-linear influence on sensitivity as a function of absorbed dose. Charge kinetics and the implications for radioluminescence efficiency are discussed in § 2.2.4 and § 2.2.7. The primary mechanism of radiation damage is creation and amalgamation of F–centres, which is introduced in § 2.2.8.

6.1.1 Priming Irradiations

For the evaluation of the impact of sensitivity changes following exposure to radiation, a parameter of interest is the rate of change in RL sensitivity as a function of absorbed dose, denoted δ_L herein. This is defined as the first derivative of the observable surrogate for RL emission intensity, L, with respect to absorbed dose to water, D_w, normalised to the value of L at the dose of interest. Experimentally, δ_L is determined by localised curve fitting to luminescence measured under constant dose rate in order to analytically define $L(D_\mathrm{w})$, to which equation 6.1 is then applied. Dose to water is chosen as the most relevant yardstick in the context of radiotherapy. It is also more convenient to experimentally determine than dose to the luminescent material.

$$\delta_L(D_\mathrm{w}) = \frac{\mathrm{d}L}{\mathrm{d}D_\mathrm{w}} \frac{1}{L(D_\mathrm{w})} \qquad (\mathrm{Gy}^{-1}) \tag{6.1}$$

Previously unexposed dosimeters exhibit initial δ_L on the order of 1% per Gy of absorbed dose, represented by the initial portion of the dose-sensitivity curves presented in figure 6.1. These plots show the response of all four first generation dosimeter probes to 6 MV and 10 MV FFF under constant dose rates of 17.7 Gy/min and 74.7 Gy/min respectively. This level of dose history dependency is untenable even for more typical dose rates of a few Gy/min occurring in radiotherapy treatments, but was reduced substantially below 0.1% per Gy after priming doses, $D_\mathrm{w,p}$, on the order of 1 kGy. The experimental values of δ_L are given in table 6.1 at the initiation and termination of priming irradiation. In the case of the Eu^{2+} activated samples AE00519 and AE00562, saturation occurs after doses comparable to that for which the OSL linearity of these samples is known to fail.[187]

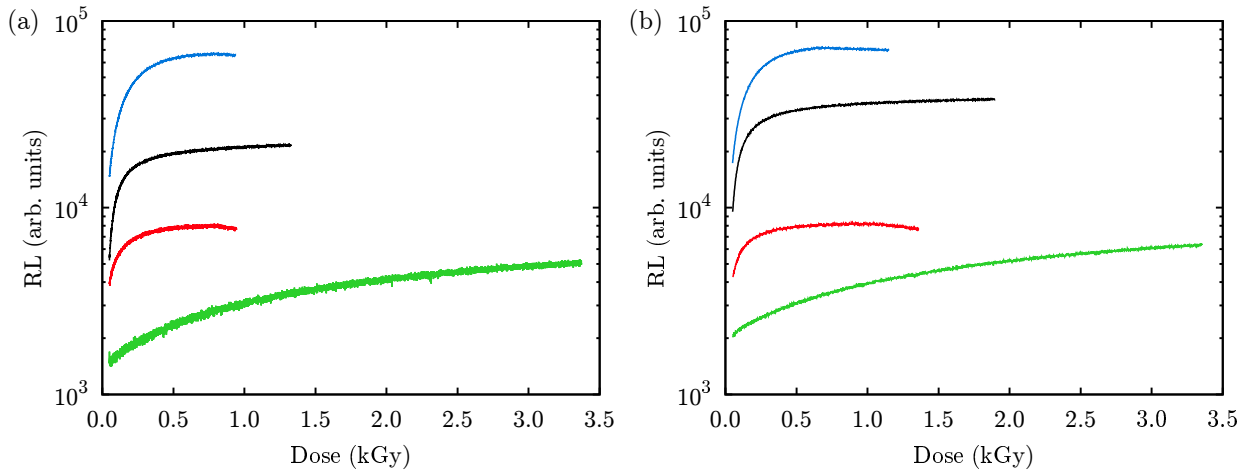

Figure 6.1: Changing radioluminescence response observed during priming under constant dose rate with (a) 6 MV photons at 17.7 Gy/min and with (b) 10 MV photons Gy/min at 74.7 Gy/min. Signal recorded for $NaMgF_3$:Eu (red), $NaMgF_3$:Mn (green), $RbMgF_3$:Eu (blue), and $RbMgF_3$:Mn (black) are plotted together to allow comparison.

Overall change in sensitivity, ΔL, was approximately a factor of 2 and 4 for the $NaMgF_3$:Eu and $RbMgF_3$:Eu dosimeters respectively, which is significantly less than the factor of 37 reported for α-Al_2O_3:C.[66] This was not quantified for $NaMgF_3$:Mn or $RbMgF_3$:Mn as these dosimeters were not saturated at the doses achievable, although it is apparent from the curves in figure 6.1 that a similar magnitude of ΔL may be expected. The required priming dose appears loosely dependant on dopant concentration, with the $NaMgF_3$:Mn dosimeter for which saturation was not achieved, having a molar concentration of the optically active ion up to 5 times higher. This introduces an additional factor into the matter of optimal dopant concentration, which is already a compromise between useful sensitivity, concentration quenching effects, and the impact of the dopant on radiological properties.

For an unsaturated dosimeters the dominant cause of dose history dependence is most likely competition between trapping and recombination of delocalised charge. This is supported by the observation that the dose response curves shown herein are relatively repeatable, with those presented in each of figures 6.1a and 6.1b being acquired with the same set of dosimeters immediately after bleaching with a 405 nm laser. Initial and final values of δ_L are also comparable within the uncertainty in fitting, which is as high as $0.3\delta L$ (see figure 6.2a) in the steep low dose region. A similar response is seen for each dosimeter when exposed to ^{192}Ir γ-rays.

While a dose history dependence after priming constrained to 10^{-4} Gy^{-1} is sufficient to carry out the characterisation measurements presented herein, it remains significant enough to preclude absolute dosimetry, as the instrument will not hold a calibration. It is also a source of uncertainty for any measurement spanning doses to water of more than a few Gy. For comparison, sensitivity changes with accumulated dose for

			$\delta_L(0)$ (Gy^{-1})		$\delta_L(D_{w,p})$ (Gy^{-1})	
	$D_{w,p}$ (kGy)	ΔL	6 MV	10 MV FFF	6 MV	10 MV FFF
$NaMgF_3$:Eu (0.1%)	0.894	~ 2	1.0×10^{-2}	7.2×10^{-3}	-2.2×10^{-4}	-2.2×10^{-4}
$NaMgF_3$:Mn (0.5%)	3.322	—	1.4×10^{-3}	1.3×10^{-3}	1.1×10^{-4}	1.1×10^{-4}
$RbMgF_3$:Eu (0.2%)	0.885	~ 4	1.9×10^{-2}	1.7×10^{-2}	-2.6×10^{-4}	-3.5×10^{-4}
$RbMgF_3$:Mn (0.2%)	1.275	—	2.9×10^{-2}	2.2×10^{-2}	6.4×10^{-5}	3.8×10^{-5}

Table 6.1: Summary of priming irradiation data including doses required to achieve useful stability, the overall change in sensitivity for the saturated Eu^{2+} dosimeters, and the initial and final changes in sensitivity per Gy of absorbed dose. Values for δ_L are determined by fitting to the measured dose-sensitivity curves in figure 6.1, for which each dosimeter was optically bleached prior to exposure.

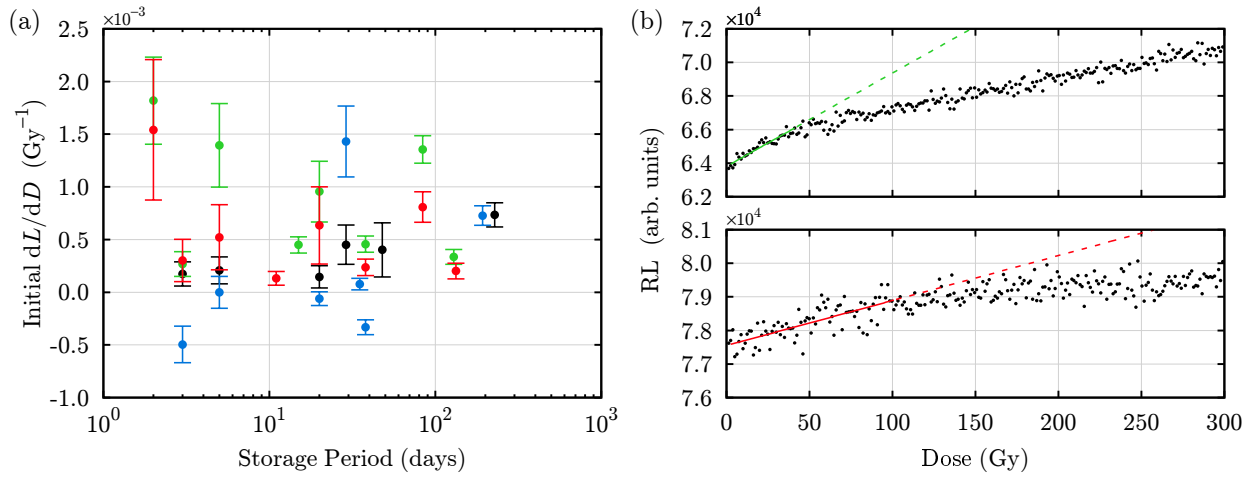

Figure 6.2: Response data for previously primed dosimeters, including (a) dependence of $\delta_L(0)$ values, or lack thereof, on duration of storage since priming, and (b) examples of the response after 20 days storage. Fits for $NaMgF_3$:Mn (green) and $NaMgF_3$:Eu (red) are shown to illustrate the determination of $\delta_L(0)$.

dosimetry diodes have been reported to be as high as 3.4×10^{-4} Gy^{-1}, and are the result of permanent radiation damage.[383]

The behaviour of the $NaMgF_3$:Mn was explored to higher absorbed doses in soft x-rays using sample AE01020, see § 4.6.2 and figure 4.10c.

6.1.2 Stability of Primed State

In the charge kinetics model the observable quantity of interest, L, is proportional to the recombination term $n_c m_j A_j^{mn}$ in equation 2.30. More generally, L depends on the populations of delocalised charge carriers of one sign, and those of the other sign trapped at luminescence centres. A central feature of the charge kinetics model is that the time evolution of these populations is governed not only by external energy input but also by the population levels themselves. Under constant dose rate, derivatives in both time and dose are numerically proportional, and so it follows that the magnitude of δ_L should be related to the population of trapped charge carriers. As encapsulated in equation 2.28, the primary means by which these populations are reduced in the model is by optical or thermal stimulation. This is reflected in the data shown in figures 6.1a and 6.1b, between which the population of trapped charge was decimated by high power laser stimulation prior to exposure, resulting in near complete restoration of earlier values for $\delta_L(0)$.

If priming is to be part of the solution to the difficulty presented by dose history dependence then the minimised δ_L attained after priming doses must persist for a useful period of time, ideally months to years. Priming could then be undertaken once, perhaps using an industrial irradiator prior to assembly rather than a therapy unit. While the stability of the primed state was not the subject of a controlled experiment, all characterisation measurements undertaken were preceded by a short repeat priming on the order of a few hundred Gy. The $\delta_L(0)$ values from each of these exposures are plotted in figure 6.2a against the period of storage in darkness since the previous exposure to radiation. Error bars represent estimations of the range of acceptable fits, examples of which are illustrated in figure 6.2b. There appears to be no significant dependence of $\delta_L(0)$ on storage period, except to note that in many cases it is larger than the values given in table 6.1 recorded immediately after priming.

A partial recovery of δ_L during storage indicates that the primed state is subject to decay, despite the dosimeters being sealed from ambient light. Theoretically, the long term stability of a light tight dosimeter should be influenced only by the concentration of trapping defects thermally accessible at or near the temperature of storage. The presence of traps accessible at room temperature is implied by a significant 'afterglow' observed in all dosimeters except $NaMgF_3$:Eu upon termination of priming irradiation. This is also loosely reflected in the magnitude of $\delta_L(0)$ after storage periods ranging from 2 days to over 7 months (figure 6.2a), for which the variability is lowest for the dosimeter with the lowest magnitude of room temperature TSL,

$NaMgF_3$:Eu.

Loss of optimal δ_L is primarily due to a fractional loss of the trapped population and therefore should be readily recoverable. As can be seen in figure 6.2b this is in fact the case, with gradient similar to those depicted in figure 6.1 restored after exposure to as little as 50 Gy for $NaMgF_3$:Mn. This dose can be achieved a few minutes with a modern accelerator producing unflattened x-ray beams and so presents much less of a barrier than does the magnitude initial priming doses. For samples in which the bulk of the glow peak intensity occurs well above room temperatures the majority of trapped charge carriers should be retained across long term storage in darkness

The dose dependency upon completion of repeated priming exposures were also collated. For $D_{\mathrm{w,p}}$ varying between approximately 120 Gy and 400 Gy, $\delta_L(D_{\mathrm{w,p}})$ is again reduced below 0.1% Gy^{-1} in all cases. While this has permitted further characterisation measurements, the relative instability of the primed state in all but the $NaMgF_3$:Eu dosimeter does render the specific fluoroperovskite samples used here as impractical for applications in radiotherapy. The room temperature TSL implicated in this instability not only limits the effectiveness of high dose priming irradiation, but may also exacerbate temperature dependence.

A few methods to mitigate the problem are worth mentioning. In $NaMgF_3$ the electron traps are believed to be F–centres,[2] with aggregates of these centres a likely candidate for the problematic shallow traps. Heating of sintered $NaMgF_3$:Eu to 900 °C followed by rapid cooling in liquid nitrogen has been demonstrated to significantly reduce room temperature glow peak intensity.[187] The reduced concentration of shallow traps is attributed to F–centres thermalised by elevation well above room temperature being unable to aggregate prior to being localised as the lattice thermal energy is lost to the cryogen. Unfortunately, subsequent exposure to ionising radiation is an effective way to reintroduce F–centre aggregate defects.[78]

An alternative solution lies in the use of nanoparticle $NaMgF_3$:Eu and $NaMgF_3$:Mn, for which RL sensitivity exhibits a markedly different shaped dose-sensitivity curve. In this form of the materials, the Eu^{3+} emission is more prominent and decreases in intensity with absorbed dose by up to 10% before plateauing at doses beyond 10 kGy.[79]

6.1.3 Radiation Damage

Figure 6.3 depicts two repeated exposures of the $RbMgF_3$:Eu dosimeter to γ-rays at a separation of 2 ± 0.5 mm from an ^{192}Ir brachytherapy source, nominal activity of 370 GBq. A similar response is exhibited by $NaMgF_3$:Eu. Dose rate under this geometry can be neither calculated nor measured with much accuracy but is estimated to be of similar magnitude to that in figure 6.1b. After 84 minutes of exposure the ^{192}Ir source was removed and the dosimeter bleached for 16 hours using the built in LED source, followed by a second exposure under the same conditions. As the changes in radioluminescence sensitivity attributed to charge kinetics discussed in the preceding sections are in principle completely reversible by bleaching, the permanent reduction in response observed is attributed to radiation damage.

There are three obvious targets for damage at high doses: the dosimeter itself, the directly exposed length of optical fibre, and the adhesive optically coupling these together. Cyanoacrylate adhesive is known to undergo additional crosslinking when irradiated, which can impact bond strength once doses reach into the region of 100 kGy,[384] but little is published regarding the impact on optical properties. Radiation induced optical absorptions in the adhesive have been tentatively eliminated following exposure of thin layers of adhesive cured on glass to soft x-ray doses on the order of several kGy. Only colour centre absorptions in the glass were observed. Even if the adhesive were to experience significant optical degradation, the path length through the bond is considerably shorter than in the active element or collection fibre and the impact is most likely negligible.

PMMA fibre optics of the type used for the dosimeter stem exposed to high doses are subject to radiation degradation with detectable changes in optical absorption for doses from tens of Gy through to about 50 kGy.[385] The primary mechanism of radiation damage is chain scissation following the generation of free radicals from the fragmentation of the $COOCH_3$ ester side chain,[386] and to a lesser extent radiation induced cross linking.[384, 387, 388] A pronounced reduction in transmitted power occurs for MV x-rays and

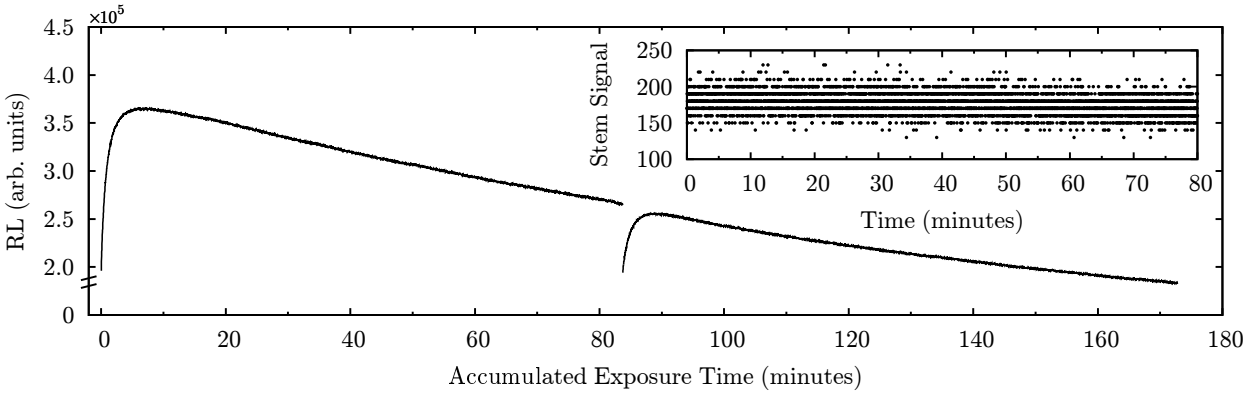

Figure 6.3: Significant changes in RL sensitivity after exposure to very high doses from a 370 GBq ^{192}Ir source. The dosimeter is bleached after 84 minutes prior to a second exposure, illustrating the sensitivity reduction is semi-permanent. This is attributed to radiation damage in the dosimeter active element and possibly also the optical fibre immediately adjacent to the dosimeter. Inset plot shows the stem signal detected at 360 nm for a similar exposure.

^{60}Co exposures on the order of kGy, with strong wavelength dependence[385, 389] and partial recovery of the unirradiated performance in the 650 nm window one month after exposure.[390] At doses on the order of MGy, PMMA is reduced to hydrogenated amorphous carbon[386] with a presumed complete loss of useful optical properties. There is no literature on the effects at the Eu^{2+} emission wavelength in the near ultraviolet where the transmittance of PMMA is marginal, even prior to irradiation. Under exposure to ^{192}Ir photons the stem signal observed at 360 nm was not observed to change significantly after 80 minutes (see figure 6.3), indicating that at least for shorter wavelengths, degradation of the polymer optics is not the dominant cause of sensitivity loss.

In the dosimeter itself, radiation induced ultraviolet absorption is expected due to the creation of colour centres, predominantly *F*–centres.[72, 78] The most intense absorption occurs at 290 nm and substantially overlaps the Eu^{2+} emission. Across all the dopants investigated in $NaMgF_3$ (see chapter 4) there is a clear trend towards dose-sensitivity curves similar to those in figure 6.3 for blue and ultraviolet emissions, even for irradiation scenarios where only the fluoroperovskite was exposed. The radiolytic generation of *F*–centres and related defects is therefore considered the dominant pathway for radiation damage, with excess loss in the directly exposed polymer optics and adhesives a secondary if not negligible effect.

Such effects are not detectable with the Mk-II prototype for either of the $NaMgF_3$:Mn or $RbMgF_3$:Mn dosimeters due to their longer emission wavelength being clear of the primary *F*–centre absorption. This is not to imply that these materials are immune, more likely that a much smaller effect is masked by the higher saturation dose. In undoped $NaMgF_3$ exposed to similarly high doses, a slight reduction in transparency attributed to *F*–centre amalgamations is also detectable overlapping the emission Mn^{2+}. This is reported in the literature[78] and confirmed by experiment for samples fabricated by the methods used in this study, see § 4.1.2.

6.2 Stem Signal

It is telling, if somewhat discouraging, that even after being actively researched[85, 226, 234, 235, 237, 241, 245] over several decades, a truly robust solution to the Čerenkov problem arguably does not yet exist. The problem is far more complex than will be treated in this chapter, and as the equipment used sports only the long since abandoned techniques of background fibre subtraction and spectral filtering, it is not surprising that this work makes no advances on the matter. In this section it is attempted simply to account the observed stem signal in order to understand the impact on the characterisation measurements undertaken.

6.2.1 Dose Rate Proportionality of Stem Signal

Stem signal observed through both the 360/12 nm and 590/20 nm band pass filters was found linear with respect to dose rate across the available range of pulse repetition rates. This was anticipated, given the geometry of exposure is static and both Čerenkov and fluorescence emissions have lifetimes many orders of magnitude shorter than the period between radiation pulses. Linear fits to this response data, which intersect the origin at L_0 within experimental uncertainty, are shown in figures 6.4a and 6.4b. Fit gradients, m, are given on the plots.

These stem signal measurements are the same as used to correct the radioluminescence data shown in figure 6.6. While seemingly trivial, this verification is a component of the overall system linearity and so must be validated separately.

6.2.2 Variation of Stem Signal with Depth and Field Size

A simple model to account for the non-linear dependence of stem signal magnitude on irradiation geometry is given in equation 6.2. The first term in this equation reflects exposure of the length of fibre embedded in the phantom, while the second term approximates the signal induced by scatter to the fibre outside the phantom. The latter is taken as a function of the directly irradiated volume. Definitions for the relative dosimetric quantities used are given in § 2.1.8 and details of experimental irradiation geometry illustrated in figure 3.9c. Beam data used to evaluate the model can be found in appendix A.

$$L(r,d) = C_0 \mathrm{TPR}\,(r,d)\, S_{c,p}\,(r) \int \mathrm{OAR}(r,d,x)\,\mathrm{d}x + \frac{r^2 C_1}{3\,\mathrm{SAD}^2}\left[(\mathrm{SAD}+b)^3 - (\mathrm{SAD}-d)^3\right] \tag{6.2}$$

This model deliberately contains a minimum of free parameters, with only C_0 and C_1 adjusted during fitting. These constants represent the contribution to stem signal from the directly and peripherally exposed fibre respectively. C_1 has units of signal per unit volume while C_0 has the same units as L, in this case none. All remaining values are fixed or dictated by the dependent variables r and d.

Equation 6.2 was fitted to the experimentally measured values of L using Levenberg-Marquardt non-linear regression. The consistency of fitted values for C_0 between experiments exploring field size and depth dependence suggests the model takes reasonable account of in field effects. Furthermore, the relative magnitude of C_0 and C_1, at approximately 10^4, is in reasonable agreement with typical ratios of in field to peripheral dose rate.[391] For stem signal detected at 360 nm, residuals to the fit are in excess of uncertainty for $r < 3$ cm, which is possibly a product of positional error in either the inactive fibre tip or secondary collimation. Neither was likely achieved with precision much better than 1 mm.

A number of secondary effects have been deliberately neglected in order to constrain the number of fitting parameters. Examples include interplay between field divergence and the angular dependence for capture of Čerenkov photons, and the impact of spectral changes with depth and distance off axis on Čerenkov emission angle. The divergence in the largest field accommodated by the phantom is small compared to the critical angle for guided modes in EH4001 optical fibre[318] ($\sim 70°$), which captures Čerenkov and fluorescence emissions over more than 80% of all possible emission trajectories. It can be seen from figure 2.9 than the Čerenkov emission angle and spectral intensity is largely invariant for electron energies above 1 MeV, and so neither is strongly depth dependent for megavoltage photons or electrons.[243] These effects may well become significant for less constrained irradiation geometries.

The practical use of this model likely does not extend far beyond providing a basis for the behaviour depicted in figures 6.4c through 6.4f. It would be expected that experimental agreement breaks down at different gantry angles, phantom sizes, and extremes of depth. The value of C_1 might also prove sensitive to the specific arrangement of the collection fibre, which would be consistent with the wider variation in fitted values than observed for C_0.

When the inactive fibre was pushed throught the full width of the plastic water phantom and subjected to the same range of field sizes as shown in figures 6.4e and 6.4f, a very similar response occurs. In doubling both the length of fibre in the primary beam and within the phantom, an increase in stem signal of only 40–

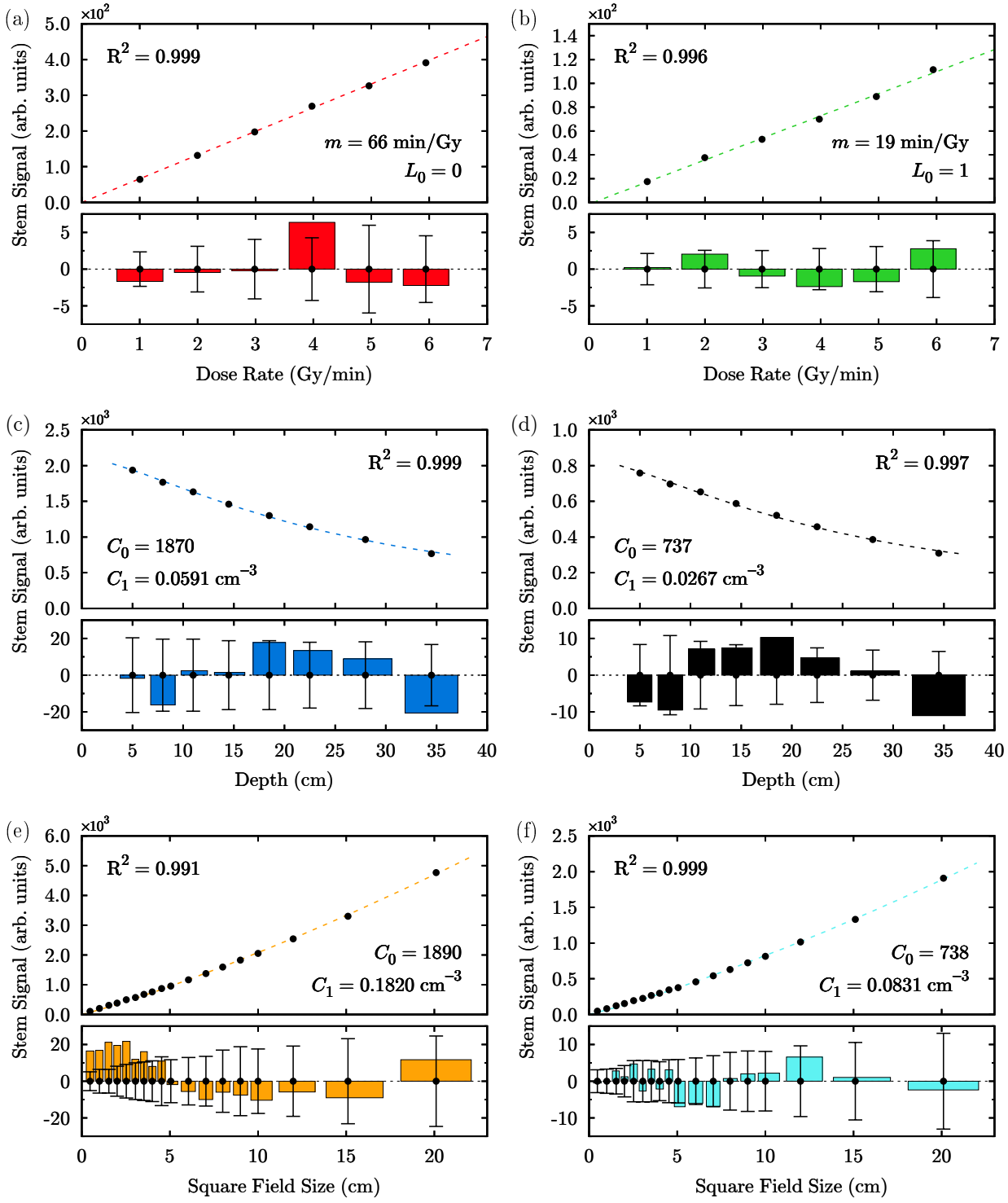

Figure 6.4: Čerenkov stem signal dependence on dose rate with (a) 360/12 nm and (b) 590/20 nm band pass filters with linear fits, variation with depth for (c) 360/12 nm and (d) 590/20 nm filters, and dependence on field size with (e) 360/12 nm and (f) 590/12 nm filters, fitted to equation 6.2.

50% was observed. This indicates that the direction of propogation of captured fluorescence and Čerenkov photons is to some extent dictated by field divergance, with those travelling towards the fibre tip detected with lower efficiency.

6.2.3 Inequivalence of Active and Inactive Fibres

Following the loss of the original inactive fibre while the Mk-II unit was at Industrial Research Limited mid 2012 for the retrofit of light sources (see § 5.1.2), the signal generated in the replacement was found to differ

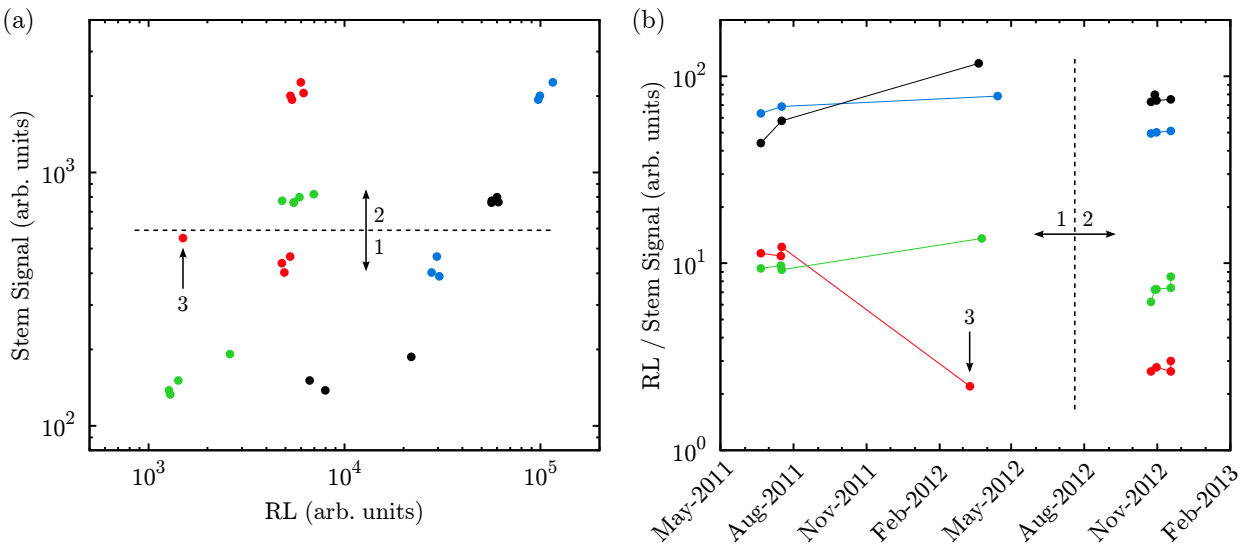

Figure 6.5: Observed stem signal for all measurements made under 6 MV reference conditions plotted with respect to (a) the corresponding RL signal and (b) the date of the measurement. Points are coloured according to the dosimeter for which the RL was recorded: $NaMgF_3$:Eu (red), $NaMgF_3$:Mn (green), $RbMgF_3$:Eu (blue), or $RbMgF_3$:Mn (black). Data in (b) is expressed as the ratio of RL to stem signal to normalise out changes in overall system sensitivity. Grouping of measurements (1) prior to and (2) after the dosimeter light source refit and replacement of the inactive dosimeter probe in mid 2012 is evident in (a). The outlier for $NaMgF_3$:Eu dosimeter (3) is discussed in the text. Statistical uncertainty is contained within the marker radii, spread in measurements arises from poor optical reproducibility.

in proportion to the measured RL. Consequently, some doubt was cast over whether stem signal magnitude obtained with either inactive fibre was representative of that occurring for the fluoroperovskite dosimeters.

Figure 6.5 summarises the system response for all measurements made under 6 MV reference conditions throughout the investigation. It can be seen clearly in figure 6.5a that a substantial shift in system sensitivity occurred across the hardware refit. This most likely arose following the replacement of the fibre splice when new light sources were installed, the photomultiplier gain control voltage having been verified at 800 mV throughout. Except for one $NaMgF_3$:Eu data point identified in the figure, the separate groupings of stem signal and RL response before and after this event lies within the limited reproducibility of sensitivity across filter changes.

A reduction in the ratio of RL to stem signal is also seen across the refit (figure 6.5b), reflecting a relative increase in stem signal after the replacement of the inactive fibre. The ESKA EH4001 polymer fibre used in the first generation dosimeters was by this time obsolete and the replacement probe was made using the closest available product, ESKA GH4001. For the Mn^{2+} emission in the region of 600 nm the nominal attenuation is improved in the latter by almost 50 dB/km,[317,318] with no specification given in the near ultraviolet. For the one metre length used this amounts to about 1% signal increase, and so the larger observed change is attributed instead to the loss of common dose history and the associated radiation damage effects.

An anomalous response of the $NaMgF_3$:Eu dosimeter is identified in both figures 6.5a and 6.5b, for which a marked reduction in RL sensitivity is accompanied by an increase in stem signal. This does not appear to be an outlier but rather a permanent change, with the sensitivity shift shown in figure 6.5a clearly taking reference from this point rather than the previous response. The cause of this is and will likely remain unknown. Mechanical damage to the dosimeter probe is one possibility.

In § 6.1.1 it was indicated that while usable values of δ_L were obtained, complete saturation of the Mn^{2+} dosimeters was not achieved. As additional dose is accumulated, the sensitivity of these two dosimeters is therefore expected to continue to rise. For both $NaMgF_3$:Mn and $RbMgF_3$:Mn this results in a larger spread in RL response shown in figure 6.5a and the increasing trend in the ratio of RL to stem signal, at least prior to the replacement of the inactive fibre. By the end of the study, the $NaMgF_3$:Eu, $NaMgF_3$:Mn, $RbMgF_3$:Eu,

and $RbMgF_3$:Mn dosimeters had received total doses since the most recent bleaching of 3.4 kGy, 5.0 kGy, 2.5 kGy, and 3.3 kGy respectively. These figures are in excess of the saturation dose observed during the bulk crystal characterisation measurements (see figures 4.8c, 4.10c, 4.24b, and 4.25b respectively) for all except $NaMgF_3$:Mn.

For many of the experiments undertaken only linearity in some quantity is of interest, and so the impact of discrepancies between absolute stem signal magnitude in the active and inactive fibres is a secondary consideration. The principle concern in these cases is inflated uncertainty in the fitted values of α. Of these measurements, this is of real consequence only for temperature dependency for which the fit values, rather than just residuals, are interpreted as a performance metric. However, for experiments in which the measured quantity is a ratio of the RL component of L observed with the $NaMgF_3$ dosimeters, an accurate correction for stem signal is critical. In this work, such measurements all concern energy dependence, and the sensitivity to stem signal is considered on a case by case basis in § 6.5. For the $RbMgF_3$:Eu and $RbMgF_3$:Mn dosimeters, stem effects are rendered almost negligible by the relative magnitude to the RL response under reference conditions.

On the timeline depicted in figure 6.5b, dose rate linearity and tissue phantom ratio experiments were carried out in mid 2011, followed by temperature dependence in early 2012, then by dose per pulse response, radiation quality dependence, and total scatter factors in late 2012. With the exception of the anomalous response of the $NaMgF_3$:Eu highlighted in figure 6.5, stem signal quantified in the inactive ESKA EH4001 probe was taken as representative of that in the dosimeter fibre. Increased uncertainty may be anticipated with the Eu^{2+} dosimeters for which radiation damage effects are more significant, but this is not readily quantifiable. All stem signal corrections obtained using data from the ESKA GH4001 inactive fibre in late 2012 are considered suspect.

6.3 Linearity

The assumption of dose rate linearity is often implicit in the interpretation of many of the results in this chapter. In the tests that follow, response was declared to be linear if the residuals with respect to the first order fit, $L(x) = mx + L_0$, of the measured response under the variable of interest, x, all fall within experimental uncertainty. The magnitude of L_0 is also expected to be comparable to said uncertainties.

6.3.1 Dose Rate Dependence

Linearity with pulse rate is a crucial property for dosimetry of dynamic radiotherapy deliveries, where dose modulation is often achieved by gating of individual radiation pulses.[310,311] Dose rate linearity for continuous irradiation is expected from a theoretical standpoint, as L is proportional to the population of delocalised charge carriers which is in turn proportional to the ionising radiation fluence rate (see equation 2.26). In addition, the photon counting readout system can reasonably be expected to maintain linearity provided that count rates are maintained within the limits determined by of the preamplifier bandwidth and discriminator dead time,[256] in this case at least 10^6 cps. For dose rate set by adjustment of pulse repetition rate, linearity was established within measurement uncertainty at up to 6 Gy/min for $NaMgF_3$:Mn, $NaMgF_3$:Eu, and $RbMgF_3$:Mn. This is illustrated in figure 6.6.

Residuals of the $RbMgF_3$:Eu dose rate data with respect the linear fit exhibit a systematic trend and are in excess of the measurement uncertainty at nominal dose rates of 1 Gy/min and 3 Gy/min. Errors in stem signal subtraction and any effect from the higher Z_{eff} of this sample are eliminated by comparison to the response of $NaMgF_3$:Eu and $RbMgF_3$:Mn respectively. The excess residuals range from approximately 0.3% to 0.8% of the RL signal after correction for stem signal. This is comparable to the product of the total experimental dose, some 36 Gy, and the δ_L reported in table 6.1 for $RbMgF_3$:Eu. Thus it seems that residual dose history dependence, which is not factored into the calculation of error bars[i], is the most likely explanation.

[i] This omission is deliberate, it reduces the likelyhood of masking such effects.

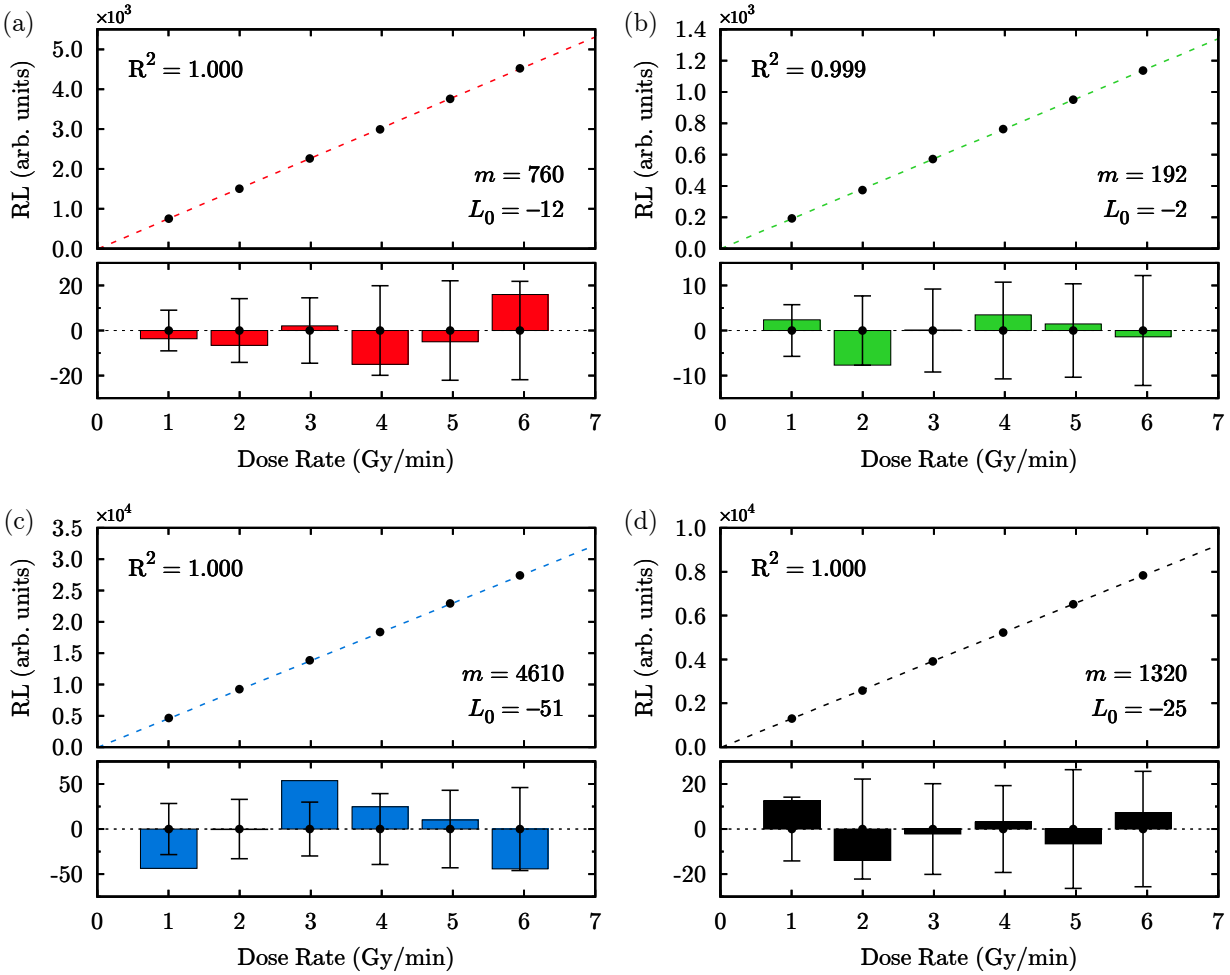

Figure 6.6: Dose rate response of (a) $NaMgF_3$:Eu, (b) $NaMgF_3$:Mn, (c) $RbMgF_3$:Eu, and (d) $RbMgF_3$:Mn. Lower subplots compare residuals with respect to the fit (dashed line) against the type A statistical uncertainty.

6.3.2 Dose per Pulse Effects

Linearity with dose per pulse was only established in $NaMgF_3$:Mn, with linear regression of the data sets for $NaMgF_3$:Eu, $RbMgF_3$:Mn, and $RbMgF_3$:Eu, producing residuals well in excess of the experimental uncertainty. When the response was fitted for the five lowest doses per pulse only, as was done for figures 6.7b through 6.7d, L_0 is minimised. When presented so, these discrepancies are interpreted as a consequence of changes in radiation spectrum incurred when dose per pulse is lowered by the addition of water equivalent attenuation. These spectral changes arise from a non-trivial interplay between primary fluence hardening and the build up of lower energy scatter and secondary bremsstrahlung.[308]

The impact of these processes is understood to a certain extent by Monte Carlo simulation.[308, 392, 393] In the 10×10 cm^2 6 MV radiation field used to investigate dose per pulse dependency, a reduction in mean photon energy from approximately 1.40 MeV at the surface to 1.25 MeV at $d = 10$ cm occurs, with recovery to 1.35 MeV by $d = 28$ cm. In terms of fluence spectra, the beam is progressively softened by the build up of scattered photons with energies down to about 50 keV, which are largely absent from the incident radiation. The peak energy is also shifted to higher energies by hardening of the primary fluence. Qualitatively, this is in agreement with the observed dose per pulse dependence in both $RbMgF_3$ activated fluoroperovskites, in that the trend in the experimental data is appropriate for an over response to the increased lower energy scatter expected for the lower doses per pulse encountered at larger depth. Over-response to these softer radiations is anticipated in light of the enhanced x-ray mass attenuation of $RbMgF_3$ between 10 keV to 100 keV. This is addressed in more detail in § 6.5.1.

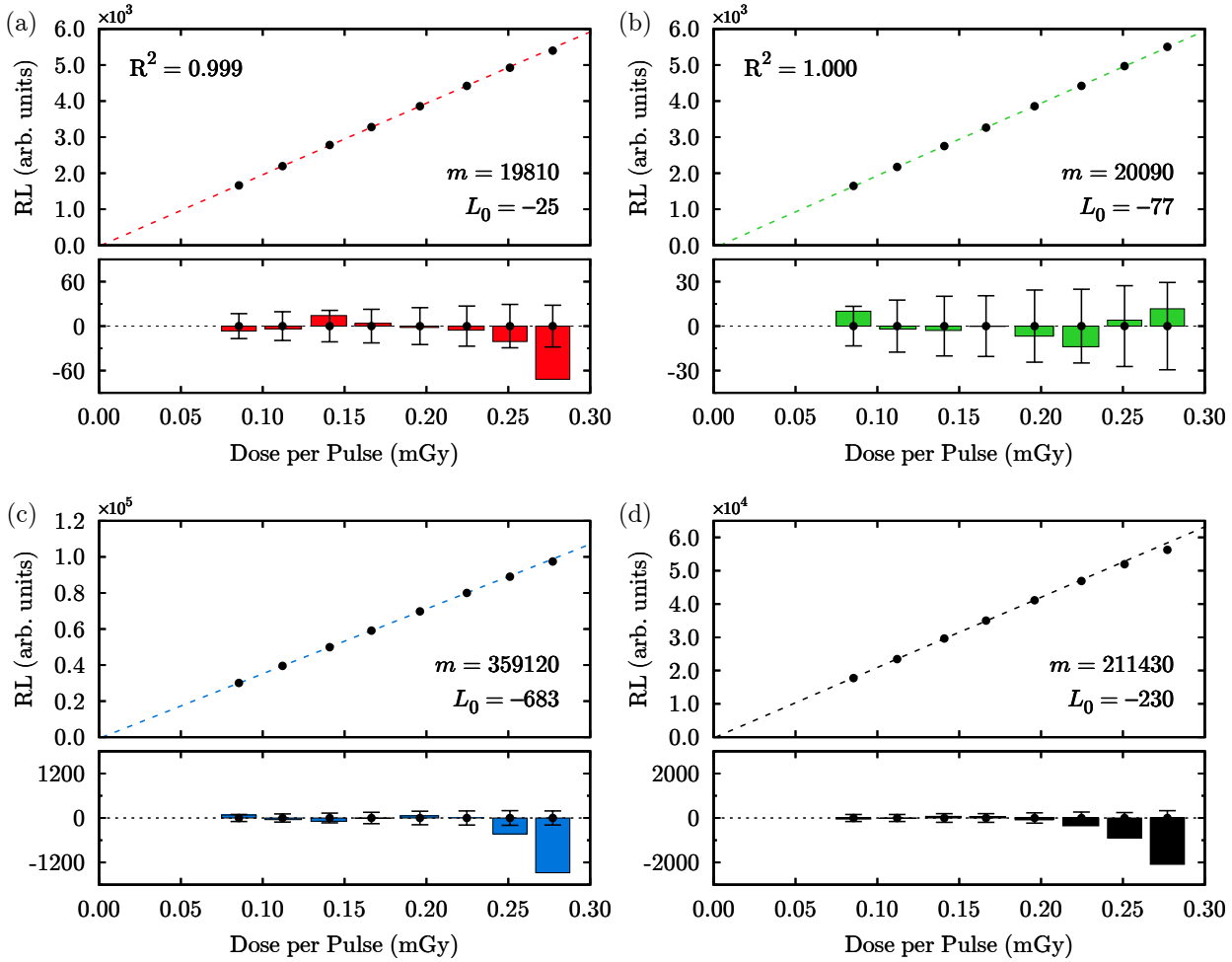

Figure 6.7: Dose per pulse response of (a) $NaMgF_3$:Eu, (b) $NaMgF_3$:Mn, (c) $RbMgF_3$:Eu, and (d) $RbMgF_3$:Mn. As dose per pulse was controlled by addition of attenuators, failure of linearity in $RbMgF_3$:Eu and $RbMgF_3$:Mn is almost certainly a product of enhanced mass attenuation coefficient for $RbMgF_3$ at lower photon energies

.

6.3.3 Integrated Dose Measurements

Performance when integrating RL emissions to determine absorbed dose at 6 Gy/min was generally poor due to the efficiency limitations of the current prototype discussed in § 5.1.3. While integrated measurements are linear with machine monitor units within uncertainty, for doses near 1 Gy this uncertainty is inflated to almost 20% by the reduced acquisition time. This is a property of the current prototype hardware more than it is of the materials under investigation. If this mode of operation is to be useful a significant reduction of the present transmission and insertion losses will be required as these doses and dose rates are highly relevant to current radiotherapy practice.

6.4 Temperature Dependence

Most measurement systems are influenced by ambient temperature in some manner, including many of the detector technologies currently used in radiotherapy.[12,14] To be useful in this field dosimeters should have minimal temperature dependence, say less than 1% response change per degree, but most importantly the effect should have a physically understood cause amenable to accurate modelling. In essence, temperature dependence is acceptable provided that it can be corrected without introducing undue additional uncertainty.

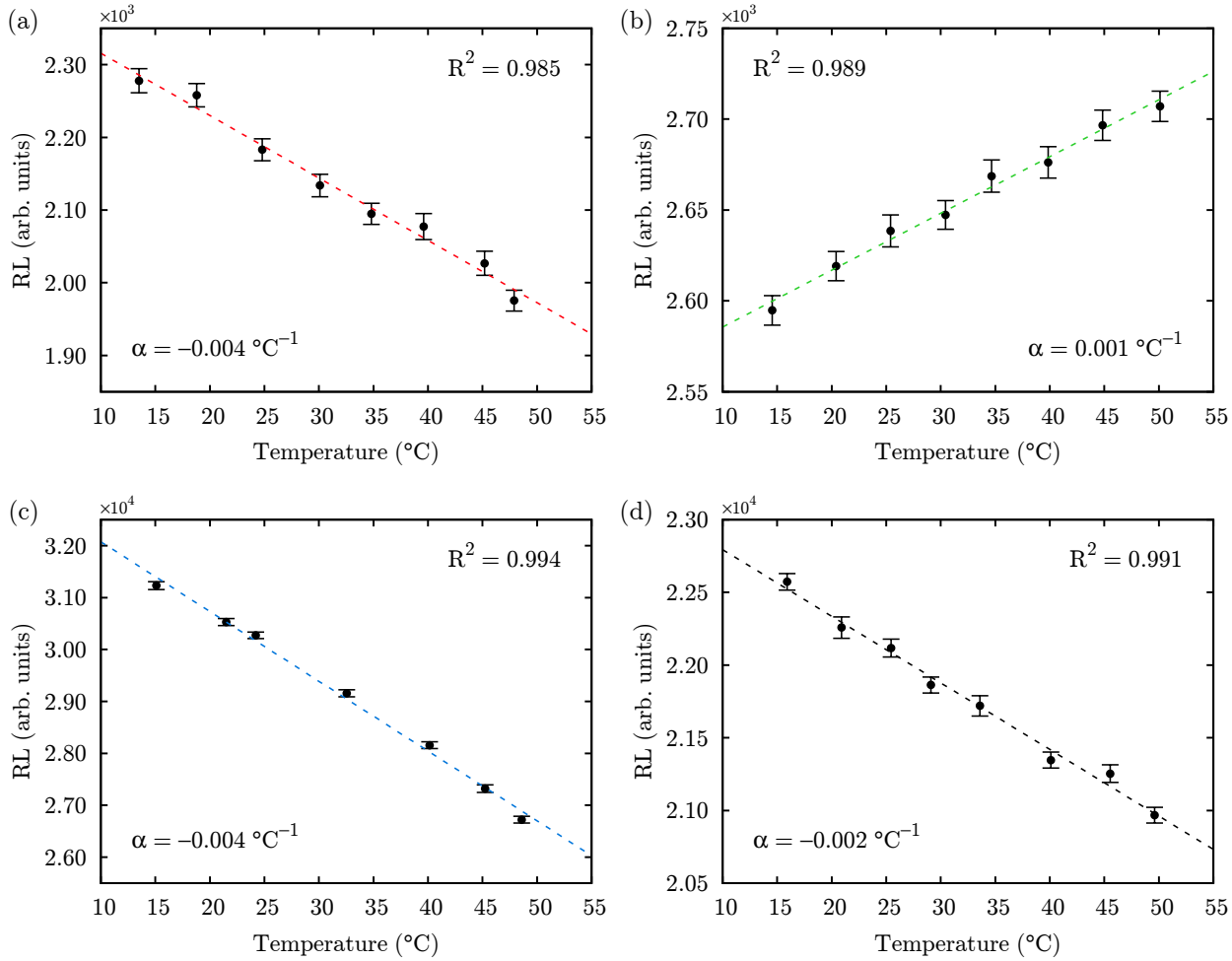

Figure 6.8: Temperature response in 6 MV photons of the Mk-II prototype with the (a) $NaMgF_3$:Eu, (b) $NaMgF_3$:Mn, (c) $RbMgF_3$:Eu, and (d) $RbMgF_3$:Mn dosimeters. Linear temperature coefficients are marked on each plot for a reference temperature of 20 °C.

6.4.1 System Temperature Response

A linear model of temperature dependency was applied to describe the response of RL sensitivity from approximately 15 °C to 50 °C in $NaMgF_3$:Mn, $NaMgF_3$:Eu, and $RbMgF_3$:Mn. Temperature coefficients are shown on the respective graphs in figure 6.8 for a reference temperature of 20 °C. These coefficients indicate a response which, at less than 0.5% per degree, depends weakly on temperature. This level of temperature dependence is comparable in magnitude to many existing commercial dosimeters.[319] Minor corrections would be required for absolute dosimetry.

In both $NaMgF_3$:Eu and $RbMgF_3$:Eu the RL emission detected through the 360/12 nm bandpass filter is dominated by the line emission of the intraconfigurational $^6P_{7/2} \rightarrow {}^8S_{7/2}$ transition of the Eu^{2+} ion. This emission exhibits a marked reduction in intensity with increasing temperature consistent with the data shown in figures 6.8a and 6.8c. This is discussed in more detail in § 4.5.2 and illustrated in figure 4.9 for sample AE00519.

The detectable emission from $NaMgF_3$:Mn and $RbMgF_3$:Mn is the portion of the wider band emission from the $^4T_{1g}(^4G) \rightarrow {}^6A_{1g}(^6S)$ transition of the MnF_6 complex which overlaps the transmitting region of the 590/20 nm bandpass filter. As shown in figure 5.1c this is the low and high energy sides of the peak RL intensity for $NaMgF_3$:Mn and $RbMgF_3$:Mn respectively. With the 3*d* orbitals of the Mn^{2+} ion interacting strongly with the crystal field, both the emission intensity and energy are found to depend on temperature, with the latter observed to increase at elevated temperatures for both $NaMgF_3$:Mn and $RbMgF_3$:Mn. Thus the sign and magnitude of α for the Mn^{2+} dosimeters is dictated as much by the choice of band pass filter as the RL emission itself. Temperature dependence of the Mn^{2+} RL emission spectrum is also described in

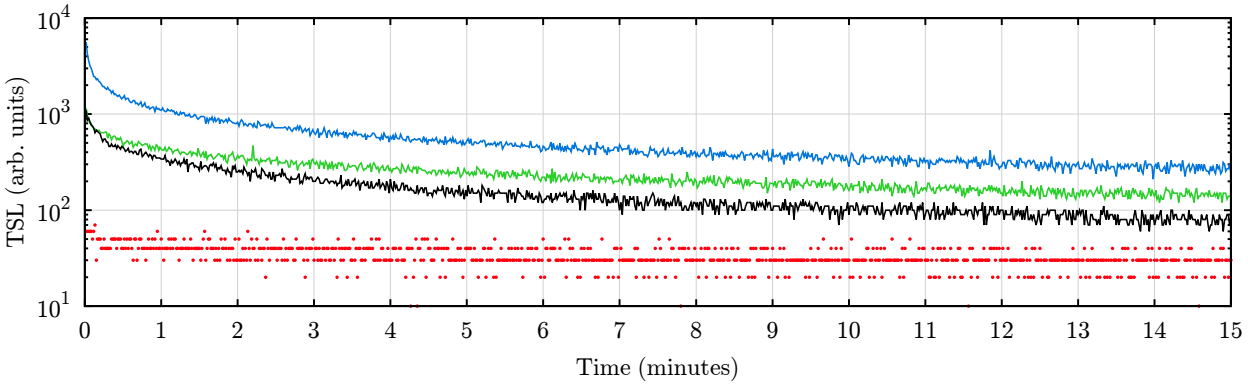

Figure 6.9: Thermally stimulated afterglow observed after 10 MV priming irradiations at room temperature for $NaMgF_3$:Eu (red), $NaMgF_3$:Mn (green), $RbMgF_3$:Eu (blue), and $RbMgF_3$:Mn (black).

§ 4.6.2 and illustrated in figure 4.11 for sample AE01020.

Temperature dependence in α-Al_2O_3:C is comparable to the figures for each fluoroperovskite shown in figure 6.8, reported at 0.2% per °C for RL with comparable but negative coefficients for OSL.[117] Organic PS systems were initially thought temperature independent, but more recent publications[394,395] report dependence on the order of 1% per °C for BCF-12 and BCF-60 which is reflected in current documentation from the manufacturer.[100]

6.4.2 Temperature Independence of Stem Signal

Stem signal appears uninfluenced by changes in temperature over the range of 15 °C to 50 °C when employing either the 360/12 nm or 590/20 nm band pass filters. This is consistent with the insignificant changes in optical loss and refractive index in PMMA over this temperature range. Specifically, the refractive index near 600 nm is reduced[316] from 1.49 at 15 °C to 1.48 at 40 °C, which has no significant impact on Čerenkov threshold energy or emission angle. Scattering losses in PMMA also have no significant temperature dependence provided the glass temperature is not exceeded,[218] which ranges widely from 85 °C to 165 °C across commercial grades of PMMA.[315] Accordingly, both ESKA EH4001 and GH4001 polymer fibres are specified for operation up to 85 °C without substantial change in optical properties.[317,318]

6.4.3 Thermally Stimulated Afterglow

All of the fluoroperovskite samples used in first generation dosimeter probes exhibit TSL at room temperature after irradiation, the decay of which is plotted in figure 6.9. For $NaMgF_3$:Eu this is negligible, at just a few times the background count rate, and in all cases decays below detectability following storage at room temperature for one day. Observed intensity scales with recently delivered dose, and was typically observed immediately after irradiation to be at least an order of magnitude below the RL signal level for each dosimeter.

Over the temperature range reported in figure 6.8 the primary effect of this is to degrade the primed state, increasing dose history dependence as discussed in § 6.1.2. At temperatures overlapping glow peaks, TSL emission is also detected during irradiation and the temperature dependency of RL intensity is perturbed. For $NaMgF_3$:Eu and $NaMgF_3$:Mn room temperature glow peaks are of relatively low intensity, see figures 4.8d and 4.10d.

6.5 Energy Response

Few detector technologies are strictly water equivalent, with $NaMgF_3$ being no exception. In figure 2.8d it can be seen that this material exhibits a level of over-response to photons below 100 keV, intermediate to LiF and Al_2O_3 but significantly improved with respect to silicon. These materials are all used in radiotherapy dosimeters, and so it is not unreasonable to expect that $NaMgF_3$ might prove viable for selected applications.

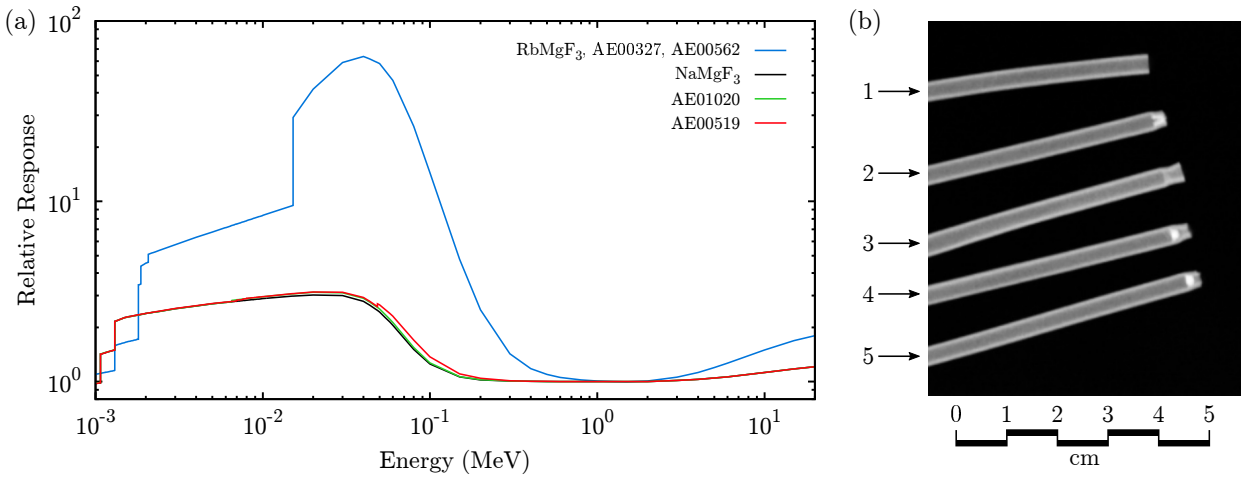

Figure 6.10: (a) Theoretical energy dependence calculated using equation 2.18 for the samples used in the first generation fibre coupled dosimeters. For $RbMgF_3$ the effect of the dopant is negligible at the concentrations shown for samples AE00327 and AE00562 in table 3.1. (b) Radiographic image illustrating (1) inactive fibre optic used for the correction of the Čerenkov background and the (2) $NaMgF_3$:Eu, (3) $NaMgF_3$:Mn, (4) $RbMgF_3$:Eu, and (5) $RbMgF_3$:Mn dosimeters, taken with a tube potential of 50 kV. For $NaMgF_3$:Eu a high density or atomic number encapsulation of the active element is clearly resolved.

The $RbMgF_3$ based dosimeters are clearly not water equivalent, their inclusion here provides an indication of sensitivity for the tests undertaken.

6.5.1 Radiation Quality Dependence

A comparison of response across all available megavoltage photon radiations is presented in table 6.2. From the energy fluence spectra shown in figure A.4, it can be seen that additional energy fluence extends into the photoelectric regime for the radiations with lower NAP, and that the unflattened 10 MV radiation is softer still, due to the lack of flattening filter. Only $NaMgF_3$:Mn was found independent of these radiation qualities, with a general trend of declining response relative to 6 MV with higher acceleration potentials for the remaining dosimeters.

In both $RbMgF_3$:Mn and $RbMgF_3$:Eu the reason for this is clear upon consideration of the energy dependence of $RbMgF_3$ presented in figure 6.10a, which is significantly inflated below approximately 500 keV by the K, L, and M edges of rubidium. This increases the response to the softer radiation qualities, with the relative response in the harder radiations consequently reduced by normalisation to 6 MV.

The cause of the less pronounced but similar trend for $NaMgF_3$:Eu is less clear. From figure 6.10a it can be seen that while the presence of 0.1% europium in sample AE00519 results in a slightly larger perturbation of the $NaMgF_3$ baseline energy dependence than does the 0.5% manganese present in sample AE01020, the europium content is insufficient to explain the data in table 6.2. Specifically, the integral of $\psi\epsilon$ using the energy fluence spectrum shown in figure A.4[ii] is 1.0147 and 1.0149 for the $NaMgF_3$:Mn and $NaMgF_3$:Eu

[ii] At best a crude approximation of the actual energy fluence at depth in water. In this case the conclusions drawn are insensitive to this parameter, with a similar outcome using $\psi = 1$ for $E < 6$ MeV and $\psi = 0$ elsewhere.

	6 MV	10 MV FFF	10 MV	18 MV
$TPR_{20,10}$	0.670	0.707	0.739	0.783
$NaMgF_3$:Mn	1.000(2)	0.999(2)	1.000(2)	1.001(2)
$NaMgF_3$:Eu	1.000(2)	1.002(2)	0.981(2)	0.975(2)
$RbMgF_3$:Mn	1.000(5)	0.994(4)	0.959(5)	0.933(4)
$RbMgF_3$:Eu	1.000(3)	1.004(5)	0.963(3)	0.946(3)

Table 6.2: Relative sensitivity of each fluoroperovskite dosimeter in a range of high energy photon radiation qualities, normalised to 6 MV. Energy fluence spectra for each radiation can be found in appendix A

dosimeters respectively, and 1.0679 and 1.0682 for $RbMgF_3$:Mn and $RbMgF_3$:Eu. Thus the $NaMgF_3$:Mn and $NaMgF_3$:Eu dosimeters should not differ substantially in radiological terms.

Other factors which may influence the response of $NaMgF_3$:Eu with respect to $NaMgF_3$:Mn include inaccuracies in stem signal quantification and differences in physical construction. A radiograph of the first generation dosimeter probes is included in figure 6.10b. This image was taken with a tube potential of 50 kV for which the high atomic number of $RbMgF_3$ is captured as high intensity and the $NaMgF_3$ detector elements are poorly resolved. The encapsulation of the $NaMgF_3$:Mn and $NaMgF_3$:Eu active elements clearly differs, with the latter appearing to be of unexpectedly high density or atomic number. Either would increase the secondary electron fluence at the location of the dosimeter itself and generate additional photoelectric electrons if of high atomic number, in which case a perturbation of energy response would be expected. This is considered the most likely cause of the excess energy dependence observed with respect to the $NaMgF_3$:Mn detector. Difficulties encountered in stem signal management are discussed in § 6.2.3. While inaccurate stem signal correction would change the relative magnitude of the figures in table 6.2 the observed trend is expected to be preserved after normalisation.

The independence from radiation quality exhibited by $NaMgF_3$:Mn is a desirable quality. Relative dosimetry is typically performed under conditions where ψ is not precisely known, for which detector energy dependence generates additional, typically uncaptured, experimental uncertainty. This is not necessarily a significant problem, with many ionisation chambers exhibiting a variation in response of a few percent across the range of x-ray qualities typically encountered in radiotherapy clinics. For example, the PTW type TW31014 small volume ionisation chamber which is widely used in radiotherapy, exhibits a 3% shift in sensitivity between the extremes of $TPR_{20,10}$ listed in table 6.2[17] yet performs acceptably for many tasks involving a single radiation quality.[396, 397]

6.5.2 Tissue Phantom Ratios

In figure 6.11 the response of each fluoroperovskite dosimeter is compared to the TW31015 small field ionisation chamber for field sizes $r = [3, 10, 20]$ cm, and depths of $d = [5, 30]$ cm in plastic water. These conditions should capture the extremes of variation in ψ for 6 MV x-rays along the central beam axis in a homogeneous absorber. Results were plotted as the ratio of response at 30 cm to 5 cm depth ($TPR_{30,5}$) to reduce data dimensionality. The ionisation chamber response was reproduced by the $NaMgF_3$:Mn dosimeter only, as shown in figure 6.11b.

Substantial discrepancies between the chamber response and both of the $RbMgF_3$ based dosimeters (figures 6.11c and 6.11d) are accounted for again by enhanced photoelectric absorption, significant in this case due to the changes in radiation spectra which occur under changes of field size. Large x-ray fields generated by medical electron accelerators generally become softer as field size is increased due to the collimation devices no longer occluding sources of extra-focal scattered radiation.[29] When a larger field impinges on the plastic water phantom, the larger irradiated volume also gives rise to a much more pronounced build up of low energy scatter, with energy fluence below 100 keV significantly inflated in larger fields at depth.[308, 393] The significant discrepancies in $TPR_{30,5}$ as measured with both $RbMgF_3$ dosimeters in larger fields is consistent with such changes in x-ray quality.

The response of the $NaMgF_3$:Eu dosimeter is intermediate to that of $NaMgF_3$:Mn and both $RbMgF_3$ detectors. This is similarly anomalous to the findings presented in § 6.5.1 and so is assumed to have the same origin. The trend in residuals with respect to dose per pulse for $NaMgF_3$:Eu plotted in figure 6.7a may also be a manifestation of the same problem.

6.5.3 Total Scatter Factors

Figure 6.12a compares a set of total scatter factors measured with the $NaMgF_3$:Mn dosimeter against the same data obtained with the TW31014 and TW31015 ionisation chambers and TW60012 silicon dosimetry diode. A normalisation field size of 5×5 cm^2 has been selected to accommodate the silicon diode which is known to over-respond at the reference field size.[29] The fluoroperovskite dosimeter appears in better

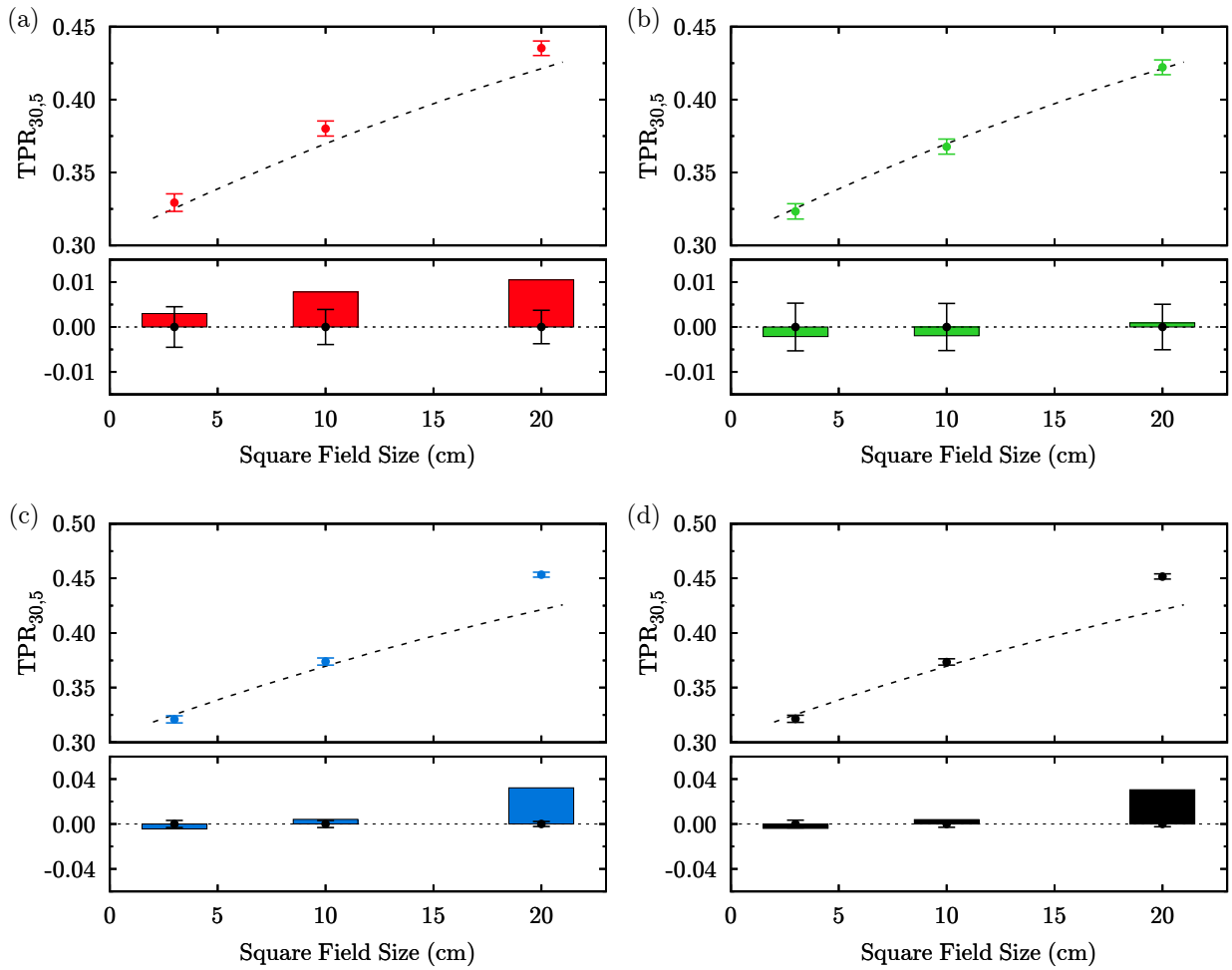

Figure 6.11: $TPR_{30,5}$ in 3×3 cm^2, 10×10 cm^2, and 20×20 cm^2 fields as determined from radioluminescence of (a) $NaMgF_3$:Eu, (b) $NaMgF_3$:Mn, (c) $RbMgF_3$:Eu, and (d) $RbMgF_3$:Mn, and small volume air filled ionisation chambers (dashed line). Good agreement between $NaMgF_3$:Mn and the ionisation chamber suggests acceptable energy dependence in this material.

agreement with the silicon detector than the ionisation chamber, a finding which is inconsistent with all other results presented for $NaMgF_3$:Mn in this chapter, in particular that in figure 6.11b.

It is almost certain that this inconsistency arises from the use of two different inactive fibres for the measurement of $TPR_{30,5}$ and $S_{c,p}$, the implications of which are detailed in § 6.2.3. The sensitivity of the $S_{c,p}$ data acquired using the $NaMgF_3$:Mn dosimeter to errors in stem signal correction is illustrated in figure 6.12b, in which the data is presented with stem signal corrections scaled to ±10%, ±20%, and +50% of that determined with the ESKA GH4001 inactive fibre. If it is assumed on the basis of the data presented in figure 6.11b that the TW31014 ionisation chamber and the $NaMgF_3$:Mn dosimeter should agree at least for $r \in [3, 20]$ cm, it can be inferred that an increase in stem signal of approximately 20% could account for the observed disagreement. This is relatively consistent with the change in the ratio of RL to stem signal observed between the ESKA EH4001 and GH4001 inactive fibres, see figure 6.5b.

This problematic set of results has been reported in order to highlight the inadequacy of the stem signal correction method available with the Mk-II prototype and the limitations it places on the practicable characterisation work. It is considered unlikely that the response illustrated in figure 6.12a is a consequence of the energy dependence of $NaMgF_3$:Mn.

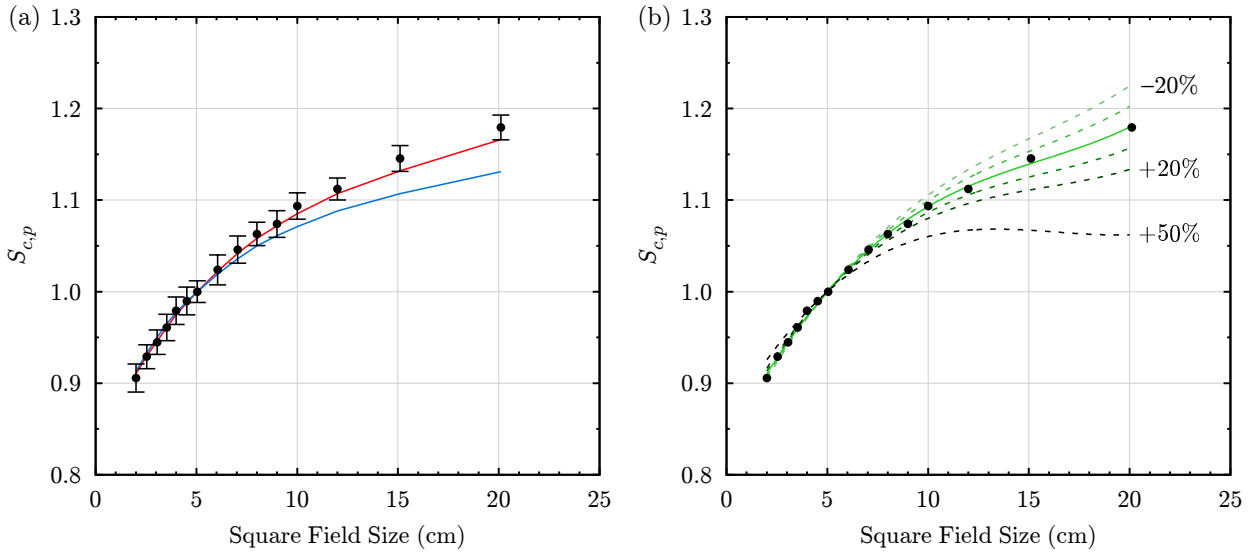

Figure 6.12: (a) 6 MV total scatter factors measured with small field ionisation chambers (blue), electron dosimetry diode (red), and $NaMgF_3$:Mn (black). (b) Indication of the sensitivity of data measured with $NaMgF_3$:Mn to the relative magnitude of stem signal (green), with percentages marked on the plot indicating the scaling of the stem signal correction for the same RL response.

6.6 Summary

While many of the results presented in this chapter are promising, there is little doubt that the Mk-II prototype is not a system suitable for dosimetry in radiotherapy. The chosen means of stem signal correction is ineffective, the system repeatability is poor, and the optical efficiency is inadequate to obtain the required precision for clinically relevant radiation doses. For the most part these are technical issues addressed in the design of the as yet untested Mk-III system outlined in § 5.2.

Assuming that engineering solutions can be found to remaining difficulties encountered, such as the Čerenkov problem, the $NaMgF_3$ based detectors show promise for use in radiotherapy. $NaMgF_3$:Mn in particular has been shown to be linear with dose rate and dose per pulse, to have manageable temperature dependence, and appropriate energy response for radiotherapy applications. Residual dose history dependency remains unaddressed but would not preclude relative dosimetry after saturation.

Chapter 7

Conclusions

This work has sought to evaluate synthetic $NaMgF_3$ as a potential luminescence material for radiotherapy dosimetry applications, with a focus on the fibre coupled dosimeter configuration. A range of luminescent species were surveyed in this host in the hope of isolating those well suited to the specific challenges of megavoltage x-ray fibre coupled dosimetry, while those identified by a previous study[2] were assessed in therapeutic radiation qualities using the Mk-II prototype system described in § 5.1. The radiotherapy characterisation did not uncover any fundamental problems with materials based on $NaMgF_3$ which might otherwise render further study futile.

Experience gained with the Mk-II system has highlighted a few key difficulties which heavily influenced the materials research and prompted the design of the Mk-III prototype. These included a need for an effective means of suppressing the Čerenkov stem signal, a means to minimise or correct for the long term changes in sensitivity due to radiation damage, and for improvements in efficiency and repeatability in the dosimeter optical train. To address stem signal and radiation damage effects, dopants yielding long lived near infrared emissions were sought, with $NaMgF_3$:Ni identified as the most promising. This material exhibits a broad emission centred near 1600 nm, for which the Čerenkov to signal ratio is theoretically improved by an order of magnitude with respect to the near ultraviolet. The decay lifetime of this emission is approximately 150 μs, which may prove marginal for temporal gating of the remaining Čerenkov signal, but effective suppression via the well established chromatic discrimination method should be possible.

Dependence of sensitivity on dose history has been established to arise from a complex interplay between the effect of charge trapping on luminescence efficiency and the impact of radiation induced colouration of the host crystal on the detectable emission intensity. The latter was characterised for both the kilovoltage x-rays used in material characterisation experiments and the megavoltage x-rays used in radiotherapy applications. It was found to be qualitatively predictable but dependent on both radiation quality and dose rate. Charge kinetics models were developed to describe these effects in $NaMgF_3$:Ni and $NaMgF_3$:Sm and successfully fitted to experimental data for doses in excess of 10 kGy. These models are necessarily simplified, and so it is doubtful that they could be used to accurately correct for changes in sensitivity with accumulated dose. Fortunately, at the wavelength of the $NaMgF_3$:Ni emission of interest the effect of colour centre absorptions is negligible and the dose history dependence is reduced to the level of 10^{-6} Gy^{-1}. This is acceptable for use in radiotherapy.

A range of additional rare earth and transition metal ions were doped into $NaMgF_3$ and luminescence observed in all cases. Many of these materials were eliminated as candidates for fibre coupled dosimetry applications during the course of this work, most often on the basis of emission intensity being too weak or not of the desired energy. In many cases, significant TSL at or below room temperature was also observed, which would be expected to exacerbate temperature dependency and compromise the stability of any reduced dose history dependence achieved through high dose priming. Nonetheless, a substantial body of experimental data has been gathered regarding these materials, some of which may have applications in other areas. For many of the studied materials this data, particularly RL emission spectra, does not appear elsewhere in the literature at this time.

The materials used in testing of the Mk-II dosimeter remain of interest, particularly $NaMgF_3$:Mn which has the most desirable radiological properties, the longest emission lifetime, and with only one emitting level is possibly the most efficient $NaMgF_3$ based material in the study. The Mn^{2+} emission energy in this host is not ideal but has been proven viable for use with the bi-alkali photocathodes common in single photon counting detectors. With a relatively long lived emission, it is also a good candidate for temporal discrimination of Čerenkov stem signal. With a principal emission at near ultraviolet wavelengths where the Čerenkov background is most intense, $NaMgF_3$:Eu does not lend itself to RL dosimetry but would likely have utility in OSL applications, including dose imaging. Such applications are beyond the scope of this work.

A significant effort was also invested in redevelopment of the prototype dosimeter to address the many short comings of the Mk-II system. While the Mk-III system has not yet seen testing in megavoltage radiations with any of the aforementioned materials, the individual optical, mechanical, and detector systems have been tested as detailed in appendix B, and the bulk of the electronics and software development completed. In addition to much improved mechanical repeatability and the reduction of optical loss from upwards of 20 dB to less than 10 dB, the Mk-III design also accommodates the array of detectors required to support the wide range of emission energies from the selected materials.

In summary, a number of $NaMgF_3$ based luminescence dosimeters have been tested with a prototype dosimeter and found to have potential for applications as dosimeters for radiotherapy. The difficulties presented by dose history dependence, Čerenkov stem signal, and the limitations of the Mk-II prototype have essentially been addressed through engineering refinements and further materials research, leading to the selection of more appropriate dopants and a better understanding of the mechanisms of radiation damage. Some work remains to integrate these findings into the redesigned Mk-III prototype before further applications testing can be undertaken.

Further Investigations

The following investigations would be of immediate interest as follow up to the work reported herein:

- Refinement of the materials fabrication process to improve optical quality and establish optimal dopant concentrations.
- Further magnetisation experiments of the type reported in § 4.10.4 to more precisely quantify radiation induced changes in the population of luminescence ions.
- Additional characterisation of RL emission temperature dependency for $NaMgF_3$:Ni, particularly for the $^3T_{2g}(^3F) \rightarrow {}^3A_{2g}(^3F)$ emission which was not captured in the temperature characterisation reported in § 4.8.2.
- Quantitative characterisation of the dependence of radiation induced colouration on dose rate and radiation quality for doped rather than pure $NaMgF_3$ in the range of megavoltage radiations used in radiotherapy.
- Attempt characterisation of absolute emission intensity for the materials of interest for applications to assist in the determination of optimal dopant concentration.

Appendix A

Nominal Beam Data

The data in this appendix is included to support the interpretation of results presented in chapter 6. It represents the relevant subset of beam data for the x-ray radiation qualities available on any of the treatment units at the Wellington Blood and Cancer Centre. Each of these accelerators were tuned to match one another when first commissioned, and so a single set of nominal data adequately describes them all. Furthermore, each is subject to periodic quality assurance checks to ensure constancy in all operating parameters which influence delivered dose.

Profile and depth dose data was measured with a PTW MP3 scanning water phantom. For measurement of profiles a small volume liquid ionisation chamber, PTW type TW31018, was used to maximise spatial resolution in the field penumbra. All profile data was measured at 100 cm SSD and has been corrected for beam divergence to represent isocentrically defined field sizes. This approach has been taken for both convenience and consistency as profiles at isocentre cannot readily be measured at greater depths due to mechanical interference between the water phantom and the accelerator gantry.

Rather than attempt to measure TPR directly, percentage depth dose data was measured and TPR calculated using the well established formalism published in BJR supplement 25.[28] A selection of air filled ionisation chambers were used for the measurement of depth dose data, including PTW types TW31010 (0.125 cm^3), TW31015 (0.030 cm^3), and TW31014 (0.015 cm^3), as appropriate for each square field size. The calculation method (see equation A.1) was adapted slightly to make use of isocentrically measured phantom scatter factors. This permitted the use of locally measured data over published peak scatter factor data and also avoids the difficulties presented by electron contamination as the local data is measured at d_{ref} rather than d_{max}.[17, 398]

$$\mathrm{TPR}\,(d,r) = \mathrm{PDD}_{d_{\mathrm{ref}}}\,(d, r\,[\mathrm{SAD}/\,(\mathrm{SAD}+d)])\,\frac{S_p\,(r\,[\mathrm{SAD}/\,(\mathrm{SAD}+d)])}{S_p\,(r\,[\mathrm{SAD}/\,(\mathrm{SAD}+d_{\mathrm{ref}})])}\left(\frac{\mathrm{SAD}+d}{\mathrm{SAD}+d_{\mathrm{ref}}}\right)^2 \tag{A.1}$$

As this approach differs slightly from convention, calculated TPRs were spot checked by measurement. Definition of terms in equation A.1 can be found in § 2.1.8 and figure 3.9, or in the referenced literature.[12–14, 28, 398]

Energy fluence spectra for the MV photon radiations used in this study are plotted in figure A.4. These were generated from parametrised fits to published Monte Carlo data,[399] which are reproduced by the fit with at most 1.7% RMS error.[400] Off axis spectra are given at the limit of the largest possible field size, capturing the worst case off axis softening. All plots show emitted energy fluence, changes with depth in water are discussed in § 6.5.

Off axis softening is a product of both the angular energy dependence of bremsstrahlung emission from the x-ray target and the selective beam hardening incurred by the use of a flattening filter for all but 10 MV FFF. The profiles for 6 MV in figure A.3 also reflect radial spectral changes in the slightly increased dose deposition at larger distances off axis. This is characteristic of flattened therapeutic x-ray radiations, for which the flattening filter is optimised to produce the most uniform profile at 10 cm depth.

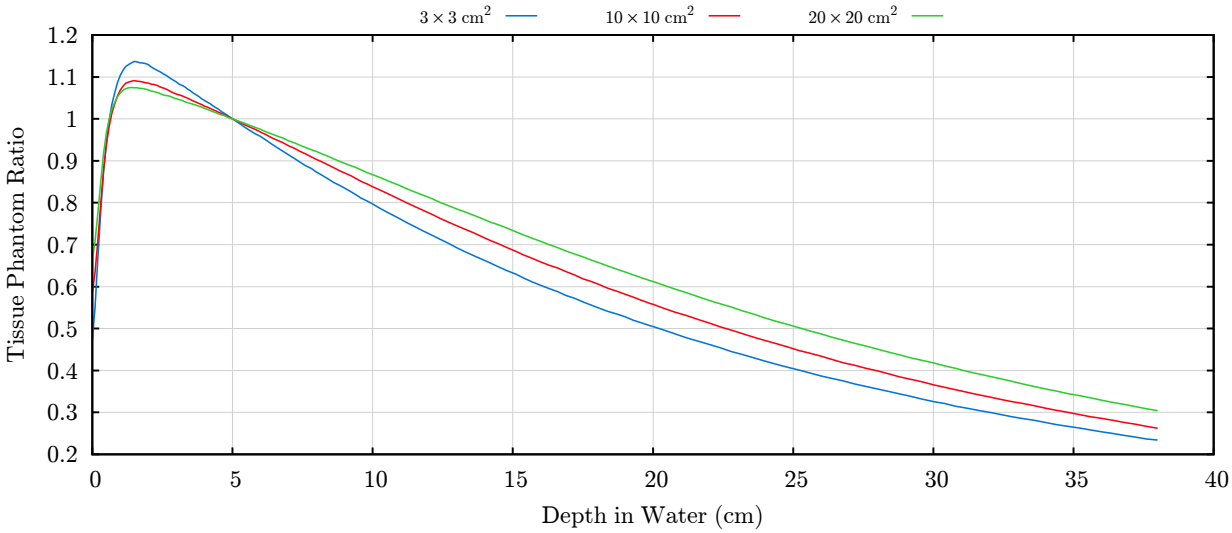

Figure A.1: Calculated TPR curves for 6 MV at the field sizes explored in § 6.5.2.

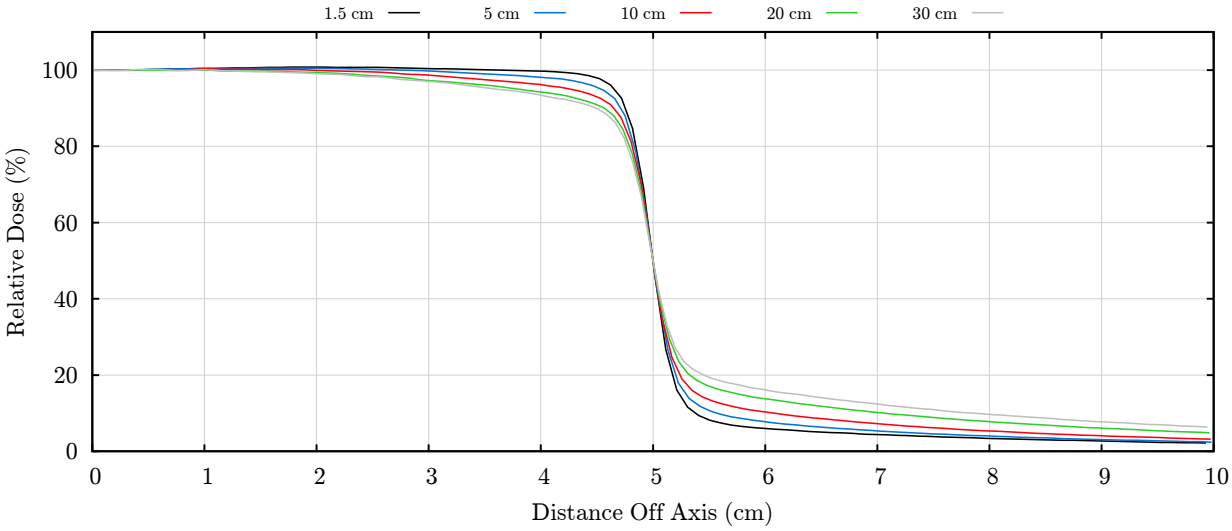

Figure A.2: Relative dose profiles for 6 MV at 10×10 cm^2 field size and a range of isocentric depths.

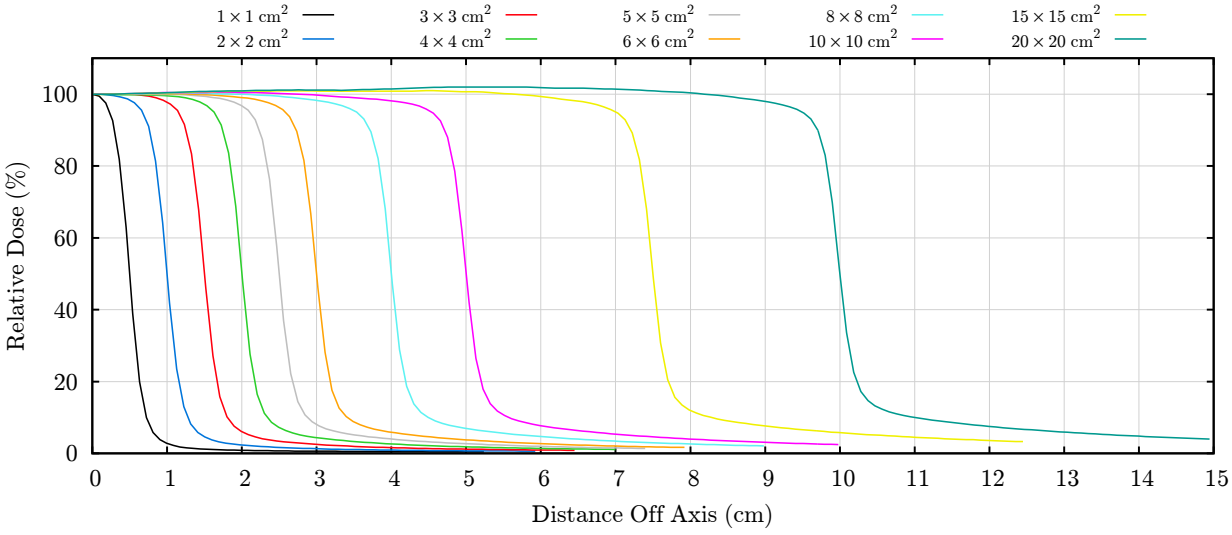

Figure A.3: Relative dose profiles for 6 MV at a depth of 5 cm in a range of isocentric field sizes.

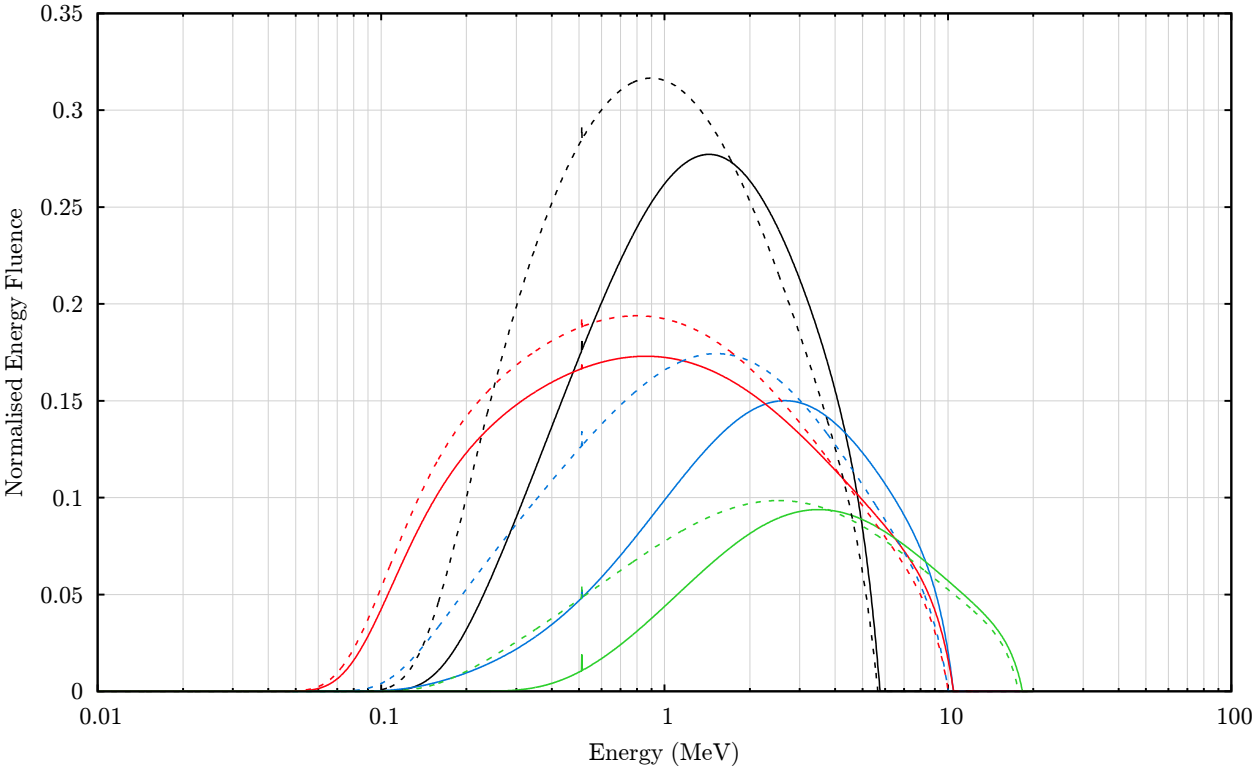

Figure A.4: Emitted energy spectra for 6 MV (black), 10 MV (blue), unflattened 10 MV (red), and 18 MV (green), each normalised to unit energy fluence. Solid curves represent spectra on the central beam axis while dashed curves illustrate softening at 20 cm off axis. The 511 keV annihilation peak has been slightly emphasised.

r (cm^2)	3×3	4×4	5×5	6×6	8×8	10×10	12×12	15×15	20×20
$S_{c,p}(r)$	0.878	0.904	0.925	0.942	0.973	1.000	1.014	1.034	1.059

Table A.1: Total scatter factors ($S_{c,p}$) for a subset of the achievable square field sizes contained within the plastic water slab phantoms used in chapter 6.

Appendix B

Dosimeter Performance Testing

Selected results from the operational testing of various components of the Mk-III prototype are included here. This data is not scientific in nature and is presented in support of the viability of the revised design, as it was not possible within the available time frame to progress the development to a stage where testing in MV x-ray radiations could be undertaken. A high level overview with selected details of the revised design is given in § 5.2.

The transimpedance amplifier and photon counting discriminator circuits described herein were designed by i2M Labs specifically for use in the Mk-III prototype.

Linearity of Photodetectors, Transimpedance Amplifier, and Photon Counter

The transimpedance amplifier linearity was tested separately using known currents injected from a resistor divider, as measured using a Keithly 6485 picoammeter. The resistor divider circuit used is illustrated in figure B.1a. A test of the S1087-01 in combination with the transimpedance amplifier was made using a fibre coupled $NaMgF_3$:Sm sample (see figure B.1b), confirming the linearity of the combined system of x-ray source, fluoroperovskite dosimeter, photodetector, and transimpedance amplifier. A transfer ratio of 9.87×10^8 V/A was determined for the transimpedance amplifier, which is consistent with the calculated value of 10^9 V/A in the low frequency limit for the nominal feedback resistance of 1 GΩ.

Prior to these tests the amplifier circuit board was rinsed in isopropyl alcohol, dried with compressed air, and housed in a grounded screen of aluminium foil. Cleaning removes dust and debris from the circuit which, if lodged near the high impedance node, can induce leakage currents which lead to output offset. While the amplifier is inherently stable as a consequence of relatively low bandwidth, the extremely high gain renders the system susceptible to electromagnetic interference. The error bars shown reflect the observed RMS noise and are not indicative of the limiting SNR achievable in the Mk-III design.

Linearity of output from the Philips PW1730 x-ray generator was established separately by monitoring the photocurrent generated in S1087-01 (figure B.1c) and G12180-110A (figure B.1d) photodiodes operated in photovoltaic mode. These devices are linear in current output when operated under low illumination,[258] and the intensity of radioluminescence has been established to be linear with dose rate in chapter 6 for the types of dosimeter materials tested. A similar test was made for the H10721-10 current mode photomultiplier module in conjunction with sample AE01020 ($NaMgF_3$:Mn). The x-ray generator was operated at 40 kVp with no filtration and photocurrent was measured using a Keithly 6485 picoammeter.

The photon counting discriminator was tested using the H5783P photomultiplier module recovered from the Mk-II prototype, re-terminated with an SMA connector for coupling to the Mk-III electronics, and operated with a control voltage of 900 mV for a nominal internal gain of 2×10^6. Optical stimulation was provided by sample AE1020 ($NaMgF_3$:Mn) mounted on EH4001 polymer optical fibre and exposed to unfiltered 40 kVp x-rays at a focus-dosimeter separation similar to that described in § 3.2.1. Average count rate was estimated using the mean frequency statistics reported by a Tektronix DPO2024 digital oscilloscope, which has an input bandwidth of at least 200 MHz. No loss of linearity was observed within the range of x-ray

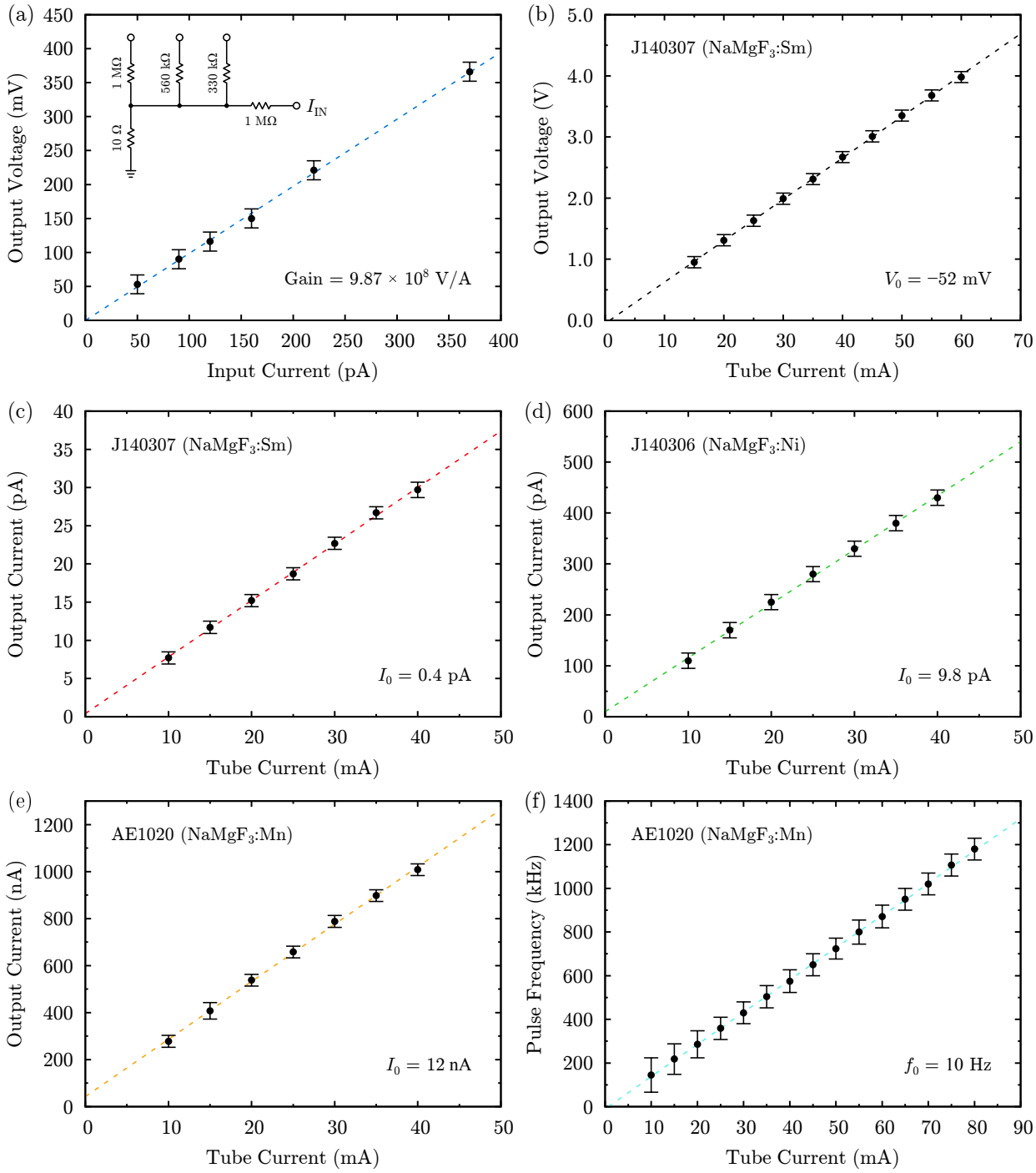

Figure B.1: Linearity of transimpedance amplifier when sourcing current from (a) the illustrated resistive divider network, and (b) the S1087-01 photodiode illuminated by the radioluminescence of sample J140307 ($NaMgF_3$:Sm). Linearity of the photodetector-fluoroperovskite combination in response to x-ray dose rate is also depicted for the (c) S1087-01 and (d) G12180-110A photodiodes, and the (e) H10721-10 photomultiplier in current mode and (f) H5783P photomultiplier in single photon mode, all as a function of tube current. Error bars are estimated from measurement noise specific to these tests and are not indicative of achievable uncertainty for the Mk-III design.

tube currents tested, for which the average pulse frequency produced by the discriminator reached almost 1.2×10^6 Hz. This is considered acceptable performance for a photon counting system, in which linearity is generally expected to fail in the range of 10^6 to 10^7 cps in the absence of dead time compensation.[256] Dark counts on the order of 10 Hz are consistent with that observed during operation of the Mk-II system, which used the Hamamatsu C9744 discriminator in conjunction with the same photomultiplier module. This test is summarised in figure B.1f.

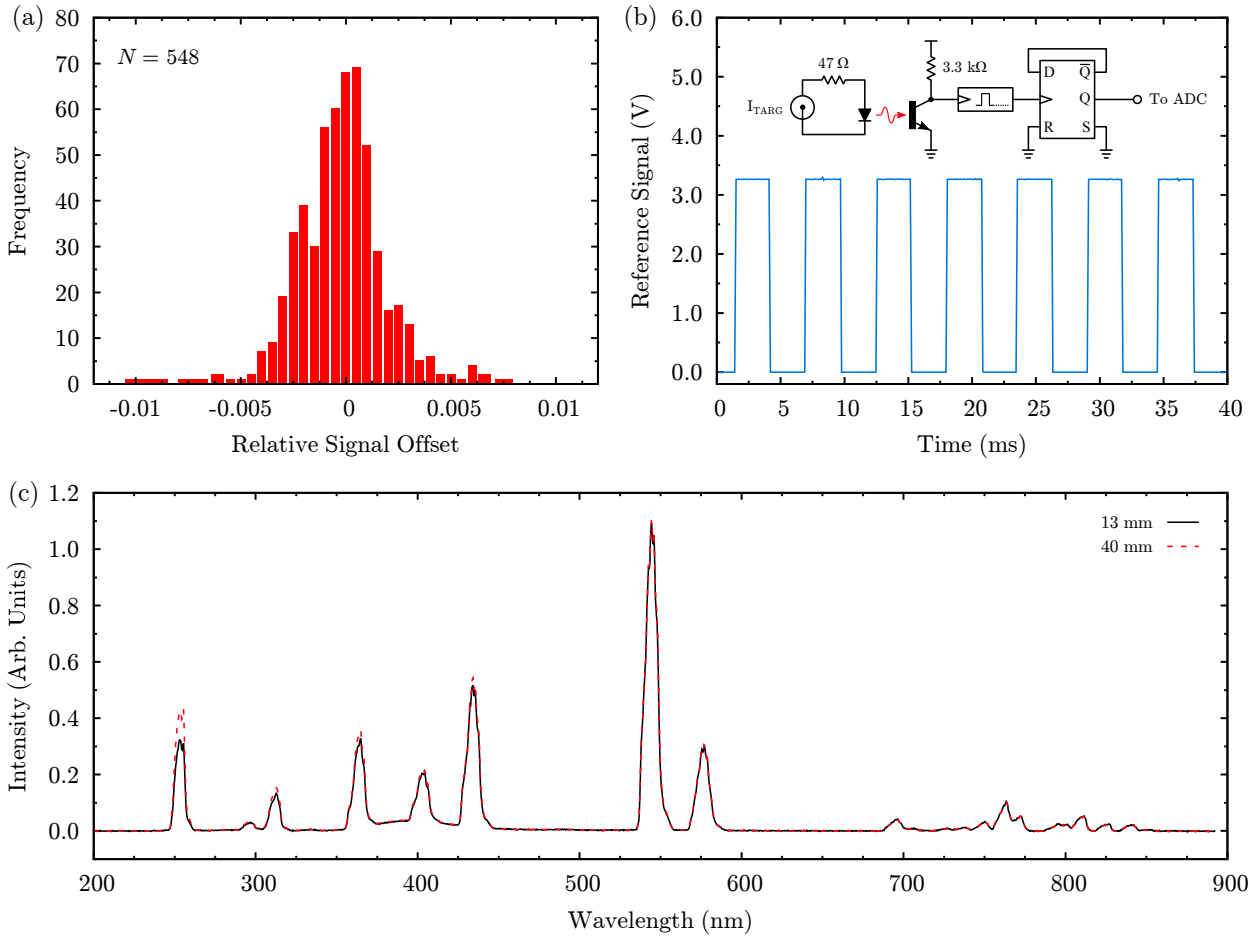

Figure B.2: Miscellaneous test results, including (a) histogram of relative signal changes across detector stage realignment, (b) detection of beam pulses using the at a sample rate of 10 kHz, and (c) spectral changes in efficiency across the pair of fibre optic collimator lenses used for the filter carousel as a function of lens separation. The spectrum shown in (c) is that of a He-Ar wavelength calibration source (Ocean Optics CAL-2000).

Optical Repeatability of Linear Stage

PL emission from sample J140306 was used during this test, being spectrally comparable to the RL signal of interest. Emission was detected by the G12181-110K photodiode after passing through an RG-830 long pass filter. The filter was placed in-line with the fibre optics using collimator lenses, rather than directly in front of the detector, this being more representative of the Mk-III design. A 2-axis micrometer stage was used to set vertical and axial position of the fibre face relative to the photodiode sensitive area with lateral alignment provided by the LTM 60P-75 linear stage under test. The Mk-III firmware was re-programmed to periodically move to a random lateral position and then re-align the optical fibre to the detector. The position of optimal alignment was always approached from the same direction to mitigate the impact of mechanical backlash. Intensity of the excitation source and the PL detected in the photodiode were synchronously sampled at 1 Hz throughout. The test was run for approximately 9 hours for a total of 548 realignments.

The distribution of relative signal offsets across realignments is shown in figure B.2a. It appears approximately normally distributed, with a mean of 6×10^{-5}, a standard deviation of 2×10^{-3}, and only one 4σ event for a sample size of 548. The vast majority of realignments resulted in a sensitivity change of less than 0.5%, while over the course of 9 hours of continual realignments the most significant sensitivity change was 0.9%. This level of performance is adequate for use of the Mk-III prototype as a research platform and for relative clinical dosimetry. Absolute dosimetry would require further refinement, probably in the form of a larger sensitive area for the photo detector, or a mechanism for correcting for small changes in optical performance, such as probing PL intensity.

Monitoring of X-ray Pulse Delivery

X-ray pulse timing was monitored on a Varian Clinac EX producing 6 MV x-rays at 6 Gy/min. The nominal pulse frequency was 360 Hz. Data was acquired using the I-TARG reference channel of the Mk-III electronics. In the relevant part of the circuit, a high speed opto-isolator is driven by the current sourced from accelerator x-ray target, producing digital pulses of approximately 4 μs in duration, which are used to clock a D-type flip-flop. The resulting signal is routed to the ADC via the multiplexer on the reference arm in the analogue front end and digitised synchronously with the signal generated by the active detector (not shown). A subset of this circuit is reproduced in figure B.2b along with the reference channel signal acquired at 10 kHz. Each transition corresponds to an x-ray pulse generated by the accelerator, for which the immediately adjacent samples in the signal channel are expected to contain an unknown fraction of stem signal.

No detector was present in the x-ray beam as the test was only intended to verify the function of the target monitor circuit. Correct operation of the illustrated circuit was also verified with 18 MV x-rays. Beam current for MeV electron modalities is insufficient to forward bias the LED in the opto-isolator.

Fibre Optic Collimator Lenses

The OceanOptics UV-74 fibre collimator lenses used in the filter carousel were mounted on micrometer stages then focused and aligned using a 470 nm LED source. A 1000 μm fibre illuminated by a He-Ar discharge lamp (OceanOptics CAL-2000) was attached to one collimator and the OceanOptics USB2000+ CCD spectrometer to the other. The separation between the collimators was then adjusted from 13 mm to 40 mm, with spectrum at each extreme shown in figure B.2c.

At wavelengths longer than 544 nm the intensity captured by the upstream fibre optic was independent of the lens separation, while for shorter wavelengths larger separations are more efficient. Between 40 mm and 13 mm separation, approximate efficiency losses of 30%, 14%, 8%, and 5% were observed at 254 nm, 312 nm, 364 nm, and 434 nm respectively. This loss accumulates more or less linearly with distance. In the Mk-III design, the collimator separation is 20 mm when mounted in the filter wheel retaining bracket.

Using the same experimental arrangement, approximate scattering losses measured when a bandpass interference filter is interposed in the collimated beam were 13%, 3%, and 1% for 360/12 nm, 585/75 nm, and 405/10 nm filters respectively. These figures are very close to the manufacturer reported nominal bandpass losses.

Detection of $NaMgF_3$:Ni Radioluminescence

As shown in figure 5.5b, cooling the sensitive element of the InGaAs photodiodes results in a shift in the material band gap and so also an increase of the low energy detection limit. Neither photodiode covers the entire $^3T_{2g}(^3F) \rightarrow {}^3A_{2g}(^3F)$ emission from Ni^{2+} and so a loss in system sensitivity is incurred under TE cooling. The G12180-110A and G12181-110K photodiodes have long wavelength limits of 1700 nm and 1900 nm respectively at 20 °C, each reduced by approximately 50 nm at −20 °C. An apparent sensitivity loss of 11% and 14% was observed when the G12180-110A was operated at −10 °C and −15 °C respectively. The corresponding figures for the G12181-110K were 2% and 3% apparent sensitivity loss.

RL from sample J140306 ($NaMgF_3$:Ni) was captured in a 1000 μm silica fibre optic and transmitted through a pair of UV-74 collimator lenses bracketing an RG-830 long pass filter, and finally through another silica optic to the G12180-110A InGaAs photodiode. Photocurrent was measured using the Keithly 6845 picoammeter during irradiation with 40 kVp x-rays at 40 mA tube current in the geometry described in § 3.2.1 and § 3.2.7. The sample was then irradiated for approximately 9 hours, revealing a response in the NIR very similar to that reported for visible emissions in § 4.8.2.

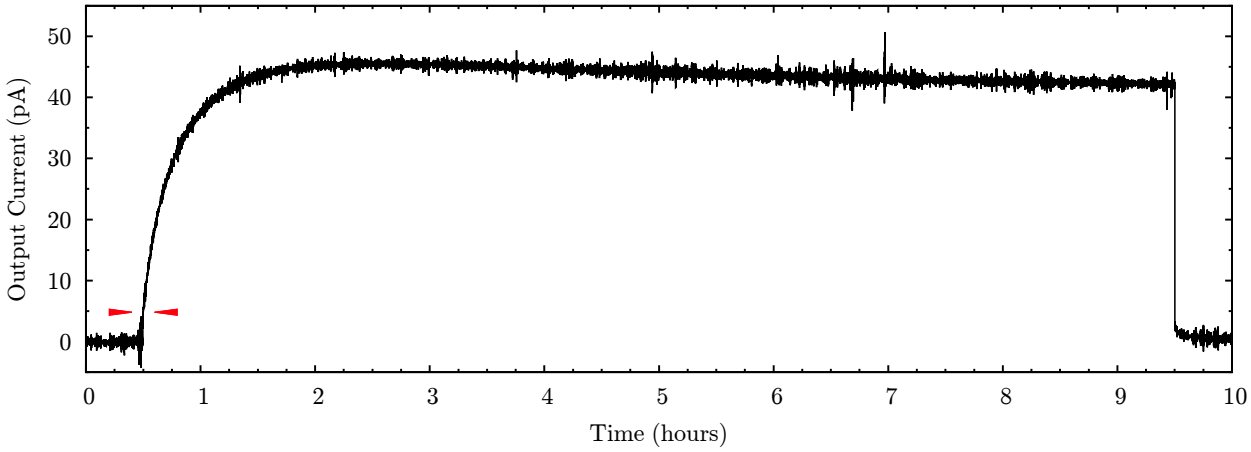

Figure B.3: High dose response of $^3T_{2g}(^3F) \rightarrow {}^3A_{2g}(^3S)$ emission of $NaMgF_3$:Ni (J140306) monitored using the Hamamatsu G12181-110A InGaAs photodiode, demonstrating a SNR of 64 after priming and a dose history dependence on the order of 10^{-6}. The initial RL intensity generates a photocurrent of approximately 5 pA, as indicated with red arrows.

Appendix C

Publications

The following works have been accepted for publication or presented at scientific meetings during the course of the research reported herein.

Peer Reviewed Articles

J. Donaldson, and G. V. M. Williams (2016). 'Photoluminescence, radioluminescence, and thermoluminescence in $NaMgF_3$ activated with Ni^{2+} and Er^{3+}', *Journal of Luminescence*, vol 173, pp 179–285.

J. Donaldson, and G. V. M. Williams (2017). 'A luminescence study of $NaMgF_3$:Dy^{3+} and $NaMgF_3$:Nd^{3+} for applications in radiation dosimetry', *International Journal of Nanotechnology*, vol 14, pp 558–565.

Conference Presentations

J. Donaldson, G. V. M. Williams, L. Greig, S. G. Raymond, J. Steel, C. Gaedtke, and J. Meyer (2011).'Radioluminescence of Fluoroperovskites as Fibre Coupled Dosimeters for Radiotherapy', *Engineering and Physical Sciences in Medicine*, Darwin: Australia.

J. Donaldson, G. V. M. Williams, L. Greig, J. Meyer, C. Gaedtke, and S. G. Raymond (2012). 'Radioluminescence of Fibre Coupled Fluoroperovskites: Characterisation for Radiotherapy', *New Zealand Physics and Engineering in Medicine*, Hamilton: New Zealand.

J. Donaldson, G. V. M. Williams, S. G. Raymond, and C. Gaedtke (2013). 'Radioluminescence of Fibre Coupled Fluoroperovskites: Characterisation for Radiotherapy', *New Zealand Institute of Physics Annual General Meeting*, Nelson: New Zealand.

J. Donaldson, G. V. M. Williams, and S. G. Raymond (2014). 'Characterisation of a Fluoroperovskite Based Fibre Coupled Optical Dosimeter for Radiotherapy', *Annual Condensed Matter and Materials Meeting*, Auckland: New Zealand.

J. Donaldson, and G. V. M. Williams (2015). 'Luminescence Properties of $NaMgF_3$:Er^{3+} for Fibre Optic Dosimetry in Radiotherapy', *Advanced Materials and Nanotechnology*, Nelson: New Zealand.

Bibliography

[1] R. Boyle, "Experiments and Considerations Touching Colours," *Transactions of the Royal Society*, pp. 413–421, 1664.

[2] C. J. Dotzler, *Optically Stimulated Luminescence in Fluoroperovskites for Dosimetric Applications*. PhD thesis, Victoria University of Wellington, Wellington: New Zealand, 2008.

[3] T. Kron, "Thermoluminescence Dosimetry and its Applications in Medicine - Part 2: History and Applications," *Australasian Physical & Engineering Sciences in Medicine*, vol. 18, no. 1, pp. 1–25, 1995.

[4] M. L. Taylor, *et al.*, "A Contemporary Review of Stereotactic Radiotherapy: Inherent Dosimetric Complexities and the Potential for Detriment," *Acta Oncologica*, vol. 50, pp. 483–508, 2011.

[5] J. Valentin, "ICRP Publication 103: The 2007 Recommendations of the International Commission on Radiological Protection," tech. rep., Elsevier, Amsterdam: Netherlands, 2007.

[6] E. J. Hall, & A. J. Giaccia, *Radiobiology for the Radiologist*. Lippincott Williams & Wilkins, Philadelphia: USA, Sixth ed., 2006.

[7] M. Joiner, & A. Kogel, *Basic Clinical Radiobiology*. Hodder Arnold, London: England, Fourth ed., 2009.

[8] W. P. M. Mayles, *et al.*, *IPEM Report 81: Physics Aspects of Quality Control in Radiotherapy*. IPEM, York: England, 1999.

[9] B. J. Mijnheer, *et al.*, "What Degree of Accuracy is Required and Can Be Achieved in Photon and Neutron Therapy?," *Radiotherapy and Oncology*, vol. 8, no. 3, pp. 237–252, 1987.

[10] B. Mijnheer, *et al.*, "Quality Assurance of Treatment Planning Systems: Practical Examples for Non-IMRT Photon Beams," tech. rep., European Society for Therapeutic Radiation Oncology, 2004.

[11] A. Allisy, *et al.*, "ICRU Report 60: Fundamental Quantities and Units for Ionising Radiation," tech. rep., International Commission on Radiation Units and Measurements, 1998.

[12] E. B. Podgorsak, *Radiation Oncology Physics: A Handbook for Teachers and Students*. IAEA, Vienna: Austria, 2005.

[13] H. E. Johns, & J. R. Cunningham, *The Physics of Radiology*. Charles C. Thomas, Springfield, Illinois: USA, Fourth ed., 1983.

[14] F. M. Khan, *The Physics of Radiation Therapy*. Williams & Wilkins, Baltimore, Maryland: USA, Fourth ed., 2010.

[15] J. A. Haider, *et al.*, "A General Cavity Theory," *Physics in Medicine and Biology*, vol. 42, no. 3, pp. 491–500, 1997.

[16] P. R. Almond, *et al.*, "AAPM TG-51: Protocol for Clinical Reference Dosimetry of High-energy Photon and Electron Beams," *Medical Physics*, vol. 26, no. 9, pp. 1847–1870, 1999.

[17] P. Andreo, *et al.*, "IAEA TRS-398: Absorbed Dose Determination in External Beam Radiotherapy, An International Code of Practice for Dosimetry Based on Standards of Absorbed Dose to Water," tech. rep., International Atomic Energy Agency, 2000.

[18] T. K. Kumar, & K. V. Reddy, "Effective Atomic Numbers for Materials of Dosimetric Interest," *Radiation Physics and Chemistry*, vol. 50, no. 6, pp. 545–553, 1997.

[19] A. Allisy, *et al.*, "ICRU Report 44: Tissue Substitutes in Radiation Dosimetry and Measurement," tech. rep., International Commission on Radiation Units and Measurements, 1989.

[20] J. H. Hubbell, & S. M. Seltzer, "NISTIR 5632: Tables of X-ray Mass Attenuation Coefficients and Mass Energy-Absorption Coefficients from 1 keV to 20 MeV for Elements Z = 1 to 92 and 48 Additional Substances of Dosimetric Interest," tech. rep., National Institute of Standards and Technology, 1995.

[21] J. Van Dyk, *et al.*, *The Modern Technology of Radiation Oncology: A Compendium for Medical Physicists and Radiation Oncologists.* Medical Physics Publishing, Madison, Wisconsin: USA, 1999.

[22] R. Ravichandran, "Has the Time Come for Doing Away with Cobalt-60 Teletherapy for Cancer Treatments?," *Journal of Medical Physics*, vol. 34, no. 2, pp. 63–65, 2009.

[23] J. Van Dyk, & J. J. Battista, "Cobalt-60: An Old Modality, a Renewed Challenge," *Current Oncology*, vol. 3, pp. 8–17, 1996.

[24] Ministry of Health, "Code of Safe Practice for the Use of Irradiation Apparatus in Medical Therapy," tech. rep., Office of Radiation Safety, New Zealand, 2010.

[25] T. Aalbers, *et al.*, *IAEA TECDOC-1585: Measurement Uncertainty, A Practical Guide for Secondary Standard Dosimetry Laboratories.* IAEA, Vienna: Austria, 2008.

[26] J. W. Boag, "Ionisation Measurements at Very High Intensities: Pulse Radiation Beams," *British Journal of Radiology*, vol. 23, no. 274, pp. 601–611, 1950.

[27] H. Tölli, *et al.*, "A Two-Dose-Rate Method for General Recombination Correction for Liquid Ionisation Chambers in Pulsed Beams," *Physics in Medicine and Biology*, vol. 55, no. 15, pp. 4247–4260, 2010.

[28] J .E. Burns, *et al.*, *BJR Supplement 25: Central Axis Depth Dose Data for Use in Radiotherapy.* British Institute of Radiology, London: England, 1996.

[29] M. M. Aspradakis, *et al.*, *IPEM Report 103: Small Field MV Photon Dosimetry.* IPEM, York: England, 2010.

[30] X. A. Li, *et al.*, "Lateral Electron Equilibrium and Electron Contamination in Measurements of Head-scatter Factors using Mini-phantoms and Brass Caps," *Medical Physics*, vol. 22, no. 7, pp. 1167–1170, 1996.

[31] R. Alfonso, *et al.*, "A New Formalism for Reference Dosimetry of Small and Nonstandard Fields," *Medical Physics*, vol. 35, no. 11, pp. 5179–5186, 2008.

[32] P. W. Atkins, *Physical Chemistry.* Oxford University Press, Oxford: United Kingdom, Fifth ed., 1994.

[33] R. A. Serway, *et al.*, *Modern Physics.* Brooks/Cole - Thomson Learning, California: USA, Third ed., 2005.

[34] L. Bøtter-Jensen, *et al.*, *Optically Stimulated Luminescence Dosimetry.* Elsevier Science B. V., Amsterdam: The Netherlands, 2003.

[35] E. G. Yukihara, & S. W. S. McKeever, *Optically Stimulated Luminescence: Fundamentals and Applications.* John Wiley & Sons Ltd, Sussex: England, First ed., 2011.

[36] D. J. Griffiths, *Introduction to Quantum Mechanics.* Pearson Education Inc., New Jersey: USA, Second ed., 2005.

[37] J. G. Solé, *et al.*, *An Introduction to the Optical Spectroscopy of Inorganic Solids.* John Wiley & Sons Ltd, Sussex: England, 2005.

[38] E. Crabb, *et al.*, *Concepts in Transition Metal Chemistry.* Royal Society of Chemistry, Cambridge: England, 2010.

[39] M. J. Winter, *d-Block Chemistry.* Oxford University Press, Oxford: United Kingdom, 1994.

[40] R. Reisfeld, *et al.*, "Europium Probe for Estimation of Site Symmetry in Glass Films, Glasses and Crystals," *Molecular Physics*, vol. 102, no. 11, pp. 1319–1330, 2004.

[41] G. Blasse, "Luminescent Materials: Is There Still News?," *Journal of Alloys and Compounds*, vol. 225, pp. 529–533, 1995.

[42] H. J. Pain, *The Physics of Vibrations and Waves.* John Wiley & Sons Ltd, Sussex: England, Fifth ed., 2005.

[43] V. Levitin, *High Temperature Strain of Metals and Alloys: Physical Fundamentals.* Wiley-VCH, Weinheim: Germany, 2006.

[44] S. W. S. McKeever, & R, Chen, "Luminescence Models," *Radiation Measurements*, vol. 27, no. 5-6, pp. 625–661, 1997.

[45] M. Jong, *et al.*, "Resolving the Ambiguity in the Relation Between Stokes Shift and Huang-Rhys Parameter," *Physical Chemistry Chemical Physics*, vol. 17, pp. 16959–16969, 2015.

[46] B. Henderson, & G. F. Imbusch, *Optical Spectroscopy of Inorganic Solids.* Oxford University Press, Oxford: United Kingdom, 2006.

[47] N. Kaltsoyannis. & P. Scott, *The f Elements.* Oxford University Press, Oxford: United Kingdom, 1999.

[48] G. H. Dieke, *Spectra and Energy Levels of Rare Earth Ions in Crystals.* John Wiley & Sons Ltd, Sussex: England, 1969.

[49] J. McCleverty, *Chemistry of the First Row Transition Metals.* Oxford University Press, Oxford: United Kingdom, 1999.

[50] P. A. Jursinic, "Characterisation of Optically Stimulated Luminescent Dosimeters, OSLDs, for Clinical Dosimetric Measurements," *Medical Physics*, vol. 34, no. 12, pp. 4594–4604, 2007.

[51] P. A. Jursinic, "Changes in Optically Stimulated Luminescent Dosimeter (OSLD) Dosimetric Characteristics with Accumulated Dose," *Medical Physics*, vol. 37, no. 1, pp. 132–140, 2010.

[52] D. J. Huntley, "An Explanation of the Power-law Decay of Luminescence," *Journal of Physics: Condensed Matter*, vol. 18, pp. 1359–1365, 2006.

[53] A. K. Jonscher, & A. de Polignac, "The Time Dependence of Luminescence in Solids," *Journal of Physics C: Solid State Physics*, vol. 17, pp. 6493–6519, 1984.

[54] J. C. Polf, *et al.*, "Real-time Luminescence from Al_2O_3 Fibre Dosimeters," *Radiation Measurements*, vol. 38, pp. 227–240, 2004.

[55] R. B. Hughes-Currie, *et al.*, "Site-selective Transient Photoluminescence Enhancement of Impurity-trapped Excitons in $NaMgF_3$:Yb^{2+}," *Physical Review B*, vol. 88, pp. 104302:1–11, 2013.

[56] G. A. Kumar, *et al.*, "Intense Visible and Near Infrared Up-conversion in M_2O_2S:Er (M=Y, Gd, La) Phosphor Under 1550 nm Excitation," *Materials Letters*, vol. 68, pp. 395–398, 2012.

[57] M. Wang, *et al.*, "Up-conversion Nanoparticles: Synthesis, Surface Modification, and Biological Applications," *Nanomedicine: Nanotechnology, Biology and Medicine*, vol. 7, pp. 710–729, 2011.

[58] J. Barthe, D. Blanc, "Model for the Establishment of Radiophotoluminescence in Silver-activated Meta-phosphate Glasses," *Journal of Luminescence*, vol. 18/19, pp. 396–401, 1979.

[59] Y. Ihara, *et al.*, "A Compact System for Measuring Radiophotoluminescence of Phosphate Glass Dosimeter," *Radiation Measurements*, vol. 43, pp. 542–545, 2008.

[60] J. H. Schulman, *et al.*, "Dosimetry of X-Rays and Gamma-Rays by Radiophotoluminescence," *Journal of Applied Physics*, vol. 22, no. 12, pp. 1479–1487, 1951.

[61] M. Ranogajek-Komor, *et al.*, "Characterisation of Radiophotoluminescence Dosimeter for Environmental Monitoring," *Radiation Measurements*, vol. 43, pp. 392–396, 2008.

[62] Asahi Glass Co., Ltd., *RPL Glass Dosimeter / Small Element System; Dose Ace Technical Guide*, 2007.

[63] M. S. Akselrod, *et al.*, "Thermal Quenching of F-centre Luminescence in Al_2O_3:C," *Journal of Applied Physics*, vol. 84, no. 6, pp. 3364–3373, 1998.

[64] S. Vincellér, *et al.*, "Influence of Thermal Quenching on the Thermostimulated Process in α-Al_2O_3. Role of F and F+ Centres," *Radiation Protection Dosimetry*, vol. 100, no. 1-4, pp. 79–82, 2002.

[65] M. S. Akselrod, *et al.*, "Optically Stimulated Luminescence and it's use in Medical Dosimetry," *Radiation Measurements*, vol. 41, pp. S78–S99, 2007.

[66] A. R. Beierholm, *et al.*, "A Comparison of BCF-12 Organic Scintillators and Al_2O_3:C Crystals for Real-time Medical Dosimetry," *Radiation Measurements*, vol. 43, pp. 898–903, 2008.

[67] S. R. Cherry, *et al.*, *Physics in Nuclear Medicine*. Saunders, Pennsylvania: USA, Third ed., 2003.

[68] M. J. Weber, "Inorganic Scintillators: Today and Tomorrow," *Journal of Luminescence*, vol. 100, pp. 35–45, 2002.

[69] A. R. Beierholm, *et al.*, "Organic Scintillators with Long Luminescent Lifetimes for Radiotherapy Dosimetry," *Radiation Measurements*, vol. 46, pp. 1982–1984, 2011.

[70] V. N. Salimgareeva, & S. V. Kolesov, "Plastic Scintillators Based on Polymethyl Methacrylate: A Review," *Instruments and Experimental Techniques*, vol. 48, no. 3, pp. 273–282, 2005.

[71] H. C. Sharma, & R. Kharb, *Comprehensive Physics for Engineers*. Firewall Media, Delhi: India, Fourth ed., 2005.

[72] A. I. Popov, *et al.*, "Basic Properties of the *F*-type Centres in Halides, Oxides and Perovskites," *Nuclear Instruments and Methods in Physics Research B*, vol. 268, pp. 3084–3089, 2010.

[73] R. A. Johnson, & A. N. Orlov, *Modern Problems in Condensed Matter Sciences, Vol 13: Physics of Radiation Effects in Crystals*. North-Holland Physics Publishing, Amsterdam: The Netherlands, 1986.

[74] D. Y. Smith, & G. Graham, "Oscillator Strengths of Defects in Insulators: The Generalisation of Smakula's Equation," *Journal de Physique*, vol. 41, no. 7, pp. 80–83, 1980.

[75] D. L. Dexter, "Absorption of Light by Atoms in Solids," *Physical Review*, vol. 101, no. 1, pp. 48–55, 1956.

[76] C. R. Riley, & W. A. Sibley, "Colour Centres in $KMgF_3$," *Physical Review B*, vol. 1, no. 6, pp. 2789–2798, 1970.

[77] W. B. Fowler, "Phonon-induced Optical Transitions in Colour Centres in Ionic Solids," *Journal of Luminescence*, vol. 1-2, pp. 755–765, 1970.

[78] J. R. Seretlo, *et al.*, "Optical Absorption of Radiation-produced Defects in $NaMgF_3$ and $RbCaF_3$," *Physical Review B*, vol. 14, no. 2, pp. 5404–5412, 1976.

[79] G. V. M. Williams, *et al.*, "Observation of Photoluminescence and Radioluminescence in Eu and Mn Doped $NaMgF_3$ Nanoparticles," *Journal of Luminescence*, vol. 143, pp. 219–225, 2013.

[80] T. Kron, "Thermoluminescence Dosimetry and its Applications in Medicine - Part 1: Physics, Materials and Equipment," *Australasian Physical & Engineering Sciences in Medicine*, vol. 17, no. 4, pp. 175–199, 1994.

[81] E. M. Yoshimura, & E. G. Yukihara, "Optically Stimulated Luminescence: Searching for New Dosimetric Materials," *Nuclear Instruments and Methods in Physics Research, Section B: Beam Interactions with Materials and Atoms*, vol. 250, pp. 337–341, 2006.

[82] D. R. Lide, *et al.*, *CRC Handbook of Chemsitry and Physics*. Chemical Rubber Publishing Company: USA, 73^{rd} ed., 1992.

[83] E. Bulur, & B. E. Saraç, "Time-resolved OSL Studies on BeO Ceramics," *Radiation Measurements*, vol. 59, pp. 129–138, 2013.

[84] C. Arun, *et al.*, "Monte Carlo Based Energy Response Studies of Diode Dosimeters in Radiotherapy Photon Beams," *Radiological Physics and Technology*, vol. 6, no. 1, pp. 151–156, 2012.

[85] S. F. de Boer, *et al.*, "Optical Filtering and Spectral Measurements of Radiation-induced Light in Plastic Scintillation Dosimetry," *Physics in Medicine and Biology*, vol. 38, pp. 945–958, 1993.

[86] E. C. T. Chao, *et al.*, "Neighbourite, $NaMgF_3$, a New Mineral From the Green River Formation, South Ouray, Utah," *The American Mineralogist*, vol. 46, pp. 379–393, 1961.

[87] M. A. Clift, *et al.*, "Water Equivalence of Plastic Organic Scintillators in Megavoltage Radiotherapy Bremsstrahlung Beams," *Physics in Medicine and Biology*, vol. 45, pp. 1185–1195, 2000.

[88] G. Erfurt & M. R. Krbetschek, "A Radioluminescent Study of Spectral and Dose Characteristics of Common Luminophors," *Radiation Protection Dosimetry*, vol. 100, pp. 403–406, 2002.

[89] L. He, *et al.*, "Effects of the Vacancy Point-defect on the Refractive Index and Equation of State (EOS) of LiF at High Pressure: A First Principles Investigation," *Physica B*, vol. 407, pp. 697–697, 2012.

[90] S. M. Hosseini, *et al.*, "First-principles Study of the Optical Properties of Pure α-Al_2O_3 and La Aluminates," *The European Physical Journal B*, vol. 43, pp. 439–444, 2005.

[91] T. Kurobori, *et al.*, "Lifetime of F_2 and F_3^+ Centres in LiF Crystals Doped with Magnesium," *Optics Communications*, vol. 64, no. 3, pp. 259–263, 1987.

[92] T. Kurobori, *et al.*, "Lifetimes of some Excited F-aggregate Centres in LiF," *Journal of Physics C: Solid State Physics*, vol. 21, no. 12, pp. L397–L402, 1988.

[93] M. Moscovitch, & Y. S. Horowitz, "Thermoluminescent Materials for Medical Applications: LiF:Mg,Ti and LiF:Mg,Cu,P," *Radiation Measurements*, vol. 41, pp. S71–S77, 2007.

[94] A. J. D. Scott, *et al.*, "Characterising the Effect of Detector Density on Dosimeter Response in Non-equilibrium Small Photon Fields," *Physics in Medicine and Biology*, vol. 57, pp. 4461–4476, 2012.

[95] E. G. Yukihara, "Luminescence Properties of BeO Optically Stimulated Luminescence (OSL) Detectors," *Radiation Measurements*, vol. 46, pp. 580–587, 2011.

[96] Saint-Gobain Crystals, *Premium Plastic Scintillators; BC-400, BC-404, BC-408, BC-412, BC-416*, 2008.

[97] Saint-Gobain Crystals, *Green Emitting Plastic Scintillator; BC-428*, 2008.

[98] Saint-Gobain Crystals, *Red Emitting Premium Plastic Scintillator; BC-430*, 2008.

[99] Saint-Gobain Crystals, *Organic Scintillation Materials*, 2011.

[100] Saint-Gobain Crystals, *Scintillating Optical Fibres*, 2011.

[101] Saint-Gobain Crystals, *Long Timing Constant Plastic Scintillator; BC-444*, 2008.

[102] V. Dauer, "Optical Constants of Lithium Fluoride Thin Films in the Far Ultraviolet," *Journal of the Optical Society of America B: Optical Physics*, vol. 17, no. 2, pp. 300–303, 2000.

[103] C. J. Karzmark, *et al.*, "Lithium Fluoride Thermoluminescence Dosimetry," *Physics in Medicine and Biology*, vol. 9, no. 3, pp. 273–286, 1964.

[104] E. H. Melvin, "The Transparency of Sodium Fluoride and Lithium Fluoride in the Extreme Ultraviolet," *Physical Review*, vol. 37, pp. 1230–1232, 1931.

[105] V. Kvatchadze, *et al.*, "Thermally Stimulated Luminescence Origin in LiF Crystals Irradiated in a Reactor at Different Temperatures," *Radiation Effects & Defects in Solids*, vol. 170, no. 6, pp. 477–483, 2015.

[106] L. Oster, *et al.*, "Optically Stimulated Luminescence in LiF:Mg,Ti: Application to Solid-state Radiation Dosimetry," *Nuclear Instruments and Method sin Physics Research A*, vol. 648, pp. 261–265, 2011.

[107] A. Abtahi, *et al.*, "Laser Stimulated Thermoluminescence," *Journal of Applied Physics*, vol. 58, no. 4, pp. 1626–1639, 1985.

[108] P. Bräunlich, *et al.*, "Laser Heating of Thermoluminescence Dielectric Layers," *Applied Physics Letters*, vol. 39, no. 9, pp. 769–771, 1981.

[109] J. Gasiot, *et al.*, "Laser Heating of Thermoluminescence Dosimetry," *Journal of Applied Physics*, vol. 53, no. 7, pp. 5200–5209, 1981.

[110] R. E. Nyswander, & B. E. Cohn, "Trbiothermoluminescence," *Physical Review*, vol. 36, pp. 1257–1260, 1930.

[111] E. Carinou, *et al.*, "Energy Dependence of TLD 100 and MCP-N Detectors," *Radiation Measurements*, vol. 43, no. 2-6, pp. 599–602, 2008.

[112] J. G. Holt, *et al.*, "Energy Dependence of the Response of Lithium Fluoride TLD Rods in High Energy Electron Fields," *Physics in Medicine and Biology*, vol. 20, no. 4, pp. 559–570, 1975.

[113] K. Momma, & F. Izumi, "VESTA 3 for Three-dimensional Visualisation of Crystal, Volumetric and Morphology Data," *Journal of Applied Crystallography*, vol. 44, pp. 1272–1276, 2011.

[114] C. E. Andersen, *et al.*, "Characterisation of a Fibre-coupled Al_2O_3:C Luminescence Dosimetry System for Online *in vivo* Dose Verification During ^{192}Ir Brachytherapy," *Medical Physics*, vol. 36, no. 3, pp. 708–718, 2009.

[115] J. M. Edmund, *et al.*, "CW-OSL Measurement Protocols Using Optical Fibre Al_2O_3:C Dose-meters," *Radiation Protection Dosimetry*, vol. 119, no. 1-4, pp. 368–374, 2006.

[116] E. G. Yukihara, *et al.*, "The Effects of Deep Trap Population on the Thermoluminescence of Al_2O_3:C," *Radiation Measurements*, vol. 37, pp. 627–638, 2003.

[117] C. E. Andersen, *et al.*, "Temperature Coefficients for *in vivo* RL and OSL Dosimetry Using Al_2O_3:C," *Radiation Measurements*, vol. 43, pp. 948–953, 2008.

[118] C. E. Andersen, *et al.*, "Precision of RL/OSL Medical Dosimetry with Fibre-coupled Al_2O_3:C: Influence of Readout Delay and Temperature Variations," *Radiation Measurements*, vol. 45, pp. 653–657, 2010.

[119] S. M. S. Damkjær, & C. E. Andersen, "Memory Effects and Systematic Errors in the RL Signal from Fibre Coupled Al_2O_3:C for Medical Dosimetry," *Radiation Measurements*, vol. 45, pp. 671–673, 2010.

[120] J. M. Edmund, & C. E. Andersen, "Temperature Dependence of the Al_2O_3:C Response in Medical Luminescence Dosimetry," *Radiation Measurements*, vol. 42, pp. 177–189, 2007.

[121] R. Gaza, *et al.*, "A Fibre-dosimetry Method Based on OSL from Al_2O_3:C for Radiotherapy Applications," *Radiation Measurements*, vol. 38, pp. 809–812, 2004.

[122] C. S. Reft, "The Energy Dependence and Dose Response of a Commercial Optically Stimulated Luminescence Detector in Kilovoltage, Megavoltage, Photon, and Electron, Proton, and Carbon Beams," *Medical Physics*, vol. 36, no. 5, pp. 1690–1699, 2009.

[123] C. J. Marckmann, *et al.*, "Optical Fibre Dose-meter Systems for Clinical Applications Based on Radioluminescence and Optically Stimulated Luminescence from Al_2O_3:C," *Radiation Protection Dosimetry*, vol. 120, no. 1-4, pp. 28–32, 2006.

[124] S. W. S. McKeever, *et al.*, "Recent Advances in Dosimetry Using the Optically Stimulated Luminescence of Al_2O_3:C," *Radiation Protection Dosimetry*, vol. 109, no. 4, pp. 269–276, 2004.

[125] E. G. Yukihara, *et al.*, "Development of New optically Stimulated Luminescence (OSL) Neutron Dosimeters," *Radiation Measurements*, vol. 43, pp. 309–314, 2008.

[126] V. Schembri, & B. J. M. Heijman, "Optically Stimulated Luminescence (OSL) of Carbon-doped Aluminium Oxide (Al_2O_3:C) for Film Dosimetry in Radiotherapy," *Medical Physics*, vol. 34, no. 6, pp. 2113–2118, 2007.

[127] J. M. Edmund, *et al.*, "Optically Stimulated Luminescence from Al_2O_3:C Irradiated with 10-60 MeV Protons," *Nuclear Instruments and Methods in Physics Research A*, vol. 580, pp. 210–213, 2007.

[128] R. Gaza, *et al.*, "The Response of Thermally and Optically Stimulated Luminescence from Al_2O_3:C to High-energy Heavy Charged Particles," *Radiation Measurements*, vol. 38, pp. 417–420, 2004.

[129] G. O. Sawakuchi, *et al.*, "Overlap of Heavy Charged Particle Tracks and the Change in Shape of Optically Stimulated Luminescence Curves of Al_2O_3:C Dosimeters," *Radiation Measurements*, vol. 43, pp. 194–198, 2008.

[130] E. G. Yukihara, *et al.*, "Optically Stimulated Luminescence and Thermoluminescence Efficiencies for Higher-energy Heavy Charged Particle Irradiation in Al_2O_3:C," *Radiation Measurements*, vol. 38, pp. 59–70, 2004.

[131] M. S. Akselrod, *et al.*, "Highly Sensitive Thermoluminescent Anion-defective α-Al_2O_3:C Single Crystal Detectors," *Radiation Protection Dosimetry*, vol. 32, no. 1, pp. 15–20, 1990.

[132] Landauer Inc., *Luxel+ Dosimeter for X, Gamma, Beta, and Neutron Radiation*, 2005.

[133] A. Viamonte, *et al.*, "Radiotherapy Dosimetry Using a Commercial OSL System," *Medical Physics*, vol. 35, no. 4, pp. 1261–1266, 2008.

[134] S. Mo, *et al.*, "Electronic and Structural Properties of Bulk γ-Al_2O_3," *Journal of the American Ceramic Society*, vol. 80, no. 5, pp. 1193–1197, 1997.

[135] L. A. Aslanov, "Crystal-chemical Model of Atomic Interactions. 2. Hexagonal, Trigonal, and Tetragonal Systems," *Acta Crystallographica B*, vol. 44, no. 5, pp. 458–462, 1988.

[136] E. N. Maslen, *et al.*, "Synchrotron X-ray Study of the Electron Density in α-Al_2O_3," *Acta Crystallographica B*, vol. 49, no. 6, pp. 973–980, 1993.

[137] J. N. Mitchell, *et al.*, "Radiation Effects in Corundum Structure Derivatives," *Nuclear Instruments and Methods in Physics Research B*, vol. 141, pp. 461–466, 1998.

[138] A. Vijay, *et al.*, "Structure of the (001) Surface of γ Alumina," *Journal of Chemical Physics*, vol. 117, no. 9, pp. 4509–4516, 2002.

[139] K. H. Lee, & J. H. Crawford, "Luminescence of the F Centre in Sapphire," *Physical Review B*, vol. 19, no. 6, pp. 3217–3221, 1979.

[140] X. B. Yang, *et al.*, "Influence of Carbon on the Thermoluminescence and Optically Stimulated Luminescence of α-Al_2O_3:C Crystals," *Journal of Applied Physics*, vol. 104, pp. 123112:1–6, 2008.

[141] R. D. Shannon, "Revised Effective Atomic Radii and Systematic Studies of Inter-atomic Distances in Halides and Chalcogenides," *Acta Crystallographica A*, vol. 32, pp. 751–767, 1976.

[142] G. Erfurt, *et al.*, "Radioluminescence (RL) Behaviour of Al_2O_3:C - Potential for Dosimetric Applications," *Radiation Measurements*, vol. 32, pp. 735–739, 2000.

[143] M. F. Ahmed, *et al.*, "Comparison Between Different Readout Approaches for Aluminium Oxide Radiophotoluminescent Crystals," *Radiation Measurements*, vol. 56, pp. 361–364, 2013.

[144] M. S. Akselrod, & G. J. Sykora, "Fluorescent Nuclear Track Detector Technology - A New Way to do Passive Solid State Dosimetry," *Radiation Measurements*, vol. 46, pp. 1671–1679, 2011.

[145] S. A. Eller, *et al.*, "Radiophotoluminescence Properties of Al_2O_3:C,Mg Crystals," *Radiation Measurements*, vol. 56, pp. 179–182, 2013.

[146] G. Busuoli, *et al.*, "TL Personnel Dosimeter with BeO," *Nuclear Instruments and Methods*, vol. 140, pp. 385–388, 1977.

[147] G. Scarpa, "The Dosimetric Use of Beryllium Oxide as a Thermoluminescent Material: A Preliminary Study," *Physics in Medicine and Biology*, vol. 15, no. 4, pp. 667–672, 1970.

[148] E. Bulur, & H. Y. Göksu, "OSL from BeO Ceramics: New Observations From an Old Material," *Radiation Measurements*, vol. 29, no. 6, pp. 639–650, 1998.

[149] E. Bulur, "Photo-transferred Luminescence from BeO Ceramics," *Radiation Measurements*, vol. 42, pp. 334–340, 2007.

[150] E. Bulur, & A. Yeltik, "Optically Stimulated Luminescence from BeO Ceramics: An LM-OSL Study," *Radiation Measurements*, vol. 45, pp. 29–34, 2010.

[151] M. Sommer, & J. Henniger, "Investigation of a BeO-based Optically Stimulated Luminescence Dosimeter," *Radiation Protection Dosimetry*, vol. 119, no. 1-4, pp. 394–397, 2006.

[152] M. Sommer, *et al.*, "New Aspects of a BeO-based Optically Stimulated Luminescence Dosimeter," *Radiation Measurements*, vol. 42, pp. 617–620, 2007.

[153] M. Sommer, *et al.*, "Beryllium Oxide as Optically Stimulated Luminescence Dosimeter," *Radiation Measurements*, vol. 43, pp. 353–356, 2008.

[154] A. Jahn, *et al.*, "2D-OSL-dosimetry with Beryllium Oxide," *Radiation Measurements*, vol. 45, pp. 674–676, 2010.

[155] A. Jahn, *et al.*, "Progress in 2D OSL Dosimetry with Beryllium Oxide," *Radiation Measurements*, vol. 46, pp. 1908–1911, 2011.

[156] A. Santos, *et al.*, "BeO Fibre Optic Dosimeter," in *EPSM-ABEC Conference Proceedings*, 2011.

[157] A. Santos, *et al.*, "Characterisation of an RL/OSL Beryllium Oxide (BeO) Ceramic Fibre-coupled Luminescence Dosimeter in 6 MV X-ray Beams," in *Engineering & Physical Sciences in Medicine Conference*, 2012.

[158] American Beryllia Inc., *Material Safety Data Sheet: Beryllium Oxide Sintered Ceramic*, 1986.

[159] J. W. Downs, *et al.*, "The Effects of Extinction on the Refined Structural Parameters of Crystalline BeO: a Neutron and X-ray Diffraction Study," *Acta Crystallographica B*, vol. 41, no. 6, pp. 425–431, 1985.

[160] T. M. Sabine, & S. Hogg, "The Wurtzite Z Parameter for Beryllium Oxide and Zinc Oxide," *Acta Crystallographica B*, vol. 25, no. 11, pp. 2254–2256, 1969.

[161] V. Y. Ivanov, *et al.*, "Time-resolved Spectroscopy of Natural and Synthetic BeO Crystals," *Journal of Surface Investigations*, vol. 4, no. 4, pp. 671–674, 2010.

[162] A. V. Kruzhalov, *et al.*, "Metastable Defects in Beryllium Oxide Crystals," *Nuclear Instruments and Methods in Research A*, vol. 486, pp. 325–329, 2002.

[163] A. D. Bross, "Scintillating Plastic Optical Fibre Radiation Detectors in High Energy Particle Physics," in *SPIE Conference on Optical Fibre Technology*, 1991.

[164] A. S. Beddar, *et al.*, "Water-equivalent Plastic Scintillation Detectors for High-energy Beam Dosimetry: I. Physical Characteristics and Theoretical Considerations," *Physics in Medicine and Biology*, vol. 37, no. 10, pp. 1883–1900, 1992.

[165] A. S. Beddar, *et al.*, "Water-equivalent Plastic Scintillation Detectors for High-energy Beam Dosimetry: II. Properties and Measurements," *Physics in Medicine and Biology*, vol. 37, no. 10, pp. 1901–1913, 1992.

[166] Z. Li, *et al.*, "Properties of Plastic Scintillators After Irradiation," *Nuclear Instruments and Methods in Physics Research A*, vol. 552, pp. 449–445, 2005.

[167] V. G. Vasil'chenko, *et al.*, "New Results on Radiation Damage Studies of Plastic Scintillators," *Nuclear Instruments and Methods in Physics Research A*, vol. 369, pp. 55–61, 1996.

[168] G. H. Schmid, *Organic Chemistry*. Mosby Year-Book, Inc., Missouri: USA, 1996.

[169] S. W. Moser, *et al.*, "Principles and Practice of Plastic Scintillator Design," *Radiation Physics and Chemistry*, vol. 41, no. 1/2, pp. 31–36, 1993.

[170] P. A. Cahill, "Toward Red-emitting Radiation Tolerant Chromophores," *Radiation Physics and Chemistry*, vol. 41, no. 1/2, pp. 351–363, 1993.

[171] R. Alcala, *et al.*, "Optical Transitions of Eu^{2+} Ions in $RbMgF_3$ Crystals," *Journal of Luminescence*, vol. 27, pp. 273–284, 1982.

[172] R. Francini, *et al.*, "Two-photon Spectroscopy of Eu^{2+} in Cubic Perovskite $KMgF_3$," *Journal of Luminescence*, vol. 72-74, pp. 188–189, 1997.

[173] J. Garcia M., *et al.*, "Optical Properties of Eu^{2+}, Eu^{3+} and Mn^{2+} in Cubic Perovskite Crystals," *Journal of Luminescence*, vol. 42, pp. 35–42, 1988.

[174] J. Garcia M., & W. A. Sibley, "Energy Transfer Between Europium Ions in Fluoroperovskite Crystals," *Journal of Luminescence*, vol. 42, pp. 109–116, 1988.

[175] F. Rodriguez, *et al.*, "Luminescence Properties of Mn^{2+} in $KMgF_3$ and $KZnF_3$ Perovskite Crystals: Evidence of a Dynamical Jahn-Teller Effect," *Journal of Luminescence*, vol. 50, pp. 101–110, 1999.

[176] D. K. Sardar, *et al.*, "Radiation-defect-perturbed Er^{2+} and Mn^{2+} Optical Transitions in $RbMgF_3$," *Physical Review B*, vol. 26, no. 5, pp. 2382–2389, 1982.

[177] D. K. Sardar, *et al.*, "Optical Absorption and Emission From Irradiated $RbMgF_3$:Eu^{2+} and $KMgF_3$:Eu^{2+}," *Journal of Luminescence*, vol. 27, pp. 401–411, 1982.

[178] M. D. Shinn, *et al.*, "Optical Transitions of Er^{3+} Ions in $RbMgF_3$ and $RbMgF_3$:Mn," *Physical Review B*, vol. 26, no. 5, pp. 2371–2381, 1982.

[179] M. D. Shinn, & W. A. Sibley, "Eu^{2+}-sensitised Mn^{2+} Luminescence in $RbMgF_3$:Mn,Eu," *Physical Review*, vol. 29, no. 7, pp. 3834–3842, 1984.

[180] J. L. Sommerdijk, & A. Bril, "On the Luminescence of $CsCaF_3$:Eu^{2+}," *Journal of Luminescence*, vol. 10, pp. 145–147, 1975.

[181] J. L. Sommerdijk, & A. Bril, "On the Luminescence of $LiBaF_3$:Eu^{2+}," *Journal of Luminescence*, vol. 10, pp. 411–413, 1975.

[182] J. L. Sommerdijk, & A. Bril, "Divalent Europium Luminescence in Perovskite-like Alkaline-earth Alkaline Fluorides," *Journal of Luminescence*, vol. 11, pp. 363–367, 1975.

[183] J. L. Sommerdijk, *et al.*, "Luminescence of Eu^{2+}-activated Cs(Ca, Mg)F_3 and Rb(Ca, Mg)F_3," *Journal of Luminescence*, vol. 15, pp. 115–118, 1977.

[184] E. G. Valyashko, *et al.*, "Spectra of Eu^{2+} in $KMgF_3$ and $NaMgF_3$ Crystals," *Translated from Zhurnal Prikladnoi Spektroskopii (Journal of Applied Spectroscopy)*, vol. 2, no. 5, pp. 876–822, 1977.

[185] G. I. Dallas, "Correlation Between TL and OSL Signals in $KMgF_3$:Ce^{3+}: Bleaching Study of Individual Glow-peaks," *Radiation Measurements*, vol. 45, pp. 537–539, 2010.

[186] C. Dotlzer, *et al.*, "The Effect of x-ray, γ-ray, and UV Radiations on the Optical Properties of $RbCdF_3$:Mn^{2+}," *Journal of Applied Physics*, vol. 100, pp. 033102:1–7, 2006.

[187] C. Dotzler, *et al.*, "Optically Stimulated Luminescence in $NaMgF_3$:Eu^{2+}," *Applied Physics Letters*, vol. 91, pp. 121910:1–3, 2007.

[188] C. Dotzler, *et al.*, "$RbCdF_3$:Mn^{2+}: A Potential Ultraviolet Dosimeter Material," *Applied Physics Letters*, vol. 91, pp. 181909:1–3, 2007.

[189] C. Dotzler, *et al.*, "Thermoluminescence, Photoluminescence and Optically Stimulated Luminescence Properties of X-ray Irradiated $RbMgF_3$:Mn^{2+}," *Physica Status Solidi C*, vol. 4, no. 3, pp. 992–995, 2007.

[190] C. Dotzler, *et al.*, "Dosimetric Properties of $RbCdF_3$:Mn^{2+}," *Radiation Measurements*, vol. 42, pp. 586–589, 2007.

[191] C. Dotzler, *et al.*, "Radiation-induced Optically and Thermally Stimulated Luminescence in $RbCdF_3$ and $RbMgF_3$," *Current Applied Physics*, vol. 8, pp. 447–450, 2008.

[192] C. Dotzler, *et al.*, "Photoluminescence, Optically Stimulated Luminescence, and Thermoluminescence Study of $RbMgF_3$:Eu^{2+}," *Journal of Applied Physics*, vol. 105, pp. 023107:1–7, 2009.

[193] G. V. M. Williams, *et al.*, "Radiation-induced Optically Stimulated Luminescence in Mn^{2+} and Eu^{2+} doped $RbMgF_3$," *Physica Status Solidi C*, vol. 6, no. S1, pp. S198–S201, 2009.

[194] G. V. M. Williams, & S. G. Raymond, "Fibre-optic-coupled $RbMgF_3$:Eu^{2+} for Remote Radiation Dosimetry," *Radiation Measurements*, vol. 46, pp. 1099–1102, 2011.

[195] M. Johnsson, & P. Lemmens, "Crystallography and Chemistry of Perovskites," in *Handbook of Magnetism and Advanced Magnetic Materials*, John Wiley & Sons Ltd, Sussex: England, 2007.

[196] R. D. Shannon, & C. T. Prewitt, "Effective Ionic Radii in Oxides and Fluorides," *Acta Crystallographica B*, vol. 25, pp. 925–946, 1969.

[197] J. Rubio, "Doubly-valent Rare Earth Ions in Halide Crystals," *Journal of Physics and Chemistry of Solids*, vol. 52, no. 1, pp. 101–174, 1991.

[198] H. J. Seo, *et al.*, "Eu^{3+} Luminescence in Eu-doped $KMgF_3$ Crystals Investigated by Site-selective Laser-excitation Spectroscopy," *Physical Review B*, vol. 70, no. 20, pp. 205113:1–8, 2004.

[199] J. A. Sommerdijk, & A. Bril, "On the Position of the $^5D_0$ Level of Eu^{3+} in $AMgF_3$ (A = K, Rb, Cs)," *Journal of Luminescence*, vol. 12/13, pp. 669–673, 1976.

[200] A. L. Huston, *et al.*, "Remote Optical Fibre Dosimetry," *Nuclear Instruments and Methods in Physics Research B*, vol. 184, pp. 55–67, 2001.

[201] G. Espinosa, *et al.*, "Commercial Optical Fibre as TLD Material," *Radiation Protection Dosimetry*, vol. 119, no. 1-4, pp. 197–200, 2006.

[202] M. Azadeh, *Fibre Optics Engineering*. Springer Science+Business Media, New York: USA, 2009.

[203] E. Hecht, *Optics*. Addison Wesley, San Francisco: USA, Fourth ed., 2002.

[204] O. Ziemann, *et al.*, *POF Handbook: Optical Short Range Transmission Systems*. Springer-Verlag, Berlin: Germany, Second ed., 2008.

[205] A. S. Beddar, "Plastic Scintillation Dosimetry: Optimisation of Light Collection Efficiency," *Physics in Medicine and Biology*, vol. 48, pp. 1141–1152, 2003.

[206] R. L. Freeman, *Fibre-optic Systems for Telecommunications*. Wiley Interscience: USA, 2002.

[207] R. H. French, *et al.*, "Absorption Edge and Band Gap of SiO_2 Fused Silica Glass," *Ceramic Transactions*, vol. 28, pp. 63–80, 1992.

[208] H. M. Zidan, & Z. Abu-Elnader, "Structural and Optical Properties of Pure PMMA and Metal Chloride-doped PMMA Films," *Physica B*, vol. 355, pp. 308–317, 2005.

[209] Thorlabs, *0.48 NA Hard Polymer Clad Multi-mode Fibre*, 2013.

[210] D. F. Edwards, & R. H. White, *Handbook of Optical Constants of Solids II*. Academic Press, Orlando: USA, 1991.

[211] T. Depireux, *et al.*, "Measurement of the Complex Refractive index of Polyvinyl-toluene in the UV, Visible, and Near IR: Application to the Size Determination of PVT Lattices," *Journal of Colloid and Interface Science*, vol. 118, no. 2, pp. 314–325, 1987.

[212] I. H. Malitson, "Inter-specimen Comparison of the Refractive Index of Fused Silica," *Journal of the Optical Society of America*, vol. 55, no. 10, pp. 1205–1208, 1965.

[213] I. H. Malitson, & M. J. Dodge, "Refractive Index and Birefringence of Synthetic Sapphire," *Journal of the Optical Society of America*, vol. 62, no. 11, p. 1405, 1972.

[214] D. C. Miller, *et al.*, "Analysis of Transmitted Optical Spectrum Enabling Accelerated Testing of CPV Designs," in *Society of Photographic Instrumentation Engineers Solar Energy + Technology Conference*, 2009.

[215] N. Sultanova, *et al.*, "Dispersion Properties of Optical Polymers," *Acta Physica Polonica A*, vol. 116, pp. 585–587, 2009.

[216] L. Zhen-Li, *et al.*, "First-principles Study of the Electronic Structure and Optical Properties of Cubic Perovskite $NaMgF_3$," *Chinese Physics B*, vol. 23, no. 3, pp. 037104:1–6, 2014.

[217] National Institute of Standards and Technology, "Stopping Power and Range Tables for Electrons." Retrieved from *http://physics.nist.gov/PhysRefData/Star/Text/ESTAR.html*, December 2012.

[218] J. C. Salamone, *et al.*, *Polymeric Materials Encyclopedia: Volume 7*. Chemical Rubber Publishing Company: USA, 1996.

[219] D. L. Pavia, *et al.*, *Introduction to Spectroscopy*. Brooks/Cole, Belmont, California: USA, 2009.

[220] Y. Koike, "High-Speed Polymer Optical Fibre Network," *Molecular Crystals and Liquid Crystals Science and Technology A*, vol. 316, pp. 1–6, 1998.

[221] P. Predeep, *et al.*, *Optoelectronics - Devices and Applications*. InTech, Rijeka: Croatia, 2011.

[222] P. S. Kumar, *et al.*, "A Fibre Optic Evanescent Wave Sensor Used for the Detection of Trace Nitrites in Water," *Journal of Optics A: Pure and Applied Optics*, vol. 4, pp. 247–250, 2002.

[223] P. A. Čerenkov, "Visible Radiation Produced by Electrons Moving in a Medium with velocities Exceeding that of Light," *Physical Review*, vol. 52, p. 378, 1937.

[224] J. V. Jelly, "Čerenkov Radiation and its Applications," *British Journal of Applied Physics*, vol. 6, pp. 227–232, 1955.

[225] L. Fülöp, & T. Biró, "Cherenkov Radiation Spectrum," *International Journal of Theoretical Physics*, vol. 31, no. 1, pp. 61–74, 1992.

[226] A. S. Beddar, *et al.*, "Čerenkov Light Generated in Optical Fibres and Other Light Pipes Irradiated by Electron Beams," *Physics in Medicine and Biology*, vol. 37, no. 4, pp. 925–935, 1992.

[227] C. J. Marckmann, *et al.*, "Influence of the Stem Effect on Radioluminescence Signals from Optical Fibre Al_2O_3:C Dose-meters," *Radiation Protection Dosimetry*, vol. 119, no. 1-4, pp. 363–367, 2006.

[228] R. Nowotny, "Radioluminescence of some Optical Fibres," *Physics in Medicine and Biology*, vol. 52, pp. N67–N73, 2007.

[229] Z. W. Bell, & L. A. Boatner, "Neutron Detection via the Cherenkov Effect," *IEEE Transactions on Nuclear Science*, vol. 57, no. 6, pp. 3800–3806, 2010.

[230] A. S. Beddar, *et al.*, "Plastic Scintillation Dosimetry for Radiation Therapy: Minimising Capture of Cerenkov Radiation Noise," *Physics in Medicine and Biology*, vol. 49, pp. 783–790, 2004.

[231] A. S. Beddar, "Plastic Scintillation Dosimetry and it's Application to Radiotherapy," *Radiation Measurements*, vol. 41, pp. S124–S133, 2007.

[232] B. Lee, *et al.*, "Measurement and Elimination of Cherenkov Light in Fibre-optic Scintillator Detector for Electron Beam Therapy Dosimetry," *Nuclear Instruments and Methods in Research A*, vol. 579, pp. 334–348, 2007.

[233] P. Z. Y. Liu, *et al.*, "Plastic Scintillation Dosimetry: Comparison of Three Solutions for the Čerenkov Challenge," *Physics in Medicine and Biology*, vol. 56, pp. 5805–5821, 2011.

[234] M. A. Clift, *et al.*, "Dealing with Cerenkov Radiation Generated in Organic Scintillator Dosimeters by Bremsstrahlung Beams," *Physics in Medicine and Biology*, vol. 45, pp. 1165–1182, 2000.

[235] J. Lambert, *et al.*, "Cerenkov-free Scintillation Dosimetry in External Beam Radiotherapy with an Air Core Light Guide," *Physics in Medicine and Biology*, vol. 53, pp. 3071–3080, 2008.

[236] J. Lambert, *et al.*, "A Prototype Scintillation Dosimeter Customised for Small and Dynamic Megavoltage Radiation Fields," *Physics in Medicine and Biology*, vol. 55, pp. 1115–1126, 2010.

[237] M. A. Clift, *et al.*, "A Temporal Method of Avoiding the Cerenkov Radiation Generated in Organic Scintillator Dosimeters by Pulsed Mega-voltage Electron and Photon Beams," *Physics in Medicine and Biology*, vol. 47, pp. 1421–1433, 2002.

[238] L. R. Lindvold, *et al.*, "An Organic Dye in a Polymer Matrix - A Search for a Scintillator with Long Luminescent Lifetime," *Radiation Measurements*, vol. 45, pp. 615–617, 2010.

[239] J. A. Tanyi, *et al.*, "Performance Characteristics of a Gated Fibre-optic-coupled Dosimeter in High-energy Pulsed Photon Radiation Dosimetry," *Applied Radiation and Isotopes*, vol. 68, pp. 364–369, 2010.

[240] J. M. Fontbonne, *et al.*, "Scintillating Fibre Dosimeter for Radiation Therapy Accelerator," *IEEE Transactions on Nuclear Science*, vol. 49, no. 2, pp. 2223–2227, 2002.

[241] A. M. Frenlin, *et al.*, "Spectral Discrimination of Čerenkov Radiation in Scintillating Dosimeters," *Medical Physics*, vol. 32, no. 9, pp. 3000–3006, 2005.

[242] G. Kertzscher, *et al.*, "Stem Signal Suppression in Fibre-coupled Al_2O_3:C Dosimetry for ^{192}Ir Brachytherapy," *Radiation Measurements*, vol. 46, pp. 2020–2024, 2011.

[243] F. Therriault-Proulx, *et al.*, "On the Nature of the Light Produced within PMMA Optical Light Guides in Scintillation Fibre-optic Dosimetry," *Physics in Medicine and Biology*, vol. 58, no. 7, pp. 2073–2084, 2013.

[244] P. Z. Y. Liu, *et al.*, "Twisted Pair of Optic Fibres for Background Removal in Radiation Fields," *Applied Optics*, vol. 52, no. 22, pp. 5500–5507, 2013.

[245] I. Veronese, *et al.*, "Infrared Luminescence for Real Time Ionising Radiation Detection," *Applied Physics Letters*, vol. 106, pp. 061103:1–4, 2014.

[246] C. E. Andersen, *et al.*, "Time-resolved *in vivo* Luminescence Dosimetry for Online Error Detection in Pulsed Dose-rate Brachytherapy," *Medical Physics*, vol. 36, no. 11, pp. 5033–5043, 2009.

[247] A. M. C. Santos, *et al.*, "Characterisation of a Real-time Fibre-coupled Beryllium Oxide (BeO) Luminescence Dosimeter in X-ray Beams," *Radiation Measurements*, vol. 53-54, pp. 1–7, 2013.

[248] A. M. C. Santos, *et al.*, "Investigation of a Fibre-coupled Beryllium Oxide (BeO) Ceramic Luminescence Dosimetry System," *Radiation Measurements*, vol. 70, pp. 52–58, 2014.

[249] A. M. C. Santos, *et al.*, "Energy Dependence of a Water-equivalent Fibre-coupled Beryllium Oxide (BeO) Dosimetry System," *Radiation Measurements*, vol. 73, pp. 1–6, 2015.

[250] A. R. Beierholm, *et al.*, "Investigation of Linear Accelerator Pulse Delivery Using Fast Organic Scintillator Measurements," *Radiation Measurements*, vol. 45, pp. 668–670, 2010.

[251] D. M. Klein, *et al.*, "Measuring Output Factors of Small Fields Formed by Collimator Jaws and Multi-leaf Collimator Using Plastic Scintillation Detectors," *Medical Physics*, vol. 37, pp. 5541–5549, 2010.

[252] M. Cararra, *et al.*, "Stem Effect of a Ce^{3+} doped SiO_2 Optical Dosimeter Irradiated with a ^{192}Ir HDR Brachytherapy Source," *Radiation Physics and Chemistry*, vol. 104, pp. 175–179, 2013.

[253] L. Archambault, *et al.*, "Comment on 'Plastic Scintillation Dosimetry: Comparison of Three Solutions for the Čerenkov Challenge'," *Physics in Medicine and Biology*, vol. 57, pp. 3661–3665, 2012.

[254] F. Lacroix, *et al.*, "A Design Methodology using Signal-to-noise Ratio for Plastic Scintillation Detectors Design and Performance Optimisation," *Medical Physics*, vol. 36, no. 11, pp. 5214–5220, 2009.

[255] F. Lacroix, *et al.*, "Simulation of the Precision Limits of Plastic Scintillation Detectors using Optimal Component Selection," *Medical Physics*, vol. 37, no. 2, pp. 412–418, 2010.

[256] Hamamatsu Photonics K. K., *Photomultiplier Tubes: Basics and Applications*. Hamamatsu Photonics K. K. Solid State Division: Japan, 2007.

[257] J. Orduna, & M. Prewitt, "Radiation Damage Studies and Operation of the DØ Luminosity Monitor," *Physics Procedia*, vol. 37, pp. 2047–2054, 2012.

[258] Hamamatsu Photonics K. K., *Opto-semiconductor Handbook*. Hamamatsu Photonics K. K. Solid State Division: Japan, 2014.

[259] L. W. Wang, *et al.*, "Monte Carlo Study of the Energy and Angular Dependence of the Response of Plastic Scintillation Detectors in Photon Beams," *Medical Physics*, vol. 37, no. 10, pp. 5279–5286, 2010.

[260] C. E. Andersen, *et al.*, "Fibre-coupled Radioluminescence Dosimetry with Saturated Al_2O_3:C Crystals: Characterisation in 6 and 18 MV Photon Beams," *Radiation Measurements*, vol. 46, pp. 1090–1098, 2011.

[261] J. Lambert, *et al.*, "A Plastic Scintillation Dosimeter for High Dose Rate Brachytherapy," *Physics in Medicine and Biology*, vol. 51, pp. 5505–5516, 2006.

[262] R. H. Mitchell, *et al.*, "A Powder Neutron Diffraction Study of the Crystal Structure of the fluoroperovskite $NaMgF_3$ (neighbourite) from 300 to 3.6 K," *Physics and Chemistry of Minerals*, vol. 34, no. 10, pp. 705–712, 2007.

[263] A. Rečnik, "Twins in Barium Titanate," *Acta Chimica Slovenica*, vol. 48, pp. 1–50, 2001.

[264] S. Lizzo, *et al.*, "On the Luminescence of Divalent Ytterbium in $KMgF_3$ and $NaMgF_3$," *Journal of Physics and Chemistry of Solids*, vol. 56, no. 7, pp. 959–964, 1995.

[265] N. Kristianpoller, & B. Trieman, "Irradiation Effects in Perovskite-type Fluorides," *Radiation Effects*, vol. 72, pp. 201–208, 1983.

[266] S. N. Bodrug, & V. A. Timoshenkov, "Absorption Spectrum of $KMgF_3$:Sm^{2+} and $NaMgF_3$:Sm^{2+} Single Crystals in the Excited State," *Translated from Zhurnal Prikladnoi Spektroskopii (Journal of Applied Spectroscopy)*, vol. 12, no. 1, pp. 117–120, 1970.

[267] J. C. Gácon, & A. Gros, "New Measurements of the Emission Spectra of Sm^{2+} in $KMgF_3$ and $NaMgF_3$ Crystals," *Journal of Physics and Chemistry of Solids*, vol. 42, pp. 587–593, 1981.

[268] N. Kristianpoller, & B. Trieman, "X-ray Induced Luminescence of Rare-earth Doped Fluoroperovskite Crystal," *Journal of Luminescence*, vol. 24/25, pp. 285–288, 1981.

[269] S. Lizzo, *et al.*, "Luminescence of Cu^+ in some Fluoride Perovskites," *Chemical Physics Letters*, vol. 253, pp. 108–112, 1996.

[270] N. J. M. Le Masson, *et al.*, "Optically and Thermally Stimulated Luminescence of $KMgF_3$:Ce^{3+} and $NaMgF_3$:Ce^{3+}," *Radiation Protection Dosimetry*, vol. 100, no. 1-4, pp. 229–234, 2002.

[271] N. J. M. Le Masson, *et al.*, "Ce^{3+} and Pr^{3+} $5d$ Energy Levels in the (Pseudo) Perovskites $KMgF_3$ and $NaMgF_3$," *Journal of Luminescence*, vol. 101, pp. 175–183, 2003.

[272] M. L. Reynolds, & G. F. J. Garlick, "The Infrared Emission of Nickel Ion Impurity Centres in Various Solids," *Infrared Physics*, vol. 7, pp. 151–167, 1967.

[273] E. van der Kolk, *et al.*, "Luminescence Excitation Study of the Higher energy States or Pr^{3+} and Mn^{2+} in $SrAlF_5$, $CaAlF_5$, and $NaMgF_3$," *Journal of Applied Physics*, vol. 95, no. 12, pp. 7867–7872, 2004.

[274] M. O'Keeffe, & J. O. Bovin, "Solid Electrolyte Behaviour of $NaMgF_3$: Geophysical Implications," *Science*, vol. 206, pp. 599–600, 1979.

[275] Sigma-Aldrich, *Material Safety Data Sheet: Magnesium(II) Fluoride*, 2013.

[276] B. P. Sobolev, *The Rare Earth Trifluorides - Part 1: The High Temperature Chemistry of the Rare Earth Trifluorides*. Institut d'Estudis Catalans, Barcelona: Spain, 2000.

[277] Best Theratronics, *Gammacell 1000 Elite / 3000 Elan*, 2013.

[278] G. H. Stout & L. H. Jensen, *X-ray Structure Determination*. Wiley Interscience: USA, Second ed., 1989.

[279] L, V, Azároff, & M. J. Buerger, *The Powder Method in X-ray Crystallography*. McGraw-Hill Book Company, New York: USA, 1958.

[280] A. R. Chakhmouradian, *et al.*, "The Crystal Chemistry of Synthetic Potassium Bearing neighbourite $(Na_{1-x}K_x)MgF_3$," *Physics and Chemistry of Minerals*, vol. 28, pp. 277–284, 2001.

[281] V. A. Zabolotnyi, "Methods of Determining Unit Cell Parameters from Powder Patterns (Review)," *Zhurnai Strukturnoi Khimii*, vol. 33, no. 5, pp. 116–136, 1991.

[282] P. E. Werner, *et al.*, "TREOR, a Semi-exhaustive Trial and Error Powder Indexing Program for all Symmetries," *Journal of Applied Crystallography*, vol. 18, pp. 367–370, 1985.

[283] T. J. H. Holland, & S. A. T Redfern, "Unit Cell Refinement from Powder Diffraction Data: the use of Regression Diagnostics," *Mineralogical Magazine*, vol. 61, pp. 65–77, 1997.

[284] Hamamatsu Photonics Corporation, *Photomultiplier tubes R928, R955*, 1997.

[285] Horiba Scientific, *Fluorolog-3: How to Build a Spectrofluorometer*, 2011.

[286] J. R. Lacowicz, *Principles of Fluorescence Spectroscopy*. Springer Science, New York: USA, Third ed., 2006.

[287] Shimadzu Corporation, *Instruction Manual: UV-2100 UV-VIS Recording Spectrophotometer*, 1996.

[288] J. W. Quilty, *et al.*, "Thermoluminescence Apparatus using PT100 Resistors as the Heating and Sensing Elements," *Review of Scientific Instruments*, vol. 78, pp. 083905:1–6, 2007.

[289] Fisher Scientific, *Material Safety Data Sheet: Silicone Oil*, 2009.

[290] Ocean Optics, *USB2000+ Fibre Optic Spectrometer: Installation and Operation Manual*, 2010.

[291] Sony Corporation, *ILX511B: 2048-pixel CCD Linear Sensor (B/W) for Single 5V Power Supply Barcode Reader*, 2003.

[292] Toshiba Corporation, *TCD1304AP: Toshiba CCD Linear Image Sensor*, 2001.

[293] H. Oliver, & H. Moseley, "The use of Diode Array Spectroradiometers for Dosimetry in Phototherapy," *Physics in Medicine and Biology*, vol. 47, no. 23, pp. 4411–4421, 2002.

[294] G. Kitis, *et al.*, "Thermoluminescence glow-curve deconvolution functions for first, second and general orders of kinetics," *Journal of Physics D: Applied Physics*, vol. 31, pp. 2636–2641, 1998.

[295] M. McElfresh, "Fundamentals of Magnetism and Magnetic Measurements Featuring Quantum Design's Magnetic Property Measurement System," tech. rep., Quantum Design, Inc., 1994.

[296] P. Stamenov, & J. M. D. Coey, "Sample Size, Position, and Structure Effects on Magnetisation Measurements using Second-order Gradiometer Pickup Coils," *Review of Scientific Instruments*, vol. 77, pp. 015106:1–11, 2006.

[297] A. Zieba, "Image and Sample Geometry Effects in SQUID Magnetometers," *Review of Scientific Instruments*, vol. 64, pp. 3357–3375, 1993.

[298] Quantum Design, "MPMS Application Note 1014-204: Variation of magnetic Field over the Scan Length," tech. rep., Quantum Design, Inc., 1997.

[299] Quantum Design, "MPMS Application Note 1014-201: Sample Mounting Considerations," tech. rep., Quantum Design, Inc., 2000.

[300] M. Sawicki, *et al.*, "Sensitive SQUID Magnetometry for Studying Nanomagnetism," *Semiconductor Science and Technology*, vol. 26, pp. 064006:1–16, 2011.

[301] B. D. Cullity, & C. D. Graham, *Introduction to Magnetic Materials*. John Wiley & Sons Ltd, Sussex: England, 2nd ed., 2009.

[302] J. H. Van Vleck, *The Theory of Electric and Magnetic Susceptibilities*. Oxford University Press, Oxford: United Kingdom, 1932.

[303] K. K. Rao, *et al.*, "Preparation, Infrared and Magnetic Susceptibility Studies of LnB_3O_6 (Ln = Gc, Eu, and Sm)," *Journal of Magnetism and Magnetic Materials*, vol. 253, p. 2002, 2002.

[304] C. L. Seaman, *et al.*, "Magnetic and Superconducting Properties of the Electron Doped Compounds $Ln_{2-x}M_xCuO_{4-y}$ (Ln = Pr, Nd, Sm, Eu, Gd; M = Ce, Th)," *Physica C*, vol. 159, pp. 391–403, 1989.

[305] N. Uryu, "On the Paramagnetic Susceptibility of Sm^{3+} Ion," *Journal of the Physical Society of Japan*, vol. 15, no. 11, pp. 2041–2050, 1960.

[306] Varian Medical Systems, *TrueBeam High-Intensity Energy Configurations: Performance and Operational Characteristics*, 2012.

[307] Varian Medical Systems, *TrueBeam Technical Reference Guide - Volume 1: TrueBeam, TrueBeam STx, Edge Radiosurgery System*, 2013.

[308] P. Metcalfe, *et al.*, *The Physics of Radiotherapy X-Rays from Linear Accelerators.* Medical Physics Publishing, Madison, Wisconsin: USA, 2004.

[309] C. J. Karzmark, *et al.*, *Medical Electron Accelerators.* McGraw-Hill Book Company, New York: USA, 1993.

[310] Varian Medical Systems, *Clinac 2100C/D, 2300C/D, 21EX, 23EX Systems manual*, 1998.

[311] Varian Medical Systems, *Portal Vision Databook*, 2008.

[312] P. Castro, *et al.*, "Study of the Uncertainty in the Determination of Absorbed Dose to Water During External Beam Radiotherapy Calibration," *Journal of Applied Clinical Medical Physics*, vol. 9, no. 1, pp. 70–86, 2008.

[313] J. Laban, "Certificate of Calibration for a Radiation Dose-meter; s/n 3500," tech. rep., New Zealand National Radiation Laboratory, 2010.

[314] J. Perez-Calatayud, *et al.*, "Dose Calculation for Photon-emitting Brachytherapy Sources with Average Energy Higher than 50 keV: Full Report of the AAPM and ESTRO," tech. rep., American Association of Physicists in Medicine, 2012.

[315] M. F. Ashby, *Materials Selection in Mechanical Design.* Butterworth-Heinemann, Burlington: USA, Third ed., 2005.

[316] J. M. Cariou, *et al.*, "Refractive-index Variations with Temperature of PMMA and Polycarbonate," *Applied Optics*, vol. 25, no. 3, pp. 334–336, 1986.

[317] Mitsubishi International Corporation, *ESKA Premier Polyethylene Jacketed Optical Fibre Cord: GH4001*, 2010.

[318] RS Components, *PMMA Fibre Optics Datasheet*, 1998.

[319] PTW Freiburg GmbH, *Small Field Dosimetry: Application Guide*, 2012.

[320] W. C. Martin, *et al.*, *Atomic Energy Levels - The Rare-Earth Elements.* US Government Printing Office, Washington: USA, 1978.

[321] Schott Glasswerke, "Optical Glass Filters," 1988.

[322] V. Pischedda, *et al.*, "Single-crystal X-ray Diffraction Study on Neighbourite ($NaMgF_3$) from Gjerdingselva, Norway," *Neues Jahrbuch fr Mineralogie, Abhandlungen*, vol. 182, pp. 23–29, 2005.

[323] Y. Zhao, *et al.*, "High-pressure Crystal Chemistry of Neighbourite, $NaMgF_3$: An Angle-dispersive Diffraction Study using Monochromatic Synchrotron X-radiation," *Americal Mineralogist*, vol. 70, pp. 615–621, 1994.

[324] E. Sonder, & W. A. Sibley, "Radiation Equilibrium of F and M centres in KCl," *Physical Review*, vol. 129, no. 4, pp. 1578–1582, 1963.

[325] F. C. Brown, *The Physics of Solids.* W. A. Benjamin, Inc., 1967.

[326] K. Knox, "Structures of Chromium(III) Fluoride," *Acta Crystallography*, vol. 13, pp. 507–508, 1960.

[327] K. A. Gschneidner, *et al.*, *Handbook on the Physics and Chemistry of Rare Earths: Volume 33.* Elsevier Science, Amsterdam: The Netherlands, 2003.

[328] D. L. Perry, & S. L. Phillips, *Handbook of Inorganic Compounds.* CRC Press, Boca Raton, Florida: USA, First ed., 1995.

[329] O. Greis, *PhD Thesis (no copy obtained).* PhD thesis, University of Freiburg, Freiburg: Germany, 1976.

[330] B. M. Anghelov, "Energy Levels and Intensity Parameters of Dy^{3+} in $LiDyP_4O_{12}$," *Materials Letters*, vol. 9, no. 12, pp. 547–549, 1990.

[331] F. Faoro, *et al.*, "Energy Levels and Emission Parameters of the Dy^{3+} Ion Doped into the YPO_4 Host Lattice," *Journal of Physics: Condensed Matter*, vol. 21, pp. 275501:1–7, 2009.

[332] J. B. Gruber, *et al.*, "Energy Levels of Dy^{3+} ($4f^9$) in Ortho-aluminate Crystals," *Journal of Applied Physics*, vol. 9, no. 2, pp. 1030–1034, 2003.

[333] K. Lemański, & P. J. Dereń, "Spectroscopic Properties of Dy^{3+} Ions in $CaTiO_3$ Nano-perovskites," *Journal of Luminescence*, vol. 145, pp. 661–664, 2014.

[334] R. S. Rana, *et al.*, "Optical Spectra and Energy Level Analysis of Dy^{3+}:$LaCl_3$," *Journal of Chemical Physics*, vol. 88, pp. 2242–2248, 1988.

[335] V. Vidyadharan, *et al.*, "Spectroscopic and Photoluminescence Characterisation of Dy^{3+} in $Sr_{0.5}Ca_{0.5}TiO_3$ Phosphor," *Luminescence*, vol. 31, pp. 202–209, 2016.

[336] R. Chen, P. L. Leung, "The Decay of OSL Signals as Stretched-exponential Functions," *Radiation Measurements*, vol. 37, pp. 519–526, 2003.

[337] J. Blanusa, *et al.*, "Magnetic Properties of $Er_xY_{1-x}F_3$ Solid Solutions," *Solid State Communications*, vol. 133, no. 3, pp. 157–161, 2005.

[338] J. B. Gruber, *et al.*, "Modelling Optical Spectra and Van Vleck Paramagnetism in Er^{3+}:$YAlO_3$," *Journal of Applied Physics*, vol. 105, pp. 023112:1–13, 2009.

[339] C. Xueyuan, *et al.*, "Energy Levels and Optical Spectroscopy of Er^{3+} in Gd_2O_3 Nanocrystals," *Journal of Physical Chemistry*, vol. 111, pp. 10404–10411, 2007.

[340] Y. Du, *et al.*, "Single-Crystalline and Near-Monodispersed $NaMF_3$ (M = Mn, Co, Ni, Mg) and $LiMAlF_6$ (M = Ca, Sr) Nanocrystals from Cothermolysis of Multiple Trifluoroacetates in Solution," *Chemistry - An Asian Journal*, vol. 2, pp. 965–974, 2007.

[341] G. V. M. Williams, *et al.*, "Optically Re-writable Bragg Gratings in Mn^{2+}," *Journal of Materials Science: Materials in Electronics*, vol. 20, 2009.

[342] A. Ellens, *et al.*, "^{6}I Emission and Vibronic Transitions of Eu^{2+} in $KMgF_3$," *Journal of Luminescence*, vol. 59, pp. 293–301, 1994.

[343] G. Blasse, "Reminiscences of a Quenched Luminescence Investigatory," *Journal of Luminescence*, vol. 100, pp. 65–67, 2002.

[344] S. Janssens, *et al.*, "Synthesis and Characterisation of Rare Earth and Transition Metal Doped $BaMgF_4$ Nanoparticles," *Journal of Luminescence*, vol. 134, pp. 277–283, 2013.

[345] K. Lamański, *et al.*, "Spectroscopic Properties of Nd^{3+} Ions in Nano-perovskite $CaTiO_3$," *Journal of Solid State Chemistry*, vol. 184, pp. 2713–2718, 2011.

[346] I. P. Kondratyuk, *et al.*, "Neutron Diffraction Study on NdF_3," *Soviet Physics, Crystallography*, vol. 33, p. 57, 1988.

[347] H. T. Takeshita, *et al.*, "Disproportionation of $CaNi_3$ hydride: Formation of New Hydride, $CaNiH_3$," *Journal of Alloys and Compounds*, vol. 333, pp. 266–273, 2002.

[348] R. Alcala, *et al.*, "Photoluminescence of Ni^{2+} ions in $RbCdF_3$ and $RbCaF_3$," *Journal of Luminescence*, vol. 48/49, pp. 569–273, 1981.

[349] P. S. May, & H. U. Güdel, "A Previously Unobserved Luminescence of Ni^{2+} in Ni^{2+}:$KMgF_3$ and Ni^{2+}:$KZnF_3$," *Chemical Physics Letters*, vol. 175, no. 5, pp. 488–492, 1990.

[350] W. E. Vehse, *et al.*, "Ni^{2+} Emission in MgO, $KMgF_3$, $KZnF_3$, and MgF_2," *Journal of Luminescence*, vol. 10, pp. 149–162, 1975.

[351] M. J. Weber, & R. R. Monchamp, "Luminescence of $Bi_4Ge_3O_{12}$: Spectral and Decay Properties," *Journal of Applied Physics*, vol. 44, no. 12, pp. 5495–5499, 1973.

[352] O. Greis, *et al.*, "Structural Data of the Tysonite-type Superstructure Modification β-PrF_3 from X-ray Powder and Electron Single-crystal Diffraction," *Powder Diffraction*, vol. 10, no. 1, pp. 44–46, 1995.

[353] V. Naresh, & B. S. Ham, "Influence of Multiphonon and Cross Relaxations on $^3P_0$ and $^1D_2$ Emission Levels of Pr^{3+} Doped Borosilicate Glasses for Broad Band Signal Amplification," *Journal of Alloys and Compounds*, vol. 64, pp. 321–330, 2016.

[354] M. R. N. Soares, *et al.*, "Red and Infrared Luminescence from Tetragonal YSZ:Pr^{3+} Single Crystal Fibres Grown by LFZ," *Optical Materials*, vol. 24, pp. 27–29, 2011.

[355] A. Stanulis, *et al.*, "Photoluminescence of Pr^{3+}-doped Calcium and Strontium Stannates," *Journal of Luminescence*, vol. 172, pp. 323–330, 2016.

[356] G. J. Goldsmith, & H. L. Pinch, "Divalent Rare-Earth Ions in Optical Maser Materials," tech. rep., Radio Corporation of America, 1965.

[357] R. B. Hughes-Currie, *Free-Electron Laser and Synchrotron Spectroscopy of Fundamental Excitations in Ytterbium-Doped Fluoride Lattices*. PhD thesis, University of Canterbury, Christchurch: New Zealand, 2015.

[358] C. W. Thiel, *Energies of Rare-Earth Ion States Relative to Host Bands in Optical Materials from Electron Photoemission Spectroscopy*. PhD thesis, Montana State University, Montana: USA, 2003.

[359] W. Zhang, *et al.*, "Site-selective Fluorescence Excitation Spectroscopy of a $KMgF_3$:Sm^{2+} Crystal," *Journal of Alloys and Compounds*, vol. 374, pp. 32–35, 2004.

[360] A. Edgar, *et al.*, "High-resolution X-ray Imaging with Samarium-doped Fluoroaluminate and Fluorophosphate Glass," *Journal of Non-crystalline Solids*, vol. 377, pp. 124–128, 2013.

[361] Y. Liu, *et al.*, "Reddish-orange-emitting and Paramagnetic Properties of $GdVO_4$:Sm^{3+}/Eu^{3+} Multifunctional Nano-materials," *New Journal of Chemistry*, vol. 39, pp. 8282–8290, 2015.

[362] M. Shivaram, *et al*, "Synthesis and Luminescence Properties of Sm^{3+} Doped $CaTiO_3$ Nano-phosphor for Application in White LED Under NUV Excitation," *Spectrochemica Acta Part A: Molecular and Biomolecular Spectroscopy*, vol. 128, pp. 891–901, 2014.

[363] K. Mansikka, & S. Mikkola, "Diamagnetic Susceptibility for some Ionic Solids," *Journal of Physics C: Solid State Physics*, vol. 7, pp. 3737–3742, 1974.

[364] M. Grinberg, & S. Mahlik, "Impurity-trapped Excitons: Experimental Evidence and Theoretical Concept," *Journal of Non-crystalline Solids*, vol. 354, pp. 4163–4169, 2008.

[365] P. Dorenbos, "Energy of the First $4f^7 \rightarrow 4f^6$5d Transition of Eu^{2+} in Inorganic Compounds," *Journal of Luminescence*, vol. 104, 2003.

[366] Z. Barandia'an & L. Seijo, "Intervalence Charge Transfer Luminescence: Interplay Between Anomalous and $5d-4f$ emissions in Yb-doped Fluorite-type Crystals," *Journal of Chemical Physics*, vol. 141, pp. 234704:1–21, 2014.

[367] R. B. Hughes-Currie, *et al.*, "The Determination of Dopant Ion Valence Distributions in Insulating Crystals Using XANES Measurements," *Journal of Physics: Condensed Matter*, vol. 28, no. 13, pp. 135502:1–4, 2016.

[368] N. N. Greenwood, *Ionic Crystals, Lattice Defects, and Non-stoichiometry*. Chemical Publishing Company, Inc. New York: USA, 1970.

[369] Hamamatsu Photonics Corporation, *Hamamatsu Current Output Type Photo-sensor Modules: H5773/H5783/H6779/H6780 Series*, 2012.

[370] S. Wasserman, *et al.*, "Transmission and Mechanical Properties of Optical Adhesives," *Journal of Adhesion*, vol. 27, pp. 67–81, 1989.

[371] H. Mikuni, "Three Bond Technical News: Instant Adhesives (Cyanoacrylate Adhesives)," tech. rep., Three Bond Co., Ltd., 1991.

[372] Industrial Fibre Optics, Inc., *Plastic Fibre Couplers (Splitters)*, 2013.

[373] Thorlabs, *0.37 NA Hard Polymer Clad Multi-mode Fibre*, 2013.

[374] OWIS GmbH, *Motorised Filter Wheels: FRM 40*, 2011.

[375] Hamamatsu Photonics Corporation, *Hamamatsu Current Output Type Photo-sensor Modules: H10720/H10721 Series*, 2013.

[376] Hamamatsu Photonics Corporation, *Ceramic Package Photodiodes with Low Dark Current: S1087/S1133 Series*, 2013.

[377] Hamamatsu Photonics Corporation, *InGaAs PIN Photodiode with Photosensitive Area from 0.3 mm to 5 mm diameter: G12180 Series*, 2014.

[378] P. Horowitz, & H Winfield, *The Art of Electronics*. Cambridge University Press, Cambridge: England, 1989.

[379] B. E. A. Saleh, & M. C. Teich, *Fundamentals of Photonics*. John Wiley & Sons Ltd, Sussex: England, 1991.

[380] OWIS GmbH, *Precision Linear Stages: LTM 60P*, 2013.

[381] S. W. S. McKeever, *et al.*, "Pulsed Optically Stimulated Luminescence Dosimetry Using α-Al_2O_3:C," *Radiation Protection Dosimetry*, vol. 65, no. 1-4, pp. 267–272, 1996.

[382] E. Bulur, "An Alternative Technique for Optically Stimulated Luminescence (OSL) Experiment," *Radiation Measurements*, vol. 26, no. 5, pp. 701–109, 1996.

[383] E. Yorke, *et al.*, "AAPM TG-62: Diode *in vivo* Dosimetry for Patients Receiving External Beam Radiation Therapy," tech. rep., American Association of Physicists in Medicine, 2005.

[384] F. Guarion, *et al.*, "Compilation of Radiation Damage Test Data - Part IV: Adhesives for use in Radiation Areas," tech. rep., CERN: European Organisation for Nuclear Research, 2001.

[385] S. O'Keeffe, & E. Lewis, "Polymer Optical Fibre for *in situ* Monitoring of Gamma Radiation Processes," *International Journal on SMart Sensing and Intelligent Systems*, vol. 2, no. 3, pp. 490–502, 2009.

[386] L. Torrisi, "Ion Irradiation of Polymethyl methacrylate," *Radiation Effects & Defects in Solids*, vol. 145, pp. 285–296, 1998.

[387] B. W. Yates, & D. M. Shinozaki, "Radiation Degradation of Poly(methyl Methacrylate) in the Soft X-ray Region," *Journal of Polymer Science B*, vol. 31, no. 12, pp. 1779–1784, 1993.

[388] H. Yoshida, & T. Ichikawa, "Temperature Effect on the Radiation Degradation of Poly(methyl Methacrylate)," *Radiation Physics and Chemistry*, vol. 46, no. 4-6, pp. 921–924, 1995.

[389] C. Yan, *et al.*, "Radiation Damage to Polymer Optical Fibres," in 5^{th} *Australian Congress on Applied Mechanics*, 2007.

[390] Mitsubishi International Corporation, *ESKA Plastic Fibre Optic (GH4001): Influence of Radiation*, 2010.

[391] M. Stovall, *et al.*, "AAPM TG-36: Fetal Dose from Radiotherapy with Photon Beams," *Medical Physics*, vol. 22, no. 1, pp. 63–82, 1995.

[392] N. Chofor, *et al.*, "Non-reference Condition Correction Factor k_{NR} of Typical Radiation Detectors Applied for the Dosimetry of High-energy Photon Fields in Radiotherapy," *Zeitschrift fur Medizinische Physik*, vol. 16, pp. 5141–5153, 2012.

[393] S. B. Scarboro, *et al.*, "Variations in Photon Energy Spectra of a 6 MV Beam and their Impact on TLD Response," *Medical Physics*, vol. 39, no. 5, pp. 2619–2628, 2011.

[394] A. S. Beddar, "Correspondence: On Possible Temperature Dependence of Plastic Scintillator Response," *Medical Physics*, vol. 39, no. 10, p. 6522, 2012.

[395] L. Wootoon, & S. Beddar, "Temperature Dependence of BCF Plastic Scintillation Detectors," *Physics in Medicine and Biology*, vol. 58, pp. 2955–2967, 2013.

[396] S. Agostinelli, *et al.*, "Response to High-energy Photons of PTW31014 PinPoint Ion Chamber with a Central Aluminium Electrode," *Medical Physics*, vol. 35, no. 7, pp. 3293–3301, 2008.

[397] R. J. W. Louwe, *et al.*, "Time-resolved Dosimetry Using a PinPoint Ionisation Chamber as Quality Assurance for IMRT and VMAT," *Medical Physics*, vol. 42, no. 4, pp. 1625–1639, 2015.

[398] J. L. M. Venselaar, *et al.*, "A Consistent Formalism for the Application of Phantom and Collimator Scatter Factors," *Physics in Medicine and Biology*, vol. 44, pp. 365–381, 1999.

[399] E. S. M. Ali, & D. W. O Rogers, "Report CLRP11-01: Validation of a New Spectral Functional Form," tech. rep., Ottawa Medical Physics Institute, 2011.

[400] E. S. M. Ali & D. W. O. Rogers, "Functional Forms for Photon Spectra of Clinical Linacs," *Physics in Medicine and Biology*, vol. 57, pp. 31–50, 2012.